3-D Thermal Modelling Of Power Device Packaging

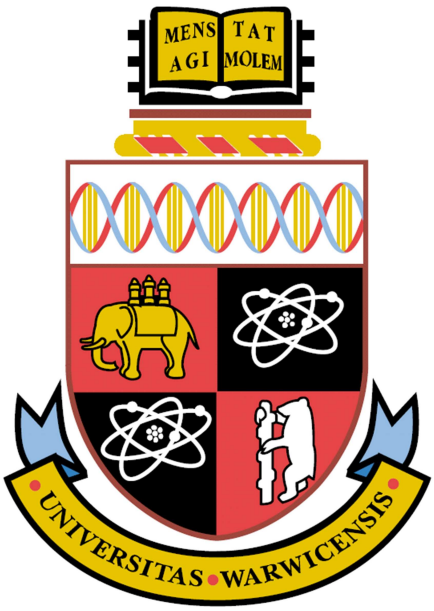

Ian Swan

School of Engineering

University of Warwick

Dissertation submitted for the degree of

Doctor of Philosophy

September 2010

Declaration

The author wishes to declare that apart from commonly understood and accepted ideas, or where reference is made to the work of others, the work in this thesis is his own. It has not been submitted in part, or in whole, to any other university for a degree, diploma or other qualification. The work presented in chapters 5, 6 and 7 have been published by the author.

I. R. Swan
School of Engineering
University of Warwick
September 2010

Acknowledgements

Firstly, I would like to acknowledge my Ph.D supervisor Professor Phil Mawby, who has shown faith in me throughout the course of the Ph.D program. I have thoroughly enjoyed my time as his Ph.D student and gained valuable experience. My Ph.D has played a key role in my personal development. Thank you Professor Mawby, for making this Ph.D possible.

I am greatly indebted to Dr. Angus Bryant for his contributions to all aspects of my work on this thesis. I feel honoured to have had mentorship from such a capable academic. Angus' advice has been invaluable during the completion of this thesis. Thank you Angus.

I would like to thank T. Ueta, T. Nisijima and K. Hamada of the Toyota motor corporation for their kind assistance in this work. I also wish to express my gratitude to Dr. Mike Jennings, Dr. Dean Hamilton and Dr. Nii Parker-Allotey for all their help and guidance. Further thanks go to all my colleagues at the University of Warwick. Particularly, to all members of the PEATER group, who have helped make the A205 laboratory a friendly and enjoyable place to work.

Beyond engineering, I would like to mention the University of Warwick rugby union club. This club has afforded me many fond memories and I believe it has given me a rounded University experience.

The final words must go to my father, who has supported me throughout all my studies at University. I hope my work will make him proud.

"*It's not that I'm so smart, it's just that I stay with problems longer.*"

Albert Einstein

Abstract

Power converters enable efficient conversion of electric power, thereby reducing power consumption and cost. The key enabling technologies inside power converters, typically used in hybrid electric vehicles, are the semiconductor devices. Device reliability is of high priority because they generate heat from the dissipation of electric power which can lead to failure if the device maximum junction temperature is exceeded. Furthermore, device temperatures can vary largely in switching applications, leading to thermal-mechanical fatigue failure. As electronic designers are pushed to deliver smaller and more powerful packages, they are finding thermal issues increasingly difficult to solve. The primary goal of this thesis is to develop a fast and accurate thermal simulation design tool which is capable of simulating realistic power converter operation.

Most commercial thermal simulators use finite-element software. Despite their perceived accuracy, they suffer from severe computational requirements and offer limited ability to explore power converter packaging converter designs during realistic converter operation. Traditional approaches using R-C networks as thermal equivalent circuits are of little use as a design tool since for every geometrical layout of the packaging structure which is tested, the designer must return to the starting point which is either a time-consuming FE simulation or a practical experiment.

The Fourier thermal model presented in this thesis is a purely conductive model requiring no parameter extraction or use of a FE simulator. The starting point for the Fourier model is the heat equation. The Fourier thermal model yields solutions to the heat equation by carrying out spatial discretisation using a truncated Fourier series and using MATLAB/Simulink to perform temporal discretisation using a dynamic ODE solver.

Validation using the finite volume thermal simulator FLOTHERM showed that the transient Fourier model could accurately simulate 3-D heat conduction through a wide range of power converter packaging structures. The Fourier thermal model is an excellent early stage design tool because its simulation speed is far superior to FLOTHERM, even though both models operate with a similar accuracy.

The use of MATLAB/Simulink as the simulation environment enabled the Fourier thermal model to operate within the framework of an electro-thermal simulator and therefore simulate realistic load conditions. This is major advantage over existing approaches which fail to simulate electro-thermal interaction. Experimental validation of the fast electro-thermal converter simulator was achieved by utilising an inverter back-to-back rig and recording transient device temperatures using an infrared camera. The similarity between the experimental and simulated results indicated that the Fourier thermal model was sufficiently accurate. The electro-thermal simulator operated at a simulation speed which was ten times real time, which is extremely fast compared to existing approaches which can take up to two days to simulate a 60 second drive cycle. 'Ten times real time' represents a significant step forward for power converter packaging design.

In the future device reliability can be accurately predicted if the electro-thermal simulator model is combined with a reliability model. The potential of the Fourier thermal model to aid numerical optimisation of the whole power converter is exciting.

Contents

List of Figures

List of Tables

Glossary

AC	Alternating current
ARTEMIS	Advanced Research and Technology for EMbedded Intelligence & Systems
BEM	Boundary Element method
CPU	Central processing unit
CTE	Coefficient of thermal expansion
CTM	Compact thermal model
DC	Direct current
DCTM	Detailed compact thermal model
DELPHI	Development of physical models for an integrated design environment
FDM	Finite Difference Method
FE	Finite element
FEM	Finite Element Method
FFT	Fast Fourier transform
FLIR	Forward looking infrared
FUDS	Federal Urban Driving Schedule
FVM	Finite Volume Method
HEV	Hybrid Electric Vehicle
IGBT	Insulated Gate Bipolar Transistor
LESIT	Leistungelektronik; Systemtechnik, Informationstechnologie
MG	Motor-generator
MMC	Metal Matrix Composite
MOR	Model-Order Reduction
MTBF	Mean time before failure(Hours)
ODE	Ordinary differential equation
PDE	Partial differential equation
PWM	Pulse width modulation
RC	Resistor-Capacitor
STPWM	Sine-triangle pulse width modulation
SVD	Single value decomposition
VVVF	Variable voltage, variable frequency

Nomenclature

A	Area normal to the n-direction (m^2)
A_1	Symbol linking the ordinary differential equations to Fig. 5.5
A_{11}	Area of a small surface (m^2)
A_i	Pre-exponential coefficient (KW^{-1})
B	Constant in equation proposed by the LESIT project
C	Thermal capacitance ($Jm^{-3}K^{-1}$)
CC	Constant in the separation of variables solution
c_p	Specific heat capacity ($JKg^{-1}K^{-1}$)
D	Constant in the separation of variables solution
dn	Change in distance along the n-direction
dx	Change in distance along the x-direction
dy	Change in distance along the y-direction
dz	Change in distance along the z-direction
E	Constant in the separation of variables solution
E_{off}	Off-state energy losses (J)
E_{on}	On-state energy losses (J)
$E_{sw(off)}$	Turn off energy losses during a switching cycle (J)
$E_{sw(on)}$	Turn on energy losses during a switching cycle (J)
E_{total}	Total energy loss during a switching cycle (J)
f_{sw}	Switching frequency (Hz)
F	System matrix
$\hat{F}$	System matrix post reduction
G	Load vector
$\hat{G}$	Load vector post reduction
G_1	Symbol linking the ordinary differential equations to Fig. 5.5
h	Heat transfer coefficient(WK^{-1})
H	Output matrix
$\hat{H}$	Output matrix post reduction
H_1	Symbol linking the ordinary differential equations to Fig. 5.5

I	Number of Fourier terms in x direction in block 1 of Fig. 6.6 and Fig. 6.11
I_F	Current during forward bias (on-state)
I_{LOAD}	Load current
$\mathrm{I_{rms}}$	root mean squared current (A)
I_{TEST}	Test current
J	Total number of Fourier terms in the y direction in block 1 of Fig. 6.11
k	Thermal conductivity ($\mathrm{Wm^{-1}K^{-1}}$)
k	Fourier coefficient in the z direction
K	Total number of Fourier terms in the z direction
L	Inductance (H)
l	Length of a rod
M	Total number of Fourier terms in the x direction
m	Fourier coefficient in the x direction
N	Total number of Fourier terms in the y direction
n	Fourier coefficient in the y direction
n	Real integers
N_f	The number of cycles to failure
P_{cond}	Conduction power losses
P_{switch}	Switching power losses (W)
P_{total}	Total power losses (W)
P	Power loss (W)
Q	Heat energy (J)
q_{12}	Net heat exchange by radiation between two surfaces (W)
Q_{act}	The activation energy per mole ($7.8\mathrm{x}10^4\mathrm{Jmol^{-1}}$)
q_c	Device heat dissipation (W)
q''_{s}	Surface heat flux (W)
$\dot{Q}_n$	Rate of heat flow in the n-direction (W)
Q_{net}	Net heat energy (J)
r	Number of ordinary differential equations post reduction
R	Thermal resistance ($\mathrm{KW^{-1}}$)
R_1	Molar gas constant (8.314 $\mathrm{Jmol^{-1}K^{-1}}$)
R_{bi-bo}	Thermal resistance between the bottom inner and bottom outer ($\mathrm{KW^{-1}}$)
R_{bo-s}	Thermal resistance between the bottom outer and side ($\mathrm{KW^{-1}}$)
R_{j-amb}	Thermal resistance between the junction and ambient temperature ($\mathrm{KW^{-1}}$)
R_{j-b}	Thermal resistance between the junction and bottom ($\mathrm{KW^{-1}}$)
R_{j-bi}	Thermal resistance between the junction and bottom inner ($\mathrm{KW^{-1}}$)
R_{j-bo}	Thermal resistance between the junction and bottom outer ($\mathrm{KW^{-1}}$)
R_{j-s}	Thermal resistance between the junction and side ($\mathrm{KW^{-1}}$)
R_{j-t}	Thermal resistance between the junction and top ($\mathrm{KW^{-1}}$)
R_{j-ti}	Thermal resistance between the junction and top inner ($\mathrm{KW^{-1}}$)

R_{j-to}	Thermal resistance between the junction and top outer (KW^{-1})
$R_{th(j-c)}$	Thermal resistance from junction to case (KW^{-1})
R_{ti-to}	Thermal resistance between the top inner and top outer (KW^{-1})
R_{to-s}	Thermal resistance between the top outer and side (KW^{-1})
t	Time (s)
t_{on}	Time taken to turn on (s)
Δt	Time of a thermal cycle (s)
Δt_{on}	Time spent in on-state (s)
Δt_{off}	Time spent in off-state (s)
T	Temperature (K)
$\dot{T}(t)$	Vector of unknown temperatures at nodes differentiation with respect to time
$\bar{T}(t)$	Vector of Fourier series termss
T_1	Absolute temperature of a small surface (K)
T_2	Absolute temperature a large surface (K)
T_{amb}	Ambient device temperature (K)
$T_{amb}(t)$	Ambient temperature (K)
t_{off}	Time taken to turn off (s)
T_{A+}	Upper insulated gate bipolar transistor in phase-leg A
T_{A-}	Lower insulated gate bipolar transistor in phase-leg A
T_{B+}	Upper insulated gate bipolar transistor in phase-leg B
T_{B-}	Lower insulated gate bipolar transistor in phase-leg B
T_{C+}	Upper insulated gate bipolar transistor in phase-leg C
T_{C-}	Lower insulated gate bipolar transistor in phase-leg C
T_j	Device junction temperature (°C)
T_{jmax}	Maximum device junction temperature (°C)
T_m	The mean temperature (°C)
T_∞	The fluid temperature away from the surface (K)
T_s	Absolute surface temperature (K)
ΔT	Peak to peak temperature (°C)
U	Internal energy (J)
$u(t)$	Input function
$\mathrm{V_{A\_control}}$	Sinusoidal voltage control signal A (V)
$\mathrm{V_{B\_control}}$	Sinusoidal voltage control signal B (V)
$\mathrm{V_{C\_control}}$	Sinusoidal voltage control signal C (V)
$\mathrm{V_{control}}$	Sinusoidal voltage control signal (V)
V_{DC}	DC line supply voltage (V)
V_F	Voltage during forward bias (on-state)
V_{LOAD}	Load voltage
$\mathrm{V_{rms}}$	root mean squared voltage (V)
$\mathrm{V_{tri}}$	Triangular switching voltage signal (V)

x	Space variable
X	A function of the space variable x
$y(t)$	Output function
$Z_{th(j-amb)}(t)$	Transient thermal impedance junction-ambient (KW^{-1})
$Z_{th(j-c)}(t)$	Transient thermal impedance from junction to case (KW^{-1})

Al	Aluminium
AlN	Aluminium nitride
AlO	Alumina
Al_2O_3	Aluminium oxide
AlSiC	Aluminum Silicon Carbide
Be	Beryllium
BeO	Beryllium oxide
Cu	Copper
CuMo	Copper molybdenum
Si	Silicon

α	Thermal diffusivity (m^2s^{-1})
β	Constant in the equation proposed by the LESIT project
ε	Emissivity
ε_1	Emissivity of a small surface
λ	Eigenvalue
ρ	Density (kgm^{-3})
ρ_1	Duty ratio
σ	Stefan-Boltzmann constant ($5.6703x10^{-8}$ ($Wm^{-2}K^{-4}$)
τ_i	Time constant

Chapter

1 Introduction

1.1 Background

Global consumption of electricity is projected to double in the next twenty years [1]. By that time, it is anticipated that nearly all electrical energy will be processed through power electronics converters [2]. Power converters enable electrical energy to be used more efficiently and flexibly, thereby reducing power consumption and cost. Within the power converters, semiconductor devices provide the means for the control and conversion of electric power by modifying voltage, current or frequency.

The Insulated Gate Bipolar Transistor (IGBT), first demonstrated by Baliga in 1979 [3], has become the power semiconductor device of choice for use in medium to high power applications. The rise in demand of consumer electronics, in addition to the increasing importance of environmental issues has forced people to take note of the IGBT power converter market. Many of its key applications are driven by energy conservation, namely renewable energy generation and automotive traction control. The Hybrid Electric Vehicle (HEV) power converter market stood at £200M in 2009 and is expected to grow strongly

at a growth rate as high as 30% until 2020 [4]. The associated need for size and cost reduction and automotive reliability has prompted research into novel device materials, structures, circuit topologies and thermal modelling.

Problems associated with the thermal dissipation and heat transfer through power converters is one of the most urgent issues that requires significant attention in order to produce efficient and reliable packaging solutions. During operation, the power devices contained in power converters never achieve 100% efficiency due to conduction and switching power losses. Conduction losses occur while the devices are on and conducting current. Switching losses represent the power dissipated during the turn-on and turn-off switching transitions. In a typical IGBT-based motor drive, 2-10% of the controlled power is dissipated as heat within the device [5]. The heat generated as a result of these losses must be conducted away from the power devices and into the environment using a heatsink. If an appropriate thermal system is not used elevated temperatures can adversely affect electronic device operation, power-handling capability, achievable packing density and, crucially, reliability.

1.1.1 Thermal Simulation

The US Air Force examined the causes for failure in electronic equipment in an investigation called the "US Air Force Avionics/Electronics Integrity Program". The investigation showed that more than 55% of the electronic failures were caused by heat [6].

Thermal simulation is necessary as a design tool in order to predict the temperature of power devices. The transient temperature changes can be used to predict the reliability. For the power semiconductor devices used in power converters there are typically two main stages in reliability estimation: 1) transient simulation of the device temperature,

and 2) estimation of the damage accumulation due to thermo-mechanical stress cycling in the device packaging. Device thermal models are essential to aid early stage design feasibility studies which can narrow the spectrum of possible design choices. Through accurate thermal simulation, it is possible to test new concepts immediately without the need to order and implement new systems which can be time-consuming and expensive. Thermal simulation can reveal information about the operating conditions which lead to failure. Critical operating temperatures prior to failure can be reproduced which makes it relatively easy to identify problematic designs. Thermal modelling is not necessarily a stand alone process, however. Thermal models can be used as part of total system optimisation if they are linked with other electrical or mechanical models in order to simulate realistic transient conditions.

It must be noted that thermal simulations often rely on assumptions and so it is up to the experience and knowledge of the design engineer to verify the usefulness and accuracy of the result. In summary, thermal simulations can reduce development time and cost by predicting and designing out the various failure modes associated with power module thermo-mechanical stresses.

1.1.2 Power Module Packaging Design Challenges

Power module technology has evolved through multiple generations each with incremental improvements. The development trends for power modules have been focused on increasing current and voltage levels to reduce the number of devices needed, increasing operational temperature to reduce the demands on the cooling system, enhancing reliability and reducing losses, as well as reducing size, weight and cost [7]. Fig. 1.1 demonstrates these trends in converter design.

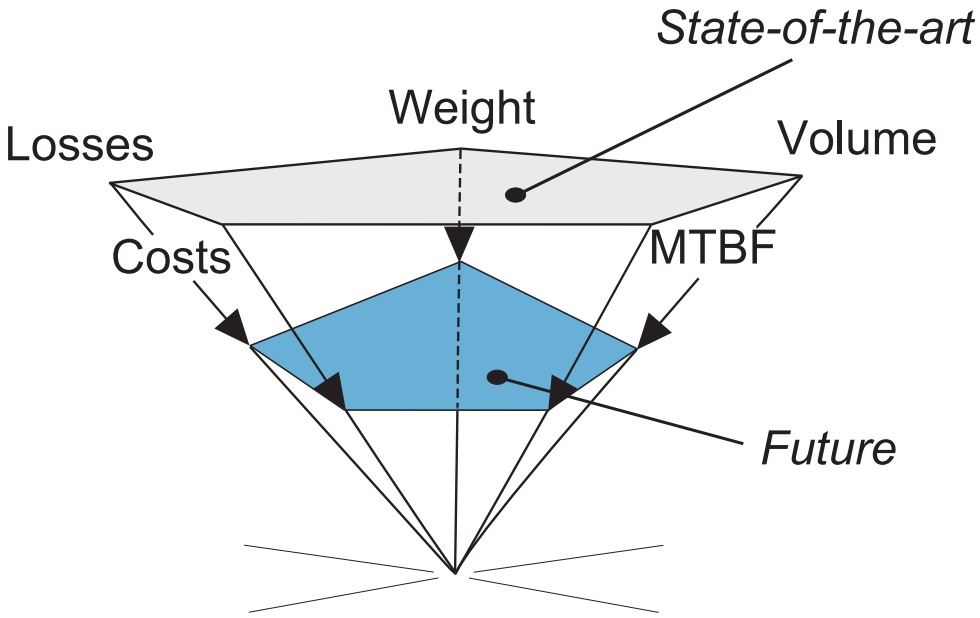

Figure 1.1: Diagram showing the development trends in power converters [8]. MTBF stands for mean time before failure.

Designers are driven to deliver increasingly efficient power modules to ensure a good utilisation of the energy resources and a low operating cost. The trend of operating losses in various power devices appears in Fig. 1.2. It can be seen from this figure that the losses are currently heading down towards 10% based on new materials.

Cost is an issue which permeates the whole of power electronics; this includes the cost of assembly as well as the cost of the materials. Power electronic modules today represent about 20% of the materials costs of hybrid vehicles, so cost is given great consideration by all the vehicle manufacturers [4].

Designers select packaging materials with high thermal conductivity, to transfer heat from the small surface area of the device to the larger surface area of the heat spreader and heatsink. It is vital for the functionality of a device that its device maximum operating temperature is not exceeded. The maximum allowed junction temperature for silicon

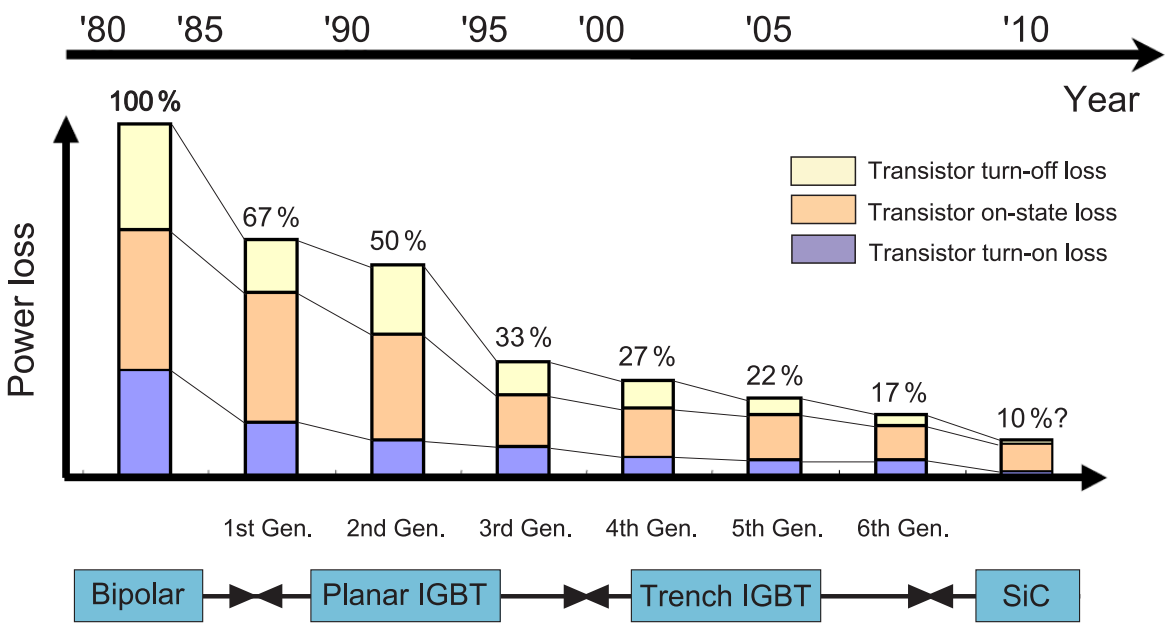

Figure 1.2: Bar chart showing the trends of operating losses of various devices [9].

IGBTs is 175°C or even 200°C for hybrid vehicle applications; however, because reliability is reduced by high temperature cycling, the operating temperatures are limited to below 150°C [10].

In addition to allowing effective heat removal from the power devices, the power module packaging must also electrically insulate the devices. It is challenging for a designer to find materials which achieve both simultaneously. Electrical insulation is essential to ensure the safe operation of the power module. The combination of different materials used in the package must also be mechanically compatible. A critical consideration in the packaging of devices is whether the bond between different materials can sustain the thermomechanical stresses it endures during its service life. The location of semiconductor devices within a power module should be optimal from a thermal management viewpoint,

although this then affects the electrical characteristics of the module.

A reduction in the volume and weight of power module packaging would reduce the complexity of the engine compartment in a hybrid vehicle, enabling simple installation, handling and maintenance, which is particularly important for hybrid vehicles. A lighter power module would result in a more fuel efficient vehicle. Weight reduction would also minismise the risk from potentially damaging stresses resulting from shock loads.

It is particularly important to optimise the size of the heat spreader and heat sink: adequate heat dissipation is necessary but overkill leads to waste. The power density of power electronic converters has roughly doubled every 10 years since 1970 [11]. The continuity of this trend has become questionable due to the fact that silicon based device technologies, more recently centering on the IGBT concept, have started to show a tendency to saturate in terms of performance improvement. The difficulty has arisen because of the desire to increase current and voltage levels while simultaneously reducing size. Unfortunately, the requirement to minimise size of the power module is constrained by the need to maintain acceptable temperatures of the power semiconductor devices used in the converter. It is for this reason that research is being conducted into new semiconductor materials such as Silicon Carbide, Gallium Nitride and Diamond. Devices based on the aforementioned materials have the potential to operate at much higher temperature although the packaging issues remain unclear.

The importance of IGBT power module reliability has significantly increased due to widespread use of these devices in fields which are associated with challenging operating conditions. The reliability of a power module is of vital importance to the user, who expects the system to operate correctly throughout its entire service life. For example, an IGBT module for railway traction has the lifetime requirement of 30 years [12]. The reliability of the whole package is tied to its temperature regime because there are many

mechanisms that lead to package degradation as a result of elevated temperatures and thermal cycling.

A package should be designed in such a way as to allow effective heat removal. A balanced engineering approach is necessary when considering the many factors involved. Final designs are typically in the form of an optimised configuration, a trade-off between reliability, cost, efficiency, size, device performance and thermal performance [9, 13].

1.1.3 Fast Electro-thermal Converter Simulation

A significant challenge in the design of a HEV powertrain is the optimisation of its power converter. The conditions expected by the power converter determine its specifications, from which the power devices and cooling design can then be selected. The converter conditions are dependent on how the HEV is driven and the vehicle's powertrain configuration. Drive cycles are standardised speed versus time profiles which can be used to simulate how a HEV is driven. Realistic converter conditions can therefore be acquired by simulation using drives cycles and a model of the HEV powertrain configuration. These converter conditions, in turn, can be fed into a converter simulator. A fast and accurate electro-thermal converter simulation is required in order to carry out converter thermal optimisation, which is one of the main drivers for this work.

Electro-thermal device models are essential since the device temperature affects the device electrical characteristics which in-turn affects the device power losses. There is feedback loop because the device power losses affect the device temperature. Electro-thermal device simulation requires accurate device models; previous attempts at electro-thermal device simulation use compact or behavioural device models in conjunction with a thermal model, see references [14–19]. These models require simulation times of a

few seconds for every device switching cycle. Therefore these models cannot be used to simulate converter operation for longer than tens of milliseconds because there are millions of switching events leading to prohibitive simulation times.

Simulation techniques have been developed which enable device power losses and device temperatures to be simulated over long drive cycles [20]. One such simulation technique has been adopted in this work; it was originally published in [21, 22]. An explanation of this technique, the 'Fast electro-thermal converter simulator', follows.

The look-up table of device losses, shown in Fig. 1.3, is critical to the operation of the electro-thermal simulator. Rather than simulating device switching at every switching event, which is time-consuming, the inverter simulator simply looks up a power loss value for the device from a look-up table. The look-up table is pre-calculated prior to an electro-thermal converter simulation taking place. The simulation controller supplies the device switching model with a number of permutations of device switching conditions (load current, duty ratio and device temperature). The device switching model runs just one switching cycle simulation for each set of switching conditions and returns the simulated power value to the simulator controller. The simulation controller is then able to populate the look-up table. The advantage of the electro-thermal converter simulator being decoupled from device switching model is that it can accurately predict device power losses while maintaining a fast simulation speed.

The inverter load conditions which feed into the electro-thermal simulator are also precalculated prior to an electro-thermal converter simulation taking place. Driving cycle data is used to determine the motor speed and torque profiles of a hypothetical electric vehicle. This is achieved by simulating the powertrain based on vehicle parameters including the mass, drag coefficients and wheel size. A simple drive model then simulates the electric motor using these speed and torque profiles. The drive model generates the

inverter load conditions (V_{rms}, I_{rms}, power factor and output modulation frequency) over the duration of a drive cycle, i.e. an inverter load cycle.

Within the electro-thermal converter simulator hightlighted in Fig. 1.3 is an inverter simulator which dynamically converts the inverter load conditions and the device temperatures, supplied by the thermal model, into device switching conditions. The inverter simulator then calculates the device power losses for a given time step, using a look-up table, and supplies it to the thermal model. The electro-thermal converter simulator demands that the instantaneous device temperature be calculated simultaneously using a thermal model, enabling the electro-thermal feedback through the devices to be simulated. In previous work, over-simplified thermal models have been entered into this framework. Such models, while accurate for a given packaging structure, can not be modified easily in order to examine different packaging geometries. Interactive optimisation of the converter packaging can therefore not cannot take place.

All stages of this simulation method are implemented in MATLAB/Simulink, giving the benefit of a common and flexible simulation environment shown in Fig. 1.3. The electro-thermal simulator allows rapid evaluation of a device's electrical performance and the thermal performance of the converter packaging.

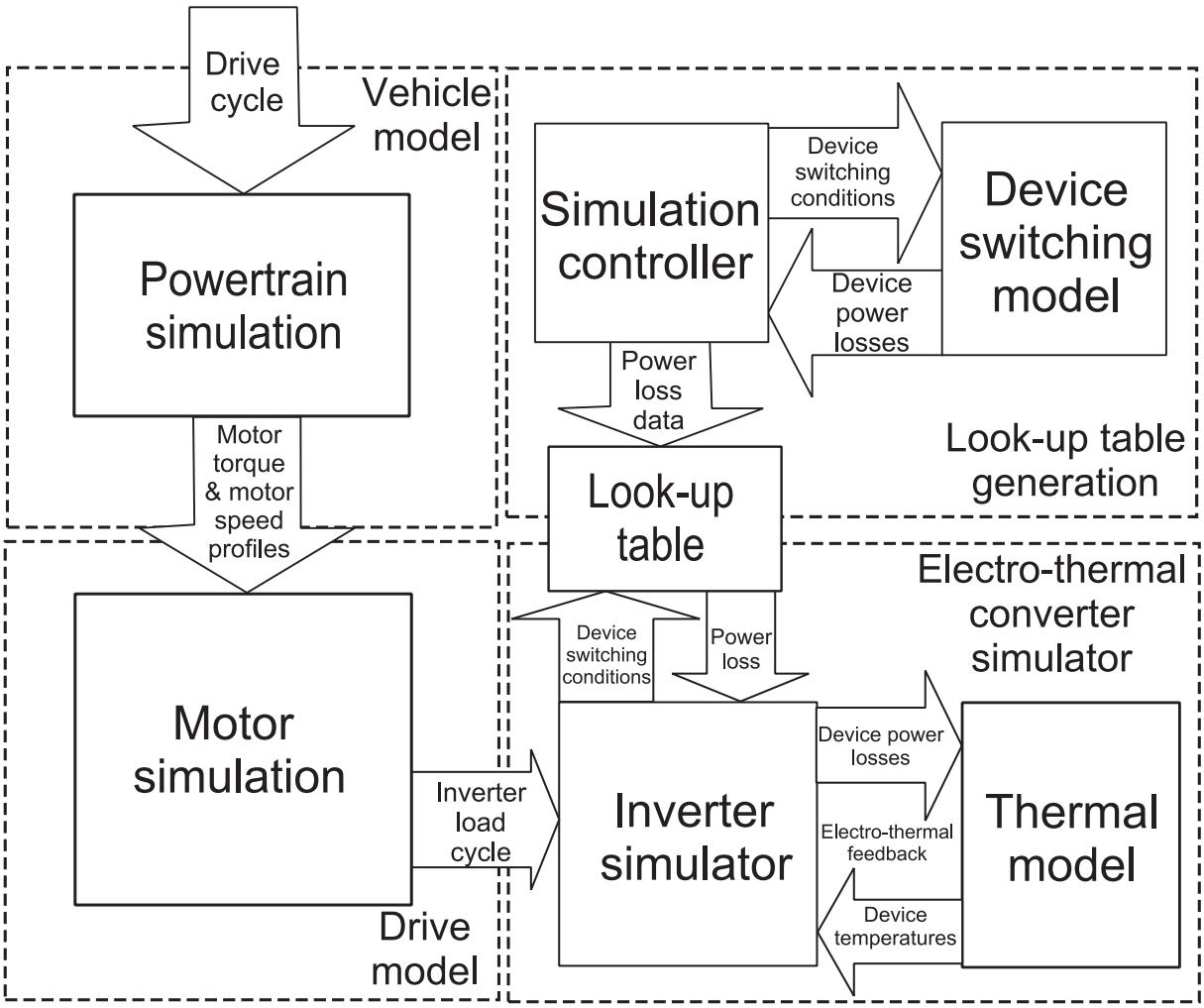

Figure 1.3: Schematic diagram showing the framework of the electro-thermal simulator.

1.2 Motivation

Engineers apply optimisation to obtain the best result under given circumstances. Trade-offs must be made depending on the factors considered in section 1.1.2. Suitable models can be used to evaluate the behaviour of the entire power train used in a hybrid electric vehicle. The aim of the work is to develop a rapid and accurate 3-D thermal model, capable of simulating and subsequently optimising the heat diffusion through power converters typically utilised in HEVs.

A fast accurate thermal model is required which is compatible with the simulation framework shown in the previous section. The thermal model must be able to co-simulate with an existing converter simulator. Therefore the thermal model should be implemented in MATLAB/Simulink to allow straightforward integration with the converter simulator. The co-simulation can be used to optimise thermal management of power module packaging and aid prediction of the reliability of the whole traction system when used in conjunction with reliability models [21, 22]. Testing for reliability under realistic converter load conditions in this manner has been identified as an important requirement for traction converter design and evaluation for automotive applications [23].

There are many requirements for a suitable thermal model. The thermal model must be able to run quickly in order to co-simulate with the inverter simulator in Fig. 1.3. In general, the faster the simulation, the more effective the simulation based design phase. Therefore a computationally efficient model is essential to calculate the transient temperature distributions in power converter packaging structures.

Another requirement of the thermal model is that it is sufficiently accurate. Accuracy is important as simulated results are meaningless if they bear no resemblance to empirical data. A full 3-D thermal model of an IGBT power module is required to accurately

evaluate a complete packaging structure. This is accomplished by computing the 3-D heat diffusion through many layers of device packaging. The thermal model must not simply provide the device temperature; the temperature distribution across the whole package is necessary to help detect hotspots. A packaging designer would also benefit from being able to visualise heat flow through a structure. It is intended to create a thermal model which will be used in the early stages of design to test design feasibility. Certain assumptions and simplifications are necessary in order for the model to achieve the required simulation speed which will inevitably lead to a degree of inaccuracy. However, a reasonably high model accuracy is required to provide a thermal designer with useful guidance.

Traditional approaches employ Resistor-Capacitor (RC) networks as thermal equivalent circuits [24–30]. RC networks are popular as they are extremely fast to simulate and can be easily integrated with an inverter simulator. However, RC networks cannot model 3-D diffusion accurately and require time consuming parameter extraction from transient results. Such transient results are either obtained by a practical experiment [31, 32] or commercial thermal simulators such as FLOTHERM, which utilises numerical methods [33–36]. Both practical experiments and commercial simulators are undesirable for a thermal designer. Commercial simulators are powerful simulation tools, which can analyse complex structures and can provide accurate results. However, they are of limited use in power module design. They require a long computation time to simulate realistic converter load cycles with sufficient accuracy, especially for 3-D simulations [31]. In addition, commercial simulators cannot be practically integrated with a inverter simulator.

Recently, there has been an emergence of Model Order Reduction (MOR) thermal models. These are able to co-simulate with a inverter simulator to enable electro-thermal simulation. Despite having many advantage over RC networks, MOR models suffer a

similar drawback. MOR models require a commercial simulator to run in order for them to be created. A designer of power module packaging wishes to test the thermal performance of many packaging layouts in an efficient manner. This is not possible using MOR models or RC networks because every design iteration would necessitate the use of a time-consuming commercial simulator.

Clearly, it is desirable to find a fast and accurate thermal model which does not rely on time-consuming commercial simulators; critically, it must be able to be integrated with a converter simulator so that total converter optimisation can take place quickly. A thermal model is therefore required which can be generated directly from the material properties and the geometry of a structure. This thesis concerns the creation of a suitable 3-D thermal simulator of power electronics packaging. A thermal model is required which can fulfil all of the stated requirements without possessing the drawbacks of existing models.

1.3 Thesis Outline

The basic operation of a power converter is examined in chapter 2, along with details of the converter power losses caused by switching and conduction losses. There is a review of the power converter packaging used in the Toyota Prius HEV and the reliability issues of power converters are highlighted.

The concepts of the physics of heat diffusion are introduced in chapter 3, followed by a derivation of the heat conduction equation. The customary separation of variable technique, used to solve the heat equation, is presented and there is an explanation of why it is unsuitable for use this work.

A discussion on the choice of thermal model and the important issues in thermal modelling is provided in chapter 4. Continuation of the work initiated by Bin Du et al

[37, 38], which involves developing a Fourier thermal model, is then identified as a suitable way to proceed with the thesis.

Chapter 5 presents the basic 1-D, 2-D and 3-D Fourier thermal model used to simulate heat conduction through a single block. Results generated by the basic Fourier thermal model are compared with results from FLOTHERM simulations in order to validate the Fourier thermal model.

The method employed to enable the Fourier thermal model to simulate the material interfaces present in the packaging layers of power converters are presented in chapter 6. Results generated by the Fourier thermal model when simulating material interfaces is, once again, validated by results from the software package FLOTHERM.

Chapter 7 shows the Fourier thermal model which is embedded into the power converter simulator framework set out in section 1.1.3 in order to simulate a single inverter phase leg during realistic load conditions. Experimental results are generated by a single phase leg from a Toyota Prius inverter supplied with realistic load conditions by a 'back-to-back' inverter test rig. Experimental results of transient device temperatures are recorded using an infrared camera and then compared with the simulated results in order to achieve experimental validation.

The thesis conclusions are given in chapter 8. Suggestions for further research, which would possibly serve to increase the capabilities of the Fourier thermal model featured in this thesis, are also described.

Chapter

2 The Power Converter

Chapter 1 stated that the motivation for this thesis was to create a fast and accurate 3-D thermal model of a HEV power converter package. This chapter begins by examining the operation of a power converter and its function within a HEV. An in depth review of the power converter packaging structure follows. The whole issue of device reliability is then addressed, which features sections concerning thermal cycling, power converter failure modes and methods of reliability estimation.

2.1 Power Converter Operation

The Power Converter has an important role in the electrical power conversion processes which take place in a HEV. Fig. 2.1 shows the location of the power converter in the powertrain of a Toyota Prius HEV. In Fig. 2.1 a pair of electric motor-generators (MGs) are present, that can operate as motors or generators. Both MG1 and MG2 are permanent magnet three-phase alternating current motor generators.

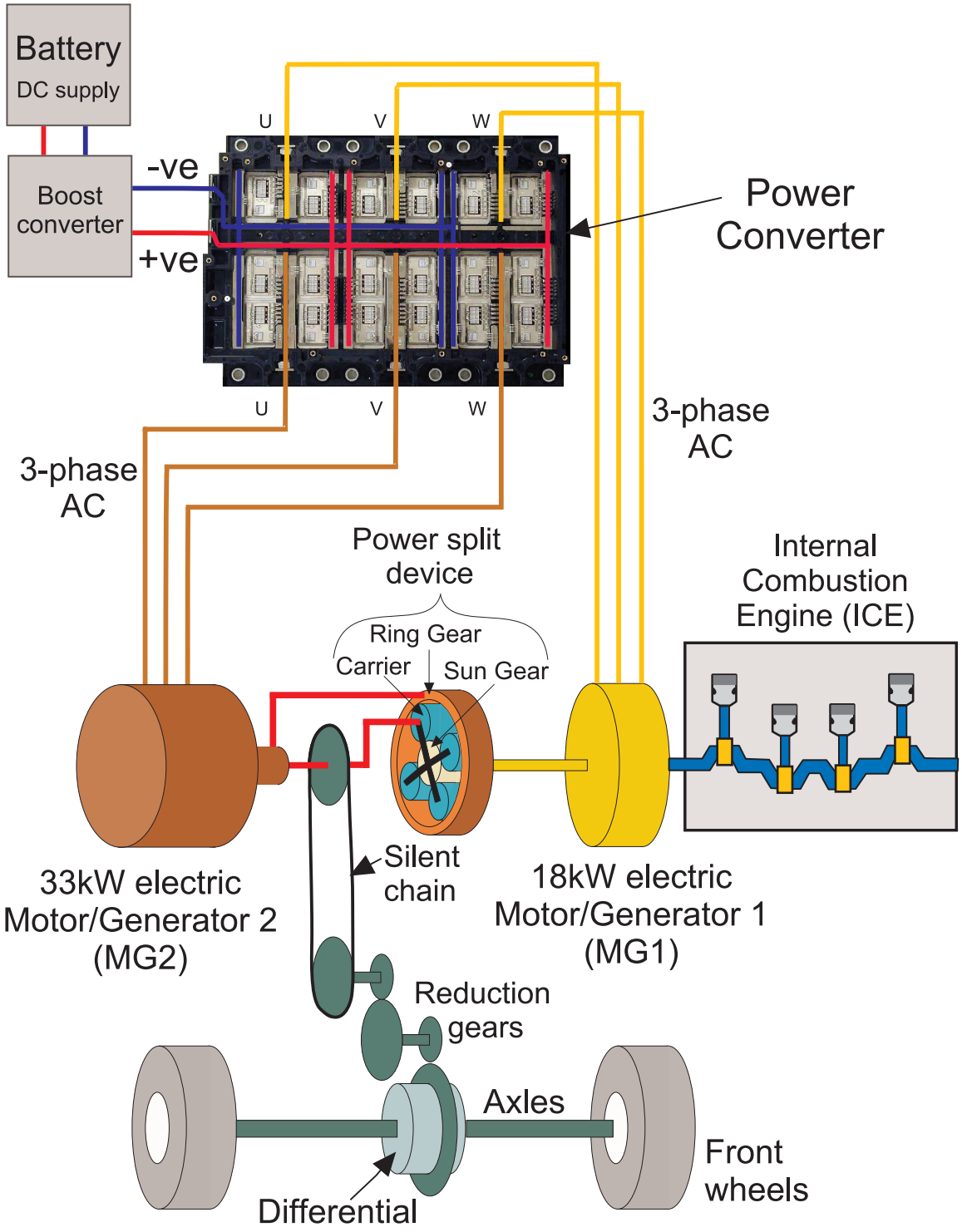

Figure 2.1: The role of the power converter within the powertrain of a Toyota Prius.

When MG assemblies run as three-phase motors, they require a variable voltage, variable frequency (VVVF) three-phase AC supply. In this instance, the power converter acts as an inverter, converting the DC line input into the AC output according to the requirements for motor speed and torque as set by the driver and vehicle powertrain. The inverter has three phase-legs each consisting of two IGBTs and two diodes (labelled with subscripts A, B and C), as shown in Fig. 2.2.

A common inverter control method is sine-triangle pulse width modulation (STPWM) control, which is displayed in Fig. 2.3. With STPWM control, the switches of the inverter are controlled based on a comparison of a sinusoidal control signal ($V_{control}$) and a triangular switching signal (V_{tri}) at the switching frequency (f_{sw}). The sinusoidal control waveform establishes the desired fundamental frequency of the inverter output, while the triangular waveform establishes the switching frequency of the inverter [39].

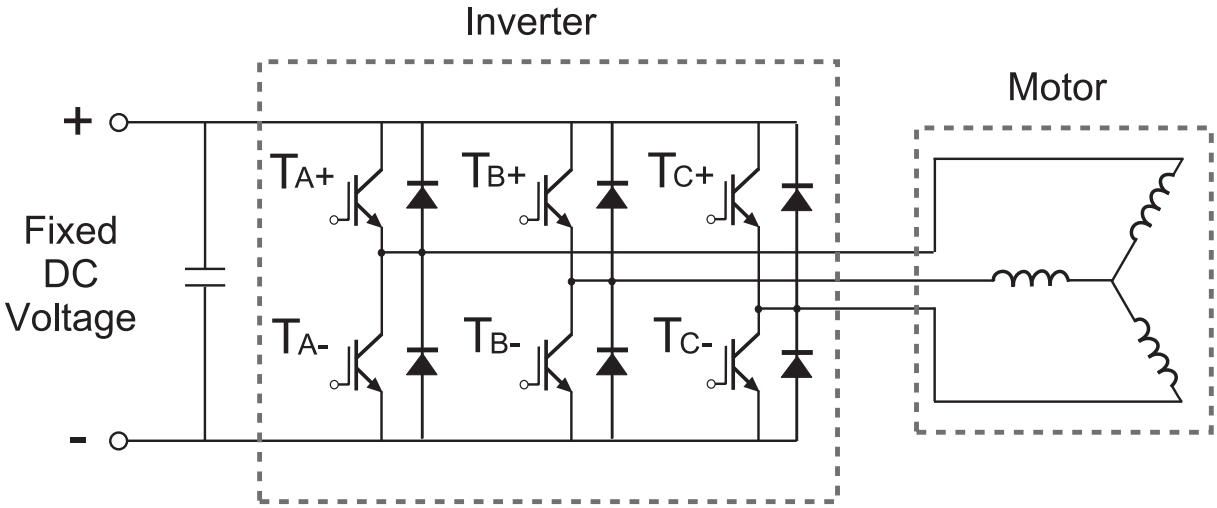

Figure 2.2: Circuit diagram of a three-phase inverter.

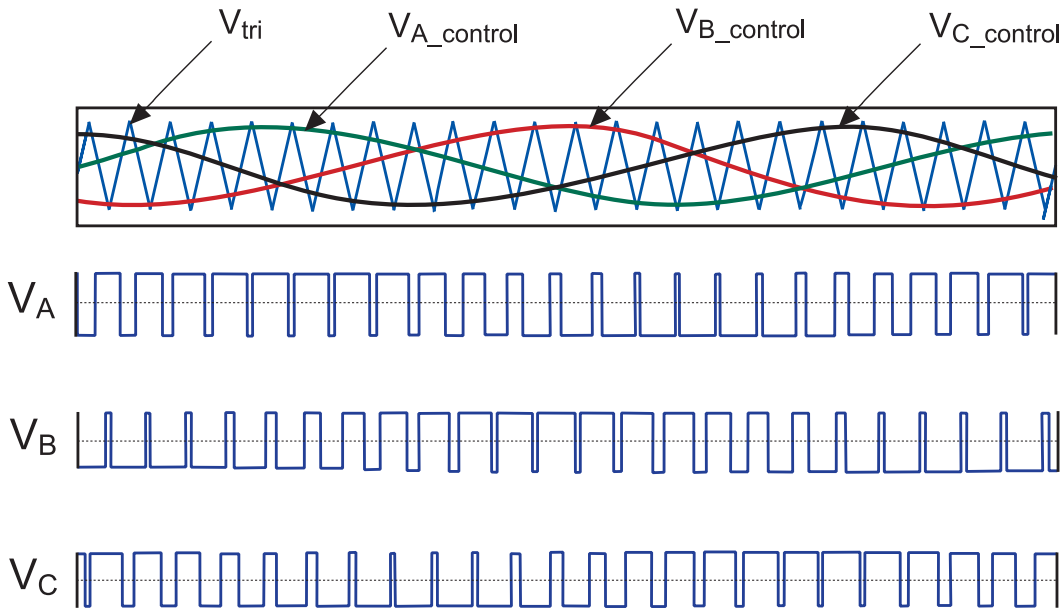

Figure 2.3: Sine-triangle pulse width modulation [40].

To achieve the pulsed output voltages in Fig. 2.3, the switches of the phase-legs are controlled based on the following comparison:

$V_{A\_control} > V_{tri}$, T_{A+} is on

$V_{A\_control} < V_{tri}$, T_{A-} is on

$V_{B\_control} > V_{tri}$, T_{B+} is on

$V_{B\_control} < V_{tri}$, T_{B-} is on

$V_{C\_control} > V_{tri}$, T_{C+} is on

$V_{C\_control} < V_{tri}$, T_{C-} is on

When the upper device T_{A+} is on, the lower device T_{A-} will be off, and vice-versa. The same is true of the other phase-legs. This ensures that there is no short-circuit between the positive and negative DC supply rails. The antiparallel diodes, connected across each of the IGBT switches, are present to provide a path for the inductive load current when the switch is turned off.

As shown in Fig. 2.3, the square wave pulses are the output from each of the inverter legs with duration proportional to the amplitude and frequency of the associated control signals. The inductance of the motor windings acts as a filter, limiting the change in current over time and therefore averages out the switched (pulsed) current through the inverter. When the switching frequency is matched to the winding inductance, and leg output frequency, it produces a low ripple sinusoidal current signal for each phase-leg of the inverter, depicted in Fig. 2.4. This low ripple sine wave is supplied to the electric motor causing it to rotate.

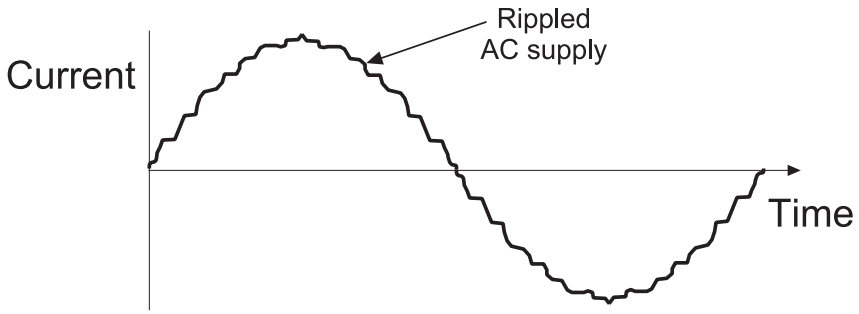

Figure 2.4: Low ripple sinusoidal current at inverter leg output with motor load.

When MG1 acts as a motor it applies direct power to drive the MG2 assembly. MG1 additionally serves as the electric motor used to start the combustion engine in the power train. In motor mode, MG2 is the primary electric drive motor. MG2 and the engine are used together or separately to drive the front wheels via reduction gears.

In Fig. 2.1, the boost converter is present to raise this DC voltage entering the inverter from the 200V of the battery to 650V (Prius 2010). The increase in DC voltage allows a greater peak-to-peak output AC voltage from the inverter. This in turn allows the motors to operate at a faster speed but at a reduced torque. Since power $P = VI$ must be conserved, the current entering the inverter is less. Therefore the I^2R heating losses in the motor and wires is less, enabling the use of thinner wires and a smaller device area.

When MG assemblies run as generators, rotated by either the combustion engine or the wheel rotation during regenerative braking, the power converter operates as a rectifier. The power converter rectifies the three-phase AC output of the MG assemblies into DC, with the diodes playing a key role. In order to gain a basic understanding, one can imagine the rectifier circuit operating solely with diodes, as shown in Fig. 2.5. This is a basic three-phase full wave bridge rectifier circuit.

When the three-phase AC is rectified, the phase-shifted pulses overlap each other to produce a DC output. Fig. 2.6 shows the full-wave rectification of a three-phase AC supply. The function of the capacitor in Fig. 2.5, is to attenuate high frequency signals which has the effect of smoothing the DC supply. After filtering and regulation (using the boost converter circuit in reverse), the recovered energy recharges the batteries in the powertrain.

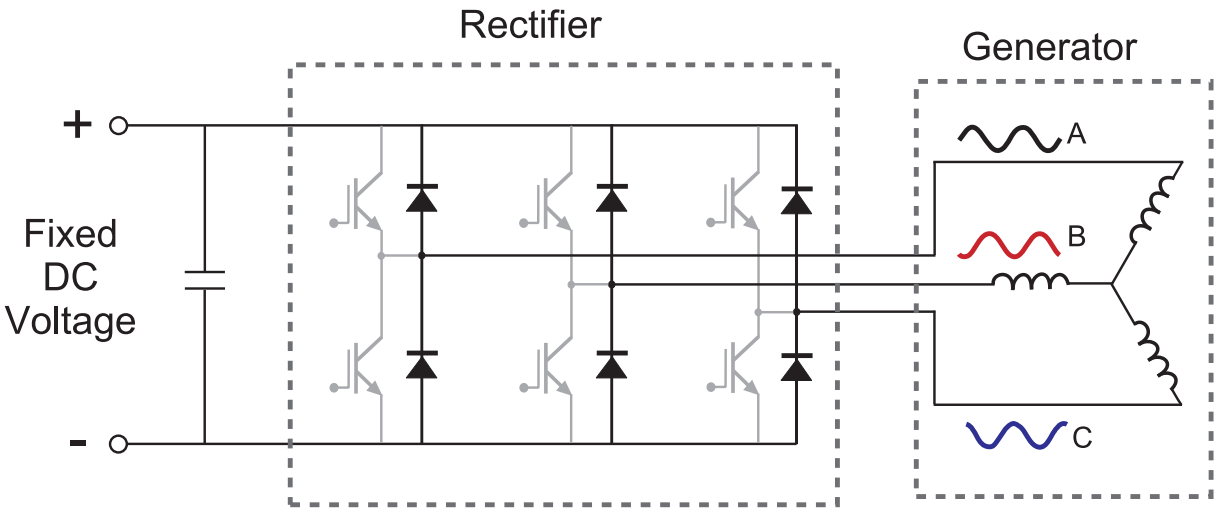

Figure 2.5: Circuit diagram of a three-phase full wave bridge rectifier.

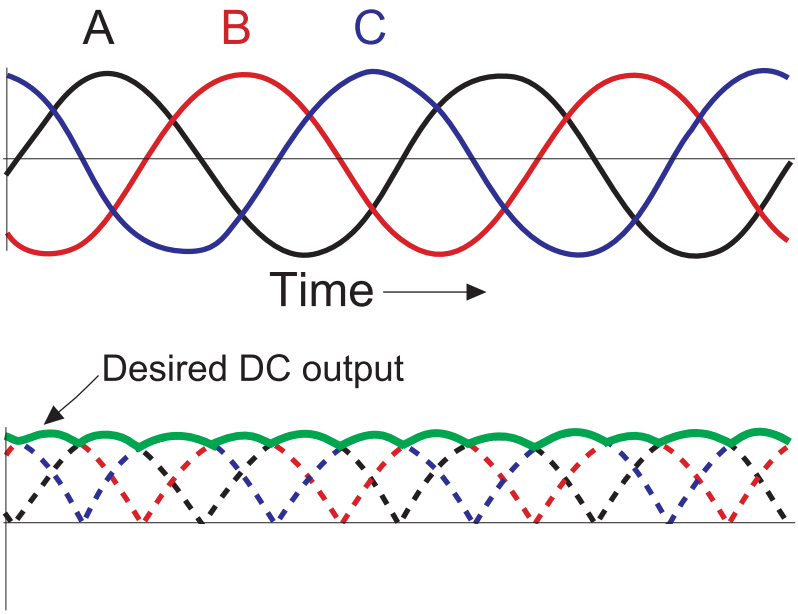

Figure 2.6: Three-phase full wave rectification.

A control system adjusts and regulates the internal combustion engine (ICE), MG1, and MG2 to meet the driving demands signalled by gear selection, accelerator pedal position and vehicle speed. Crucially, it also controls the operation of the power converter and balances the power requirements of the car.

2.1.1 Power Loss Generation in Power Devices

Semiconductor devices exhibit power losses that fall into two main categories: conduction losses and switching losses. The type of losses responsible for the majority of the overall system losses in the converter, depends on the switching frequency.

All silicon devices provide resistance to the flow of electric current that originates from the resistivity of the bulk semiconductor material. Hence, whilst the device operating in the on-state, there is conduction power loss given by:

$$P_{cond} = \rho_1 \, I_F V_F, \tag{2.1}$$

where ρ_1 is the duty ratio, I_F is the current during forward bias (on-state), while V_F represents the voltage through the device during forward bias. Duty ratio is defined as:

$$\rho_1 = \frac{\Delta t_{on}}{\Delta t_{off} + \Delta t_{on}} = \Delta t_{on} f_{sw}, \tag{2.2}$$

where Δt_{on} is the time spent in on-state, Δt_{off} is the time spent in off-state and where f_{SW} represents the switching frequency. It can be seen from Equation (2.1) and (2.2) that the conduction losses increase in proportion to the f_{sw}. Off-state leakage current can also lead to conduction losses but is negligible compared to the on-state loss.

The other form of power dissipation, coined "switching losses", originates during the device transition from the on-state to the off-state or vice versa. When a semiconductor component is turned on, the device aims to switch from the blocking state to an unblocking state. Ideally, the voltage would drop to zero and the current would reach its set level, determined by the load, instantaneously. In practice, the voltage never drops to zero and when a device is signalled to turn on or off the device current does not change instantaneously but instead rises or falls in a finite time. These dynamic non-idealities of the power devices result in switching losses and are due to the presence of stray inductance and device capacitance. There is an energy loss for every device switching event. Fig. 2.7 illustrates the non-ideal switching behaviour of a typical semiconductor device, in this instance an IGBT. $E_{sw(on)}$ represents the turn on energy losses and $E_{sw(off)}$ the turn off energy losses. The time spent in onstate t_{on} is the time taken to turn on, while t_{off} is the time taken to turn off. V_{DC} is the DC line supply voltage, which appears at the leg outputs when the associated upper switching is on.

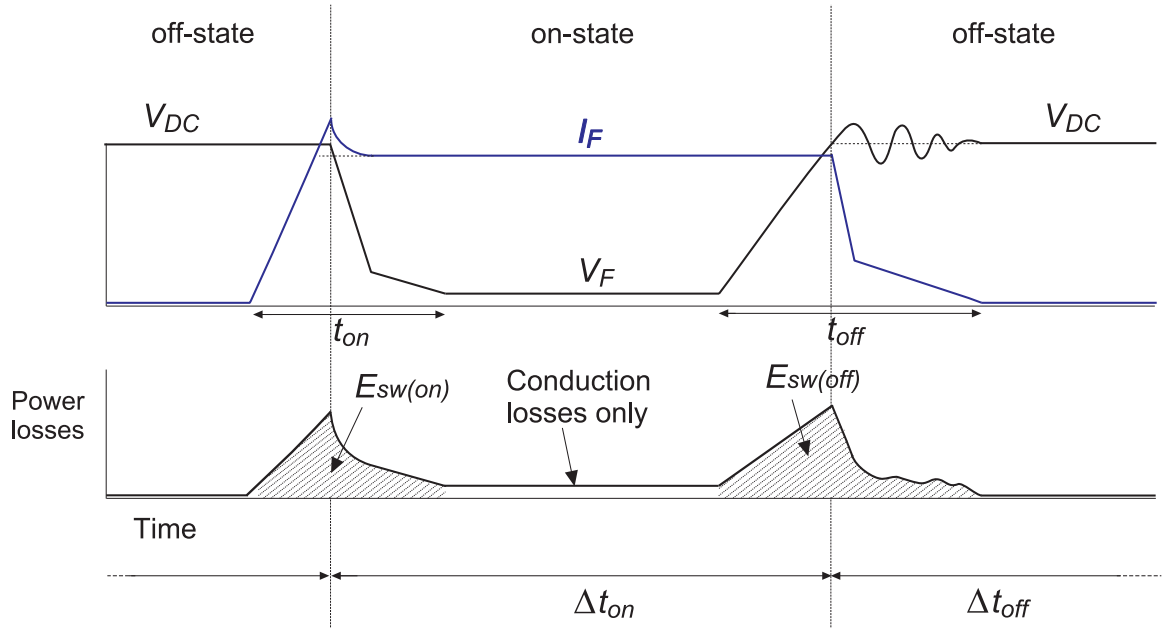

Figure 2.7: Power losses, $P(t)$, in an IGBT device during a switching cycle.

It is possible to calculate the total amount of energy lost during a switching cycle, E_{total}, since:

$$E_{total} = E_{on} + E_{off}, \tag{2.3}$$

where E_{on} represents the on-state energy losses and E_{off} is the off-state energy losses, which are defined below:

$$E_{on} = \int_{\Delta t_{on}} P(t)dt, \tag{2.4}$$

$$E_{off} = \int_{\Delta t_{off}} P(t)dt. \tag{2.5}$$

Using the relationship between energy and power, it is possible to represent P_{total} which is total power loss of the device:

$$P_{total} = f_{SW} E_{total}, \tag{2.6}$$

As an expression for P_{total} and P_{cond} exists, it is therefore possible to calculate the power switching losses P_{switch} using the equation:

$$P_{total} = P_{cond} + P_{switch} \tag{2.7}$$

Fig. 2.8 summarises the parameters which influence the total device power loss in a semiconductor device.

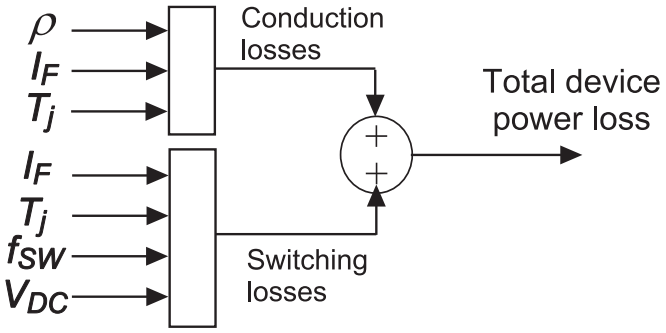

Figure 2.8: Parameters which influence the power losses in semiconductor devices.

The on-resistance of a device is temperature dependent, which explains why the device conduction losses are temperature dependent [41]. The device junction temperature T_j affects the both the I_F tail at turn-off and the diode characteristic at turn-on in Fig. 2.7, hence the switching losses are a function of device junction temperature [42]. Since T_j is dependent on the total device power losses, a coupled electro-thermal system exists with the device physics interacting with the thermal properties of the switching device and heatsink and the external load conditions. This justifies the use of the electro-thermal

converter simulator framework displayed in section 1.1.3, which is able to simulate this coupled electro-thermal system providing a suitable thermal model can be created. To recap, a thermal model is required which can produce a profile of the device junction temperature, T_j, using a device power loss profile. However, it must be able to co-simulate with the inverter simulator shown in Fig. 1.3 since simulation of the electro-thermal feedback through the devices is required as the device conduction and switching losses change with device junction temperature, as shown in Fig. 2.8. In order to create a suitable thermal model the packaging structure which is being modelled must be understood.

2.2 Power Converter Structure

The use of semiconductors in the power converter leads to heat being generated by these devices. Despite the converter efficiency being more than 90%, the large quantity of power being converted leads to significant quantities of heat being generated. Adequate cooling is paramount in order to keep the switching devices operational over the lifetime of the vehicle. Power converter installations in hybrid vehicles have their own dedicated cooling system. Part of the cooling system, the heatsink, is placed beneath the packaging of the switching devices. The heatsink, the switching devices and their packaging are collectively known as a power converter module.

The first power converter module was the SEMIPACK, introduced in 1975 [7]. Since then a significant amount of engineering time and effort has been spent on topology and packaging design. In recent years, a number of companies in the electronics industry have released power modules known as "bricks". The bricks are simply bolted to a heatsink, and electrically attached to the control and filter stages of the power converter [43]. The advantage of this modularity is reduced cost. The bricks are an attempt to standard-

ise power electronics design, thus reducing the required time for engineers to focus on electronic packaging and thermal issues.

Before a thermal model may be created for the power converter it is necessary to review the geometry of commercially available power module packages. An image of the power converter in Fig. 2.1 is given in Fig. 2.9. This power module is constructed with multiple devices electrically connected in parallel. Upon close inspection, bond wires can been seen connecting the device to bus bars and terminals. The entire transistor/diode array assembly used by the power converter is encapsulated in a sea of protective silicone gel protecting against debris, dust and moisture. The gel also protects the bond wires giving shock and vibration protection. The gel does not migrate or flow, allowing the converter mounting angle to be unrestricted.

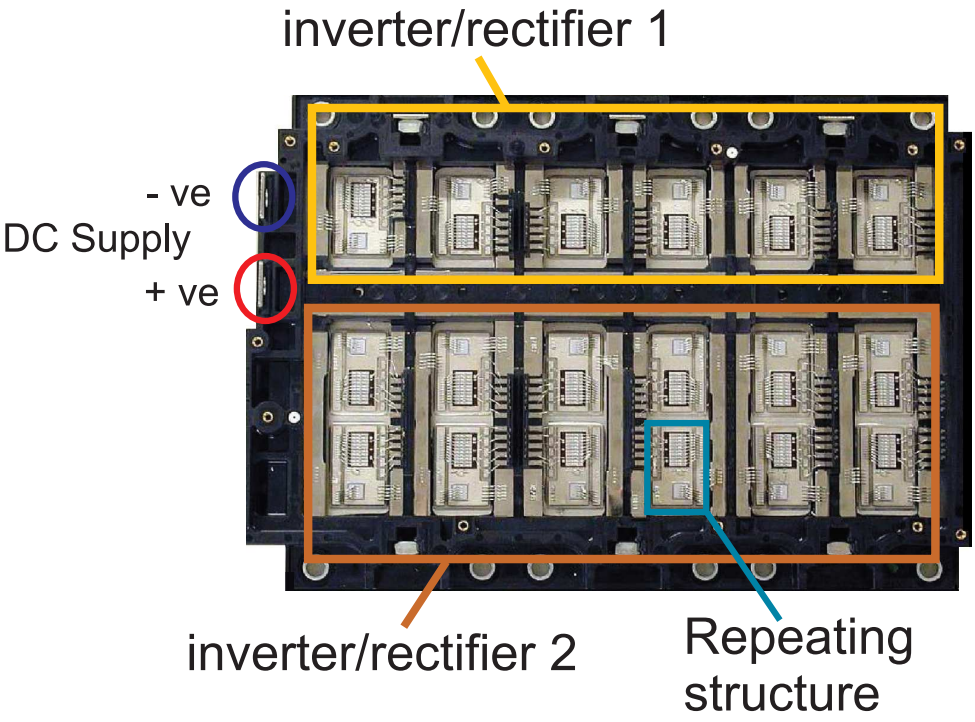

Figure 2.9: Photograph of a power converter from the Toyota Prius HEV [44]. The gate drive PCB and shielding plate have been removed.

The power semiconductor devices (IGBTs and diodes) placed in the power converter are the main components and both play the role of the switching devices. Owing to symmetry, the main objective is to simply model the structure highlighted in Fig. 2.9 which repeats throughout the power module structure. The presence of this repeated structure makes model expansion straightforward and a detailed structural view of it appears in Fig. 2.10.

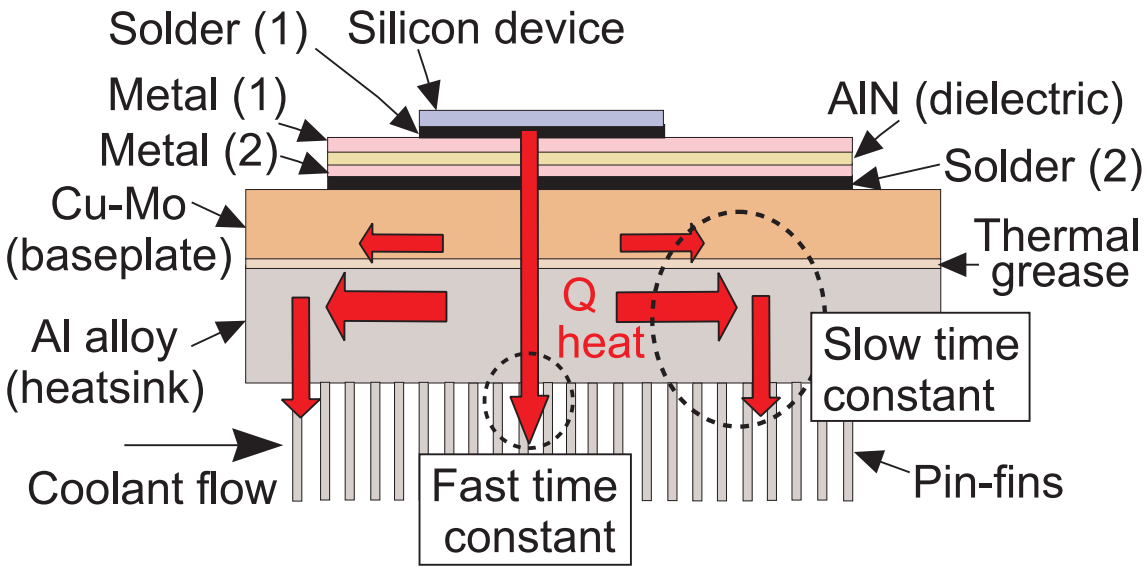

Figure 2.10: Structural view of the power module package from the power converter used in the Toyota Prius (not to scale). Heat dissipates from the silicon device at the top and travels through the packaging layers before being removed by the coolant. [45, 46].

Conventionally, high power electronic packages are of stack configuration. The configuration used in the Toyota Prius is shown in Fig. 2.10. Alternative configurations exist with AlO used in place of AlN for the dielectric and AlSiC being the material selected for the baseplate. In the Toyota Prius stack configuration, the silicon devices are soldered onto an insulating substrates of AlN, which is sandwiched between two metal layers. The substrate acts to electrically isolate the power devices from the heatsink. Beneath the

substrate is a CuMo heat spreader which moves heat away from the sensitive devices and provides proper mechanical support. The lateral heat spreading is caused by the limited cooling capability of the module, lowering the heat flux to a level suitable for further transportation to the heatsink. The important characteristics of a thermal heat spreader material are its thermal conductivity and its coefficient of thermal expansion (CTE). Copper and aluminium were formerly the industry standard heat spreaders due to their high thermal conductivity properties, as stated in table 2.1. More recently, materials such as Metal Matrix Composites (MMCs) or CuMo are preferred because they match the CTE characteristics of silicon more closely, while at the same time retaining high thermal conductivity properties.

The heatspreader is connected to the heatsink by a thin layer of grease. The inverter generally sits on a separate heatsink, thermal grease is used to provide a thermal contact which is better than air. Although Table 2.1 shows that thermal grease has a low thermal conductivity, it improves thermal contact by occupying the microscopic voids and cavities between mating surfaces. The heatsink conducts heat away from the devices. Typically, the inverter has a heatsink in which the coolant flows channels cast into the heatsink. In most inverter configurations, a clamping mechanism, such as bolts, is used in the package. This results in the thermal interface materials being subjected to a pressure of the order of 0.17 - 0.34 MPa [46].

In summary, the repeating structure labelled in Fig. 2.9 shall be modelled in order to determine the transient temperature of the switching devices used in the Toyota Prius power converter during realistic operation. The repeating structure is essentially a stack of blocks of material with their own thermal and mechanical properties. The transient temperature regime of the switching devices can promote power converter failure modes which directly affects the reliability of the power converter.

Table 2.1: Comparison of material properties.

Material	CTE (ppm/K)	Thermal Conductivity (W/mK)
Si	2.6	149
Solder		46
Al_2O_3	6.4	35
AlN	4.3	180
Aluminium	22	226
Copper	17	393
CuMo	7.2	197
Be-BeO MMC	6.8	240
Graphite-Cu MMC	0-2.0 (Directional)	356 (minimum)
Diamond	0.8-2.0	1000-2000
Gold	14	317
Thermal grease		1.09
Aluminum alloy 5086	23.7	125
Aluminum alloy 6061	23.4	167

2.3 Power Device Reliability

Reliability is the probability that the item will perform its required function under given conditions for a stated time period [47]. Device reliability may be affected by many factors, including excessive current causing heating and device destruction, cosmic radiation causing breakdown in the off-state, gate oxide breakdown, and thermal runaway. Most failures are due to thermal effects, so effective thermal management is essential.

Reliability should be examined as a function of time. Device failure rate, follows a so-called "bathtub" curve shown in Fig. 2.11. The behaviour of failure rate with time is quite revealing with respect to the causes of failure.

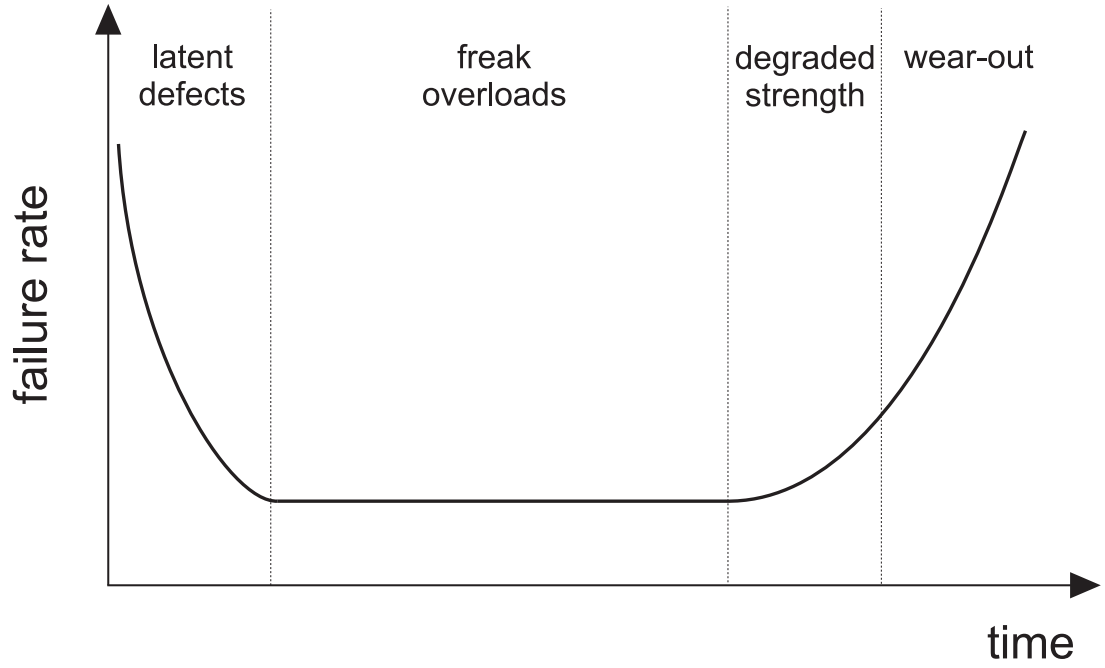

Figure 2.11: A "bathtub" curve representing a time-dependent failure rate [48].

Latent defects tend to be caused by defective components at manufacture. Missing parts, substandard material batches, components which are out of tolerance and damage in transit are a few of the quality control short comings that cause excessive failure rates

near the beginning of working life. The middle section of the bathtub curve contains the lowest failure rates; failures during this time are caused by freak overloads; power surges, vibrations, mechanical impact, temperature fluctuations and moisture variation are a few possible causes.

Towards the end of the product's working life the failure rates increase. The onset of rapidly increasing failure rates normally forms the basis for specifying a system's lifetime. The mechanism for thermally induced failure is thermo-mechanical cycling. This is the expansion and constriction of materials with dissimilar material properties, namely elastic moduli and coefficient of thermal expansion (CTE). This tends to contribute to the latter stages of degraded strength and wear out. Here thermal cycling, reliability estimation and the failure modes resulting from the cumulative effects of thermo-mechanical fatigue will be considered.

2.3.1 Thermal Cycling

Thermal cycling may be characterised by:

i) High frequency cycling - with a time period of tens of milliseconds, the device temperature varies with the load current during an inverter modulation cycle.

ii) Low frequency cycling - with a time period of many seconds, is due to the variation in average (rms) load current throughout the load cycle, as the inverter load changes.

iii) Deep thermal cycling - with a time period of many minutes or hours, it is caused by operational changes, i.e. the rise and fall in device temperature as the converter comes in and out of use.

Thermal cycling is often responsible for damage to power semiconductor devices. Fig. 2.12 defines key temperature variables which influence power module reliability. The

critical variable is ΔT which is the peak-to-peak temperature, it exposes power modules to thermo-mechanical stresses which leads to fatigue failure. The stresses are due to the mismatch of material properties such as Young's modulus and coefficient of thermal expansion (CTE). The effects of incompatible materials appear at interfaces. ΔT is two to five times more likely to be responsible for failure than the maximum junction temperature $T_{j\,\max}$ [49, 50]. In summary, the failure rate in thermal cycling is related to:

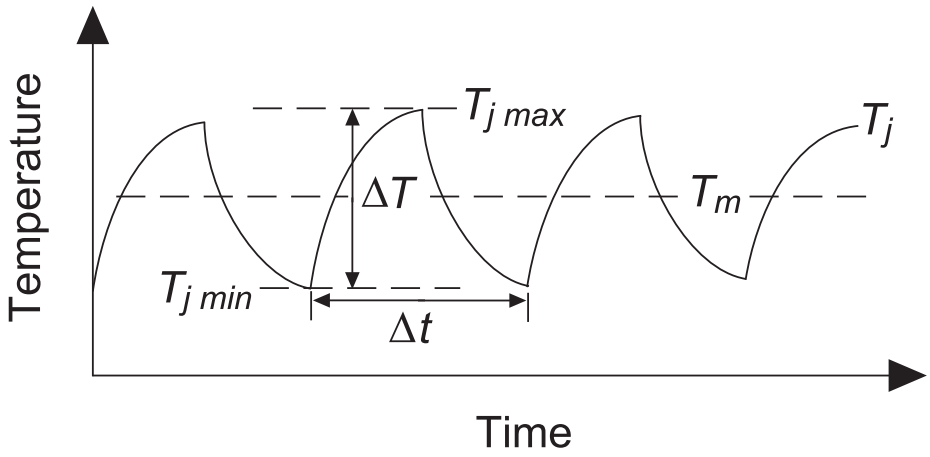

Figure 2.12: IGBT temperature profile.

1. the total number of cycles,
2. the total temperature fluctuation over the cycle, ΔT,
3. the mean temperature of the cycle, T_m,
4. the rate of temperature change, i.e. $\Delta T/\Delta t$

2.3.2 Thermally Induced Power Module Failure Modes

2.3.2.1 Bond Wire Failure

Reliability of bond wire is influenced by the bond wire length and loop height [51]. Two main types bond wire failure been reported:

a) bond wire lift-off,

b) the heel crack failure.

Bond wire lift off is caused by the large mismatch of CTE between the Al bond wire ($22x10^{-6}$/K) and the silicon device ($2.6x10^{-6}$/K). This generates a significant thermo-mechanical stress in the bonding zone during thermal cycling. This stress eventually leads to bond wire lift-off, as shown in Fig. 2.13. The current density through the surviving wires increases accordingly, accelerating their failure, resulting in the complete failure of the device [52, 53]. Poor bonding during the manufacturing process due to surface contaminants can also be a contributory factor. Thermo-mechanical stress can also lead to the mechanical deformation of the bond wire resulting in a fatigue crack, as shown in Fig. 2.14. Other contributory factors mechanical resonances caused by a combination of external field and time varying current through the bond wires [51, 54, 55]. Considerable improvements in tool design and bond wire material composition has significantly improved reliability at the device-bond wire interface.

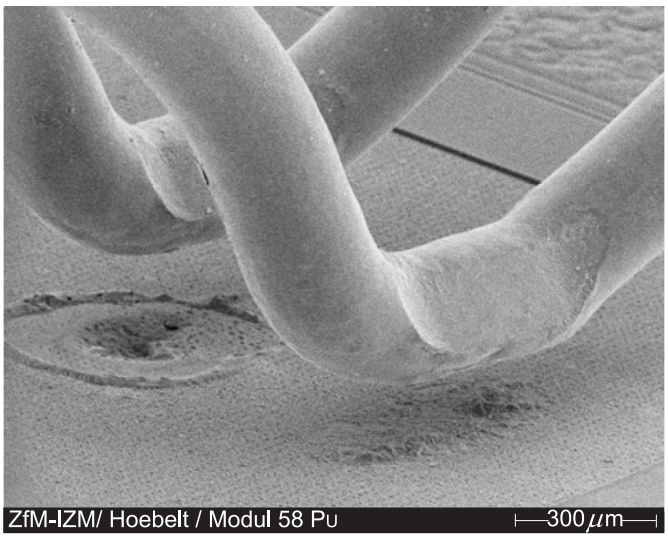

Figure 2.13: High resolution X-ray radiograph of IGBT bond wire lift-off during a power cycling test [52].

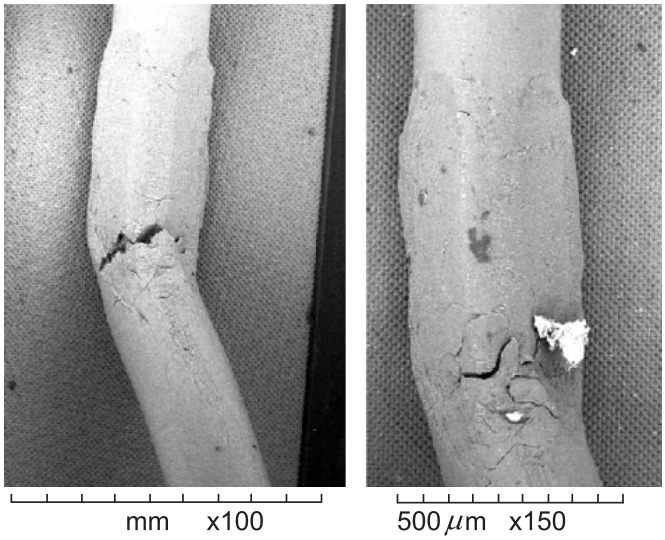

Figure 2.14: High resolution X-ray radiograph of a heel crack initiation in an IGBT bond wire [54].

2.3.2.2 Degradation of Solder Layers

Soft soldered joints are the greatest reliability limiter. Solder joint failure is mainly due to fatigue resulting from thermal cycling. A temperature swing causes stress to be applied to the solder between materials whose CTEs are different. Repeated application of this stress, as the temperature alternates between its high and low values (ΔT), causes the solder to crack, as displayed in Fig. 2.15. Both process-induced and fatigue-induced solder cracks propagate due to deformation from cyclic stresses.

In the case of IGBT power modules, failures are most likely to occur in the solder layers located between the base plate and the Metal(1)-AlN-Metal(2) insulator sandwich. These solder layers are exposed to the toughest conditions with regard to lifetime fatigue [56–59] because the materials either side have a large CTE mismatch and the solder layers occupy a large area.

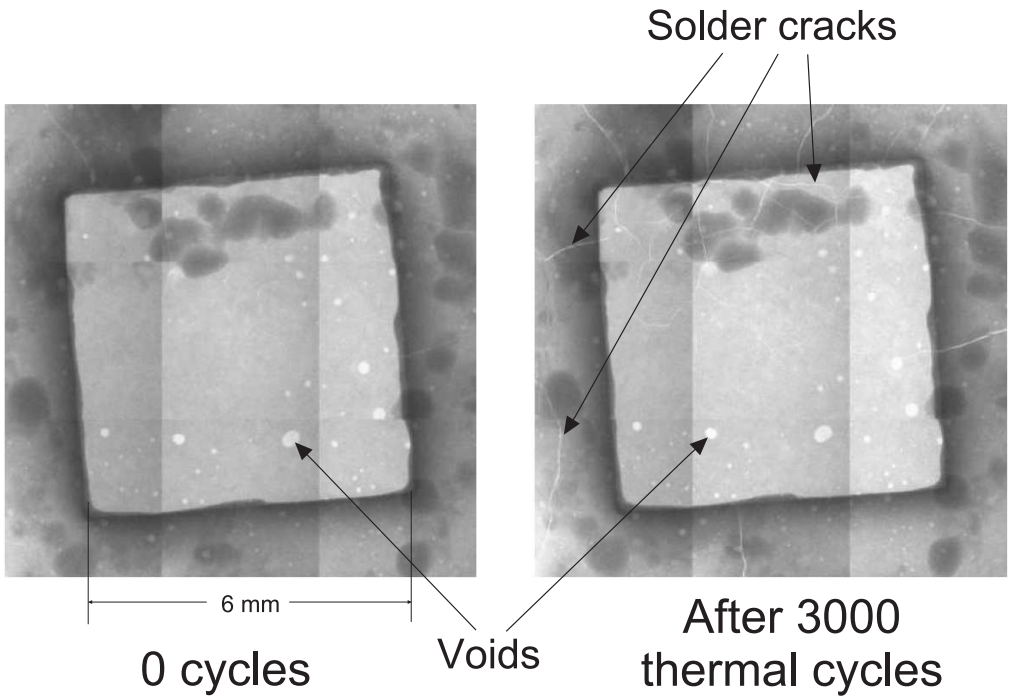

Figure 2.15: High resolution X-ray radiograph of a Au-Sn solder layer located beneath a silicon device. The solder thickness is about 75μm [60].

Solder cracks and relatively large voids in the solder layer can have detrimental effects on the heat dissipation performances of the assembly. The heat must flow around them, causing unequal flux distribution and resulting in increased device temperature and the formation of localised hotspots. This can accelerate the evolution of several other failure mechanisms, such as bond wire lift-off and solder fatigue [61, 62].

2.3.2.3 Silicon Device and Substrate Cracking

Silicon and AlN have a low CTE in the useful range for electronics. At room temperature, silicon and AlN have a CTE of 2.6x10^{-6}/K and 4.3x10^{-6}/K respectively [63]. Very few materials have such low values in this temperature range to match either Silicon or AlN. Consequently, silicon and AlN layers, within a power module structure, are often located alongside materials with a dissimilar CTE to their own. Therefore, silicon and AlN regularly endure the stresses which cause the brittle silicon and alumina to crack [64].

2.3.2.4 Delamination

The critical zones for delamination are the interfaces between the ceramic substrate AlN and the metal above and below. The difference in their CTE leads to stress within the interfaces when subjected to temperature changes. The bimetallic effect causes bending deformation which leads to delamination of the metal from the substrate [65]. Solder delamination occasionally occurs due to the presence of voids similar to those shown in Fig. 2.15. Solder delamination tends to creep from the edges inwards.

2.3.3 Reliability Estimation

Typically, device and packaging reliability has been tested by simulating or accelerating thermal cycling. This may be active, by operating and self-heating the device, or passive, where heat is supplied by an outside source. This is a means for evaluating packaging performance.

More recently, the LESIT project [66] was set up to explore power device reliability in relation to temperature. A large sample of devices were tested across a wide range of cycle conditions, but the project only considered instances when the failure mechanism was bond wire lift-off. This work provides the only known comprehensive set of data for thermal reliability of IGBT power modules and is a valuable starting point for determining power device reliability, despite only examining bond wire lift-off.

Data from the LESIT project for various combinations of N_f, T_m and ΔT is plotted in Fig. 2.16. The number of cycles to failure, N_f, is the key variable describing the average lifetime of a component. The data implied that N_f had a power law dependency on the temperature range ΔT, essentially a Coffin Manson relationship [67, 68]. The almost parallel shift in the data for various values of T_m indicated an Arrhenius approach [69].

The LESIT project put forward the following equation:

$$N_f = B\Delta T^{\beta} \exp\left(\frac{Q_{act}}{R_1 T_m}\right), \tag{2.8}$$

where R_1 is the gas constant (8.314 $\mathrm{Jmol^{-1}K^{-1}}$). Using a least square fit, values were found for the remaining constants, B = 640, β = -5, and the activation energy per mole Q_{act}=7.8x10^4 ($\mathrm{Jmol^{-1}}$). By proposing Equation (2.8), the LESIT project allowed the determination of N_f as a function of T_m and ΔT.

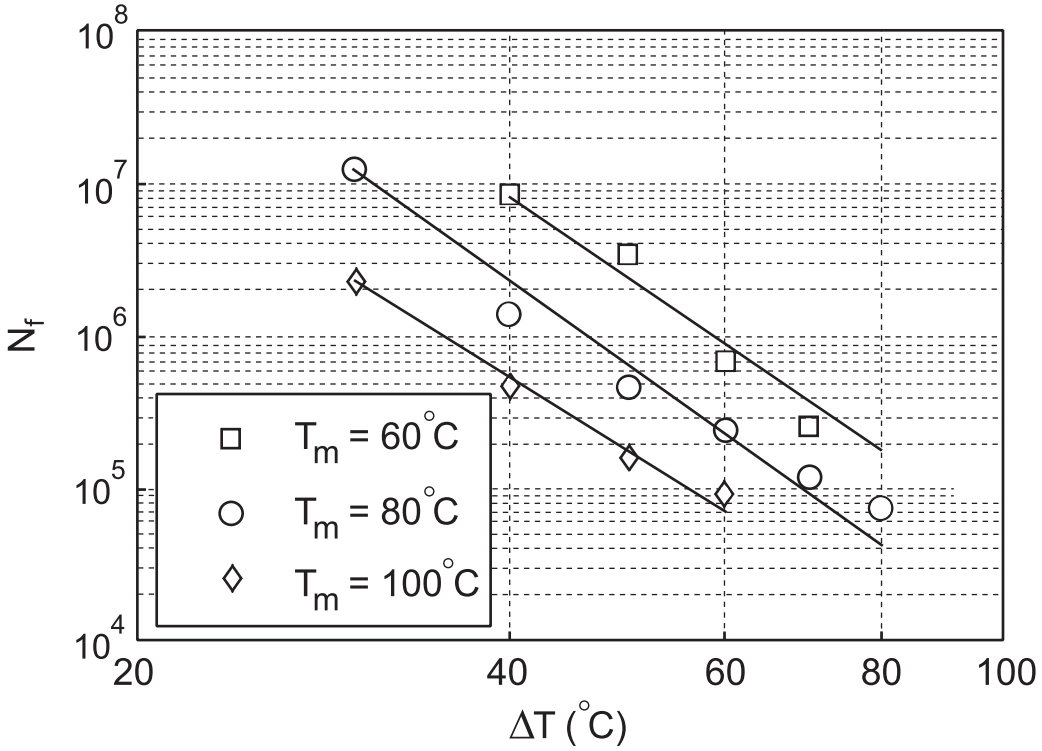

Figure 2.16: Dependence of the number of cycles to failure, N_f, on the mean (T_m) and amplitude (ΔT) of the temperature cycling taken from [66]. The lines indicate the best fit through the experimental data points.

For the solder cracking failure mechanism the relationship is more complex, and also depends on time since the solder creeps. The difficulty is that the interaction between

failure mechanisms for different temperature cycling conditions is not known with certainty [70]. It has been suggested in [71] that above the temperature range ΔT of 130K the dominant mechanism is solder cracking, while below 130K it is bond wire lift-off.

2.4 Summary

This chapter began by highlighting the role of the power converter, utilising the powertrain of the Toyota Prius hybrid electric vehicle. A detailed explanation of how a power converter operates, either as an inverter or rectifier followed. Semiconductor device power losses, more specifically, switching losses and conduction losses were introduced. These losses are worthy of mention because they are responsible for the increase in temperature of the power module packaging.

The structure of a power module package from the Toyota Prius HEV was reviewed. Attention was given to the structure which repeated with the packaging module that the simulation domain for the thermal model is based upon.

Consideration was given to the power device reliability; thermal cycling was addressed. The typical failure modes of power module packaging are featured. These include bond wire failure and solder layer degradation, solder cracks and delamination. The chapter concludes with a brief mention of existing methods of reliability estimation.

Thermo-mechanical stress-induced fatigue mechanisms are a direct result of the temperature cycling caused by rapid switching of a large load, typical of the conditions seen in a HEV. To keep these effects to a minimum, the device junction temperature swing (ΔT_j) has to be minimised; this required careful design and a thorough knowledge of heat diffusion and associated material properties.

Chapter

3 An introduction to the Physics of Heat Diffusion

Heat energy can be transferred from one place to another by conduction, convection and radiation. The majority of heat generated by the semiconductor devices in a power converter module is transported via conduction to the bottom of the power module. Other mechanisms are seldom sufficient to cause any noticeable change [43, 72]. Therefore convection and radiation are only covered briefly in this chapter. Conduction is addressed in more detail and Fourier's law is stated. Finally, the derivation of the heat equation is presented, followed by its solution using the customary separation of variables method.

3.1 Convection

Convective heat transfer tends to refer to the thermal interaction between a surface and an adjacent moving fluid. Convection is a combination of diffusion and advection. Diffusion is the random Brownian motion of individual particles in the fluid. Advection is when heat is transported by the larger-scale motion of currents in the fluid. Near the surface the fluid velocity is low, and diffusion dominates. Away from the surface, advection has the greatest significance [73].

Determination of the heat transfer rate between a surface and an adjacent fluid in motion is based on Newton's law of cooling:

$$q''_{\mathrm{s}} = h(T_s - T_\infty), \tag{3.1}$$

where q''_{s} (W) is the surface heat flux, T_s (K) is surface temperature, T_∞ (K) is the fluid temperature away from the surface and h (WK^{-1}) is the heat transfer coefficient [74].

3.2 Radiation

Electromagnetic radiation is continuously emitted from all substances because of the molecular and atomic agitation associated with their internal energy. Radiation travels directly to its point of absorption at the speed of light and does not require an intervening medium to carry it. The energy exchange between two surfaces depends on the geometry, shape, area, material crystal orientation, absorptivity and emissivity of the two surfaces. Emissivity ε refers to a material's ability to emit heat. The determination of the net heat exchange by radiation between two surfaces, q_{12} (W), can be complex. However, the analysis is simplified for an ideal model for which absorptivity is equal to the emissivity. For the case where a small surface is surrounded by a much bigger surface the net heat change exchange can be expressed by the Stefan-Boltzmann radiation law [75]:

$$q_{12} = \varepsilon_1 \sigma A_{11} ({T_1}^4 - {T_2}^4) \tag{3.2}$$

where ε_1 is the emissivity of the small surface, A_{11} (m^2) is its area, T_1 (K) its absolute temperature, and T_2 (K) is the absolute temperature of the larger surrounding surface. σ is called the Stefan-Boltzmann constant and has a value of $5.6703\mathrm{x}10^{-8}$ ($\mathrm{Wm}^{-2}\mathrm{K}^{-4}$).

3.3 Conduction

In this instance, conduction refers to heat conduction as opposed to the previous chapter where "conduction losses" referred losses which occurred in semiconductor devices conducting electrical current.

Conduction describes how energy is transmitted through solids. Heat conduction occurs by charge carrier transport, lattice vibrations, electromagnetic waves and spin waves. All these mechanisms contribute to the overall thermal conductivity of a material, denoted by k ($\mathrm{Wm^{-1}K^{-1}}$) [76]. Charge carrier transport and lattice vibrations are the main mechanisms by which conduction occurs.

3.3.1 Lattice Vibrations

Lattice vibration occurs when the nucleus of one atom vibrates causing energy to be passed on to nearby nuclei. There is no net motion of the media as the energy propagates through. Atoms vibrating more energetically in one part of a solid transfer that energy to less energetic neighbouring atoms. The effectiveness of lattice vibrations can be increased by cooperative motion in the form of propagating lattice waves, called phonons.

In insulators lattice vibrations are the dominant heat transportation mechanism and the magnitude of their lattice thermal conductivities k can vary over an extremely wide range. Diamond has a thermal conductivity of 900 - 2320$\mathrm{Wm^{-1}K^{-1}}$, higher than any metal, while in polymeric materials k can be as low as 0.003$\mathrm{Wm^{-1}K^{-1}}$ [77].

Fig. 3.1 aids the visualisation of lattice vibrations. Note that if heat energy is supplied to one part of a solid, the atoms vibrate faster. As they vibrate more, the bonds between atoms are shaken more. This passes vibrations on to the next atom, and so on. Eventually the energy spreads throughout the solid resulting in an overall temperature increase.

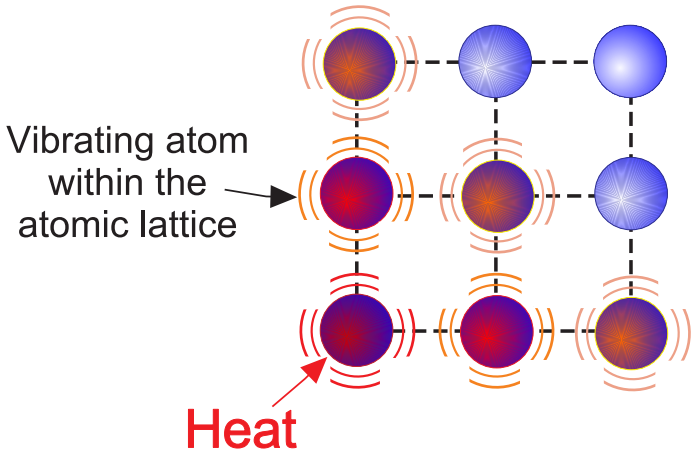

Figure 3.1: Diagram showing heat conduction due to lattice vibrations in a solid material.

3.3.2 Charge Carrier Transport

This heat transport mechanism occurs in metals. The unique feature of metals, as far as their structure is concerned, is the presence of charge carriers, specifically conduction electrons. The conduction electrons in a metal are non-localized, i.e. they are not tied to any particular atom. The same mobile electrons which participate in electrical conduction also take part in the transfer of heat. Factors which determine the heat conductivity of a metal include:

i) the density of conduction electrons,

ii) the average speed of conduction electrons,

iii) the distances that the electrons travel before they suffer a collision.

It is noteworthy that even in pure metals there is some 'thermal scattering' since the atoms are always vibrating out of position because of the energy linked with their temperature (lattice vibration). In a pure metal, the heat current associated with the flow of electrons far exceeds the small contribution due to lattice vibration. Fig. 3.2 depicts how conduction electrons become excited by the heat source and transport energy through the material.

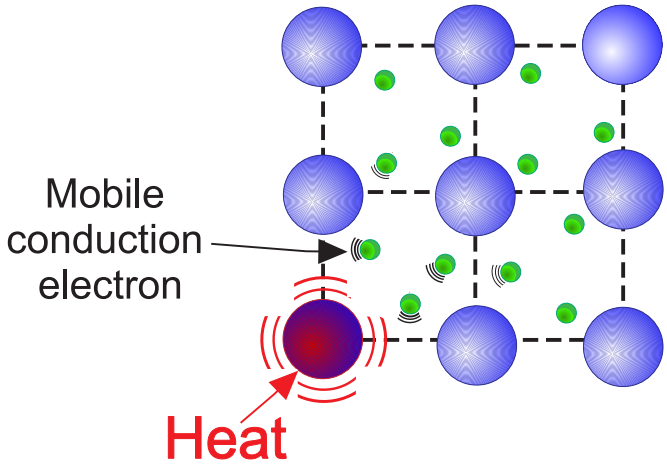

Figure 3.2: Diagram showing heat conduction in a metal due to carrier charge transport. Conduction electrons move freely within the atomic lattice.

3.3.3 Fourier's Law of Conduction

The empirical law of heat conduction states that the rate of heat flow by conduction in a given direction is proportional to the area normal to the direction of heat flow and to the gradient of temperature in that direction. It is known as the Fourier rate equation and appears in Equation (3.3).

$$\dot{Q}_n = -kA\frac{dT}{dn}, \tag{3.3}$$

where $\dot{Q}_n$ (W) is the rate of heat flow in n-direction, k ($\mathrm{Wm^{-1}K^{-1}}$) is the thermal conductivity of the material and A ($\mathrm{m^2}$) is the area normal to the n-direction. The sign convention implies that the direction of heat flow between two neighbouring points is in the direction of the lower temperature.

3.4 Derivation of the Heat Conduction Equation

The heat equation is derived from Fourier's law and the law of conservation of energy [78–80]. Consider the volume of heat conducting material in Fig. 3.3. It is a rectangular parallelepiped whose sides are parallel to the axes of coordinates and are of lengths dx, dy and dz. The solid is assumed to be homogenous, isotropic and to have thermal conductivity k which is dependent on temperature only. Q (W) represents the heat energy.

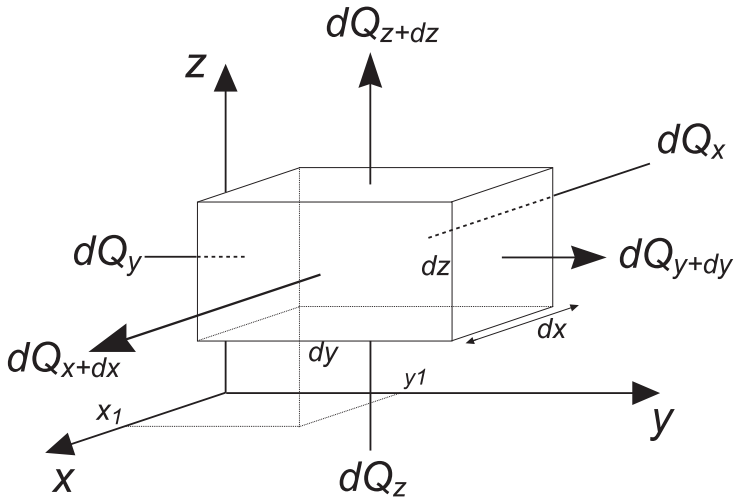

Figure 3.3: Rectangular parallelepiped of heat conducting material

According to Fourier's Law, the total quantity of heat flowing through the face $dydz$ at x_1 in time dt is:

$$dQ_{x_1} = -dydzk(T)\frac{\partial T}{\partial x}dt, \tag{3.4}$$

while the rate of loss of heat through the face $dydz$ at $x_1 + dx$ is:

$$dQ_{x_1+dx} = dQ_{x_1} + \frac{\partial}{\partial x}(dQ_{x_1})dx. \tag{3.5}$$

Substituting Equation (3.4) into the parenthesis in Equation (3.5) yields:

$$dQ_{x_1} - dQ_{x_1+dx} = dydz\left[\frac{\partial}{\partial x}\left(k(T)\frac{\partial T}{\partial x}\right)dx\right]dt. \tag{3.6}$$

Similarly from the other faces we obtain the following equations

$$dQ_{y_1} - dQ_{y_1+dy} = dxdz\left[\frac{\partial}{\partial y}\left(k(T)\frac{\partial T}{\partial y}\right)dy\right]dt, \tag{3.7}$$

$$dQ_{z_1} - dQ_{z_1+dz} = dydx\left[\frac{\partial}{\partial z}\left(k(T)\frac{\partial T}{\partial z}\right)dz\right]dt. \tag{3.8}$$

Assuming that the material does not generate its own heat, the basic law of conservation of heat energy for the volume states that the rate of change of heat inside the volume is equal to the net flow of heat through the boundaries. Therefore:

$$dQ_{net} = dQ_{x_1} - dQ_{x_1+dx} + dQ_{y_1} - dQ_{y_1+dy} + dQ_{z_1} - dQ_{z_1+dz}. \tag{3.9}$$

Using elementary physics, a change in the internal energy U of the volume in time dt can be described by:

$$dU = \rho_1 c_p dxdydz\left(\frac{\partial T}{\partial t}\right)dt, \tag{3.10}$$

where ρ (kgm^{-3}) is the density and c_p (JKg^{-1}K^{-1}) is specific heat capacity .

In the absence of work done, the first law of thermodynamics becomes:

$$dU = dQ_{net}. \tag{3.11}$$

Now substitute each of the expressions from Equations (3.6), (3.7) and (3.8) into Equation (3.9). Substituting the resulting expression and Equation (3.10) into Equation

(3.11) leads to the following expression:

$$\underbrace{c\rho\frac{\partial T}{\partial t}}_{\text{Change in thermal energy storage}} = \underbrace{\left(\frac{\partial}{\partial x}\left[k(T)\frac{\partial T}{\partial x}\right] + \frac{\partial}{\partial y}\left[k(T)\frac{\partial T}{\partial y}\right] + \frac{\partial}{\partial z}\left[k(T)\frac{\partial T}{\partial z}\right]\right)}_{\text{Net transfer of thermal energy into the control volume (inflow − outflow)}} . \quad (3.12)$$

Assuming the physical properties are constant (i.e. k is independent of temperature) results in the following 3D heat equation:

$$\frac{\partial T(x,y,z,t)}{\partial t} = \alpha\left(\frac{\partial^2 T(x,y,z,t)}{\partial x^2} + \frac{\partial^2 T(x,y,z,t)}{\partial y^2} + \frac{\partial^2 T(x,y,z,t)}{\partial z^2}\right), \quad (3.13)$$

where $\alpha = k/(c\rho)$. α is known as thermal diffusivity and represents the ratio of thermal conductivity to thermal capacity. It is a measure of how quickly heat spreads through a given material.

In order to be able to simulate heat conduction through solid matter, such as power module packaging, it is necessary to solve the 3-D heat equation. By doing so, it is possible to generate an expression for $T(x,y,z,t)$, which is the temperature distribution in a structure over time.

3.4.1 Solving the 1-D Heat Equation.

Consider the 1-D heat conduction problem in Fig. 3.4 which is the classical problem of heat conduction through a simple rod. The solution to the 1-D heat equation is an expression of $T(x,t)$. The initial temperature distribution and heat flux boundary conditions are known, called Neumann conditions. The assumption is that the rod is perfectly insulated, i.e. there is no heat flow out of the boundaries.

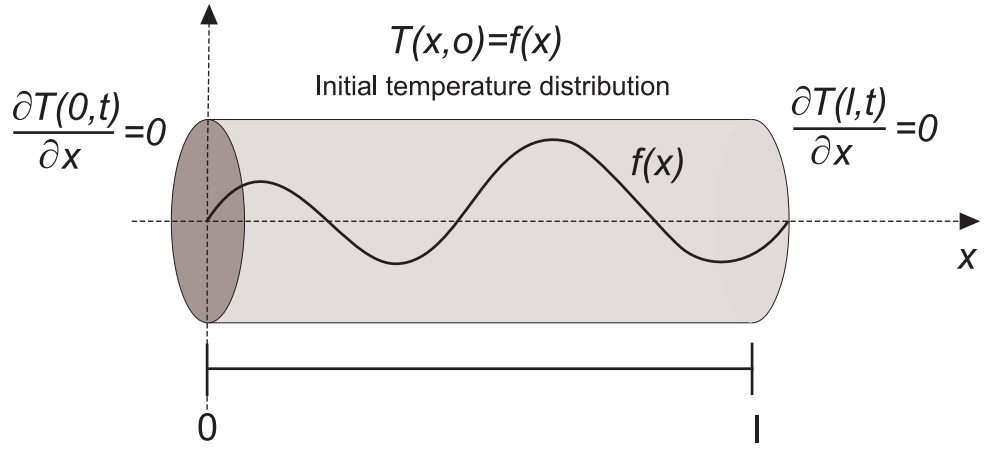

Figure 3.4: Heat conduction in a rod with known boundary conditions.

Assuming that heat energy is neither created nor destroyed in the interior of the rod, the following 1-D Heat equation applies:

$$\frac{\partial T(x,t)}{\partial t} = \alpha \left(\frac{\partial^2 T(x,t)}{\partial x^2} \right) \qquad \text{for all } 0 < x < l \text{ and } t > 0. \tag{3.14}$$

Boundary conditions:

$$\frac{\partial T(0,t)}{\partial x} = \frac{\partial T(l,t)}{\partial x} = 0. \tag{3.15}$$

Initial condition:

$$T(x,0) = f(x). \tag{3.16}$$

3.4.1.1 Linearisation of the Heat Equation

When material properties, k, c and ρ, are constant in the heat equation, it is called linear. There are many mathematical benefits; for example one can use the superposition principle. Computationally, it is much easier to solve a linear partial differential equation (PDE) than a non-linear PDE. Almost all analytical solutions require the heat equation to be linear. For numerical methods it is not a requirement but is still desirable.

3.4.1.2 Separation of Variables Method

The heat equation is a partial differential equation (PDE) which can be solved by the classical method called the *separation of variables*. The separation of variables method represents one of the most powerful and most used analytical techniques for solving a variety of PDEs. The following approach was first proposed by Fourier in his classical work *Thorie analytique de la chaleur* (1822; The Analytical Theory of Heat) [81].

Assume the solution can be separated, i.e.:

$$T(x,t) = X(x)T(t). \tag{3.17}$$

Begin by substituting (3.17) into (3.14), giving:

$$\frac{\partial}{\partial t}\left[X(x)T(t)\right] = \alpha\frac{\partial^2}{\partial x^2}\left[X(x)T(t)\right]. \tag{3.18}$$

Separate the equation so that the one side depends only on t, while the other depends only on x. Both sides must be equal to a constant (λ) since one side depends only on t and the other only on x, so the equation becomes:

$$\frac{T'(t)}{\alpha T(t)} = \frac{X''(x)}{X(x)} = -\lambda. \tag{3.19}$$

The minus sign appears for convenience. The equation in (3.19) contains a pair of separate ordinary differential equations (ODEs). The first ODE to solve is:

$$T'(t) + \lambda\alpha T(t) = 0. \tag{3.20}$$

This is straightforward to solve, rearranging and integrating leads to:

$$\int \frac{1}{T(t)} dT(t) = \int -\lambda\alpha dt. \tag{3.21}$$

Therefore:

$$T(t) = CCe^{-\lambda\alpha t}, \tag{3.22}$$

and using the law of indices:

$$T(t) = CCe^{\alpha}e^{-\lambda t}. \tag{3.23}$$

As a constant multiplied by a constant generates another constant, the expression in Equation (3.23) can simply be written as:

$$T(t) = CCe^{-\lambda t}. \tag{3.24}$$

Eigenvalues and eigenfunctions must be found for the second ODE which is:

$$X''(x) + \lambda X(x) = 0. \tag{3.25}$$

When $\lambda < 0$, there exists real numbers D, E such that:

$$X'(x) = \sqrt{-\lambda}De^{\sqrt{-\lambda}x} - \sqrt{-\lambda}Ee^{-\sqrt{-\lambda}x}. \tag{3.26}$$

Applying boundary conditions from (3.15) means that $D = E = 0$, which implies $X(x)$

is identically 0. Also, suppose that $\lambda = 0$, then there exists real numbers D, E such that:

$$X(x) = Dx + E. \tag{3.27}$$

From (3.15), in the same manner as in the previous case, it can be concluded that that $D = 0$. So every constant function $X_0(x) = E$ is an eigenvalue $\lambda_0 = 0$.

When $\lambda > 0$ there exists real numbers D, E such that:

$$X'(x) = -D\sqrt{\lambda}\sin(\sqrt{\lambda}x) + E\sqrt{\lambda}\cos(\sqrt{\lambda}x). \tag{3.28}$$

The boundary condition $X'(0) = 0$ means $E = 0$, and the boundary condition $X'(l) = 0$ provides the expression:

$$D\sin(\sqrt{\lambda}l) = 0 \tag{3.29}$$

To avoid having a trivial solution, $\sqrt{\lambda}l$ must be equal to $n\pi$. Therefore, the eigenvalues and eigenfunctions are:

$$\lambda_n = \left(\frac{n\pi}{l}\right)^2 \qquad \text{n} = 0, 1, 2...., \tag{3.30}$$

and

$$X_n(x) = \cos\left(\frac{n\pi x}{l}\right) \qquad \text{n} = 0, 1, 2..... \tag{3.31}$$

Notice the result from $\lambda = 0$ case is incorporated into this solution. The resulting functions associated with (3.24) are:

$$T_n(t) = CC_n e^{-\lambda_n t} \tag{3.32}$$

The linear combination of (3.31) and (3.32), written as the formal infinite sum for any integer N and constants $\{CC_n\}_{n=0}^{N}$, is:

$$T_n(x,t) = \frac{1}{2}CC_0 + \sum_{n=1}^{\infty} CC_n e^{\left(\frac{n\pi}{l}\right)^2 t} \cos\left(\frac{n\pi x}{l}\right), \qquad \text{n} = 0, 1, 2..... \tag{3.33}$$

The initial condition (3.16) means the following must be satisfied:

$$T(x,0) = f(x) = \frac{1}{2}CC_0 + \sum_{n=1}^{\infty} CC_n \cos\left(\frac{n\pi x}{l}\right), \qquad \text{n} = 0, 1, 2..... \tag{3.34}$$

This is nothing more than a *Fourier cosine series* expansion of the function $f(x)$ over the interval $(0, l)$. Fourier's successful approach was to substitute the expression for $\{CC_n\}_{n=0}^{N}$, from the Fourier series definition, into (3.33). This gave rise to a solution to 1D heat equation in terms of $T(x,t)$. Prior to Fourier's work there was no known solution to the heat equation.

The problem with the customary separation of variables technique is that it can only provide a solution to the 1-D heat equation, in terms of $T(x,t)$, for known analytic time-varying boundary conditions. For non-analytic time-varying boundary conditions the traditional separation of variables approach is inappropriate for the task. It merely reduces the 1D heat equation into a set of two ODEs, one ODE in terms of $T(x)$ and the other in terms of $T(t)$, which can not be solved. Therefore it is not worth incorporating the customary separation of variable technique into a thermal model to attempt to fulfil the requirements of this work. Non-analytic time-varying boundary conditions, in the form of heat fluxes, must exist to accurately simulate the material interfaces which are present in the layered structure of a power module.

Other existing thermal models should be examined to see if there are any that can fulfill all of aims set out in the motivation section of this thesis.

Chapter

4 Thermal Models for Power Converters

This chapter introduces existing thermal models which are frequently employed to calculate the temperature of power semiconductor devices used in power converters. The models are divided into separate categories; compact thermal models, dynamic compact thermal models, numerical methods and analytic solutions. The theory behind each of the thermal models and their mode of operation is considered. At the end of the chapter is a detailed discussion which examines the advantages and disadvantages of existing models. A suitable way to proceed, considering the motivation for this thesis, is then stated.

4.1 Steady State Compact Thermal Models

Compact thermal models (CTMs) provide a simple quantitative description of a modelled packaging structure. CTMs provide an abstract description of power module packaging behaviour when construction details are too detailed to be of use at the desired level of analysis. CTMs simulate quickly when compared with detailed thermal models. A requirement for a CTM is to be reasonably boundary condition independent so that the variation of the environment does not affect the compact thermal model [82].

4.1.1 Resistive Networks

Thermal resistive networks are behavioural CTMs which aim to predict steady state temperature in a package, accurately, but only at a few critical points. Resistive networks are not based on the geometry and material properties of the actual packaging. Instead, they attempt to mimic the power module packaging response to a heat source.

4.1.1.1 Single Resistor Model

A simple one-resistor network R_{j-amb} (KW^{-1}) represents the steady state thermal resistance between the junction and ambient in a packaging structure, it is defined by:

$$R_{j-amb} = \frac{(T_j - T_{amb})}{q_c} \tag{4.1}$$

where T_j (K) is junction temperature, T_{amb} (K) is the ambient device temperature, and q_c (W) is the device heat dissipation. This is analogous to Ohm's law, in which the electrical resistance is defined as the ratio of the voltage drop across a resistor to the current flow across the resistor.

This approach has been used for decades and it is still widely used today because of its simplicity and ease of application. An example of the use of this primitive network appears in [83]. According to [84, 85] a single junction-to-ambient thermal resistance is not adequate for package design, because too much information about the temperature distribution across the package is lost. If a model is to be at all useful, it should be as close as possible to reality for any boundary conditions [86, 87]. Unfortunately, the R_{j-amb} value is only valid for the one environment that it was measured in and is therefore not boundary condition independent. The one-resistor model is is not a predictive tool and therefore of little use.

4.1.1.2 Two Resistor Model

The two resistor model is derived from [88]. The two resistor network model lumps the complicated geometry of the package into two thermal resistances, as shown in Fig. 4.1.

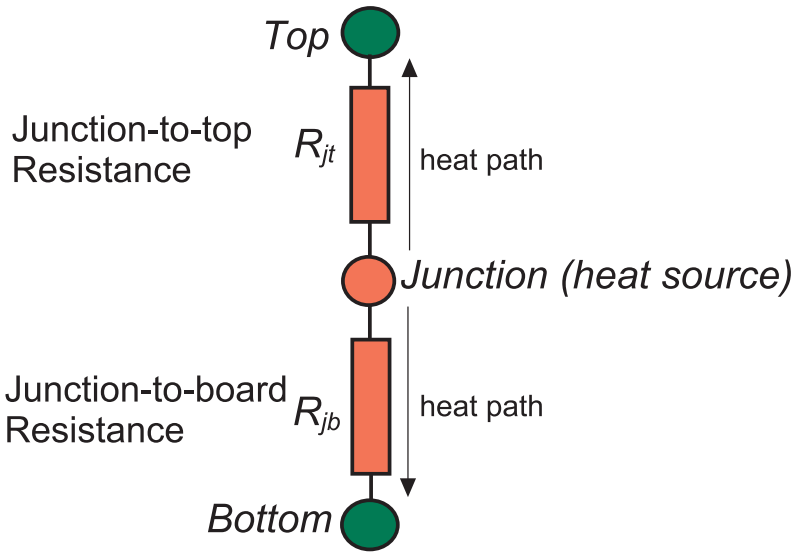

Figure 4.1: Diagram of a two resistor compact thermal model.

Attempts to create two-resistor models, in accordance with the guidelines set out by the by the JEDEC JC15.1 standards committee [89], appear in [90, 91]. Although they are not expected to provide high accuracy, two-resistor models are a major improvement in accuracy over traditional single resistor approach [92]. The advantages of the two-resistor model is its ease of generation and its low computational cost. However, the approach fails to recognise that heat may flow by more than two paths in order to leave the junction node. Model accuracy is dependent on the packaging structure and operating conditions it is modelling. In [93], the two-resistor model accuracy varied between 2-20% compared with the results from a detailed model.

4.1.1.3 Star Shaped Resistive Network

The star shaped network has a higher level of complexity than the two resistor model. The method was proposed in [84, 94, 95]. A package is characterised by a limited number of well-chosen thermal resistances. The model attempts to capture all the dominant conductive heat flow paths in a structure.

Unfortunately, many different star shaped resistive network topologies are required for each of the different packaging structures [96]. In [97], the star shaped model failed to predict accurately the junction temperature for packaging structures attached to heat sinks, which indicates the model is not fully boundary condition independent.

4.1.1.4 DELPHI Model

The DELPHI (development of physical models for an integrated design environment) model is shown in Fig. 4.2. It is an extension of the star shaped method because resistive paths are considered which are not aligned with the heat source.

In [93], the DELPHI compact model was found to have an accuracy within 5% of a detailed model. According to [99], the DELPHI model is reasonably boundary condition independent since it is not limited to certain packages or environments.

Unfortunately, the extraction of the DELPHI compact model is time-consuming because the process involves many network nodes. As stated in [97], dedicated compact model generation software is required to produce DELPHI models. This suggests a high computational cost compared with the two-resistor model.

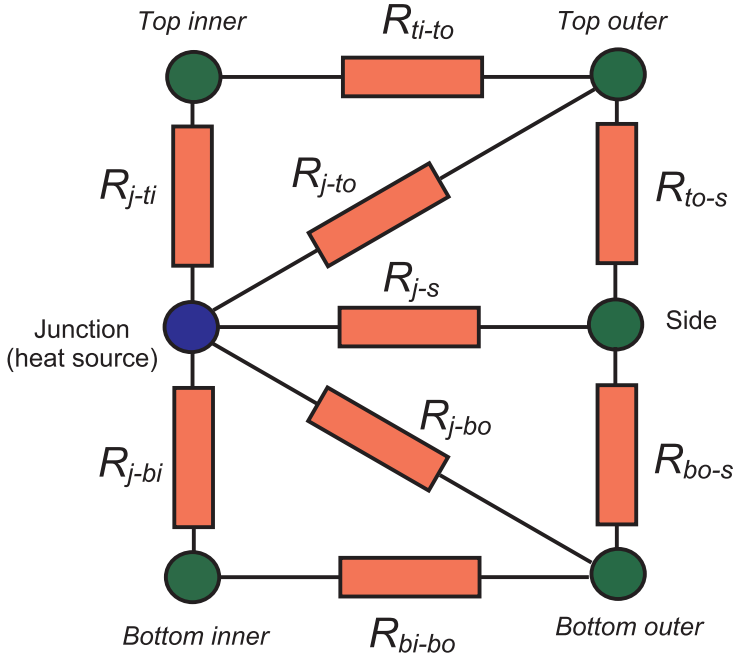

Figure 4.2: Diagram of a typical multi-resistor (DELPHI) compact thermal model [98].

4.2 Dynamic Compact Thermal Models

Dynamic Compact Thermal Models (DCTMs) can mimic the transient thermal response of a heated packaging structure. This is a clear advantage over ordinary CTMs which can only simulate a package in steady state conditions. The main methods for constructing DCTMs can be divided into two categories:

i) RC equivalent circuits,

ii) Reduction models.

4.2.1 RC Equivalent Circuits

An electrical equivalent circuit is created to provide a transient response which describes the transient thermal impedance of the packaging structure. It employs the well established thermal-electrical analogy which is stated in Table 4.1.

Table 4.1: Corressponding physical variables using the electrical-thermal analogy

Thermal		$\Longleftrightarrow$	**Electrical**	
Temperature	(K)		Voltage	(V)
Power	(W)		Current	(A)
Thermal resistance	(KW^{-1})		Electrical resistance	(Ω)
Thermal capacitance	(JK^{-1})		Electrical capacitance	(F)

Typically, a transient thermal impedance curve resulting from a step change in power is required to extract a RC network. Power module manufacturers tend to provide normalised impedance curves, as shown in Fig. 4.3. $Z_{th(j-c)}(t)$ represents the transient thermal impedance from junction-to-case. Values of $Z_{th(j-c)}$ can be obtained by multiplying the value of steady state thermal resistance $R_{th(j-c)}$ by the normalised factor taken from the curve at the time of interest. $R_{th(j-c)}$ is specified by a packaging manufacturer and is typically between 0.2-0.4 K/W for a power module [100]. Unfortunately, manufacturers tend to provide information which is unreliable. Furthermore, data concerning $Z_{th(j-c)}(t)$ does not allow for the presence of the power module heatsink.

The transient thermal impedance curve of $Z_{th(j-amb)}(t)$ is needed. This represents the transient thermal impedance between the junction and ambient conditions, therefore including the heatsink. Fortunately, a cooling/heating curve representing the junction temperature $T_j(t)$ may be generated by simulation software employing numerical methods or from experimental measurements. From a curve of $T_j(t)$ it is possible to generate a curve of $Z_{th(j-amb)}(t)$ using Equation (4.2):

$$Z_{th(j-amb)}(t) = \frac{T_j(t) - T_{amb}(t)}{P}, \tag{4.2}$$

where t (s) is time, $T_{amb}(t)$ (K) is the known ambient temperature and P (W) is the known power distribution step.

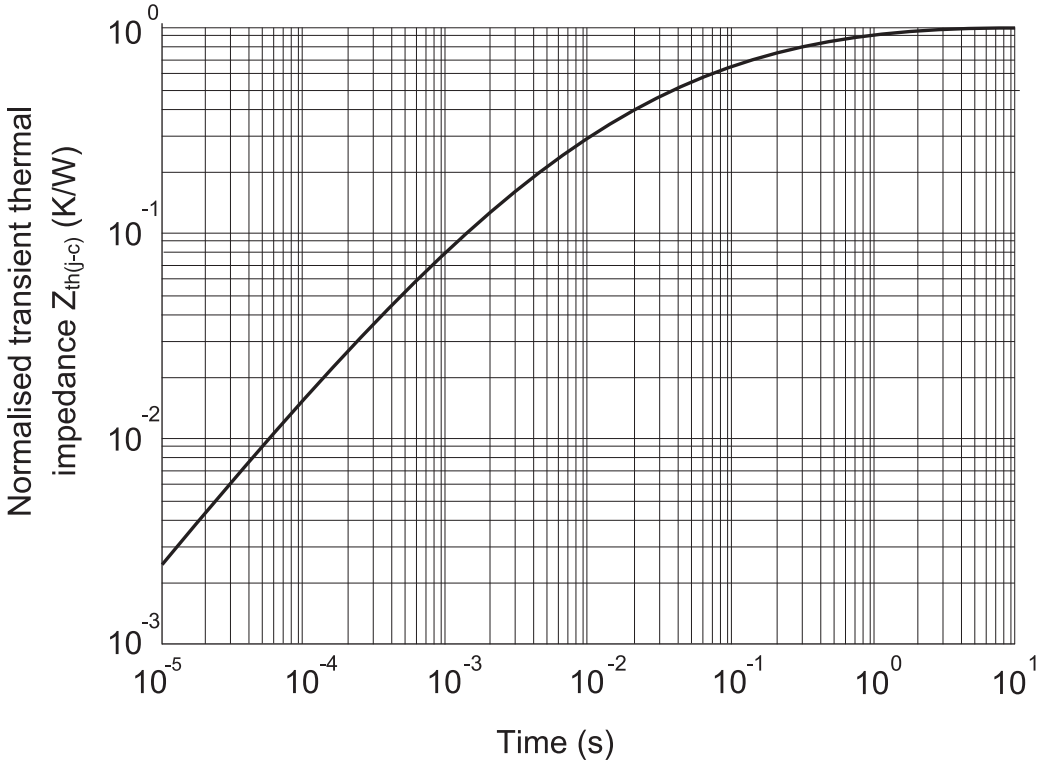

Figure 4.3: Graph showing a typical normalised transient thermal impedance curve which would be provided by a power module manufacturer.

An equivalent circuit may then be fitted to $Z_{th(j-amb)}(t)$ in light of the following approximation:

$$Z_{th(j-amb)}(t) = \sum_{i=1}^{n} A_i \left(1 - e^{-\frac{t}{\tau_i}}\right) \tag{4.3}$$

where A_i (KW^{-1}) is the pre-exponential coefficient and τ_i (s) is the time constant. Examples of this curve fitting approach appear in [24, 26, 28–30]. The two dominant types of RC equivalent circuits are the Foster (partial fraction) model and the Cauer (continued fraction) model.

4.2.1.1 Foster Model

The Foster model equivalent circuit appears in Fig. 4.4. Its networks element values are related to Equation (4.3) by: $R_i = A_i$; $C_i = \frac{\tau_i}{A_i}$.

This property simplifies determination of the values of the equivalent elements and which can be directly fitted as shown in [101]. Its computational simplicity explains the wide application and popularity of this equivalent network.

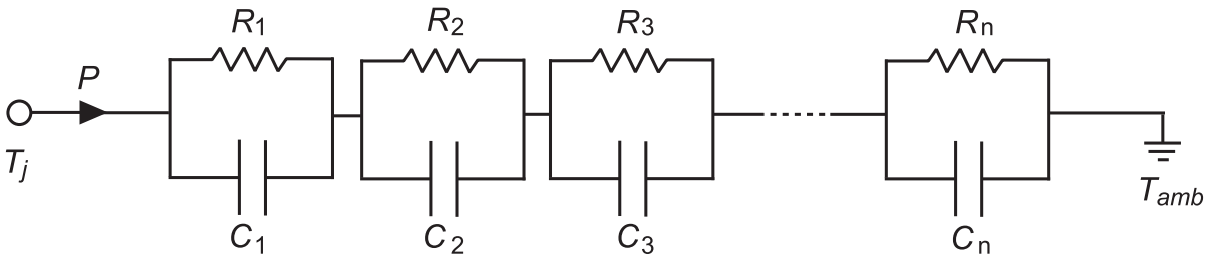

Figure 4.4: Foster RC equivalent circuit.

The Foster network is a "black box" approach. It can describe the curve of the junction temperature with any excitation but it has no physical meaning since its RC elements are not directly related to the layers in the structure. Therefore, the Foster model can not be used for physical identification of heat flow through the structure [102–104]. The reason is that the node-to-node capacitances are physically inconsistent, as stated in [25, 27, 105]. For instance, if a pulse of thermal power is injected at the model input the temperature at every internal node would change immediately due to the capacitors forming a series connection between input and the output side. This differs from reality, where there is a time delay before the heat diffuses through the structure. Another weakness of this "black box" approach is that it would be necessary to produce a new graph of the transient junction temperature, and then recalculate the values for all of the RC elements, if an extra layer was added to a structure which had been previously modelled.

4.2.1.2 Cauer Model

The Cauer model equivalent circuit appears in Fig. 4.5. The Cauer model is the transmission line equivalent circuit [106–108] containing grounded capacitors and floating resistors. It is able to describe the internal heat flow of the structure it is modelling. There is a clear correlation between the RC elements in the equivalent circuit and each physical layer of the power module package. Unfortunately, component manufacturers do not make the value of network parameters readily available.

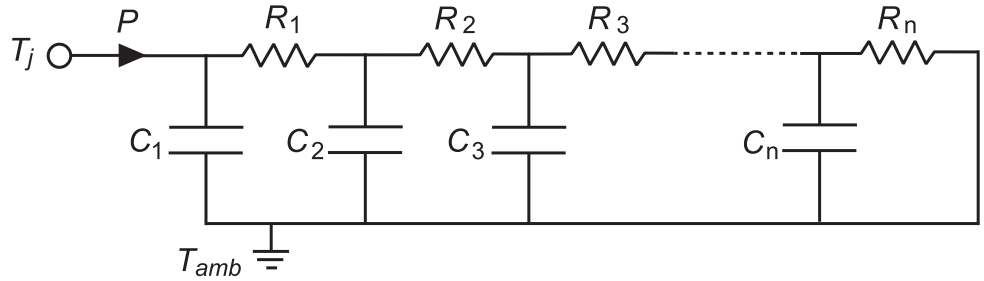

Figure 4.5: Cauer RC equivalent circuit.

Therefore it is necessary to determine values for the RC elements in the structure, a process known as parameter extraction. This is a long arduous process when using the step response of the Cauer network since it is difficult to achieve mathematically [109]. It occurred with limited success in [110], which required a Laplace transform and aid from a curve fitting algorithms.

The Cauer network can also be obtained by converting from a Foster network [111, 112]. However, this conversion should be used with caution since it is only valid when T_{amb}, labelled in Fig. 4.4 and Fig. 4.5, can be considered constant.

Unfortunately, both approaches which are used to obtain Cauer networks invoke some numerical difficulties because there is no one to one relation between any single network element and the terms in Equation (4.3), unlike the Foster network. A further drawback of the Cauer model is that it cannot accurately represent lateral heat spreading [113, 114].

4.2.2 Model Order Reduction Models

Recently there has been a surge in interest in Model Order Reduction (MOR) compact thermal models [115–121]. MOR models are an approximation of large-scale dynamic systems obtained through formal model reduction procedures based on a solid mathematical background. Fig. 4.6 outlines how MOR models are generated.

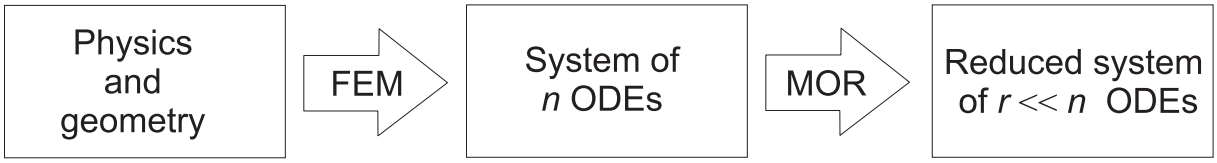

Figure 4.6: Model order reduction

The starting point is a detailed thermal model constructed in a Finite Element (FE) simulator. It is created from the known material properties and geometry of the packaging structure being modelled. Using an accurate high dimensional FE solver to discretise in space, it is possible to convert from the governing 3-D heat equation from a partial differential equation (PDE) system, to a system of n ordinary differential equations (ODEs). The system of ODEs in matrix form appears as shown in Equation (4.4):

$$\dot{T}(t) = FT(t) + GFu(t), \tag{4.4}$$

where $T(t)$ is the vector of unknown temperatures at nodes made during the discretisation, G is the load vector, F is the system matrix and $u(t)$ is the input function. An engineer rarely needs to know the temperature at every single node in the finite element structure. Using the output matrix H, the required output $y(t)$ can be expressed as:

$$y(t) = HT(t). \tag{4.5}$$

Vector $T(t)$ has a high dimensionality in a FE solver when simulating 3-D geometries.

This explains the long computation times associated with FE solvers. A solution to this problem is Model Order Reduction which creates a low-order system that reasonably well approximates the large scale dynamic system. The inputs $u(t)$ and outputs $y(t)$ remain the same size but the dimension of the state vector $T(t)$ is reduced from n to r dimensions. Fig. 4.7 shows how the dimensions of the terms in Equation 4.5 and Equation 4.4 change as a result of MOR. This drastic reduction in matrix dimensions gives rise to a compact MOR model which requires less computational work to simulate heat diffusion than a FE thermal model.

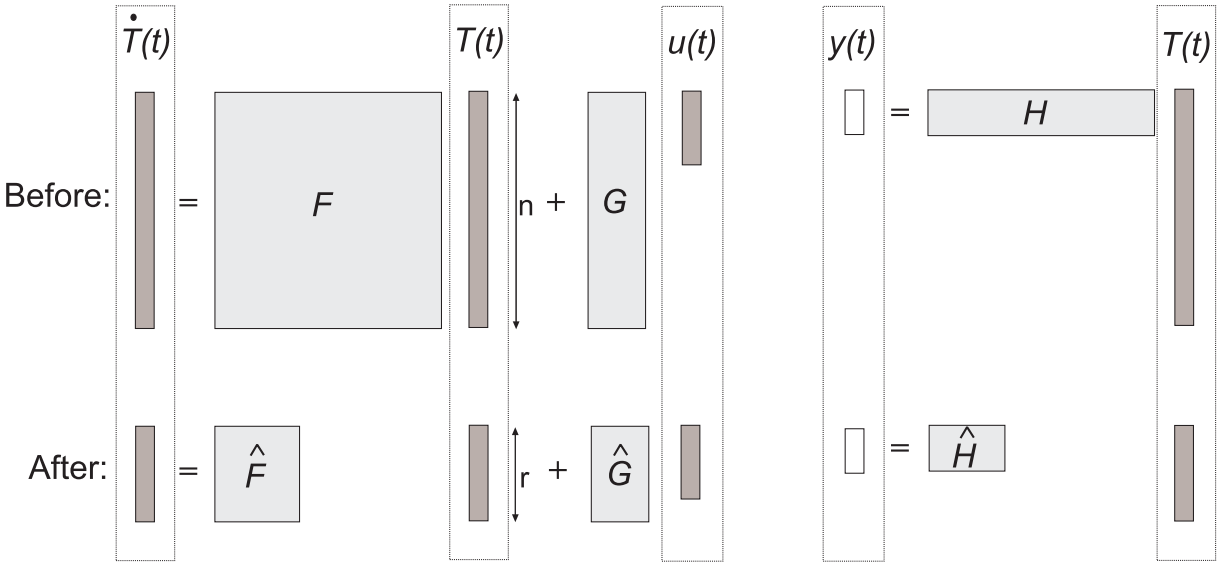

Figure 4.7: ODE system model order reduction details [115].

Every type of MOR model has the same objective which is to reduce the number of terms or functions in a FE model while preserving an acceptable level of accuracy.

4.2.2.1 Krylov Subspace-based Approaches

In Krylov subspace-based approaches [116–119] the idea is to describe the behaviour of vector $T(t)$, through the low-dimensional subspace, called Krylov subspace. This is typically achieved by means of the Arnoldi [120] process or a Lanczos algorithm [121]. These

iterative procedures reduce the system by several orders of magnitude with minimum loss of precision. Krylov subspace-based approaches are computationally fast and can be applied to very high-dimensional first order linear systems. One minor drawback is the fact the user has to select the order of the reduced system manually. There is no way to estimate the error that this approach produces.

4.2.2.2 Single Value Decomposition Approaches

Single value decomposition (SVD) approaches have a global error estimate and may be operated in a fully automatic manner. The SVD-based approaches were developed in control theory [122] and are a way of factorising matrices into a series of linear approximations that expose the underlying structure of the matrix. The downside of this approach is the level of computational complexity involved. It can only describe systems with fewer than a few thousand unknowns. There is a lack of experience in this field and no software packages have been commercially released.

4.2.2.3 Guyan Algorithm

The Guyan algorithm [123, 124] is a model order reduction method which projects a high dimensional ODE system to a lower-dimensional one. It works by eliminating equations from non-terminal nodes by means of linear algebraic operations. It is commercially available within the FE solver ANSYS [125] which has a built-in automatic "master" node selector [126]. This approach results in unnecessary large reduced order models and does not provide the required accuracy for electro-thermal simulations [127].

4.3 Numerical Methods Thermal Models

No single compact model can be 100% boundary condition independent. That is only achievable by with the use of a so-called detailed model which has an infinite number of degrees of freedom [128]. Computer-aided-design (CAD) drawings can often be exported into detailed thermal models (DTMs) which makes it possible to represent physical geometry in great detail. Thus, the DTM can look very similar to the actual package geometry. A DTM will accurately predict temperature at various points within the package regardless of the cooling environment in which it is placed. DTMs can require excessive computational resources and are time-consuming.

If the domain is split into many small pieces, that discretises the space, one can approximate the temperature field within an element by using local shape functions and express the the whole temperature field in a piecewise fashion. This solution is referred to as "numerical". Numerical methods can be described as dynamic detailed thermal models because they provide transient solutions. There are several methods associated with a mesh, which partition the arbitrary computational domain into smaller units. These are the finite difference method (FDM), the finite volume method (FVM) , the finite element method (FEM) and the boundary element method (BEM). Each of these numerical methods is described and some basic considerations associated with solving 3-D heat conduction in power module packaging is provided.

4.3.1 Finite Element Method

Despite becoming popular in the 1960s, this method was not provided with rigorous mathematical foundation until 1973 with the publication of [129]. FEM has since become a branch of applied mathematics for numerical modeling of physical systems in a wide

variety of engineering disciplines.

The method involves spatially discretising the domain under study into a mesh of polytopes. The governing PDE therefore becomes a series of smaller elements which are represented by a system of Ordinary Differential Equations (ODEs). An assembler program passes over all the elements of the mesh, passing relevant information to an appropriate element subprogram, and receives back the small ODE coefficient matrices. The behaviour over the entire problem domain is determined by adding up the element contributions into a large sparse global system of matrices. Once complete, the FE program can proceed to solve the ODE system [130].

[34] states that the main advantages of the FEM are that conservation laws are exactly satisfied even by coarse approximations. Another attractive feature of the FEM is its ability to handle complicated irregular geometries with relative ease.

In FEM local mesh refinement is necessary where the dimensions of neighbouring materials are significantly different. This process is straightforward but time-consuming. Unfortunately, mesh refinement is necessary when modelling the power modules packages because the layer thickness varies greatly throughout the structure. A further drawback of FEM is that meaningful calculations tend to come from users who have undergone appropriate FEM software training. Accurate 3-D thermal simulation of power module packaging has occurred using the software package ANSYS [125] which appears in [131–133]. The greatest problem with FEM is that it requires a great degree of computational complexity. It renders FEM too slow to be embedded in the framework of the electro-thermal simulator shown in Fig. 1.3.

4.3.2 Finite Volume Method

The first step in the FVM is to divide the domain into a number of control volumes. The meshing requirements are similar to FEM; however, there is a major difference in the way that the element matrix contributions are computed. The finite volume method is based on the integral conservation law equation rather than the governing partial differential equation [134]. Conservation is satisfied for every control volume as well as for the whole computational domain.

The Finite Volume Method (FVM) is the most versatile discretisation technique and can even be applied to compressible flows. FVM solvers are more efficient than FEM solvers and require less memory. Another advantage of the finite volume method is that it is easily formulated to allow for unstructured meshes. Accurate transient thermal 3-D finite volume models of the power module packaging, carried out using commercially available software package FLOTHERM [135], can be found in [136–138]. Whilst having many advantages over FEM, FVM suffers many of the same drawbacks, mesh refinement is necessary and it is too slow to co-simulate with the circuit simulator in Fig. 1.3.

4.3.3 Finite Difference Method

Historically, the FDM was the first numerical method. It started gaining prevalence in the 1930s following the work of *R. Courant et al* [139].

The finite difference method (FDM) is an alternative way of approximating solutions of PDEs. It relies on transforming the PDEs into a group of solvable algebraic equations [140]. FDM involves dividing the whole geometry into a mesh of discrete nodes. The mesh is essentially cartesian although the mesh may also be defined along curvilinear co-ordinates [130]. The mesh is not as versatile as that of FEM and so it can not model

all geometries accurately, which explains why it is not that popular commercially.

An advantage of FDM is its formulation of ODEs. The focus is on neighbouring nodes along mesh lines which means that discretisation is straightforward and intuitive. Very fast methods exist to solve this special case and it is simple to implement [141]. As FDM is restricted to a so called structured mesh, it may only be applied to regular geometries. Conveniently, power module packages are normally simple rectangular structures so this restriction is not an issue. In [35] and [36], FDM models have simulated heat conduction in such structures.

Unfortunately, the quality of the approximation between grid points tends to be poor in FDM, therefore many nodes are required to generate accurate results. This is inefficient and results in long simulation times which renders FDM unsuitable for use in the electro-thermal converter simulator in Fig. 1.3.

4.3.4 Boundary Element Method

Despite gaining prevalence around the same time as FEM, the boundary element method (BEM) has been slow to gain acceptance compared to FEM. In BEM, the governing PDE is rewritten as a boundary integral. In contrast to the other methods, the mesh is one dimension lower than the computational geometry because only the boundary of the geometry is discretised for 3-D analysis. This gives rise to an important time saving in the creation and modification of the mesh and it minimises the number of algebraic equations. Despite these advantages, simulation speed is still an issue. Boundary element formulations typically give rise to fully populated matrices. This means that the storage requirements and computational effort is greater per unknown than other methods leading to a slow simulation speed. The time taken to form the BEM equations also has a negative impact on the simulation speed.

BEM is applicable to problems for which Green's functions can be calculated. Therefore the use of Green's functions provides an exact analytical solution to the governing heat equation (PDE) and BEM can be used to solve transient heat conduction in 3-D electronic packages as shown in [142–144].

4.4 Analytical Solutions

Analytical methods of solving the heat equation are based on the concept of computing solutions as sums of infinite series employing different kinds of expansion techniques. Then it is possible to use these methods to obtain exact mathematical formulae describing the temperature distribution in the entire structure. Usually, analytical models suffer from the drawback that the structure geometry to be modelled is too complex. However, power module packaging has a simple rectangular geometry. The two most commonly used series expansion techniques are Green's functions and the Fourier series expansion.

4.4.1 Green's Function Technique

Green's functions are versatile mathematical tools suitable for obtaining solutions of linear heat conduction problems in power module packaging. The temperature distribution is calculated by summing all the elemental contributions. This is achieved by integrating over the sources in the directions which heat propagates.

Green's Functions can be derived using many different methods, such as the Image method [145] and from the Fourier method of separation of variables [146]. All these methods yield solutions in different but mathematically identical form.

Green's functions are capable of simulating heat diffusion from multiple heat sources. Another feature of Green's functions is that they can easily be extended from 1-D up to

2-D or 3-D Green's functions [147]. Unfortunately, Green's function do not generate a whole temperature distribution map easily and suffer from poor accuracy [148].

A further shortcoming of Green's functions is that they tend to display slow convergence [149]. Thermal models using Green's functions are too slow to be embedded into the electro-thermal converter simulator in Fig. 1.3. Although, in [150] and [104] a RC network has been generated from the results of a Green's function model to overcome the issue of slow simulation speed.

4.4.2 Fourier Series Expansion

All of the Fourier Series Expansion approaches use Fourier's separation of variables technique but not in the traditional sense of solving a PDE with a set of known analytic time-varying boundary conditions. It is called separation of variables because the space and time variables are solved separately. This is possible due to the linearity of the heat equation. The Fourier series expansion is invariably used to discretise in space.

In 1972 Lindsted and Surty [151] used the Fourier series expansion approach to evaluate the 3-D temperature distribution generated by a rectangular heat source placed on the surface of a device. A few years later Kokkas [152] presented a solution which determined the temperature distribution in the top surface of a multi-layered rectangular structure. Dorkel et al [153] advanced that work by creating a model which could simulate a structure with various cross-sectional areas. The Fourier Method was employed in simulators called Monstra [154] and Therman [155].

A major drawback of all the Fourier models mentioned so far is that they are only able to describe 3-D temperature distribution in a packaging structure at steady state. They are unable to produce a 3-D transient thermal models of a packaging structure using a purely analytical approach. In [154], an FEM simulator was used to generate transient

results, while [155] was dependent on experimental results. [152] and [153] attempted to generate transient models by using a Laplace transform to discretise temporally. Unfortunately, they were only able to generate transient results for one single block of material. Clearly, this is of limited benefit to a thermal designer. In the literature, only a limited amount of research appears on use of the Fourier series expansion for this very reason. Instead, researchers have tended to focus their effort on finite difference approaches from which transient models can be generated easily in an intuitive fashion.

The recent work of Du et al [37, 38] revisited the Fourier series expansion. In this, a transient Fourier thermal model was created which can describe the 2-D temperature distribution in a heated packaging structure over time. This purely analytical approach is able to model structures with varying cross-sectional areas. The model has been created by using the Fourier cosine expansion to discretise in space which reduces the governing heat equation (PDE) into a set of ODEs. The ODEs can be written in matrix form into a group of solvable algebraic equations. These ODEs are solved using the dynamic solver MATLAB/Simulink, which discretises temporally. This approach can accept non-analytical boundary conditions over time, and therefore simulate heat diffusion for general cases. The model can be embedded in the electro-thermal converter simulator in Fig. 1.3, and therefore the thermal model is able to model the transient device temperatures during realistic converter operation.

The Fourier model has a significant advantage over FDM. The Fourier series expansion approach can describe a device temperature distribution over a silicon device as a smooth curve even at very low resolution, especially if the shape is similar to one of the harmonics. The FDM numerical method cannot, however; it may only describe the temperature profile as a straight line between nodes, as shown in Fig 4.8. FDM requires a large number of nodes in order to model a curved distribution with sufficient accuracy. Therefore the

Fourier model tends to require fewer terms than a FDM model especially in the 3-D case which potentially gives it a faster simulation speed.

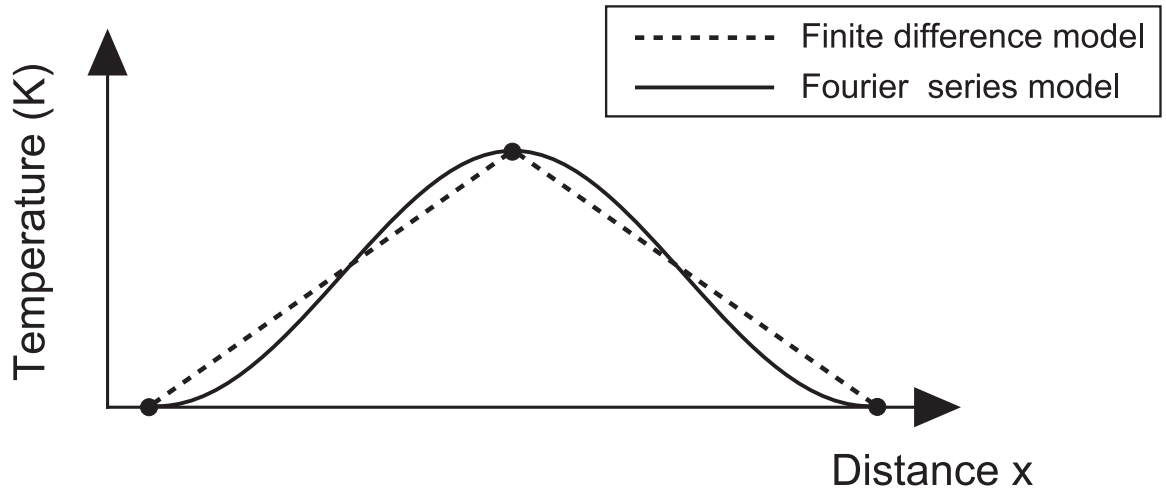

Figure 4.8: Comparison between a device temperature distribution produced by the Fourier method and finite difference model at very low resolution.

A beneficial feature of the Fourier models are that they are able to calculate the solution directly from the material properties and geometry of a structure. It is therefore likely to be a useful design tool that may be used to calculate an optimal set of geometrical parameters. The models are able to represent the whole temperature distribution in a packaging structure; in doing so the model can supply important information to a thermal designer.

In practice, only a finite number of Fourier terms can be summed using this approach. Consequently, the Fourier model relies on the truncation of the theoretically infinite Fourier series which will inevitably lead to an error. Fortunately, higher-order Fourier terms have a negligible effect on the solution because the series rapidly converges to zero. The number of expansion coefficients retained depends on the precision needed. However, there are no strict guidelines on how many Fourier coefficient to select to obtain the desired accuracy.

4.5 Discussion

None of the resistive networks featured in this chapter are suitable thermal models for power converter packaging. As pointed out by [128], the problem with all the resistive networks stem from the fact that heat does not flow from one "point" to another "point" and the flow of heat is inevitably different from 1-D flow of electrical current in wires: it is in fact 3-D diffusion.

The most significant drawback of resistive networks is that they are steady state models. Therefore they can not carry out transient thermal simulation of power converters during realistic operation, which is essential in order to predict the reliability of power module packaging. Transient temperature profiles are far more important than the steady state temperature provided by these resistive networks [156–158] because semiconductor devices in power modules are subjected to large transient heating loads that are often several orders of magnitude larger than corresponding steady state loads [159]. Such transient heating loads lead to dynamic thermal stresses which are damaging due to their repetitive nature causing fatigue [62, 160, 161]. Therefore dynamic compact thermal models are essential.

Generating transient RC equivalent circuits as thermal models is popular because the thermal models can be easily implemented in an electro-thermal circuit simulator. However, their generation is a manual process and the likelihood of human error is great, especially when attempting to model 3-D heat diffusion in the extensive RC network shown in [103]. A designer must also choose the number and position of the RC ladders without strict guidelines. The parameter extraction involved is also unattractive to a packaging designer because it is a manual time consuming process. In optimising the design of a converter and packaging, the designer must test many different layouts. For each

geometrical layout of the packaging structure which is tested, the designer must return to the starting point which is either an FEM/FDM simulation or a practical experiment [31, 32]. Both models struggle to model coupling from multiple heat sources [162–167].

Consideration has been given to the dominant Model Order Reduction (MOR) models which exist; the Krylov subspace approach appears the most suited to modelling the type of structures encountered by a converter designer as it can handle large linear models. MOR models can be embedded into electro-thermal simulators, such as that in Fig. 1.3. This was also a feature of RC networks, however, MOR models possess the following advantages over RC networks:

i) there is no time consuming parameterisation,

ii) the procedure involves following clear guidelines,

iii) it can accurately simulate multiple heat sources [168].

Nevertheless, MOR approaches do share a similar significant drawback with RC networks. MOR models are generated from FEM simulations and are therefore structure specific. MOR compact models can carry out fast transient thermal simulation for a given structure under a set of boundary conditions without being able to generalise the model and make it re-usable for all structures. Clearly, it is desirable to use compact models which do not rely on time-consuming detailed FEM simulations as a starting point. A compact thermal model is required which can be generated directly from the material properties and the geometry of a structure.

The numerical methods featured in this chapter are powerful simulation tools, which can analyse complex structures and provide accurate results. Numerical methods are not computationally efficient and demand a long computation time to simulate realistic converter load cycles with sufficient accuracy, especially for 3-D structures. In addition, the user is often required to generate a structural model and a suitable mesh which

can occupy even more time. Commercially available simulation software, which usually employ numerical methods, cannot be integrated easily into a electro-thermal converter simulator which is one of the goals of this work. Also, the cost of the software license can be expensive and the user may require training.

The most promising approach is the Fourier expansion approach used by Du et al [37, 38]. This is a purely analytic method of solving the heat equation based on the concept of computing solutions as sums of the infinite series. In this case, a geometrical 2-D Fourier expansion is employed to obtain an exact mathematical formula describing the 2-D temperature distribution in an entire packaging structure. Therefore it is possible to determine the temperature distribution across a device, rather than rely on it being represented as a node, as with some compact thermal models. The model is also able to simulate 2-D heat diffusion through boundaries where the cross-section of a structure changes. This Fourier model offers an improved trade off between simulation speed and accuracy compared to FEM/FDM simulations. The method simulates with a speed approaching that of RC networks but without the presence of artificial assumptions. Unlike previous attempts using the Fourier expansion approach, Du et al have produced a transient thermal model which is suitable to co-simulate with the circuit simulator in Fig. 1.3, enabling long mission profiles to be simulated. The approach is superior to the other main analytical model that uses Green's functions. The Green's function models are slower to converge and require a greater computational cost. This means that models based on Green's functions are not suitable to be embedded into the electro-thermal circuit simulator in Fig. 1.3. The Du et al model in [37, 38] contains some unavoidable simplifying hypotheses which enable numerical calculation to be carried out. For example, it assumes that there is zero contact resistance at a material boundary, which is clearly different from reality. However, it remains an attractive early stage design tool particularly as

it can simulate directly from the model geometry and material properties. Therefore, a packaging designer can search for optimum design configurations effectively. The need for prototyping is eliminated which reduces costs and potentially the time-to-market of a new product. There is also no parameter extraction process, making the use of FEM/FDM commercial simulators no longer necessary.

As stated, the work by Du et al [37, 38] has some very positive features, however, there are aspects of the model which require improvement. The first and obvious improvement would be to extend the model so that it could simulate full 3-D diffusion rather than 2-D. Furthermore, the approach used to model the 2-D material boundaries in [38] seems ineffective; it resorts to converting the temperature distribution of the materials either side of the boundary from the Fourier domain to the spatial domain. The material boundary is then represented as a row of nodes along where the materials come into contact. The representation of flux which is obtained is then returned into the Fourier domain. This approach to the material boundaries would not model 3-D diffusion through material boundaries with differing cross-sectional areas in both the x and y lateral directions. A more elegant approach with a firm mathematical background would be preferable. Ideally, the boundary situation would be modelled by allowing all the data to remain in the Fourier domain because this would increase the simulation speed of the model. Another failure of the approach proposed by Du et al is that it cannot easily support material boundaries where multiple heat sources come into contact with a single layer. This is the situation which occurs in power module packaging, as shown in Fig 2.9. The model also seems to use an excessive number of Fourier coefficients throughout the whole structure. One reason for this could be that it supports the existing approach to modelling the material boundaries.

A suitable way to proceed is therefore to create a 3-D Fourier thermal model based on the approach set out by Du et al in [37, 38]. The objective is to make the required improvements which have been mentioned on the previous page. This will give rise to a a fast and accurate compact 3-D thermal model which can:

- model the layered structure similar to that in Fig. 2.10,
- provide results in the form of a transient 3-D temperature distribution,
- co-simulate with the circuit simulator in Fig. 1.3.

Chapter

5 Fourier Thermal model

The next two chapters show the development of a Fourier thermal model. The model can simulate heat conduction through the whole of a power module packaging structure. Chapter 5 describes the basic model in 1-D, 2-D and 3-D. Chapter 6 describes the method used for modelling the material interfaces between packaging layers.

The Fourier thermal model relies on the assumptions stated at the start of this chapter in the model hypothesis. The remainder of this chapter demonstrates how the Fourier thermal model was developed to the stage where it could simulate 3-D heat conduction through a single block of material. Each stage of model development has been validated against the FVM commercial software package FLOTHERM.

5.1 Model Hypothesis

The Fourier thermal model is required to model power converter packaging. Fortunately, power converter packaging tends to consist of a structure - usually rectangular in nature - which is repeated many times in order to form the whole power converter packaging. The repeated structure packaging of a Toyota Prius HEV converter is highlighted in Fig. 2.9. Therefore, the simulation domain need only be the structure shown in Fig. 5.1.

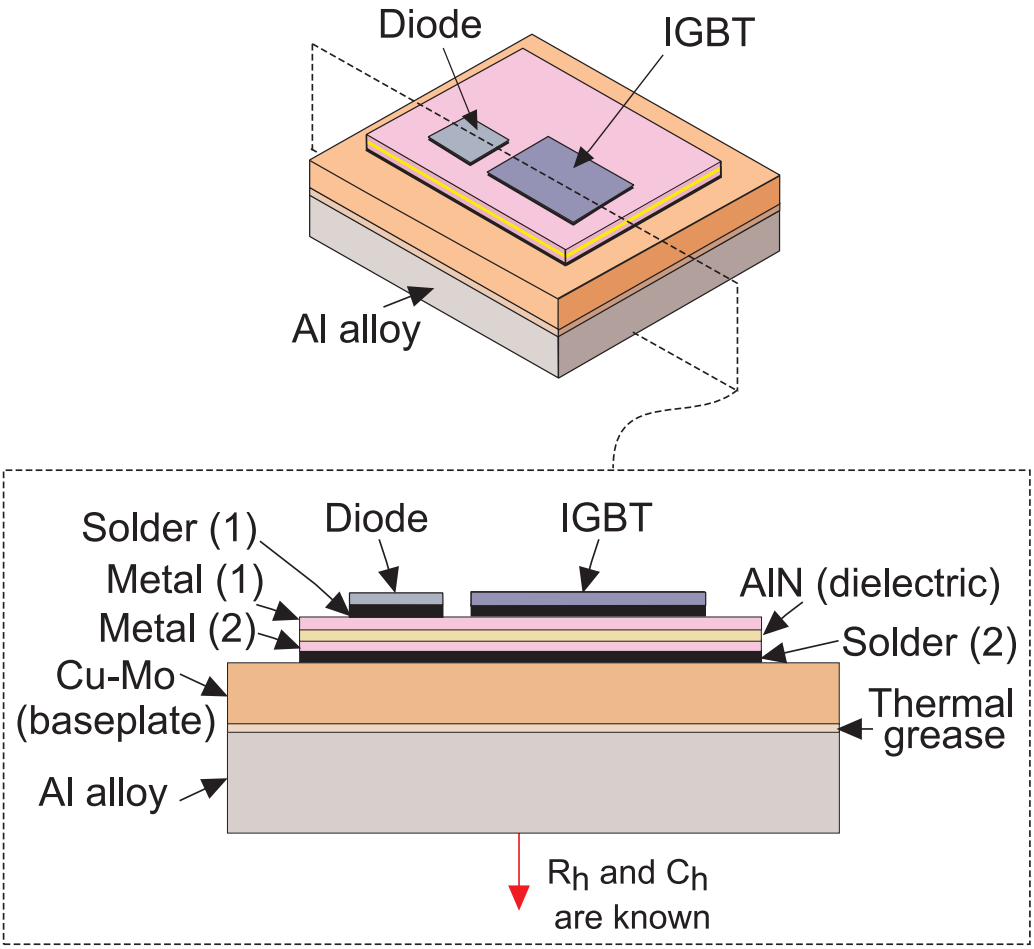

Figure 5.1: Diagram of the simulation domain - the packaging associated with one IGBT and one diode, in a ceramic isolated power converter module. Diagram not to scale.

In Fig. 5.1, R_h and C_h represent the thermal resistance and thermal capacitance at the underside of the Aluminium alloy layer respectively. If a thermal model can simulate this simulation domain, model expansion to simulate the whole power converter package is straightforward.

Certain assumptions allow the Fourier thermal model to simulate the simulation domain; each layer in the package is assumed to be a perfect cuboid. This assumption may not be true for the solder layers which are likely to have tapered edges. It is assumed that isotropic 3-D heat conduction is the only heat transfer mechanism occurring in the electronic packaging. This is a fair assumption to make, because in the range of temperatures in which power electronic equipment operates, the majority of heat generated in devices is transported via conduction to the bottom of the power module. Other mechanisms are seldom sufficient to cause a noticeable change [72][43]. The thermal material properties are assumed to be temperature independent. This is also not strictly true; however, it allows the heat equation to be treated as a linear partial differential equation. For many materials, such as Copper and Aluminium, the thermal conductivity is virtually constant over a wide temperature range, supporting the use of this assumption [169].

Heat conduction at material interfaces is assumed to be perfect, when in reality material interfaces influence thermal performance [170]. However, it is a reasonable assumption to make for an power converter module because the packaging layers have been forced together under an evenly distributed pressure by screws, minimising the contact thermal resistance. Heat is assumed to enter the packaging at the top surface of the devices only, which means that the heat generation function within the structure is zero. The side walls are assumed to be adiabatic. Heat may only leave the packaging through the heat sink despite the fact that in real modules there is heat transfer through the top surface

and wire bonds. The thermal grease layer is potentially difficult to model because of its relatively unknown thickness, its inhomogeneity over the whole interface area and its instability during the module ageing duration [171]. For modelling purposes, the thermal grease is assumed to have uniform thickness. The bond wires are ignored as well as the silicone gel used to protect the devices. The small metal (1) layer that makes a connection with the bond wire in Fig. 2.10 are ignored too. A detailed model of the heatsink with the coolant flowing through the pin fins shall not be created. Instead, only the thermal resistance R_h and capacitance C_h at the underside of the Aluminium alloy layer will be taken into account as it is provided by the manufacturers.

5.2 Modelling a Single Block of Material

As a power module package compromises of many blocks of material in contact with one another, a useful starting point is to create a thermal model which can simulate heat conduction through a single block of material. This will provide the foundations from which a full packaging model can be constructed. It necessary to solve the heat equation in order simulate heat diffusion through a single block. Therefore both spatial and temporal discretisation is necessary. The Fourier series solution can achieve spatial discretisation using by a truncated Fourier series, while MATLAB/Simulink can perform temporal discretisation using a dynamic ODE solver. The resulting Fourier thermal model can yield solutions to the heat equation using non-analytic time-varying boundary conditions. The Fourier series solution and its MATLAB Simulink implementation is presented in this section for the 1-D, 2-D and 3-D case.

5.2.1 1-D Fourier Thermal Model

5.2.1.1 Fourier Series Solution of the 1-D Heat Equation

The 1-D heat equation is a partial differential equation which describes the variation in temperature along a single dimension over time. When the heat generation function is zero and the heat diffuses in the z dimension only, the 1-D heat equation is defined as:

$$\frac{\partial T(z,t)}{\partial t} = \alpha \left(\frac{\partial^2 T(z,t)}{\partial z^2} \right), \tag{5.1}$$

where $\alpha = k/(c_p \rho)$. α is the thermal diffusivity of the medium, T is the temperature, t is the time variable and z is the space variable. k is thermal conductivity, and ρ and c_p are mass density and specific heat capacity of the material respectively.

The boundary conditions of a single block of material are labelled in Fig. 5.2. The heat fluxes are applied at $z = z_1$ and $z = z_2$ and are represented by a single numerical value. The solution to Equation (5.1) is a line which describes the temperature distribution through the depth of the block of material, i.e. between z_1 and z_2. Geometrically, the solution can be represented using the Fourier cosine series expansion for a line, defined below:

$$T(z,t) \sim \sum_{k=0}^{\infty} T_k(t) \cos \left(\frac{\pi k (z - z_1)}{(z_2 - z_1)} \right), \tag{5.2}$$

and the Fourier series harmonics $T_k(t)$ are described by:

$$T_0(t) = \frac{1}{(z_2 - z_1)} \int_{z_1}^{z_2} T(z,t) dz, \qquad k = 0, \tag{5.3}$$

$$T_k(t) = \frac{2}{(z_2 - z_1)} \int_{z_1}^{z_2} T(z,t) \cos \left(\frac{\pi k (z - z_1)}{(z_2 - z_1)} \right) dz, \qquad k \geq 1. \tag{5.4}$$

Each of the Fourier terms are represented in Fig. 5.3. The Fourier cosine series is well suited to the boundary conditions, since the DC term of a cosine series is non-zero. The temperature profile given by the Fourier series are only valid between z_1 and z_2.

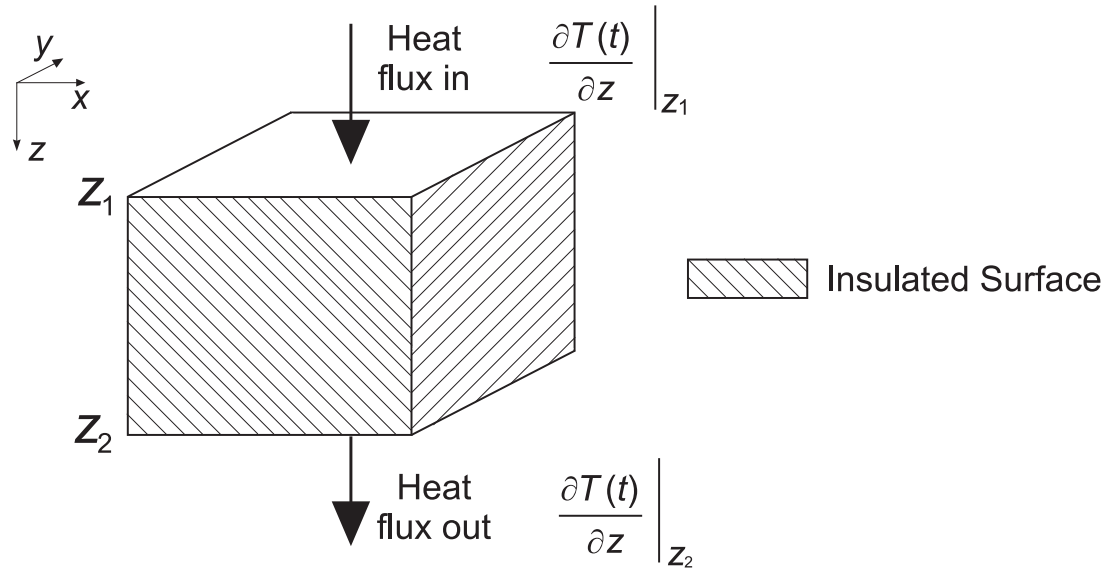

Figure 5.2: 1-D heat conduction through a block of material. Heat fluxes are represented by a single numerical value.

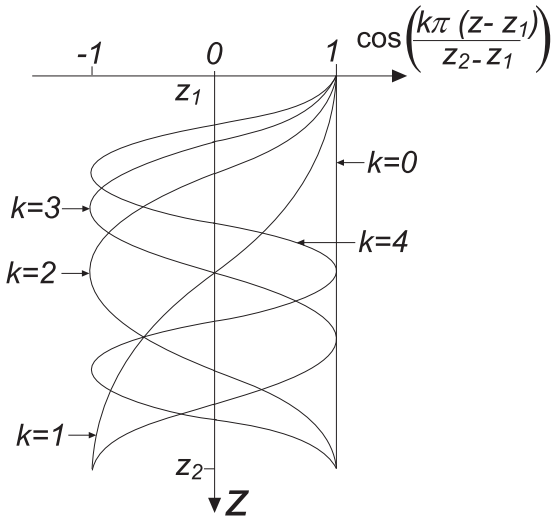

Figure 5.3: Temperature profiles for various Fourier coefficients in the Fourier cosine series.

The 1-D heat equation is the starting point of the thermal model. Each term in Equation (5.1) is multiplied through by:

$$\cos\left[\frac{\pi k(z-z_1)}{(z_2-z_1)}\right],$$

and integrated with respect to z between z_1 and z_2, giving:

$$I_1 = I_2. \tag{5.5}$$

When $k \geq 1$, the following expression represents I_1:

$$I_1 = \alpha \int_{z_1}^{z_2} \left(\frac{\partial^2 T(z,t)}{\partial z^2}\right) \cos\left(\frac{\pi k(z-z_1)}{(z_2-z_1)}\right) dz. \tag{5.6}$$

Applying integration by parts gives:

$$\begin{aligned} I_1 \quad &= \alpha \cos(\pi k) \left(\frac{\partial T(t)}{\partial z}\bigg|_{z_2}\right) - \alpha \left(\frac{\partial T(t)}{\partial z}\bigg|_{z_1}\right) \\ &+ \frac{\alpha \pi k}{(z_2-z_1)} \left[\int_{z_1}^{z_2} \left(\frac{\partial T(z,t)}{\partial z}\right) \sin\left(\frac{\pi k(z-z_1)}{(z_2-z_1)}\right) dz\right]. \end{aligned} \tag{5.7}$$

Integration by parts is now applied again to the integral in the square brackets, resulting in the expression below:

$$\int_{z_1}^{z_2} \left(\frac{\partial T(z,t)}{\partial z}\right) \sin\left(\frac{\pi k(z-z_1)}{(z_2-z_1)}\right) dz = -\frac{\pi k}{(z_2-z_1)} \int_{z_1}^{z_2} T(z,t) \cos\left(\frac{\pi k(z-z_1)}{(z_2-z_1)}\right) dz \tag{5.8}$$

Substitution of the Fourier cosine series definition for $k \geq 1$ from Equation (5.4) into Equation (5.8) leads to:

$$\int_{z_1}^{z_2} \left(\frac{\partial T(z,t)}{\partial z} \right) \sin \left(\frac{\pi k (z - z_1)}{(z_2 - z_1)} \right) dz = - \frac{\pi k}{(z_2 - z_1)} \frac{(z_2 - z_1)}{2} T_k(t). \tag{5.9}$$

Further substitution of $(-1)^k = \cos(\pi k)$, and Equation (5.9) into Equation (5.7), allows I_1 to be expressed as:

$$I_1 = \alpha \left[\left. \frac{\partial T(t)}{\partial z} \right|_{z_2} (-1)^k - \left(\left. \frac{\partial T(t)}{\partial z} \right|_{z_1} \right) \right] - \alpha \left(\frac{\pi k}{(z_2 - z_1)} \right)^2 \frac{(z_2 - z_1)}{2} T_k(t). \tag{5.10}$$

When $k \geq 1$ I_2 is represented by:

$$I_2 = \int_{z_1}^{z_2} \frac{\partial T(z,t)}{\partial t} \cos \left(\frac{\pi k (z - z_1)}{(z_2 - z_1)} \right) dz. \tag{5.11}$$

Substitution of the Fourier cosine series definition into Equation (5.11) produces the following expression:

$$I_2 = \frac{(z_2 - z_1)}{2} \frac{dT_k(t)}{dt}. \tag{5.12}$$

Substituting Equation (5.10) and Equation (5.12) into Equation (5.5) and rearranging results in the following Ordinary Differential Equation (ODE):

$$\frac{dT_k(t)}{dt} = \underbrace{\frac{2\alpha}{(z_2 - z_1)} \left[\left. \frac{\partial T(t)}{\partial z} \right|_{z_2} (-1)^k - \left. \frac{\partial T(t)}{\partial z} \right|_{z_1} \right]}_{\text{Material properties and boundary conditions}} - \underbrace{\left[\alpha \pi^2 \left(\frac{k^2}{(z_2 - z_1)^2} \right) \right]}_{\text{Diffusive terms}} T_k(t). \tag{5.13}$$

A similar process can be carried out to derive the ODE for the DC (0-th) term in the Fourier series which appears in Appendix 1. The result is this expression:

$$\frac{dT_0(t)}{dt} = \frac{\alpha}{(z_2 - z_1)} \left[\left. \frac{\partial T(t)}{\partial z} \right|_{z_2} - \left. \frac{\partial T(t)}{\partial z} \right|_{z_1} \right]. \tag{5.14}$$

5.2.1.2 1-D Implementation

Spatial discretisation has been achieved using the Fourier series solution which reduced the 1-D heat equation from a PDE to a set of ODEs. To simulate the dynamics of a thermal system over a period of time, it is necessary for the time to be discretised to a series of points. This can be achieved using a variable step stiff ODE solver in MATLAB/Simulink, either solver ode15s or ode23tb [172]; these operate using backward differentiation, known as Gear's method [173]. A benefit of using a variable step solver is that for a given accuracy the time step can then be substantially enlarged so that the computation of the integration becomes much faster. The solver ode23tb has been found to give the most stable results. The maximum step size is 10^{-2}s, the minimum step size is 10^{-6}s and the initial step size is set to *auto*. The relative tolerance is 10^{-3} and the absolute tolerance is 10^{-4}. The implementation of the equations within Simulink relied on the use of function blocks (e.g. integrators, transfer functions, mathematical functions). A benefit of this approach was that system debugging could be carried out swiftly. In order to implement the ODEs into MATLAB/Simulink, the ODEs are written in matrix form as shown in Fig. 5.4.

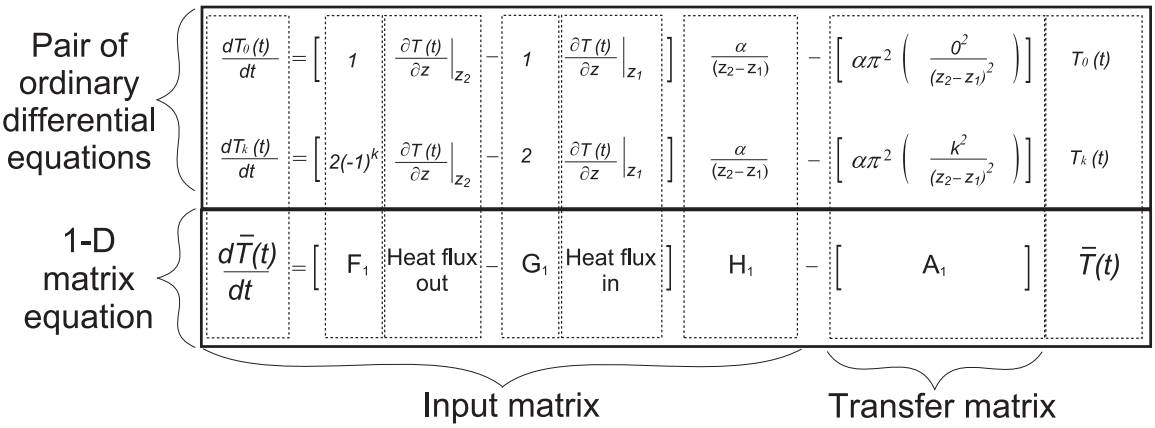

Figure 5.4: ODEs from the Fourier series solution to the 1-D heat equation written in matrix form.

$\bar{T}(t)$ is a vector of Fourier series harmonics as shown below:

$$\bar{T}(t) = \begin{Bmatrix} T_0(t) \\ \vdots \\ T_k(t) \end{Bmatrix}$$

The diffusive terms form the transfer matrix while the material properties and boundary conditions contribute to the input matrix in Fig. 5.4. The matrix equation, and therefore the ODEs, can be solved using MATLAB/Simulink. Simulink was chosen because it allows straightforward integration with the converter simulator, which is also in Simulink [22],[21].

In order to find an exact solution to the 1-D heat equation, $T_k(t)$, it would be necessary to use an infinite number of Fourier terms in every direction (K=∞). Practically, this cannot be achieved. A convenient method of finding an approximate solution to the heat equation is to truncate the theoretically infinite Fourier series. Truncation will inevitably lead to error. Fortunately, higher-order Fourier terms only have a negligible effect on the solution as the series tend to rapidly converge to zero. Therefore K can be assigned a finite number. The fewer Fourier terms used, the less computational power required to solve the heat equation, however, the greater the error in the solution [174].

Fig. 5.5 shows the basic form of the Simulink implementation. The model shown can simulate 1-D diffusion for the heat conduction problem presented in Fig. 5.2. The Fourier to space conversion matrix is a premultiplying matrix created using the relationship from Equation (5.2). The Ambient block is present to give the block of material an initial temperature. The block subsystem is highlighted to show the potential for the single block model to interact with other layers.

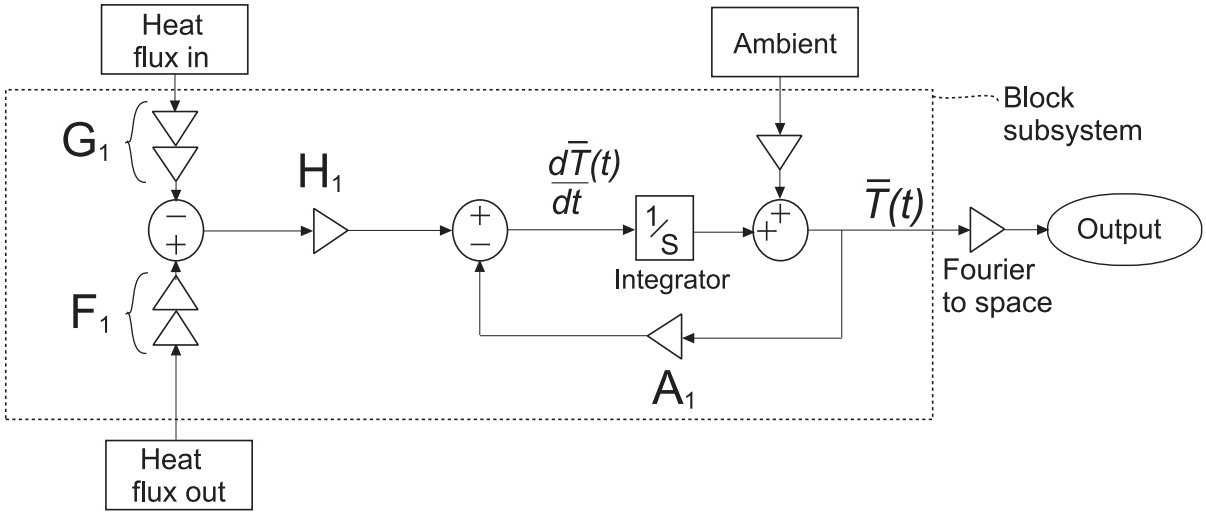

Figure 5.5: Block diagram showing the MATLAB/Simulink implementation of the Fourier series solution. The letters are defined in Fig. 5.4.

5.2.2 2-D Fourier Thermal Model

5.2.2.1 Fourier Series Solution of the 2-D Heat Equation

The 2-D heat equation is a partial differential equation which describes the variation in temperature in two dimensions over time. When the heat generation function is zero and heat diffusion occurs in the x and z dimensions, the 2-D form of the heat equation is defined as:

$$\alpha \left(\frac{\partial^2 T(z,x,t)}{\partial z^2} + \frac{\partial^2 T(z,x,t)}{\partial x^2} \right) = \frac{\partial T(z,x,t)}{\partial t}. \tag{5.15}$$

The boundary conditions labelled in Fig. 5.6 are applied to the block of material shown. The heat fluxes, $\frac{\partial T(x,t)}{\partial z}\Big|_{z_1}$ and $\frac{\partial T(x,t)}{\partial z}\Big|_{z_2}$, are represented by a line distribution which varies between x_1 and x_2.

The solution to Equation (5.15) is a x-z 2-D surface distribution. Geometrically, this can be represented using the Fourier cosine series expansion for an area, defined by:

$$T(z,x,t) \sim \sum_{k=0}^{\infty} \sum_{m=0}^{\infty} T_{km}(t) \cos\left(\frac{\pi k (z - z_1)}{(z_2 - z_1)} \right) \cos\left(\frac{\pi m (x - x_1)}{(x_2 - x_1)} \right), \tag{5.16}$$

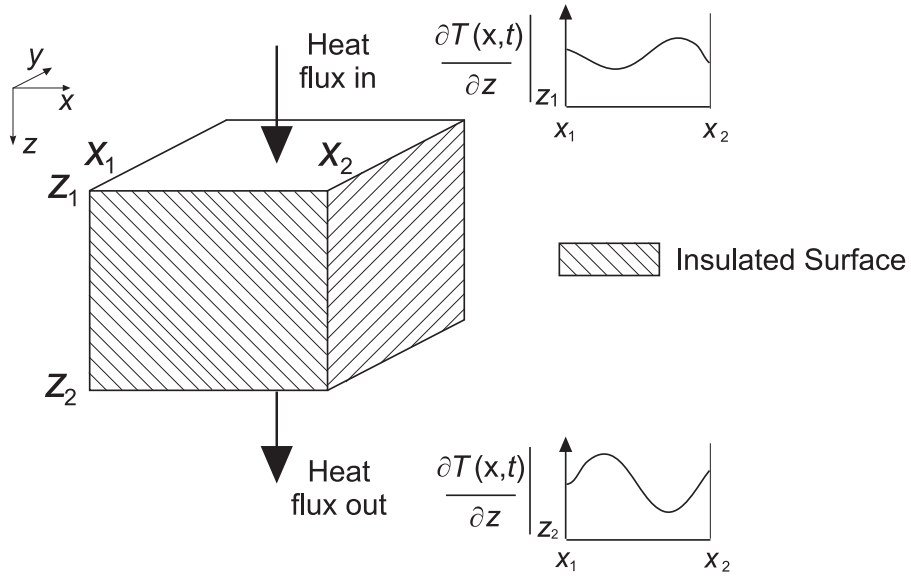

Figure 5.6: 2-D heat conduction through a block of material. The arbitrary heat fluxes are a line distribution which may vary across the x dimension.

The Fourier series harmonics associated with Equation (5.16) are:

$$T_{00}(t) = \frac{1}{(z_2-z_1)(x_2-x_1)} \int_{z_1}^{z_2} \int_{x_1}^{x_2} T(z,x,t) dx dz, \tag{5.17}$$

$$T_{k0}(t) = \frac{2}{(z_2-z_1)(x_2-x_1)} \int_{z_1}^{z_2} \int_{x_1}^{x_2} T(z,x,t) \cos\left(\frac{\pi k(z-z_1)}{(z_2-z_1)}\right) dx dz, \tag{5.18}$$

$$T_{0m}(t) = \frac{2}{(z_2-z_1)(x_2-x_1)} \int_{z_1}^{z_2} \int_{x_1}^{x_2} T(z,x,t) \cos\left(\frac{\pi m(x-x_1)}{(x_2-x_1)}\right) dx dz, \tag{5.19}$$

$$T_{km}(t) = \frac{4}{(z_2-z_1)(x_2-x_1)} \int_{z_1}^{z_2} \int_{x_1}^{x_2} T(z,x,t) \cos\left(\frac{\pi m(x-x_1)}{(x_2-x_1)}\right) \cos\left(\frac{\pi k(z-z_1)}{(z_2-z_1)}\right) dx dz. \tag{5.20}$$

The procedure is similar to the one-dimensional solution. Initially, the 2-D heat equation in multiplied by:

$$\cos\left[\frac{\pi k(z-z_1)}{(z_2-z_1)}\right] \cos\left[\frac{\pi m(x-x_1)}{(x_2-x_1)}\right], \tag{5.21}$$

and integrated with respect to z between z_1 and z_2, and with respect to x between x_1 and x_2, giving:

$$I_1 = I_2, \tag{5.22}$$

where I_1 is defined by the following equations when $k \geq 1$ and $m \geq 1$:

$$I_1 = \alpha \int_{x_1}^{x_2} \left[\int_{z_1}^{z_2} \frac{\partial^2 T(z,x,t)}{\partial z^2} \cos\left(\frac{\pi k(z-z_1)}{(z_2-z_1)}\right) dz \right] \cos\left(\frac{\pi m(x-x_1)}{(x_2-x_1)}\right) dx$$
$$+ \alpha \int_{z_1}^{z_2} \left[\int_{x_1}^{x_2} \frac{\partial^2 T(z,x,t)}{\partial x^2} \cos\left(\frac{\pi m(x-x_1)}{(x_2-x_1)}\right) dx \right] \cos\left(\frac{\pi k(z-z_1)}{(x_2-z_1)}\right) dz. \tag{5.23}$$

Breaking this expression down into constituent parts produces:

$$I_1 = I_{1z} + I_{1x}. \tag{5.24}$$

Therefore:

$$I_{1z} = \alpha \int_{x_1}^{x_2} \left[\int_{z_1}^{z_2} \frac{\partial^2 T(z,x,t)}{\partial z^2} \cos\left(\frac{\pi k(z-z_1)}{(z_2-z_1)}\right) dz \right] \cos\left(\frac{\pi m(x-x_1)}{(x_2-x_1)}\right) dx. \tag{5.25}$$

Integration by parts is applied successively to the expression in the square brackets which produces the following expression for I_{1z}:

$$I_{1z} = \alpha \left[\left.\frac{\partial T(x,t)}{\partial z}\right|_{z_2} \cos(\pi k) - \left.\frac{\partial T(x,t)}{\partial z}\right|_{z_1} \right] \int_{x_1}^{x_2} \cos\left(\frac{\pi m(x-x_1)}{(x_2-x_1)}\right) dx$$
$$- \alpha \left(\frac{\pi k}{(z_2-z_1)}\right)^2 \int_{x_1}^{x_2} \int_{z_1}^{z_2} T(z,x,t) \cos\left(\frac{\pi m(z-z_1)}{(z_2-z_1)}\right) \cos\left(\frac{\pi m(x-x_1)}{(x_2-x_1)}\right) dz dx. \tag{5.26}$$

Substitution of the expression in Equation (5.20) and $(-1)^k = \cos(\pi k)$ in Equation (5.26) leads to:

$$I_{1z} = \alpha(-1)^k \int_{x_1}^{x_2} \left.\frac{\partial T(x,t)}{\partial z}\right|_{z_2} \cos\left(\frac{\pi m(x-x_1)}{(x_2-x_1)}\right) dx - \alpha \int_{x_1}^{x_2} \left.\frac{\partial T(x,t)}{\partial z}\right|_{z_1} \cos\left(\frac{\pi m(x-x_1)}{(x_2-x_1)}\right) dx$$
$$-\alpha\left(\frac{\pi k}{(z_2-z_1)}\right)^2 \frac{(z_2-z_1)(x_2-x_1)}{4} T_{km}(t). \tag{5.27}$$

As shown in Fig. 5.6, $\left.\frac{\partial T(x,t)}{\partial z}\right|_z$ is defined along each edge at $z = z_1$ and $z = z_2$. $\left.\frac{\partial T(x,t)}{\partial z}\right|_z$ can be considered to be $\left.\frac{\partial T(t)}{\partial z}\right|_z(x)$, and therefore it can be represented as a Fourier series and take the form of any arbitrary distribution which is a function of x. $\left.\frac{\partial T_m(t)}{\partial z}\right|_z$ is the m-th term in a Fourier series of $\left.\frac{\partial T(t)}{\partial z}\right|_z(x)$. The conversion from the spatial domain to the Fourier domain for the heat fluxes is shown below:

$$\left.\frac{\partial T_m(t)}{\partial z}\right|_z = \frac{2}{(x_2-x_1)} \int_{x_1}^{x_2} \left.\frac{\partial T(x,t)}{\partial z}\right|_z (x) \cos\left(\frac{\pi m(x-x_1)}{(x_2-x_1)}\right) dx, \qquad m \geq 1 \tag{5.28}$$

The substitution of Equation (5.28) into Equation (5.27) simplifies to:

$$I_{1z} = \alpha\frac{(x_2-x_1)}{2}\left[\left.\frac{\partial T_m(t)}{\partial x}\right|_{z_2}(-1)^k - \left.\frac{\partial T_m(t)}{\partial x}\right|_{z_1}\right]$$
$$-\alpha\left(\frac{\pi k}{(z_2-z_1)}\right)^2 \frac{(z_2-z_1)(x_2-x_1)}{4} T_{km}(t). \tag{5.29}$$

Using the same approach for I_{1x}:

$$I_{1x} = \alpha\left[\left.\frac{\partial T_k(t)}{\partial x}\right|_{x_2}\cos(\pi m) - \left.\frac{\partial T_k(t)}{\partial x}\right|_{x_1}\right] \int_{z_1}^{z_2} \cos\left(\frac{\pi k(z-z_1)}{(z_2-z_1)}\right) dz$$
$$-\alpha\left(\frac{\pi m}{(x_2-x_1)}\right)^2 \frac{(z_2-z_1)(x_2-x_1)}{4} T_{km}(t). \tag{5.30}$$

However, due to the insulated surfaces at x_1 and x_2, shown in Fig. 5.6, there exists:

$$\left.\frac{\partial T_k(t)}{\partial x}\right|_{x_2} = \left.\frac{\partial T_k(t)}{\partial x}\right|_{x_1} = 0, \tag{5.31}$$

and therefore:

$$I_{1x} = -\alpha \left(\frac{\pi m}{(x_2 - x_1)}\right)^2 \frac{(z_2 - z_1)(x_2 - x_1)}{4} T_{km}(t). \tag{5.32}$$

Substitution of Equation (5.32) and (5.29) into Equation (5.24) leads to:

$$\begin{aligned} I_1 &= \alpha \frac{(x_2 - x_1)}{2} \left[\left.\frac{\partial T_m(t)}{\partial z}\right|_{z_2} (-1)^m - \left.\frac{\partial T_m(t)}{\partial z}\right|_{z_1} \right] \\ &\quad -\alpha \left(\frac{\pi^2 k^2}{(z_2 - z_1)^2} + \frac{\pi^2 m^2}{(x_2 - x_1)^2} \right) \frac{(z_2 - z_1)(x_2 - x_1)}{4} T_{km}(t). \end{aligned} \tag{5.33}$$

The expression for I_2 is:

$$I_2 = \int_{z_1}^{z_2} \int_{x_1}^{x_2} \frac{\partial T(z, x, t)}{\partial t} \cos\left(\frac{\pi m (z - z_1)}{(z_2 - z_1)}\right) \cos\left(\frac{\pi m (x - x_1)}{(x_2 - x_1)}\right) dz dx. \tag{5.34}$$

Using the Fourier series definition this simplifies to:

$$I_2 = \frac{(z_2 - z_1)(x_2 - x_1)}{4} \frac{dT_{km}(t)}{dz}. \tag{5.35}$$

Substitution of Equation (5.33) and (5.35) into Equation (5.24) followed by rearrangement produces the following ODE:

$$\begin{aligned} \frac{dT_{km}(t)}{dt} &= \frac{2\alpha}{(z_2 - z_1)} \left[\left.\frac{dT_m(t)}{dz}\right|_{z_2} (-1)^k - \left.\frac{dT_m(t)}{dz}\right|_{z_1} \right] \\ &\quad - T_{km}(t) \left[\alpha \pi^2 \left(\frac{k^2}{(z_2 - z_1)^2} + \frac{m^2}{(x_2 - x_1)^2} \right) \right]. \end{aligned} \tag{5.36}$$

A similar process can be carried out to determine the ODEs associated with the DC (0-th) terms in the Fourier series; this process appears in Appendix 1. The resulting

expression for when $k = 0$ and $m = 0$ is:

$$\frac{dT_{00}(t)}{dt} = \frac{1}{(z_2 - z_1)}\alpha \left[\left.\frac{\partial T_o(t)}{\partial z}\right|_{z_2} - \left.\frac{\partial T_o(t)}{\partial z}\right|_{z_1} \right], \tag{5.37}$$

and when $k \geq 1$ and $m = 0$ is:

$$\frac{dT_{k0}(t)}{dt} = \frac{2\alpha}{(z_2 - z_1)} \left[\left.\frac{\partial T_0(t)}{\partial z}\right|_{z_2} (-1)^k - \left.\frac{\partial T_0(t)}{\partial z}\right|_{z_1} \right] - T_{k0}(t) \left[\alpha\pi^2 \left(\frac{k^2}{(z_2 - z_1)^2} \right) \right], \tag{5.38}$$

and finally when $k = 0$ and $m \geq 1$ is:

$$\frac{dT_{0m}(t)}{dt} = \frac{\alpha}{(z_2 - z_1)} \left[\left.\frac{\partial T_m(t)}{\partial t}\right|_{z_2} - \left.\frac{\partial T_m(t)}{\partial t}\right|_{z_1} \right] - T_{0m}(t) \left[\alpha\pi^2 \left(\frac{m^2}{(x_2 - x_1)^2} \right) \right]. \tag{5.39}$$

5.2.2.2 2-D Implementation

The implementation of the 2-D Fourier series solution is very similar to the implementation for the 1-D case shown in section 5.2.1.2. On this occasion the Fourier series solution reduces the 2-D heat equation from a PDE to a set of four ODEs. The ODEs are written in matrix form as shown in Fig. 5.7.

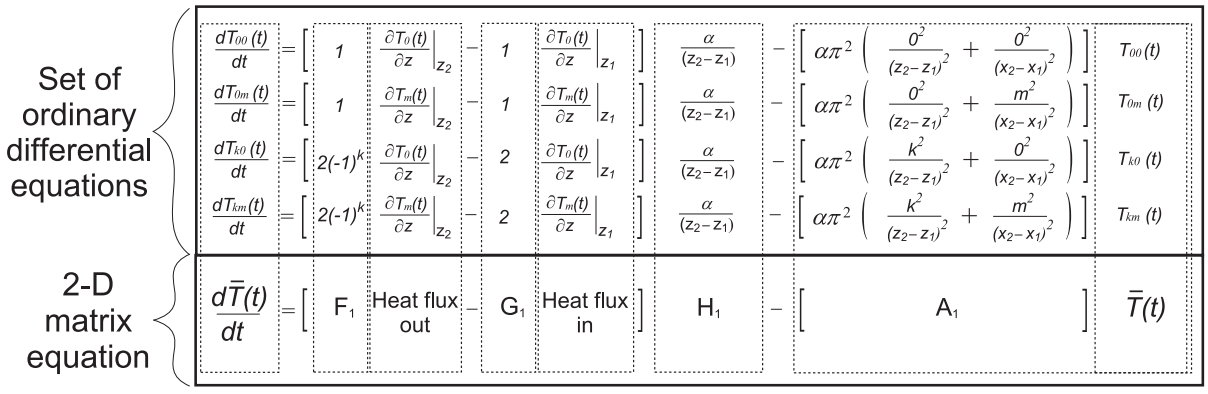

Figure 5.7: ODEs from the Fourier series solution to the 2-D heat equation written in matrix form.

$\bar{T}(t)$ is a matrix of Fourier series harmonics as shown below:

$$\bar{T}(t) = \begin{pmatrix} T_{00}(t) & \cdots & T_{0m}(t) \\ \vdots & \ddots & \\ T_{k0}(t) & & T_{km}(t) \end{pmatrix}$$

The Simulink model for the 2-D case appears as shown in Fig. 5.5. However, in this case it is simulating 2-D heat diffusion for the heat conduction problem presented in Fig. 5.6. Therefore the letters labelled in the Simulink model are now defined by Fig. 5.7 and $\bar{T}$ is a 2-D matrix as defined above. Consequently, a premultiplying matrix and post multiplying matrix, applying the relationship from Equation (5.16), was required in order to carry out the conversion from the Fourier to the space domain.

5.2.3 3-D Fourier Model

5.2.3.1 Fourier Series Solution to the 3-D Heat Equation

The 3-D heat equation is a partial differential equation which describes the variation in temperature in three dimensions over time. When the heat generation function is zero and heat diffusion occurs in the x, y and z dimensions over time, the 3-D form of the heat equation is defined as:

$$\alpha \left(\frac{\partial^2 T(x,y,z,t)}{\partial x^2} + \frac{\partial^2 T(x,y,z,t)}{\partial y^2} + \frac{\partial^2 T(x,y,z,t)}{\partial z^2} \right) = \frac{\partial T(x,y,z,t)}{\partial t}. \tag{5.40}$$

The solution to Equation (5.40) is a volume which describes the temperature distribution throughout the 3-D block of material. Geometrically, this can be represented using the Fourier cosine series expansion for a cuboid, defined overleaf:

$$T(x,y,z,t) \sim \sum_{m=0}^{\infty}\sum_{n=0}^{\infty}\sum_{k=0}^{\infty} T_{mnk}(t)\cos\left(\frac{\pi m(x-x_1)}{(x_2-x_1)}\right)\cos\left(\frac{\pi n(y-y_1)}{(y_2-y_1)}\right)\cos\left(\frac{\pi k(z-z_1)}{(z_2-z_1)}\right), \quad (5.41)$$

where the Fourier series harmonics are described by:

$$T_{000}(t) = \frac{1}{(z_2-z_1)(y_2-y_1)(x_2-x_1)}\int_{x_1}^{x_2}\int_{y_1}^{y_2}\int_{z_1}^{z_2} T(x,y,z,t)dxdydz, \quad (5.42)$$

$$T_{m00}(t) = \frac{2}{(z_2-z_1)(y_2-y_1)(x_2-x_1)}\int_{x_1}^{x_2}\int_{y_1}^{y_2}\int_{z_1}^{z_2} T(x,y,z,t)\cos\left(\frac{\pi m(x-x_1)}{(x_2-x_1)}\right)dxdydz, \quad (5.43)$$

$$T_{0n0}(t) = \frac{2}{(z_2-z_1)(y_2-y_1)(x_2-x_1)}\int_{x_1}^{x_2}\int_{y_1}^{y_2}\int_{z_1}^{z_2} T(x,y,z,t)\cos\left(\frac{\pi n(y-y_1)}{(y_2-y_1)}\right)dxdydz, \quad (5.44)$$

$$T_{00k}(t) = \frac{2}{(z_2-z_1)(y_2-y_1)(x_2-x_1)}\int_{x_1}^{x_2}\int_{y_1}^{y_2}\int_{z_1}^{z_2} T(x,y,z,t)\cos\left(\frac{\pi k(z-z_1)}{(z_2-z_1)}\right)dxdydz, \quad (5.45)$$

$$\begin{aligned} T_{mn0}(t) &= \frac{4}{(z_2-z_1)(y_2-y_1)(x_2-x_1)} \\ &\quad \times \int_{x_1}^{x_2}\int_{y_1}^{y_2}\int_{z_1}^{z_2} T(x,y,z,t)\cos\left(\frac{\pi m(x-x_1)}{(x_2-x_1)}\right)\cos\left(\frac{\pi n(y-y_1)}{(y_2-y_1)}\right)dxdydz, \end{aligned} \quad (5.46)$$

$$\begin{aligned} T_{m0k}(t) &= \frac{4}{(z_2-z_1)(y_2-y_1)(x_2-x_1)} \\ &\quad \times \int_{x_1}^{x_2}\int_{y_1}^{y_2}\int_{z_1}^{z_2} T(x,y,z,t)\cos\left(\frac{\pi m(x-x_1)}{(x_2-x_1)}\right)\cos\left(\frac{\pi k(z-z_1)}{(z_2-z_1)}\right)dxdydz, \end{aligned} \quad (5.47)$$

$$T_{0nk}(t) = \frac{4}{(z_2-z_1)(y_2-y_1)(x_2-x_1)} \times \int_{x_1}^{x_2}\int_{y_1}^{y_2}\int_{z_1}^{z_2} T(x,y,z,t)\cos\left(\frac{\pi n(y-y_1)}{(y_2-y_1)}\right)\cos\left(\frac{\pi k(z-z_1)}{(z_2-z_1)}\right)dxdydz, \quad (5.48)$$

$$T_{mnk}(t) = \frac{8}{(x_2-x_1)(y_2-y_1)(z_2-z_1)} \times \int_{x_1}^{x_2}\int_{y_1}^{y_2}\int_{z_1}^{z_2} T(x,y,z,t)\cos\left(\frac{\pi m(x-x_1)}{(x_2-x_1)}\right)\cos\left(\frac{\pi n(y-y_1)}{(y_2-y_1)}\right)\cos\left(\frac{\pi k(z-z_1)}{(z_2-z_1)}\right)dxdydz. \quad (5.49)$$

The boundary conditions shown in Fig. 5.8 are applied to the block of material. The heat fluxes are in the form of a 2-D x-y surface distribution.

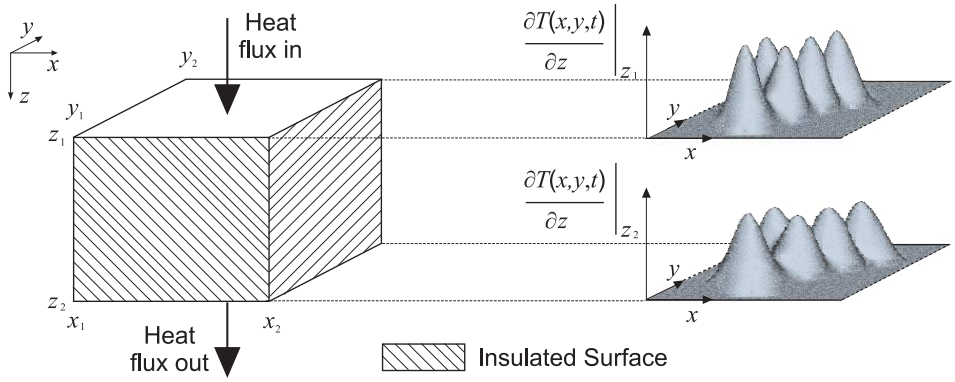

Figure 5.8: 3-D heat conduction through a block of material. Heat fluxes are represented by a 2-D function of arbitrary distribution.

The procedure for solving the 3-D heat equation is similar to the approach for solving the 1-D and the 2-D heat equation. For the 3-D case, each term in Equation (5.40) is multiplied by:

$$\cos\left[\frac{\pi m(x-x_1)}{(x_2-x_1)}\right]\cos\left[\frac{\pi n(y-y_1)}{(y_2-y_1)}\right]\cos\left[\frac{\pi k(z-z_1)}{(z_2-z_1)}\right],$$

and integrated with respect to x between x_1 and x_2, with respect to y between y_1 and y_2, and with respect to z between z_1 and z_2, giving:

$$I_1{=}I_2. \tag{5.50}$$

I_1 when $m{\geq}1$, $n{\geq}1$, $k{\geq}1$, is:

$$\begin{aligned} I_1 &= \alpha \int_{x_1}^{x_2}\int_{y_1}^{y_2}\int_{z_1}^{z_2} \left(\frac{\partial^2 T(x,y,z,t)}{\partial x^2} + \frac{\partial^2 T(x,y,z,t)}{\partial y^2} + \frac{\partial^2 T(x,y,z,t)}{\partial z^2} \right) \\ &\quad \times \cos\left(\frac{\pi m(x{-}x_1)}{(x_2{-}x_1)}\right) \cos\left(\frac{\pi n(y{-}y_1)}{(y_2{-}y_1)}\right) \cos\left(\frac{\pi k(z{-}z_1)}{(z_2{-}z_1)}\right) dxdydz, \end{aligned} \tag{5.51}$$

which is treated as:

$$I_1{=}I_{1x}{+}I_{1y}{+}I_{1z}. \tag{5.52}$$

The expression for I_{1z} is shown below:

$$\begin{aligned} I_{1z} &= \alpha \int_{y_1}^{y_2}\int_{x_1}^{x_2} \left[\int_{z_1}^{z_2} \frac{\partial^2 T(x,y,z,t)}{\partial z^2} \cos\left(\frac{\pi k(z{-}z_1)}{(z_2{-}z_1)}\right) dz \right] \\ &\quad \times \cos\left(\frac{\pi m(x{-}x_1)}{(x_2{-}x_1)}\right) \cos\left(\frac{\pi n(y{-}y_1)}{(y_2{-}y_1)}\right) dxdy \end{aligned} \tag{5.53}$$

Applying integration by parts successively produces:

$$\begin{aligned} I_{1z} &= \int_{y_1}^{y_2}\int_{x_1}^{x_2} (-1)^k \left(\frac{\partial T(x,y,t)}{\partial z}\bigg|_{z_2} \right) \cos\left(\frac{\pi m(x{-}x_1)}{(x_2{-}x_1)}\right) \cos\left(\frac{\pi n(y{-}y_1)}{(y_2{-}y_1)}\right) dxdy \\ &- \frac{\alpha\pi^2 k^2}{(z_2{-}z_1)^2} \int_{z_1}^{z_2}\int_{y_1}^{y_2}\int_{x_1}^{x_2} T(x,y,z,t) \cos\left(\frac{\pi m(x{-}x_1)}{(x_2{-}x_1)}\right) \cos\left(\frac{\pi n(y{-}y_1)}{(y_2{-}y_1)}\right) \cos\left(\frac{\pi k(z{-}z_1)}{(z_2{-}z_1)}\right) dxdydz \\ &- \int_{y_1}^{y_2}\int_{x_1}^{x_2} \left(\frac{\partial T(x,y,t)}{\partial z}\bigg|_{z_1} \right) \cos\left(\frac{\pi m(x{-}x_1)}{(x_2{-}x_1)}\right) \cos\left(\frac{\pi n(y{-}y_1)}{(y_2{-}y_1)}\right) dxdy. \end{aligned} \tag{5.54}$$

For this integral, $\left.\frac{\partial T(x,y,t)}{\partial z}\right|_{z_1} \neq 0$ and $\left.\frac{\partial T(x,y,t)}{\partial z}\right|_{z_2} \neq 0$, because the x-y surfaces at $z{=}z_1$ and $z{=}z_2$ are not insulated. These heat fluxes can be represented by any arbitrary 2-D function when in the form of a 2-D Fourier series. $\left.\frac{\partial T_{mn}(t)}{\partial z}\right|_{z_1}$ is the 2-D Fourier series for the boundary heat flux at $z{=}z_1$, and $\left.\frac{\partial T_{mn}(t)}{\partial z}\right|_{z_2}$ is the 2-D Fourier series for the boundary heat flux at $z{=}z_2$. The relationship between a 2-D boundary Fourier series and a 2-D spatial boundary function is shown below:

$$\left.\frac{\partial T_{mn}(t)}{\partial z}\right|_z = \frac{4}{(x_2{-}x_1)(y_2{-}y_1)} \times \int_{y_1}^{y_2}\int_{x_1}^{x_2} \left.\frac{\partial T(x,y,t)}{\partial z}\right|_z \cos\left(\frac{\pi n(y{-}y_1)}{(y_2{-}y_1)}\right)\cos\left(\frac{\pi m(x{-}x_1)}{(x_2{-}x_1)}\right) dxdy. \quad (5.55)$$

Substitution of Equation (5.55) and (5.49) into Equation (5.54) produces:

$$I_{1z} = (-1)^k \frac{(x_2{-}x_1)(y_2{-}y_1)}{4} \left.\frac{\partial T_{mn}(t)}{\partial z}\right|_{z_2} - \frac{(x_2{-}x_1)(y_2{-}y_1)}{4} \left.\frac{\partial T_{mn}(t)}{\partial z}\right|_{z_1} - \frac{\alpha\pi^2 k^2}{(z_2{-}z_1)} \frac{(x_2{-}x_1)(y_2{-}y_1)}{8} T_{mnk}(t) \quad (5.56)$$

The same approach is used to find an expression for I_{1x}; however, in this case the y-z plane at $x{=}x_1$ and $x{=}x_2$ is insulated. Therefore $\left.\frac{\partial T(y,z,t)}{\partial x}\right|_{x_1} = 0$, $\left.\frac{\partial T(y,z,t)}{\partial x}\right|_{x_2} = 0$ and I_{1x} becomes:

$$I_{1x} = -\frac{\alpha\pi^2 m^2 (y_2{-}y_1)(z_2{-}z_1)}{8(x_2{-}x_1)} T_{mnk}(t). \quad (5.57)$$

The same approach to get an expression for I_{1y}. The x-z plane at $y{=}y_1$ and $y{=}y_2$ is insulated and so the resulting expression is:

$$I_{1\mathrm{y}} = -\frac{\alpha\pi^2 n^2 (x_2{-}x_1)(z_2{-}z_1)}{8(y_2{-}y_1)} T_{mnk}(t). \quad (5.58)$$

In order to gain an expression for I_1, we substitute in Equation (5.57), (5.58) and (5.56) into (5.52), which produces:

$$\begin{aligned} I_1 &= (-1)^k \frac{(x_2-x_1)(y_2-y_1)}{4} \left.\frac{\partial T_{mn}(t)}{\partial z}\right|_{z_2} - \frac{(x_2-x_1)(y_2-y_1)}{4} \left.\frac{\partial T_{mn}(t)}{\partial z}\right|_{z_1} \\ &\quad -\frac{\alpha\pi^2 k^2 (x_2-x_1)(y_2-y_1)}{8(z_2-z_1)} T_{mnk}(t) - \frac{\alpha\pi^2 n^2 (x_2-x_1)(z_2-z_1)}{8(y_2-y_1)} T_{mnk}(t) \\ &\quad -\frac{\alpha\pi^2 m^2 (y_2-y_1)(z_2-z_1)}{8(x_2-x_1)} T_{mnk}(t) \end{aligned} \tag{5.59}$$

Now attention turns to the integral I_2:

$$I_2 = \int_{x_1}^{x_2}\int_{y_1}^{y_2}\int_{z_1}^{z_2} \frac{\partial T(x,y,z,t)}{\partial t} \cos\left(\frac{\pi m(x-x_1)}{(x_2-x_1)}\right) \cos\left(\frac{\pi n(y-y_1)}{(y_2-y_1)}\right) \cos\left(\frac{\pi k(z-z_1)}{(z_2-z_1)}\right) dxdydz \tag{5.60}$$

Substitution of the Fourier series definition simplifies I_2 to:

$$I_2 = \frac{(x_2-x_1)(y_2-y_1)(z_2-z_1)}{8} \frac{dT_{mnk}(t)}{dt}. \tag{5.61}$$

Equating I_1 and I_2 then rearranging produces the following Ordinary Differential Equation (ODE) for the $m \geq 1$, $n \geq 1$, $k \geq 1$ case:

$$\begin{aligned} \frac{dT_{mnk}(t)}{dt} &= \underbrace{\frac{2\alpha}{(z_2-z_1)} \left[\left.\frac{\partial T_{mn}(t)}{\partial z}\right|_{z_2} (-1)^{\mathbf{k}} - \left.\frac{\partial T_{mn}(t)}{\partial z}\right|_{z_1} \right]}_{\text{Material properties and boundary conditions}} \\ &\quad \underbrace{- \left[\alpha\pi^2 \left(\frac{m^2}{(x_2-x_1)^2} + \frac{n^2}{(y_2-\mathrm{y}_1)^2} + \frac{k^2}{(z_2-z_1)^2} \right) \right]}_{\text{Diffusive terms}} T_{mnk}(t). \end{aligned} \tag{5.62}$$

Further use of this mathematical approach appears in Appendix 1, where the ODEs associated with the DC (0-*th*) terms in the Fourier series are determined, resulting in: $m \geq 1$, $n \geq 1$, $k \geq 1$:

$$\frac{dT_{000}(t)}{dt} = \frac{\alpha}{(z_2-z_1)}\left[\left.\frac{\partial T_{00}(t)}{\partial z}\right|_{z_2} - \left.\frac{\partial T_{00}(t)}{\partial z}\right|_{z_1}\right], \tag{5.63}$$

$m \geq 1$, $n = 0$, $k = 0$:

$$\frac{dT_{m00}(t)}{dt} = \frac{\alpha}{(z_2-z_1)}\left[\left.\frac{\partial T_{m0}(t)}{\partial z}\right|_{z_2} - \left.\frac{\partial T_{m0}(t)}{\partial z}\right|_{z_1}\right] - \left[\alpha\pi^2\left(\frac{m^2}{(x_2-x_1)^2}\right)\right]T_{m00}(t), \tag{5.64}$$

$m = 0$, $n \geq 1$, $k = 0$:

$$\frac{dT_{0n0}(t)}{dt} = \frac{\alpha}{(z_2-z_1)}\left[\left.\frac{\partial T_{0n}(t)}{\partial z}\right|_{z_2} - \left.\frac{\partial T_{0n}(t)}{\partial z}\right|_{z_1}\right] - \left[\alpha\pi^2\left(\frac{n^2}{(y_2-y_1)^2}\right)\right]T_{0n0}(t), \tag{5.65}$$

$m = 0$, $n = 0$, $k \geq 1$:

$$\frac{dT_{00k}(t)}{dt} = \frac{2\alpha}{(z_2-z_1)}\left[\left.\frac{\partial T_{00}(t)}{\partial z}\right|_{z_2}(-1)^k - \left.\frac{\partial T_{00}(t)}{\partial z}\right|_{z_1}\right] - \left[\alpha\pi^2\left(\frac{k^2}{(z_2-z_1)^2}\right)\right]T_{00k}(t), \tag{5.66}$$

$m \geq 1$, $n \geq 1$, $k = 0$:

$$\begin{aligned}\frac{dT_{mn0}(t)}{dt} = & \quad \frac{\alpha}{(z_2-z_1)}\left[\left.\frac{\partial T_{mn}(t)}{\partial z}\right|_{z_2} - \left.\frac{\partial T_{mn}(t)}{\partial z}\right|_{z_1}\right] \\ & - \left[\alpha\pi^2\left(\frac{m^2}{(x_2-x_1)^2} + \frac{n^2}{(y_2-y_1)^2}\right)\right]T_{mn0}(t),\end{aligned} \tag{5.67}$$

$m \geq 1$, $n = 0$, $k \geq 1$:

$$\begin{aligned}\frac{dT_{m0k}(t)}{dt} = & \quad \frac{2\alpha}{(z_2-z_1)}\left[\left.\frac{\partial T_{m0}(t)}{\partial z}\right|_{z_2}(-1)^k - \left.\frac{\partial T_{m0}(t)}{\partial z}\right|_{z_1}\right] \\ & - \left[\alpha\pi^2\left(\frac{m^2}{(x_2-x_1)^2} + \frac{k^2}{(z_2-z_1)^2}\right)\right]T_{m0k}(t),\end{aligned} \tag{5.68}$$

$m = 0$, $n \geq 1$, $k \geq 1$:

$$\begin{aligned}\frac{dT_{0nk}(t)}{dt} = & \quad \frac{2\alpha}{(z_2-z_1)}\left[\left.\frac{\partial T_{0n}(t)}{\partial t}\right|_{z_2}(-1)^k - \left.\frac{\partial T_{0n}(t)}{\partial t}\right|_{z_1}\right] \\ & - \left[\alpha\pi^2\left(\frac{n^2}{(y_2-y_1)^2} + \frac{k^2}{(z_2-z_1)^2}\right)\right]T_{0nk}(t).\end{aligned} \tag{5.69}$$

5.2.3.2 3-D Implementation

The implementation of the 3-D Fourier series solution is similar to the implementation for the 1-D case shown in section 5.2.1.2. On this occasion the Fourier series solution reduces the 3-D heat equation from a PDE to a set of eight ODEs. The ODEs are written in matrix form as shown in Fig. 5.9.

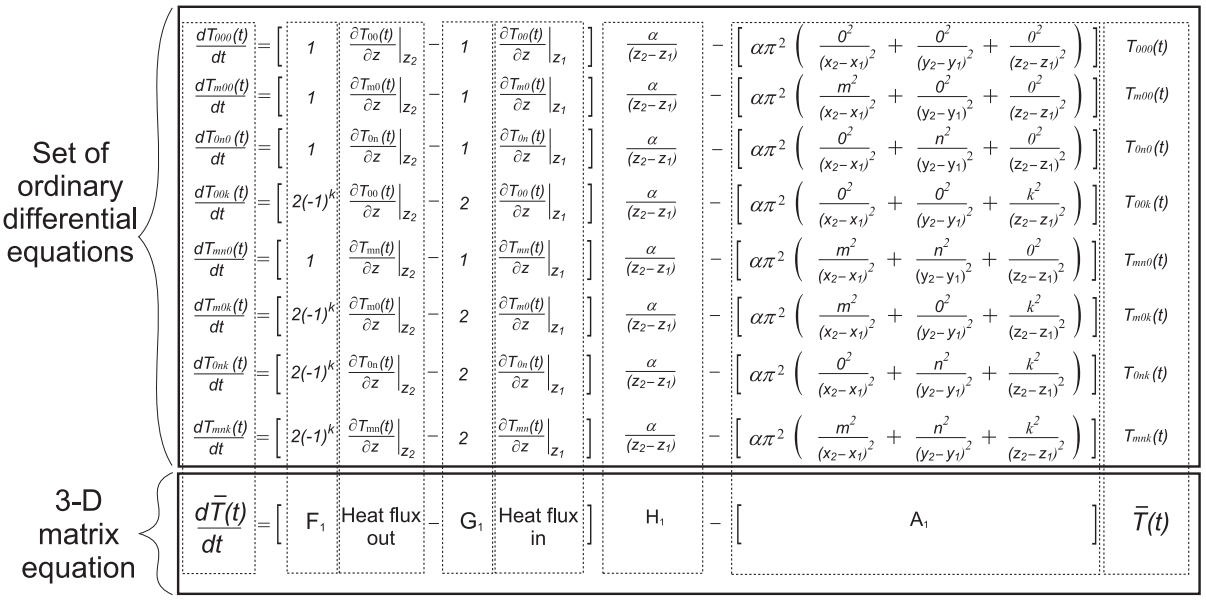

Figure 5.9: ODEs from the Fourier series solution to the 3-D heat equation written in matrix form.

Although MATLAB can handle multidimensional arrays, Simulink only accepts 2-D matrices. Therefore, for this case, 3-D matrices were represented in 2-D form, as shown in Fig. 5.10. The Simulink model for the 3-D case also appears as shown in Fig. 5.5. However, in this case it is simulating 3-D heat diffusion for the heat conduction problem presented in Fig. 5.8. Therefore the letters labelled in the Simulink model are now defined by Fig. 5.9.

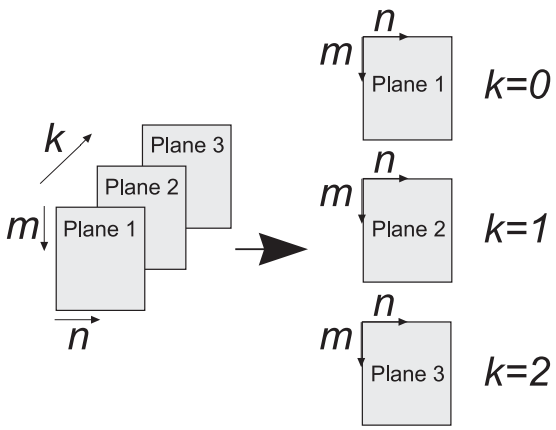

Figure 5.10: A 3-D matrix represented as a 2-D matrix.

For this 3-D case, $\bar{T}(t)$ in Fig. 5.9 appeared as shown below:

$$\bar{T}(t) = \begin{pmatrix} T_{000}(t) \cdots\cdots T_{00n}(t) \\ \vdots \qquad\qquad \ddots \\ T_{00m}(t) \qquad\quad T_{0mn}(t) \end{pmatrix} \\ \vdots \\ \begin{pmatrix} T_{k00}(t) \cdots\cdots T_{k0n}(t) \\ \vdots \qquad\qquad \ddots \\ T_{k0m}(t) \qquad\quad T_{kmn}(t) \end{pmatrix}$$

As a result of the stacked configuration of $\bar{T}$, the Fourier to space conversion process was not as straightforward as the 1-D and 2-D cases. An explanation of how the Fourier to space conversion matrices were constructed for this case, using the relationship from Equation (5.41), appears in Appendix 2.

5.3 Results

The chapter has shown the development of a Fourier thermal model to simulate heat conduction through a single block of material. This results section acts to validate the 1-D, 2-D and 3-D Fourier thermal model. Results generated by the various Fourier thermal models are compared with those from the software package FLOTHERM.

5.3.1 FLOTHERM

Simulation results produced by FLOTHERM are presented over the next two chapters. As mentioned, these results are necessary to validate the Fourier thermal model. For each validation, a FLOTHERM model was created to simulate a specific heat conduction problem. An explanation of the general procedure which was carried out to create all of the FLOTHERM thermal models now follows. The FLOTHERM solution type was set to transient and conduction only. Blocks of material were added to a root assembly and the blocks were assigned their dimensions and their location. The resulting structure could be visibly checked on the FLOTHERM drawing board. Each of the blocks were then assigned the appropriate material properties (thermal conductivity, density and specific heat capacity) and given their thermal properties, either purely conducting or acting as a heat source. For each heat conduction problem presented in this and the next chapter, the value assigned to each heat source represents the total power applied over the specified area. This allows for a clearer understanding of the data entered into the FLOTHERM model as opposed to using a value of heatflux.

The initial temperature of the whole structure also had to be determined and some block faces were set to 'insulated' in order to match the heat conduction problem being modelled by the Fourier model. The FLOTHERM mesh had to be adjusted to the desired density. On occasions, grid patches were added because the existing mesh was not suitable.

The transient grid was adjusted to determine the number of time steps FLOTHERM would use over the transient solution period. FLOTHERM's accuracy was determined by the density of both the transient grid and spatial mesh. Temperature monitoring points were positioned in the appropriate location throughout the entire structure. Upon completion of all of the above, the solver could be finally be initialised. Following the completion of the FVM solver, the transient temperature monitoring point data was transferred from FLOTHERM to MATLAB, via Excel. Plots of the FLOTHERM results could then be created in MATLAB for direct comparison with the Fourier model.

5.3.2 Validation of the 1-D Fourier Thermal Model

The 1-D Fourier thermal model and FLOTHERM simulated the 1-D heat conduction problem shown in Fig. 5.11. The block of silicon which appears in the figure is of similar size to that of the IGBT device used in the Toyota Prius power converter. The heat entering the silicon is retained within the structure.

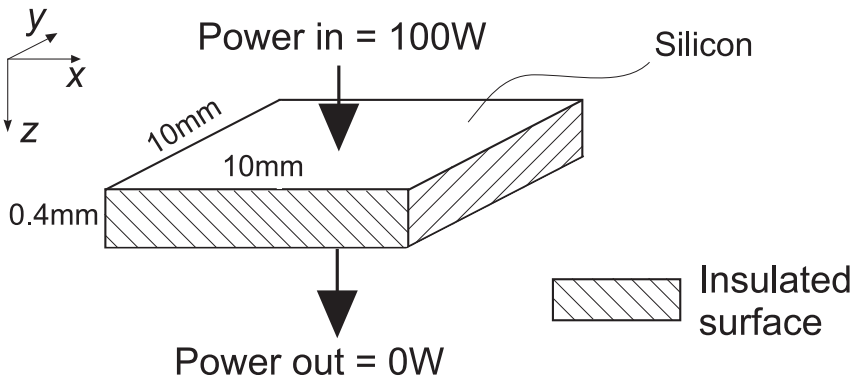

Figure 5.11: Diagram showing the 1-D heat conduction problem. The power input is applied evenly across the whole top x-y surface of the silicon, with no variation in the x or y direction, for a duration of 1.5ms. The initial temperature of the block is 0°C.

Fig. 5.12 compares results generated by the Fourier thermal model and FLOTHERM when simulating the heat conduction problem in Fig. 5.11. The total simulation time for the 1-D Fourier model was measured using the MATLAB tic function. K represents the number of Fourier terms used in the Fourier model simulation. The FLOTHERM model employed a low density mesh which contained 67072 nodes, chosen because it could deal with this relatively straightforward heat conduction problem. The FLOTHERM model simulated using 20 time steps and temperatures were recorded by positioning 7 monitoring points through the depth of the silicon block.

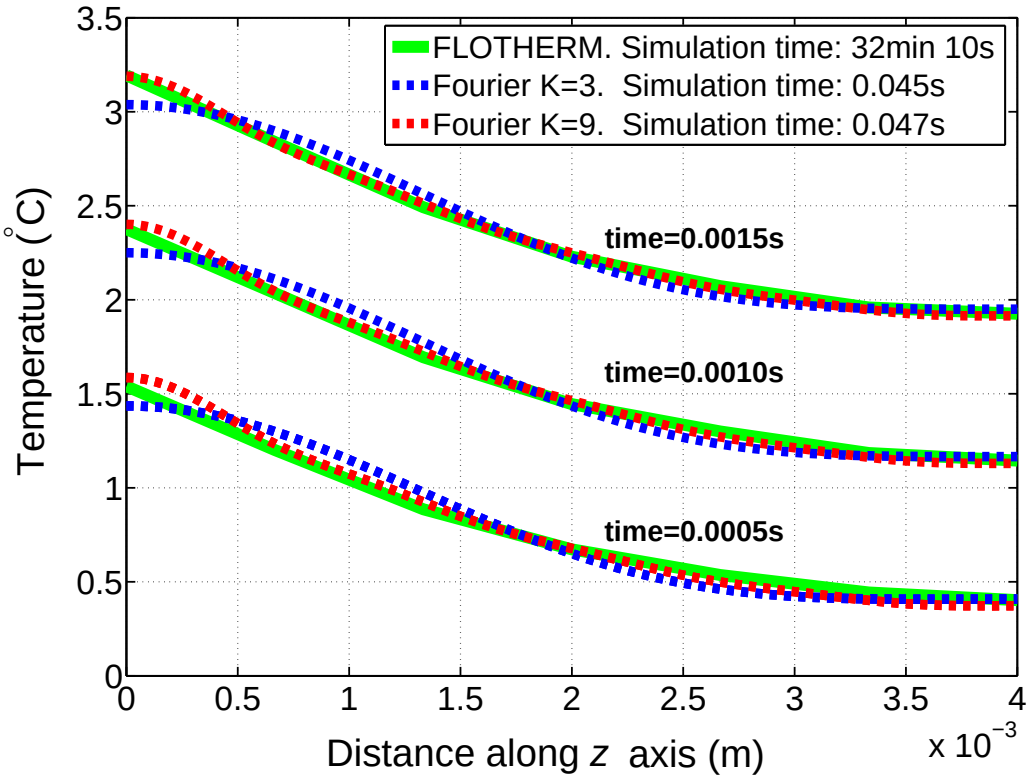

Figure 5.12: Comparison of the results generated by the 1-D Fourier thermal model and FLOTHERM. The simulation time represents the time taken to simulate 1.5ms. K represents the total number of Fourier terms used.

5.3.3 Validation of the 2-D Fourier Thermal Model

The 2-D Fourier thermal model and FLOTHERM were used to simulate a single block of solder heated at both ends, as shown in Fig. 5.13. The solder had an initial temperature of 0°C. The power inputs shown were applied for 3 seconds in order to test the Fourier model over a longer transient than in the previous validation. The FLOTHERM model employed a dense mesh model containing 226400 nodes to ensure accurate results. The FLOTHERM model contained 121 temperature monitoring points and calculated results at 50 time steps.

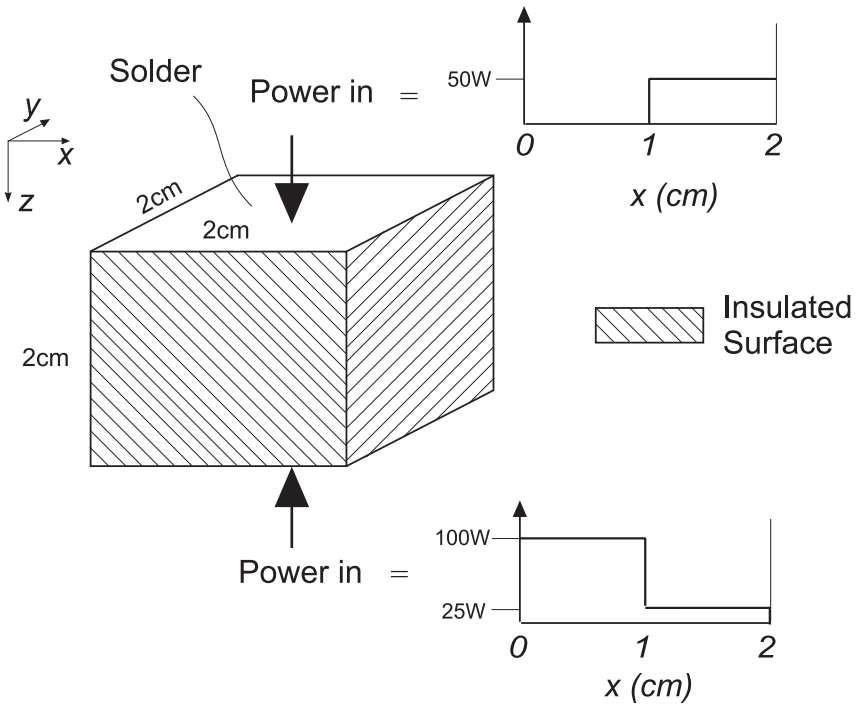

Figure 5.13: Diagram of a 2-D heat conduction problem. The power inputs span the whole x-y surface of the block and do not vary in the y direction.

The thermographs in Fig. 5.14 show results generated by the Fourier thermal model and FLOTHERM. The thermographs represent the temperature distributions over the x-z cross-section of the solder at time t=3s. K and M represent the number of Fourier coefficients used in the z and x dimension respectively. In order to enable a clearer comparison between the two models cut lines were taken from the plots shown in Fig. 5.14, appearing in Fig. 5.15.

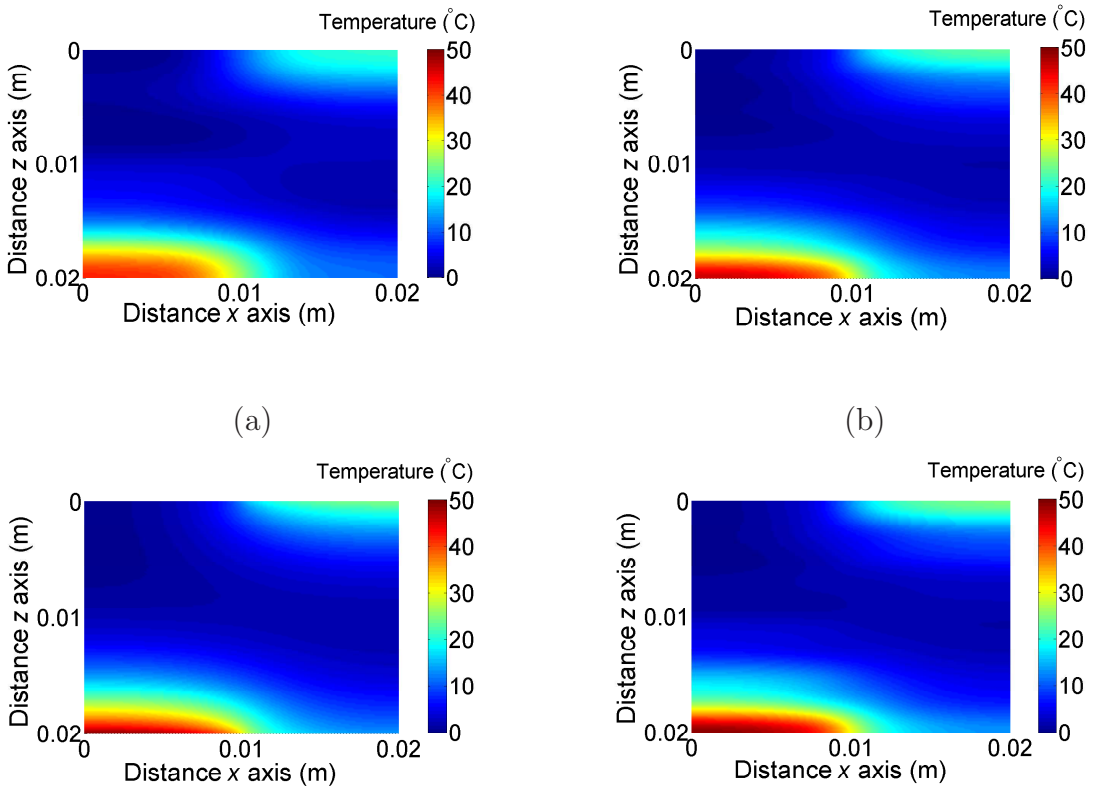

Figure 5.14: Thermographs illustrating the simulation results from modelling the heat conduction problem in Fig. 5.13. The thermographs represent the x-z plane at z=z_3, at time t=3s.
(a) Fourier model K=M=3. Simulation time: 0.029s.
(b) Fourier model K=M=6. Simulation time: 0.034s.
(c) Fourier model K=M=12. Simulation time: 0.079s.
(d) FLOTHERM model. Simulation time: 1hr 25 mins.

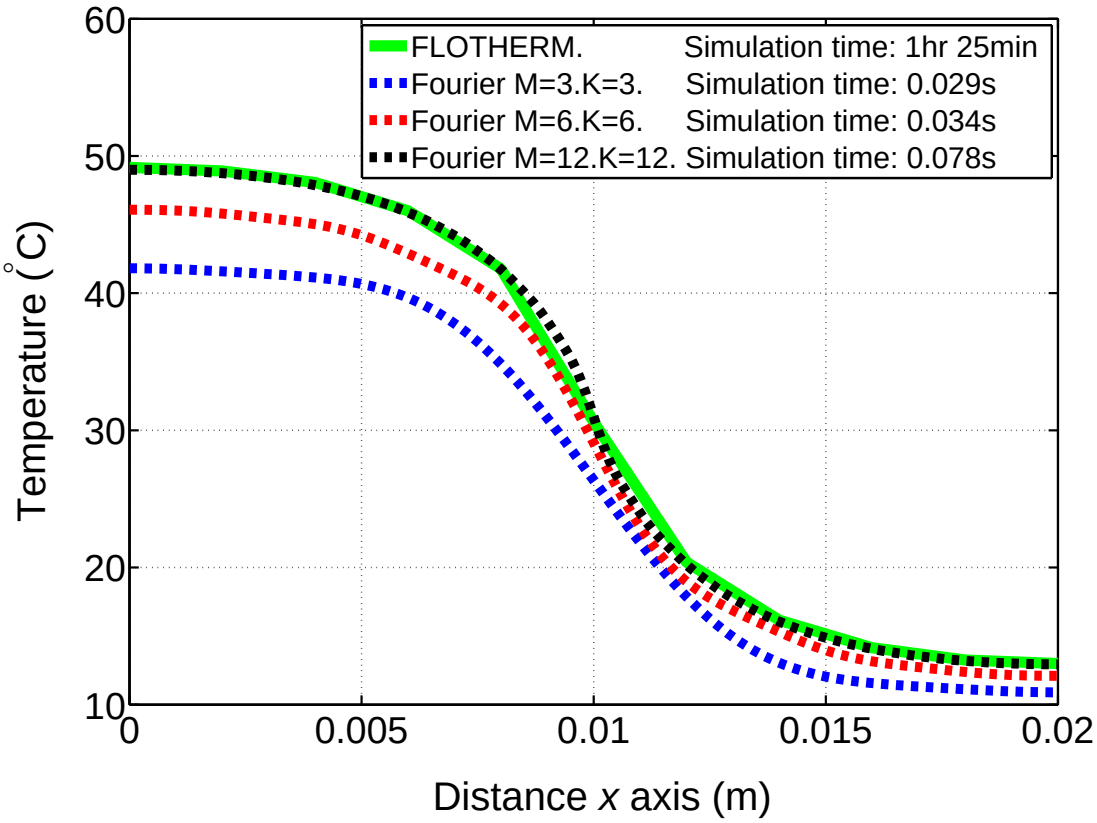

Figure 5.15: Cut lines taken from the four plots which appear in Fig. 10. The cut lines represent z=0.02m along the x dimension.

5.3.4 Validation of the 3-D Fourier Thermal Model

Fig. 5.16 shows a 3-D heat conduction problem. The top quarter of a block of silicon is heated by the 5W power source shown. The initial temperature of the silicon block was 300K. The thermographs in Fig. 5.17 represent the x-y plane at z=0, at time t=0.5s. Fig. 5.17(a) and Fig. 5.17(b) display the results from the Fourier model and FLOTHERM model respectively. The FLOTHERM model used a medium density mesh, containing 102060 cells, and 350 time steps. The Fourier model used eight Fourier terms in every direction (M=N=K=8). For further comparison between the two models, cut lines were taken along y=0m in Fig. 5.17(a) and Fig. 5.17(b). The cut lines appear in Fig. 5.18. Results generated by the Fourier thermal model with fewer Fourier terms are also included.

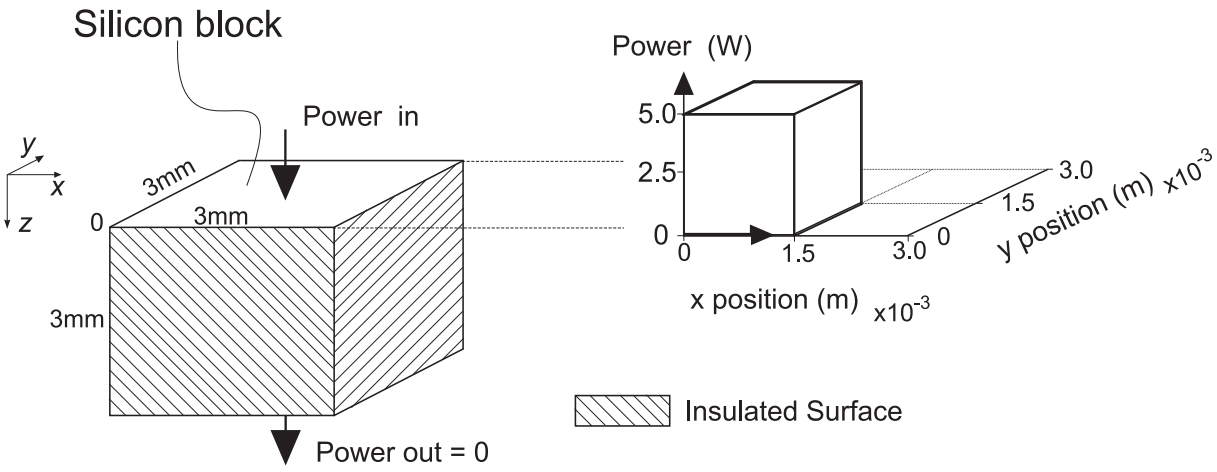

Figure 5.16: A 3-D heat conduction problem. The power source shown is to the top x-y plane of the silicon block for 0.5 seconds.

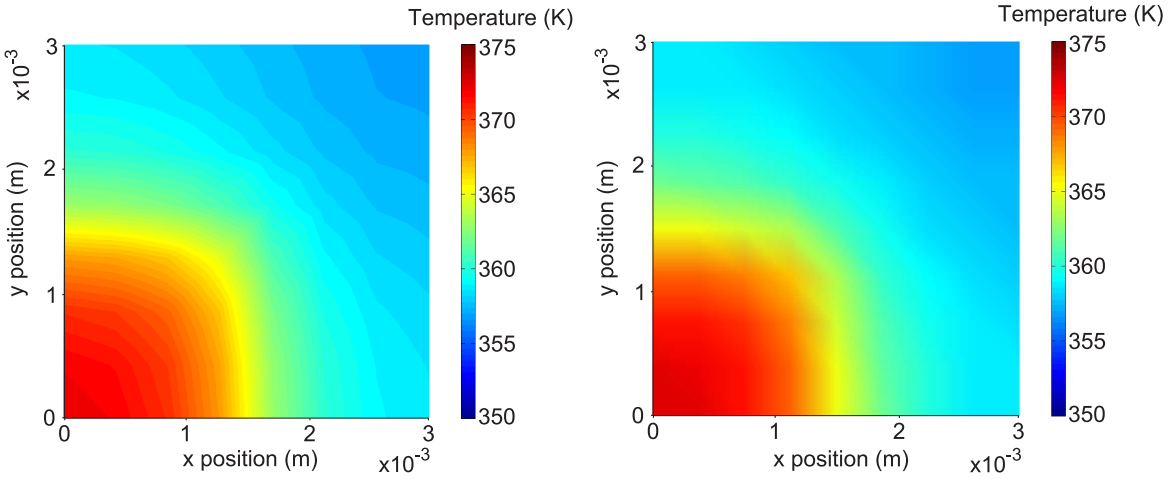

Figure 5.17: The thermographs illustrate the temperature distribution in the x-y plane at z=0 of the silicon block featured in Fig. 5.16, at time t=0.5s. Figure 5.17(a) is from the 3-D Fourier model with M=N=K=8, and the plot in Fig. 5.17(b) is from the FLOTHERM model.

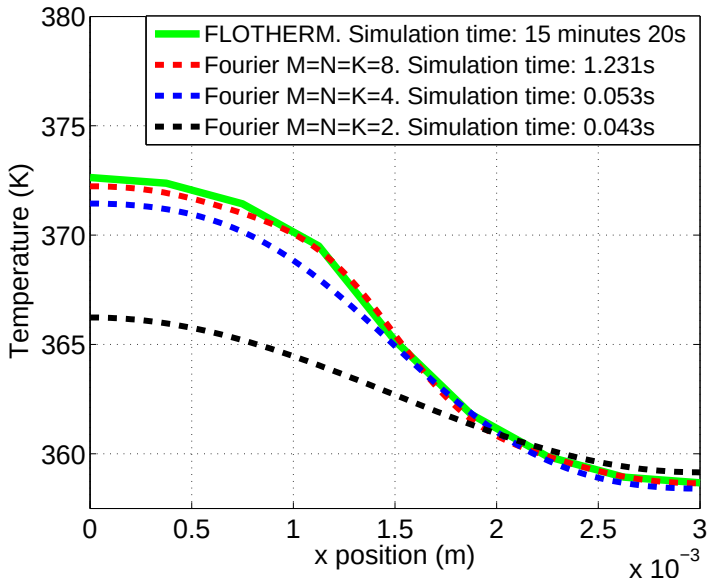

Figure 5.18: Cut lines along the x axis at depth z=0m, at time t=0.5s.

5.4 Discussion

The results from the 1-D Fourier thermal model and FLOTHERM, shown in Fig. 5.12, all agree closely over the short transient period. The Fourier model using nine Fourier terms ($K = 9$) matches the FLOTHERM result more closely than the $K = 3$ Fourier model result. The $K = 9$ Fourier result is marginally slower to simulate than the $K = 3$ Fourier result. The 1-D Fourier thermal model simulated the heat conduction problem in Fig. 5.11 in less than 0.05 seconds for both K=3 and K=9. The simulation speed of the 1-D Fourier model was therefore far superior to the FLOTHERM model which took over 32 minutes to simulate despite employing a low density mesh.

It is clear from Fig. 5.13 that the 2-D Fourier thermal model was able to simulate the 2-D heat conduction problem in Fig. 5.14 accurately. All the results from the 2-D Fourier model show evidence of capturing the thermal behaviour because all the Fourier results resemble the FLOTHERM result over a long transient period of 3 seconds. The comparison of the cut lines in Fig. 5.15 shows that when the 2-D Fourier model contained twelve Fourier terms along the z and x dimension (K=M=12), it was a near perfect match to the FLOTHERM result. It is apparent that as the number for Fourier terms used in the Fourier model increases, the accuracy of the result increases. However, the accuracy comes at the expensive of simulation speed. All the results from the 2-D Fourier thermal model simulated much more quickly than the FLOTHERM model. The 2-D validation involved simulating power entering a block at either end of the structure, which is unlikely to occur in a real power converter packaging structure. However, the result is relevant because shows that the 2-D Fourier model is correctly simulating 2-D heat diffusion and it suggests the MATLAB/Simulink implementation of the model has been a success.

The thermographs in Fig. 5.17(a) and Fig. 5.17(b) are very similar. Both temperature distributions are symmetrical about the line $y = x$, as would be expected give the power

input shown in Fig. 5.16. Therefore the 3-D Fourier thermal model appears to working successfully when using eight Fourier terms in each direction (M=N=K=8). This is also supported by the cut lines which appear in Fig. 5.18. It is clear that increasing the number of Fourier terms used in the 3-D Fourier model improves accuracy while having a detrimental affect on the simulation speed. This is what would be expected since the 3-D Fourier model with more terms is likely to provide a more accurate solution to the 3-D heat equation. However, the downside is that MATLAB/Simulink must handle a greater number of terms which leads to a slower simulation speed. It is worth noting that for the 3-D Fourier thermal model of a single block, the total number of terms is the product of KMN. This suggests that when modelling 3-D diffusion in structures which contain more than just one block, it is likely that the number of Fourier terms can quickly become excessive if care is not taken. Fig. 5.18 suggests that four Fourier terms in each dimension is a suitable compromise of simulation speed and accuracy, since the Fourier model is significantly slower when using eight Fourier terms in each dimension.

It is clear that the 1-D, 2-D and 3-D Fourier thermal models can capture the required aspects of heat diffusion through a single block. All the Fourier thermal models have proven accurate when simulating a range of transients. It is apparent that the accuracy of the 1-D, 2-D and 3-D Fourier thermal models is dependent on the number of Fourier terms used in the model. However, the benefit of using fewer terms is that the model simulates more quickly. As rapid simulation speed is vital for the thermal model, since it must be suitable for design and optimisation, it is clearly necessary to find a compromise between simulation speed and accuracy.

The Fourier thermal model is computationally efficient when compared with FLOTHERM. Regardless of the mesh employed by FLOTHERM, the Fourier model was significantly faster to simulate for every test case. A superior simulation speed was not the only advan-

tage of the Fourier model over FLOTHERM. The appearance of the results generated by the Fourier thermal model looked more realistic than those generated by FLOTHERM. The reason is that the FLOTHERM results were plotted as straight lines joining specified monitoring points whereas the Fourier model results took the form of a continuous wave. The fact that the Fourier model does not only supply temperatures at specified monitoring points is what makes the Fourier model a useful tool for hotspot detection.

The implementation of the Fourier thermal models in MATLAB/Simulink proved straightforward. The validation of the Fourier model proved a useful method of verifying the MATLAB/Simulink function blocks which were constructed and the MATLAB codes which were written. A positive indication of successful implementation was the fact that as the number of Fourier terms increased, so did the model accuracy. This is what would be expected when modelling pure heat conduction. Also, the methods used to convert between the spatial and Fourier domain which were implemented all appeared correct, which is particularly reassuring when using stacked 2-D matrices in the 3-D Fourier model. Implementing the power inputs as heat fluxes was simple because the Fourier model was created to describe any arbitrary heat flux at the top and bottom block boundary. The benefit of this feature will become more apparent when dealing with material boundaries.

This chapter has shown that the Fourier thermal model is capable of accurately simulating 1-D, 2-D and 3-D heat conduction through a single block of material. The Fourier thermal model is clearly producing the correct behaviour. Nevertheless, the Fourier thermal model is ultimately required to model the structure shown in Fig. 5.1, which is much more complicated than a single block of material in that multiple blocks of different cross-sectional areas are required to be modelled. Therefore the Fourier model requires further development in order to achieve this aim.

Chapter

6 Material Interfaces

The Fourier series thermal, which featured in chapter 5, undergoes further development in this chapter so that it is capable of modelling a whole power module package. Power module packaging structures consist of many vertically stacked blocks of material with different cross-sectional areas. Many different material interfaces are present within these structures. This chapter describes the methods employed by the Fourier thermal model to simulate these material interfaces. Every stage of Fourier series thermal model development is validated using the FVM software package FLOTHERM.

6.1 Constant Cross-sectional Area

6.1.1 1-D Heat Conduction

An appropriate place to begin is to consider the simplest of material interfaces: 1-D heat diffusion through the interface shown in Fig. 6.1. This situation, with blocks of constant x-y cross-section vertically stacked, occurs in power module packaging structures.

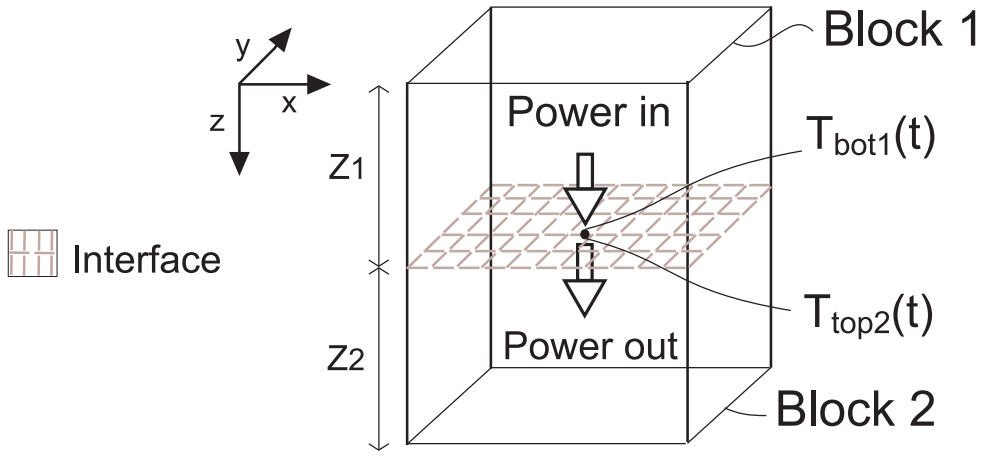

Figure 6.1: Diagram showing 1-D (z) heat conduction through a material interface. The x-y cross-sectional area is the same in block 1 and block 2.

Block 1 and block 2 have the same cross-sectional area (x-y plane). However, $z_1 \neq z_2$ and the material properties of each block are different. The point highlighted in the centre of Fig. 6.1 represents an infinitely small point in the x-y plane of the interface. The temperature of this point is the same whether considering block 1 or block 2, i.e:

$$T_{bot1}(t) = T_{top2}(t), \tag{6.1}$$

where T_{bot1} represents the temperature at the bottom of block 1 and T_{top2} represents the temperature at the top of block 2. It is also important to ensure that the total power entering the interface is equal to the total power leaving the interface. So the second constraint is:

$$P_{in} = P_{out}. \tag{6.2}$$

According to Fourier's Law for heat conduction,

$$P = -kA \left. \frac{dT(t)}{dz} \right|_z. \tag{6.3}$$

The constant of proportionality here is k (W/mK), the thermal conductivity. A is the area of the x-y plane. $\left. \frac{\partial T(t)}{\partial z} \right|_{bot1}$ is the heat flux leaving the bottom of block 1, and $\left. \frac{\partial T(t)}{\partial z} \right|_{top2}$ is the heat flux entering the top of block 2. Using Equations (6.2) and (6.3), and the fact that the area is the same in both blocks, gives:

$$\left. \frac{\partial T(t)}{\partial z} \right|_{bot1} = \frac{k_2}{k_1} \left. \frac{\partial T(t)}{\partial z} \right|_{top2}. \tag{6.4}$$

The Fourier series solution from section 5.2.1.1 can be used to calculate $T_{bot1}(t)$ from $\left. \frac{\partial T(t)}{\partial z} \right|_{bot1}$. Similarly, the Fourier series solution can calculate $T_{top2}(t)$ when given $\left. \frac{\partial T(t)}{\partial z} \right|_{top2}$. However, the outputs of the Fourier series solution are the temperatures and the inputs are the heat fluxes, so Equations (6.1) and (6.4) cannot be used directly.

The solution to the problem is to use a "Virtual Earth" feedback system based on [175] and shown in Fig. 6.2. It is given its name because it ensures that the temperature at the interface of the materials is consistent, i.e. it constrains $T_{bot1} = T_{top2}$ by using a large gain to force $e(t) \approx 0$, where $e(t)$ is the error between the temperatures on either side of the interface. It also fulfils the other system requirement because it forces the power leaving the underneath of the top block to be equal to the power entering the top of the block below. Fig. 6.2 shows that the two temperature readings, $T_{bot1}(t)$ and $T_{top2}(t)$, meet at a summing junction.

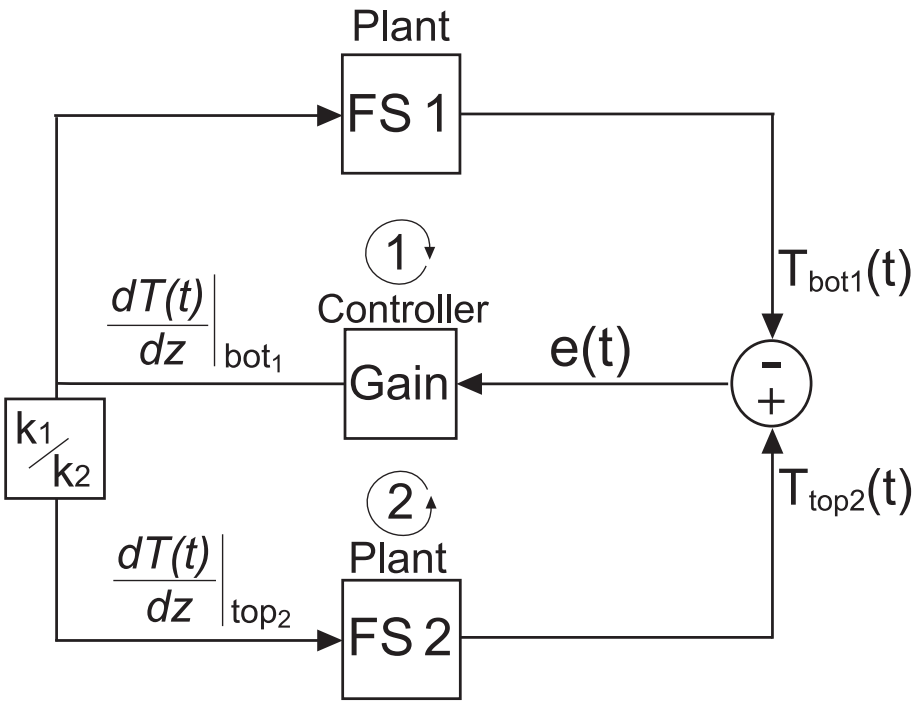

Figure 6.2: Diagram of the Virtual Earth Feedback system used to simulate the material interface in Fig. 6.1. FS1 and FS2 are the Fourier series solutions to the heat equation in block 1 and block 2 respectively.

The error $e(t)$ is obtained directly:

$$e\left(t\right) = T_{bot1}\left(t\right) - T_{top2}\left(t\right). \tag{6.5}$$

This error is available for manipulation and is the input to the controller. The controller output, $\left.\frac{\partial T(t)}{\partial z}\right|_{bot1}$, is the multiplication product of the error signal and the proportional gain. This can be mathematically expressed as:

$$\left.\frac{\partial T(t)}{\partial z}\right|_{bot1} = Gain * e(t). \tag{6.6}$$

Therefore, substituting in equation 6.4) and rearranging gives:

$$\left.\frac{\partial T(t)}{\partial z}\right|_{top2} = Gain * e(t) * \frac{k_1}{k_2}. \tag{6.7}$$

This is a simple procedure because it only involves a controller which consists entirely of a multiplying constant (gain). The controller provides the required compensation. The controller output $\left.\frac{\partial T(t)}{\partial z}\right|_{bot1}$ is then the input to plant 1. $\left.\frac{\partial T(t)}{\partial z}\right|_{top2}$ is the input to plant 2. The closed loop equations relating T_{bot1} to T_{top2} are given by:

Loop 1

$$T_{bot1} = -FS1 * \left.\frac{\partial T(t)}{\partial z}\right|_{bot1}. \tag{6.8}$$

Substitution of Equation (6.6) and Equation (6.5) into Equation (6.8) produces:

$$T_{bot1} = \left(\frac{(FS1 * Gain)}{(1 + FS1 * Gain)}\right) T_{top2}. \tag{6.9}$$

Loop 2

$$T_{top2} = FS2 * \left.\frac{\partial T(t)}{\partial z}\right|_{top2}. \tag{6.10}$$

Substitution of Equation (6.7) and Equation (6.5) into Equation (6.10) produces:

$$T_{top2} = \left(\frac{\left(FS2 * Gain * \frac{k1}{k2}\right)}{\left(1 + FS2 * Gain * \frac{k1}{k2}\right)}\right) T_{bot1}. \tag{6.11}$$

In the steady state, i.e. $t > \infty$, as long as $(FS1 * Gain) >> 1$ and $\left(FS2 * Gain * \frac{k_1}{k_2}\right) >> 1$, the output will be just about equal to the input for any type of input signal. It is clear that the gain must greatly exceed unity; this applies to all negative feedback systems regardless of system details.

In order to supplement the understanding of the system, consider what would happen at the instant at which $T_{bot1}(t)$ increased. This would cause the value of $e(t)$ to be a negative value. Therefore the value of $\frac{\partial T}{\partial z}\big|_{bot1}$ would also be negative, providing the gain was positive. This means that power would leave the underneath of block 1 (Fourier's law). Similarly, the value of $\frac{\partial T}{\partial z}\big|_{top2}$ would be negative. Therefore, heat would enter the top of block 2, causing T_{top2} to rise, therefore reducing $e(t)$ and bringing the values of T_{bot1} and T_{top2} closer together.

The gain value depends on the required accuracy. Increasing leads to a smaller error in the system, but less numerical stability. Another consequence of using increasing feedback gain is an increase in the number of steps required to find the solution, which in turn leads to a longer simulation time. An infinitely high feedback gain would be needed to simulate a 'perfect' interface [176, 177].

A whole chain of feedback loops would be required in order to model more than two packaging layers, as shown in Fig. 6.3.

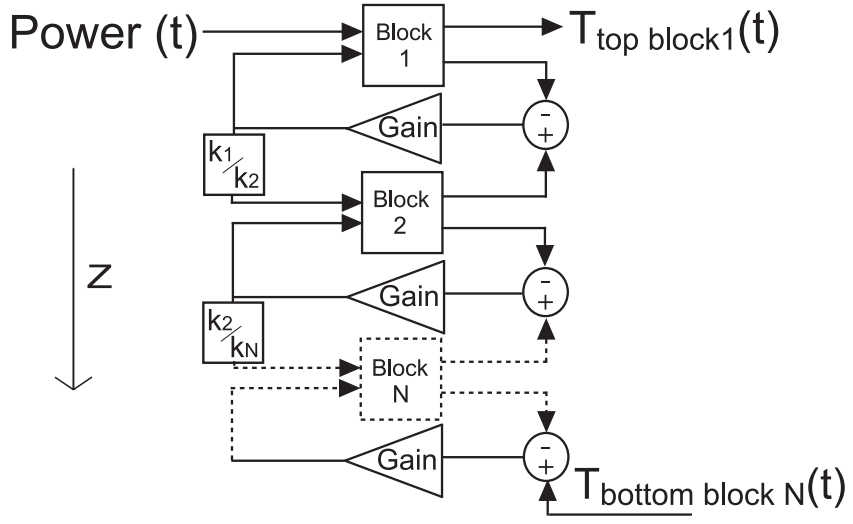

Figure 6.3: Diagram of a chain of feedback loops required to simulate the material interfaces in N layers of material with a constant x-y cross-sectional area.

6.1.2 2-D Heat Conduction

Other than an added dimension, the approach for this case is very similar to that shown in section 6.1.1. The difference is that an infinitely thin boundary line is used to represent the boundary, as shown in Fig. 6.4, rather than an infinitely small point. The data along the line is in the Fourier domain and can therefore describe any distribution along the x dimension. Therefore the boundary can model 2-D (x-z) diffusion through the two blocks.

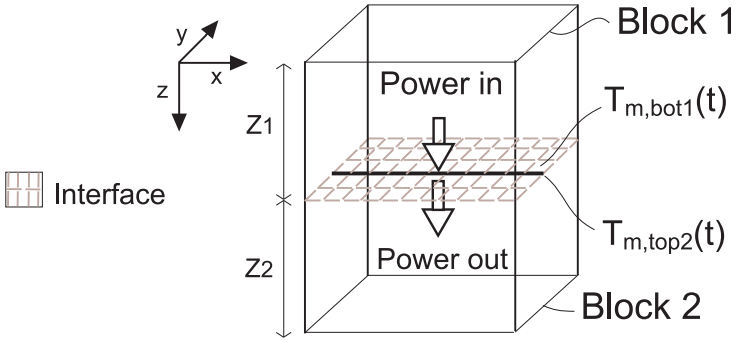

Figure 6.4: Diagram showing 2-D (x-z) heat conduction through a material interface. The x-y cross-sectional area is the same in block 1 and block 2.

There are two constraints on the system. The first is that the temperature distribution along the boundary line is the same whether considering block 1 or block 2, i.e: ,

$$T_{m,bot1}(t) = T_{m,top2}(t), \tag{6.12}$$

where $T_{m,bot1}(t)$ represents the temperature distribution along the x dimension at the bottom of block 1. $T_{m,top2}(t)$ represents the temperature distribution along the x dimension at the top of block 2. The second constraint is that the power entering the interface is equal to the power leaving the interface, giving rise to the following expression:

$$\left.\frac{\partial T_m(t)}{\partial z}\right|_{bot1} = \frac{k_2}{k_1}\left.\frac{\partial T_m(t)}{\partial z}\right|_{top2}, \tag{6.13}$$

where $\left.\frac{\partial T_m(t)}{\partial z}\right|_{bot1}$ is the heat flux at the bottom of block 1 and $\left.\frac{\partial T_m(t)}{\partial z}\right|_{top2}$ is the heat flux at the top of block 2. The "Virtual Earth" method is applied as shown in Fig. 6.2; however, the data is in the form of a line distribution along the x dimension rather than a single numerical value.

6.1.3 3-D Heat Conduction

The technique used in this case is again similar to section 6.1.1. However, an infinitely thin x-y surface is used to represent the boundary, as shown in Fig. 6.5, rather than an infinitely small point. The data describing the surface is in the Fourier domain and can therefore describe any x-y surface distribution. Therefore the boundary can model 3-D (x-z) diffusion through the two blocks. Two constraints are placed on the system. The

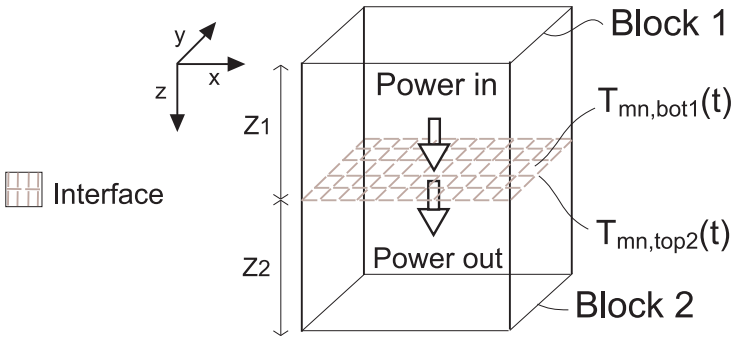

Figure 6.5: Diagram showing 3-D (x-y-z) heat conduction through a material interface. The x-y cross-sectional area is the same in block 1 and block 2.

first constraint is that the temperature distribution of the x-y boundary surface is the same whether considering block 1 or block 2, i.e:

$$T_{mn,bot1}(t) = T_{mn,top2}(t), \tag{6.14}$$

where $T_{mn,bot1}(t)$ represents the temperature distribution of the x-y surface at the bottom of block 1. $T_{mn,top2}(t)$ represents the temperature distribution of the x-y surface at the top of block 2. The second constraint is that the power entering the interface is equal to the power leaving the interface, giving rise to the following expression:

$$\left.\frac{\partial T_{mn}(t)}{\partial z}\right|_{bot1} = \frac{k_2}{k_1}\left.\frac{\partial T_{mn}(t)}{\partial z}\right|_{top2}, \tag{6.15}$$

where $\left.\frac{\partial T_{mn}(t)}{\partial z}\right|_{bot1}$ is the heat flux at the bottom of block 1 and $\left.\frac{\partial T_{mn}(t)}{\partial z}\right|_{top2}$ is the heat flux at the top of block 2. The "Virtual Earth" method, described in Fig. 6.2, is applied. However, the data is in the form of a x-y surface distribution rather than a numerical value for this case.

6.2 Different Cross-sectional Area

The vertically stacked blocks of material which make up a power module package tend to have varied x-y cross-sections. This gives rise to different material interfaces to those shown in the previous section and require simulation. When considering 2-D heat diffusion it is necessary to model a cross-sectional change in one dimension only, either the x or y dimension. However, when modelling 3-D diffusion cross-sectional changes in both the x and y dimension must be acknowledged. 1-D heat diffusion is not considered in this section since, by its very nature, it assumes a constant x-y cross-section.

6.2.1 2-D Heat Conduction

This section will demonstrate the approach to modelling 2-D diffusion for a cross-sectional change in the x dimension only, although the approach would be the same if modelling a change in the y dimension only. Therefore, in Fig. 6.6, block 1 and block 2 have different x and z dimensions but a common y dimension. The Fourier model requires the heat flux entering block 2, between x=0 and x=x_3 at z=z_1, to be accurately represented. Also, the temperature distribution across the top of block 2, between x=x_1 and x=x_2, must be extracted. To achieve this, it is necessary to transform between different Fourier domains in a way which represents the spatial change in the x dimension. This is possible through the use of a heat flux window matrix and a temperature extraction matrix. Each matrix is applied within the feedback system shown in Fig. 6.7.

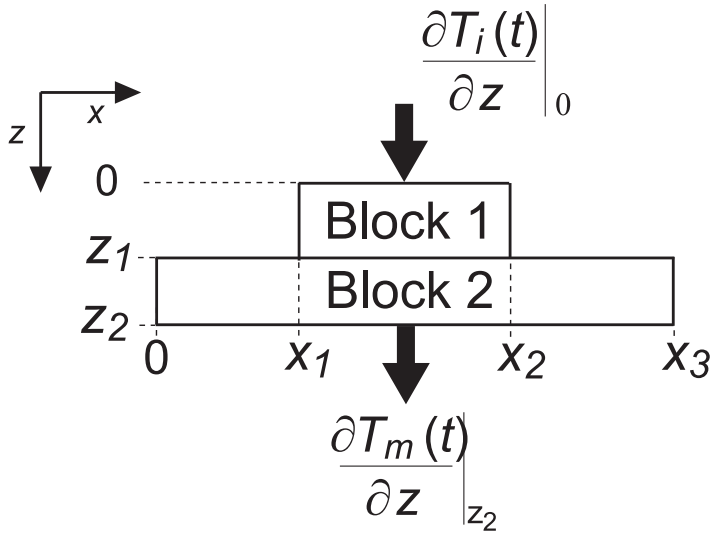

Figure 6.6: Heat diffusion through two blocks with a different x dimension. Block 1 has I Fourier harmonics, while block 2 has M Fourier harmonics, to describe a distribution in the x dimension.

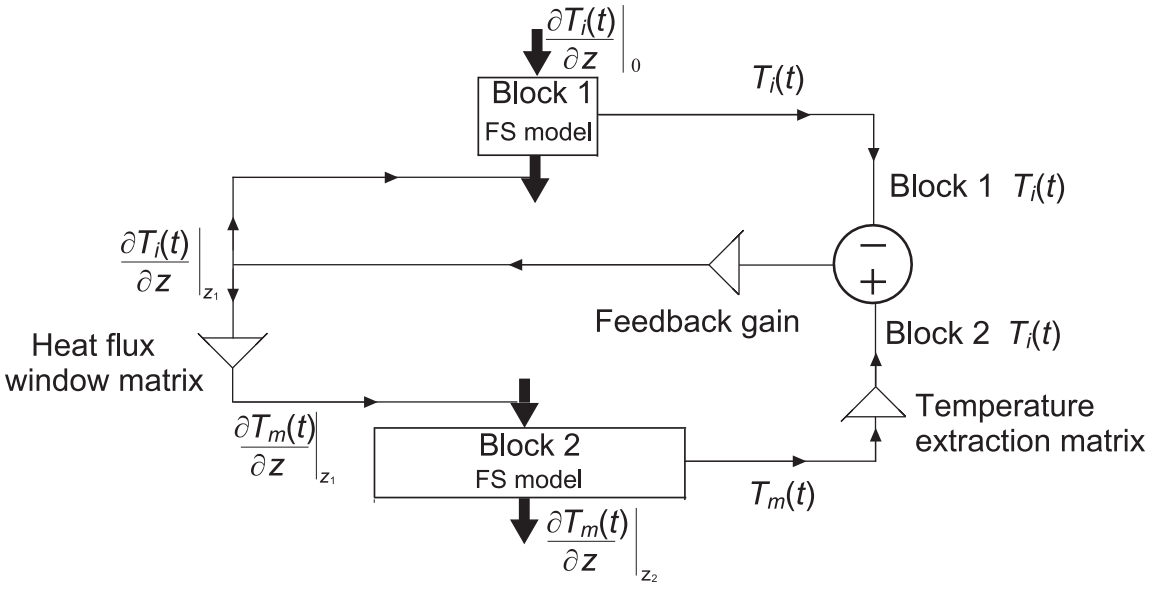

Figure 6.7: A schematic showing the approach to modelling the problem shown in Fig. 6.6. T_i are the temperature harmonics based on the domain x=x_1 to x=x_2, and T_m are those based on x=0 to x=x_3.

6.2.1.1 Heat Flux Window

In order to convert the heat flux at $z = Z_1$ in Fig. 6.6 from the block 1 domain (x=x_1 to x=x_2) to the block 2 domain (x=0 to x=x_3), a transformation between the two Fourier domains is required.

In Fig. 6.8, an arbitrary function, $f_1(x)$, represents the heat flux leaving the bottom of block 1. The function $f_2(x)$, which also appears in Fig. 6.8, represents the heat flux entering block 2. It is observed that $f_1(x)$=$f_2(x)$ for $x_1 \leq x \leq x_2$ because a perfect thermal contact is assumed at the material interface. $f_2(x)$=0 for $0 \leq x \leq x_1$ and $x_2 \leq x_3$ because the heat flux is zero where block 1 is not in contact with block 2.

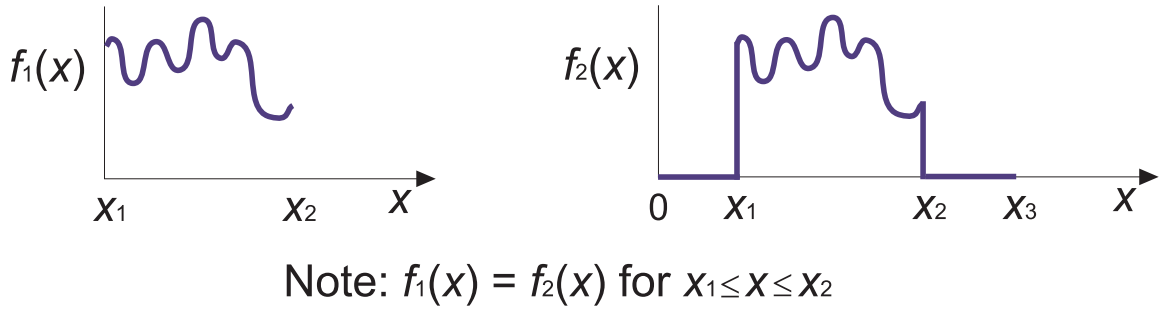

Figure 6.8: The function, $f_1(x)$, represents heat flux at the bottom of block 1 in Fig. 6.6. The function, $f_2(x)$, describes the heat flux entering the top of block 2, in Fig. 6.6.

The definition of 1-D Fourier cosine series gives: ,

$$f_1(x) = \sum_{i=0}^{\infty} F_{1i} \cos\left(\frac{i\pi(x - x_1)}{x_2 - x_1}\right), \tag{6.16}$$

where F_{1i} represents the Fourier coefficients in the block 1 domain and i is the index for the Fourier series F_{1i}. The 1-D Fourier cosine series definition of the function $f_2(x)$ is:

$$f_2(x) = \sum_{m=0}^{\infty} F_{2m} \cos\left(\frac{m\pi x}{x_3}\right), \tag{6.17}$$

where F_{2m} represents the Fourier coefficients and m is the index for the Fourier series F_{2m}. Since $f_1(x)=f_2(x)$ for $x_1 \leq x \leq x_2$, the expression for F_{2m} in terms of F_{1i} is:

$$F_{2m} = \begin{cases} \frac{1}{x_3} \int_{x_1}^{x_2} \sum_{i=0}^{\infty} F_{1i} \cos\left(\frac{i\pi(x-x_1)}{(x_2-x_1)}\right) dx, & m=0 \\ \frac{2}{x_3} \int_{x_1}^{x_2} \sum_{i=0}^{\infty} F_{1i} \cos\left(\frac{i\pi(x-x_1)}{(x_2-x_1)}\right) \cos\left(\frac{m\pi x}{x_3}\right) dx, & m>0 \end{cases} \tag{6.18}$$

The solution to Equation (6.18) is:

$$F_{2m} = \begin{cases} [(x_2 - x_1)/x_3] F_{1i}, & m=0,\ i=0 \\ \frac{2}{m\pi}\left[\sin\left(\frac{m\pi x_2}{x_3}\right) - \sin\left(\frac{m\pi x_1}{x_3}\right)\right] F_{1i}, & m>0,\ i=0 \\ [0] \sum_{i=0}^{I} F_{1i}, & m=0,\ i>0 \\ \frac{-2m}{\pi x_3^2} \left(\frac{1}{\left(\frac{i^2}{(x_2-x_1)^2}\right) - \left(\frac{m^2}{x_3^2}\right)}\right) \left((-1)^i \sin\left(\frac{m\pi x_2}{x_3}\right) - \sin\left(\frac{m\pi x_1}{x_3}\right)\right) \sum_{i=0}^{I} F_{1i}. & m>0,\ i>0 \end{cases} \tag{6.19}$$

Fig. 6.9 shows how to convert from I Fourier harmonics (block 1 domain) to M Fourier harmonics (block 2 domain) in order represent the heat flux window entering block 2. Each expression in Equation (6.19) occupies a different region within the premultiplier conversion matrix.

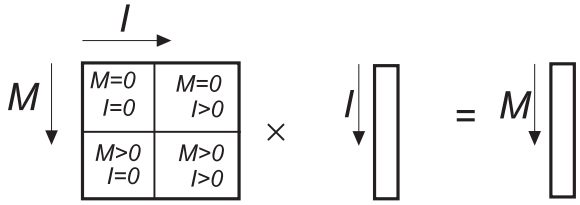

Figure 6.9: Matrix multiplication to convert from a Fourier series with I Fourier harmonics (block 1) to a Fourier series with M Fourier harmonics (block 2).

6.2.1.2 Temperature Extraction

In order for the feedback loop in Fig. 6.7 to model the situation in Fig. 6.6 correctly, the temperature distribution in block 2 between x=x_1 and x=x_2 at z=z_1 must be extracted and then compared with the temperature distribution at the bottom of block 1. To achieve this a transformation between the two Fourier domains must be performed.

The arbitrary function $f_3(x)$, in Fig. 6.10, represents the temperature distribution between x=0 and x=x_3, at z=z_1, in the block 2 domain. The function $f_4(x)$, in Fig. 6.10, is extracted from $f_3(x)$. It represents the temperature distribution between x=x_1 and x=x_2 z=z_1, in block 1 domain.

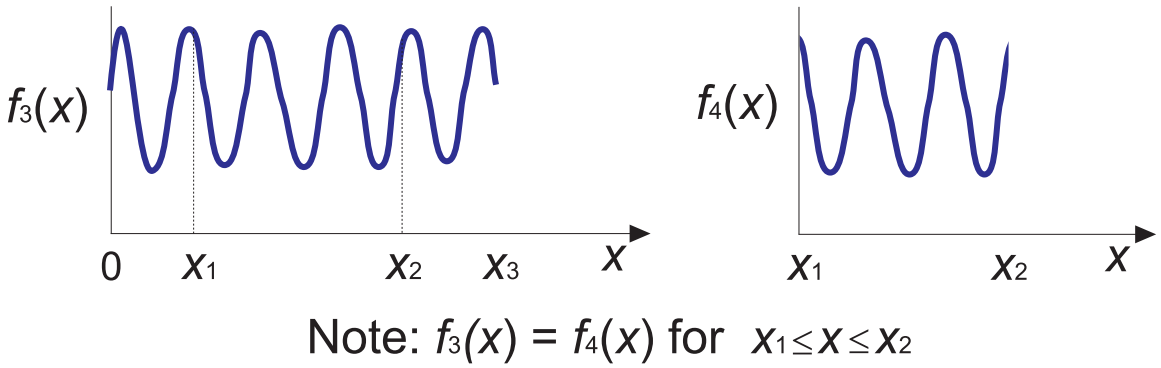

Figure 6.10: The function, $f_3(x)$, represents the temperature distribution across the top of block 2. The function $f_4(x)$ represents the temperature distribution at the top of block 2 between x=x_1 and x=x_2. $f_4(x)$ has been extracted from the function $f_3(x)$.

The 1-D Fourier cosine series of the function $f_3(x)$ is:

$$f_3(x) = \sum_{m=0}^{\infty} F_{3m} \cos\left(\frac{m\pi x}{x_3}\right), \tag{6.20}$$

where F_{3m} represents the Fourier coefficients and m is the index for the Fourier series.

The 1-D Fourier cosine series of the function $f_4(x)$ is:

$$f_4(x) = \sum_{i=0}^{\infty} F_{4i} \cos\left(\frac{i\pi(x - x_1)}{(x_2 - x_1)}\right), \tag{6.21}$$

where F_{4i} represents the Fourier coefficients and where i is the index of the Fourier series.

An expression of F_{4i} in terms of F_{3m} is required to create a pre-multiplying conversion matrix. Since $f_3(x)$=$f_4(x)$ for $x_1 \leq x \leq x_2$, the expression for F_{4m} in terms of F_{3i} is:

$$F_{4i} = \begin{cases} \frac{1}{(x_2 - x_1)} \sum_{m=0}^{\infty} F_{3m} \int_{x_1}^{x_2} \cos\left(\frac{m\pi x}{x_3}\right) dx, & i=0 \\ \frac{2}{(x_2 - x_1)} \sum_{m=0}^{\infty} F_{3m} \int_{x_1}^{x_2} \cos\left(\frac{m\pi x}{x_3}\right) \cos\left(\frac{i\pi(x - x_1)}{(x_2 - x_1)}\right) dx. & i>0 \end{cases}. \tag{6.22}$$

The solution to Equation (6.22) is:

$$F_{4i} = \begin{cases} F_{3m}, & i=0,\ m=0 \\ [0]\, F_{3m}, & i>0,\ m=0 \\ \frac{x_3}{m\pi(x_2 - x_1)} \left(\sin\left(\frac{m\pi x_2}{x_3}\right) - \sin\left(\frac{m\pi x_1}{x_3}\right)\right) \sum_{m=0}^{M} F_{3m}, & i=0,\ m>0 \\ \frac{-2m}{\pi(x_2 - x_1)x_3} \left(\frac{1}{\left(\frac{i^2}{(x_2 - x_1)^2}\right) - \left(\frac{m^2}{x_3^2}\right)}\right) \left((-1)^i \sin\left(\frac{m\pi x_2}{x_3}\right) - \sin\left(\frac{m\pi x_1}{x_3}\right)\right) \sum_{m=0}^{M} F_{3m}. & i>0,\ m>0 \end{cases} \tag{6.23}$$

Using the solution in Equation (6.23), it is now possible to construct a premultiplying conversion matrix needed to convert from M Fourier harmonics (block 2 domain) to I Fourier harmonics (block 1 domain). This conversion matrix will extract the required temperature distribution. This happens in a similar fashion to the matrix multiplication in Fig. 6.9.

6.2.2 3-D Heat Conduction

The same approach used to model the heat conduction problem in Fig. 6.6 is applied to model the situation in Fig. 6.11. Whether representing the 2-D x-y heat flux window entering block 2 or carrying out the necessary x-y temperature distribution extraction, a transformation between Fourier domains is required. To simulate the problem in Fig. 6.11 it is necessary to convert in both the x dimension and the y dimension. Therefore a post-multiplying conversion matrix is used to convert in the y dimension in addition to the pre-multiplying conversion matrix which is used to convert in the x dimension.

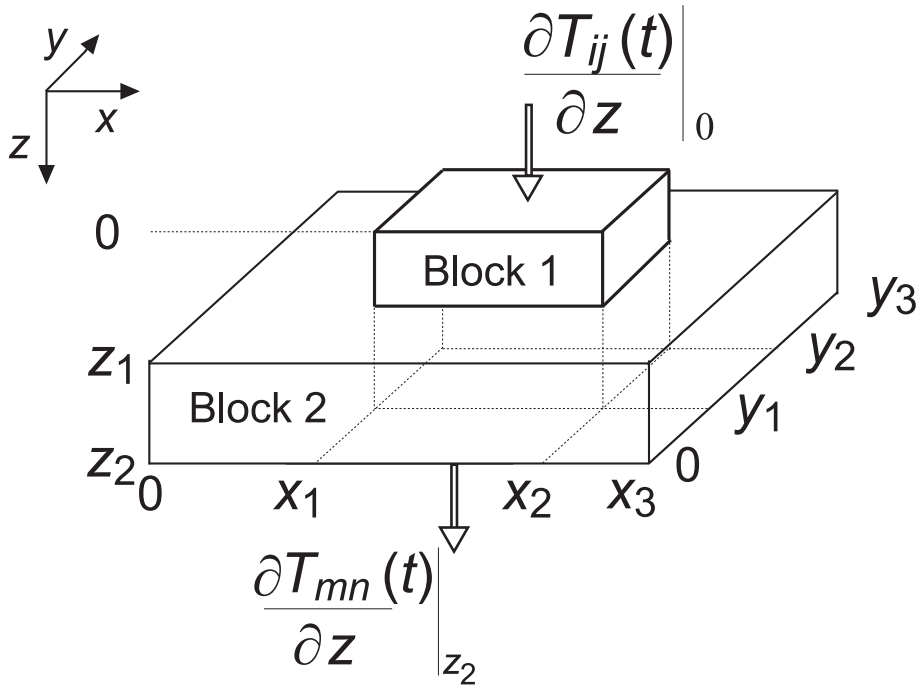

Figure 6.11: 3-D heat diffusion through two blocks with different x, y and z dimensions. The IJ Fourier domain describes the x-y distribution in block 1. The MN Fourier domain describes the x-y distribution in block 2.

6.2.2.1 Heat Flux Window

The matrix algebra associated with a change from the IJ Fourier series domain (block 1) to the MN Fourier series domain (block 2) is shown in Fig. 6.12. This is required to generate the 2-D heat flux window entering the top of block 2, in Fig. 6.11. The derivation of the MI pre-multiplying conversion matrix proceeds as in section (6.2.1.1). The derivation of the post-multiplying JN conversion matrix is similar.

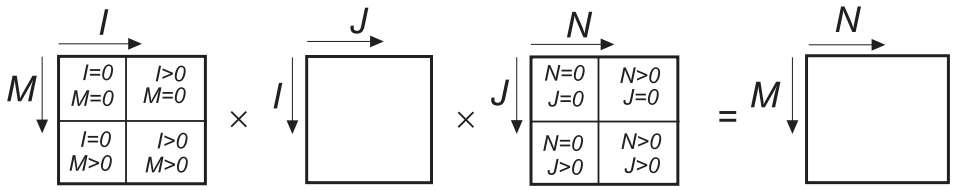

Figure 6.12: Matrix conversion from the IJ domain (block 1) to the MN domain (block 2). The M by I matrix converts in the x dimension, the J by N matrix converts in the y dimension.

6.2.2.2 Temperature Extraction

The matrix algebra associated with a change from the MN Fourier series domain (block 2) to the IJ Fourier series domain (block 1) is shown in Fig. 6.13. This is required to extract the 2-D temperature distribution from the region of block 2 which is in contact with block 1. The derivation of the pre-multiplying IM conversion matrix proceeds as in section (6.2.1.2). The derivation of post-multiplying NJ conversion matrix is similar.

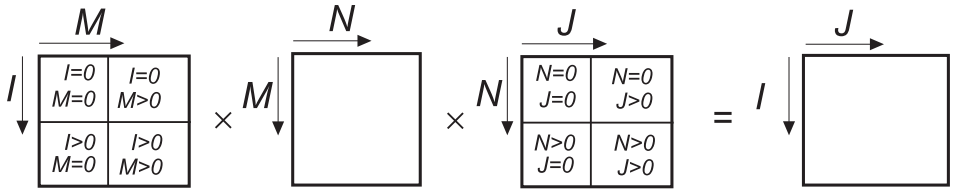

Figure 6.13: Matrix conversion from the MN Fourier domain (block 2) to the IJ Fourier domain (block 1). The I by M matrix converts in the x dimension, the N by J matrix converts in the y dimension.

6.3 Multiple Heat Sources

The principle of superposition is applied in order to model thermal interactions from multiple independent heat sources. This is achieved by simply adding the heat flux representations from the individual heat sources (i.e. adjacent devices). The use of this principle for this purpose is widely reported in literature [178–182]. Consider the metal (1) block, which appears in the packaging structure in Fig. 5.1. If both silicon devices were to dissipate heat, the heat flux reaching the metal (1) block is the sum of the flux coming down from the IGBT solder block and the flux from the diode solder block. Fig. 6.14 helps visualise superposition in the spatial domain. Simple addition also works in the Fourier domain because the heat equation is linear. Adding heat fluxes in this way ensures that the effects of thermal coupling are taken into account. It is worth mentioning that IGBT and diode in the simulation domain, shown in Fig. 5.1 of chapter 5, are never switched on at the same time during the operation of the Toyota Prius power converter. Therefore the devices do not dissipate heat at the same time because they are anti-parallel and conduct current in different directions. Nevertheless, it is essential that the Fourier model can simulate this scenario because heat continues to diffuse through the packaging structure from a hot device even when it is switched off.

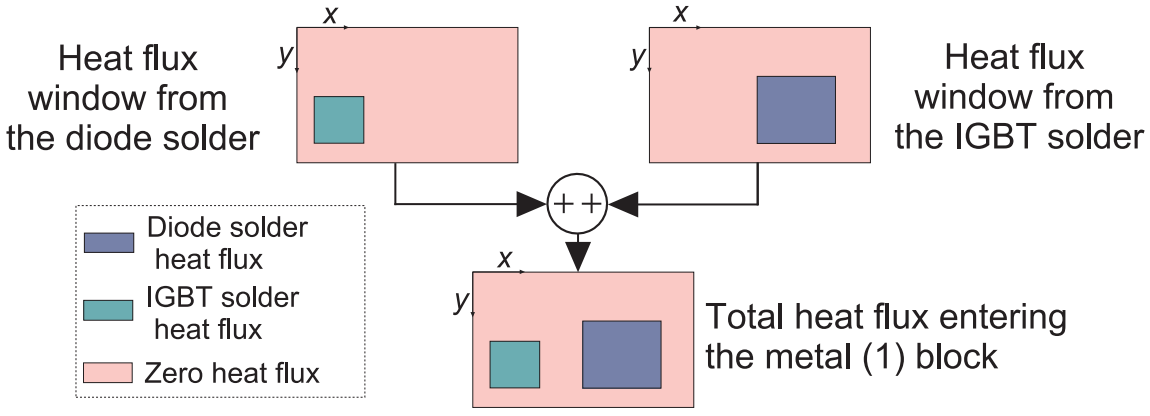

Figure 6.14: A spatial representation of the superposition principle. The heat flux into the metal (1) block, shown in Fig. 2.10, equates to the sum of the individual heat fluxes.

6.4 Results

Throughout this results section heat diffusion is simulated through a range of structures in order to test the approaches presented in this chapter for modelling various material interfaces. Validation of the Fourier thermal model is achieved by comparison between the results generated by it and FLOTHERM. The procedure for creating FLOTHERM thermal models is explained in section 5.3.1

6.4.1 Constant Cross-sectional Area

This section aims to validate the 'Virtual Earth' feedback system shown in Fig. 6.2. Only structures with non-varying x-y cross-sectional areas will be considered.

6.4.1.1 1-D Heat Conduction

Fig. 6.15 shows a 1-D heat conduction problem. The x-y cross-sectional area of the structure shown matches that of the silicon diode in a Toyota Prius power converter. The z dimensions of the materials also match those from the Toyota converter but only the material as far down as the metal (2) layer is considered. Therefore the blocks below the silicon layer have different material properties and thicknesses. The underside of the metal (2) layer is fixed at 300K. A transient power input of 50W was dissipated into the top of the silicon diode for 1 second, as shown in Fig. 6.15.

To enable comparison between the 1-D Fourier model and FLOTHERM, the transient temperatures at the centre of each block of material were plotted on log scale, as shown in Fig. 6.16. The mesh used in FLOTHERM was fine, containing 106032 nodes and it solved using 50 time steps. K represents the number of Fourier harmonics used in the Fourier model to represent each block of material. The Fourier model feedback gain was very high at 10^8 to ensure a "perfect" thermal contact at the material interfaces.

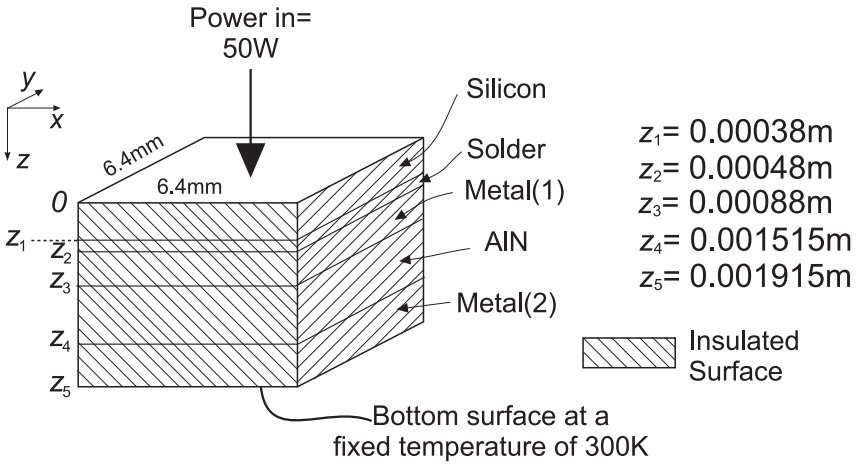

Figure 6.15: Diagram of a 1-D heat conduction problem containing vertically stacked materials with constant x-y cross-sectional area. The power input is applied evenly across the top surface for 1 second. Drawing not to scale.

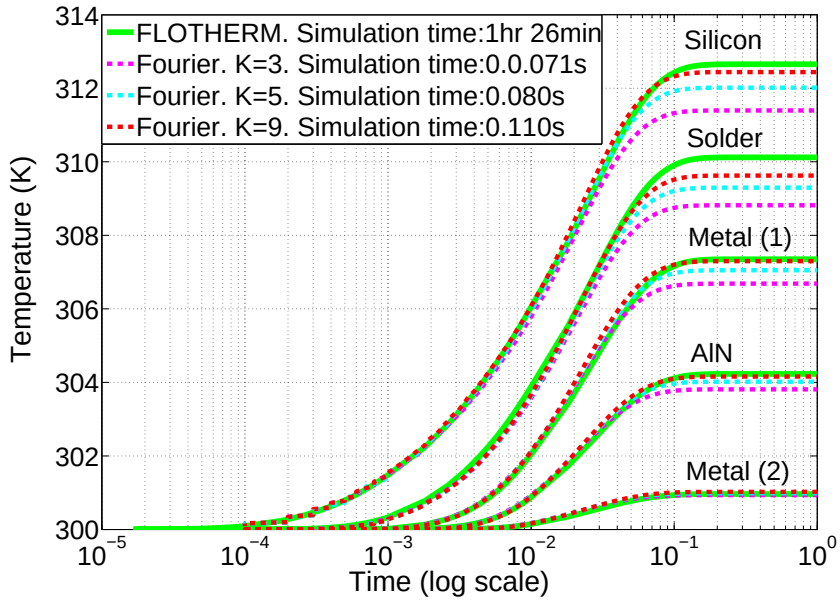

Figure 6.16: Transient temperature profiles generated by the Fourier thermal model and FLOTHERM. The temperatures represent the centre point of each block of material shown in Fig. 6.15. Results are plotted on a log scale.

6.4.1.2 2-D Heat Conduction

This simulation applies the 2-D Fourier series model and FLOTHERM to 2-D heat conduction problem shown in Fig. 6.17. The z dimensions and material properties of the materials match those which are used in a Toyota Prius power converter package. The initial temperature of the structure was 300K and the underside of the Al alloy layer is fixed at 300K.

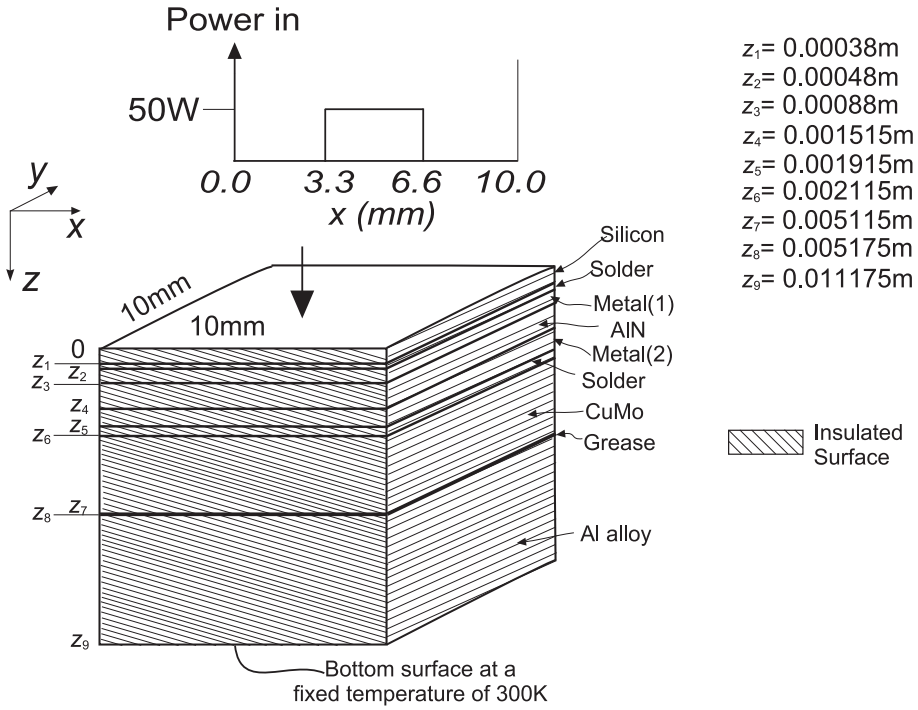

Figure 6.17: Diagram of a 2-D heat conduction problem containing vertically stacked materials with constant x-y cross-sectional area. The power input was applied across the whole of the top surface, with no variation in the y dimension for a total of 10 seconds. Diagram not to scale.

The results of modelling this structure using the 2-D Fourier model and FLOTHERM appear in the thermographs shown in Fig. 6.18. The Fourier thermal model used a high feedback gain of 10^8 to model the material boundaries. K and M represent the number of Fourier harmonics used in the Fourier model along the z and x dimension respectively. The FLOTHERM model employed a coarse mesh with 101175 nodes, and it calculated using 120 time steps. The FLOTHERM model relied on 729 temperature monitoring points in order to produce the thermograph shown in Fig. 6.18(d).

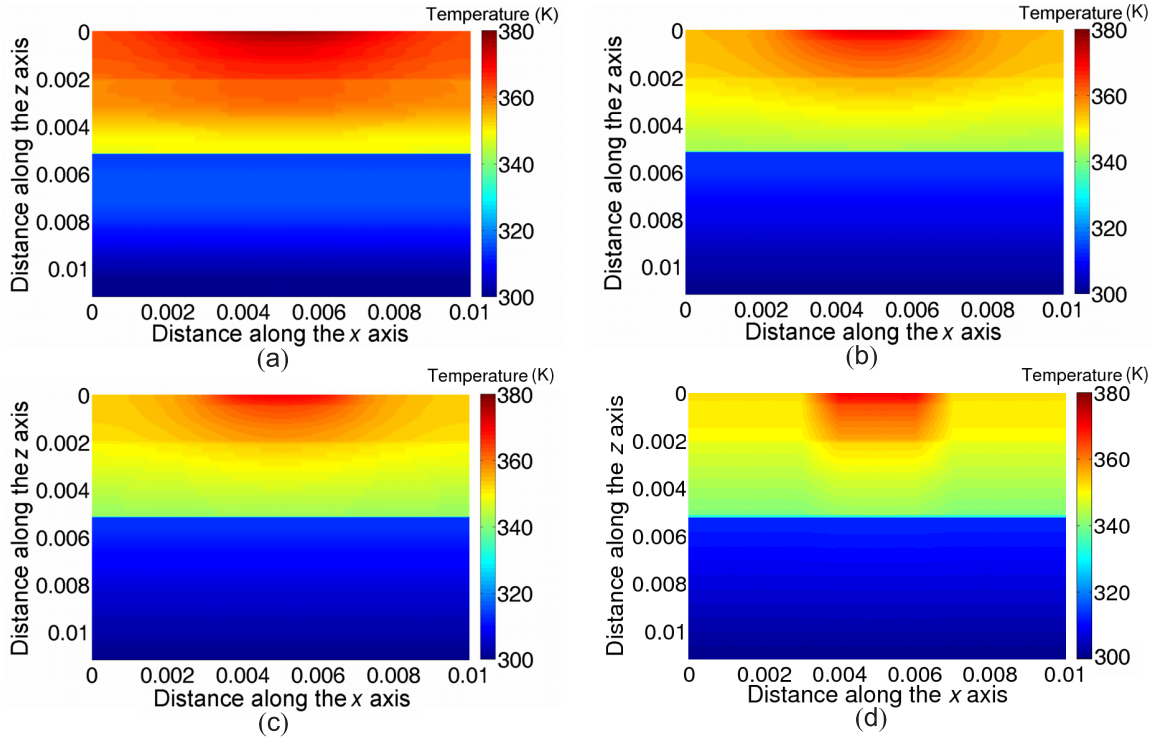

Figure 6.18: Thermographs illustrating the simulation results from modelling the heat conduction problem in Fig. 6.17. The thermographs represent the x-y plane at z=z_3, at time t=10s.
(a) Fourier model K=M=3. Simulation time: 0.015s.
(b) Fourier model K=M=5. Simulation time: 0.76s.
(c) Fourier model K=M=9. Simulation time: 4.96s.
(d) FLOTHERM model. Simulation time: 2hr 35min.

6.4.2 3-D Heat Conduction

The power source shown in Fig. 6.19 was applied for 0.5 seconds to the structure shown. The structure consists of two blocks of material which are vertically stacked. The blocks have the same x-y cross-sectional area and an initial temperature of 300K.

The 3-D heat conduction problem in Fig. 6.19 was simulated by a 3-D Fourier series model and FLOTHERM. Fig. 6.20 shows a comparison of the temperature distribution in the x-y plane at $z = z_2$ after 0.5 seconds. The FLOTHERM model contained 121 temperature monitoring points in the x-y plane at $z = z_2$. The FLOTHERM model employed a medium density mesh of 369920 nodes and calculated results over 25 time steps. K, M and N represent the number of Fourier harmonics in the z, x and y dimensions respectively. The Fourier thermal model has used a feedback gain of 10^8 at the material interface.

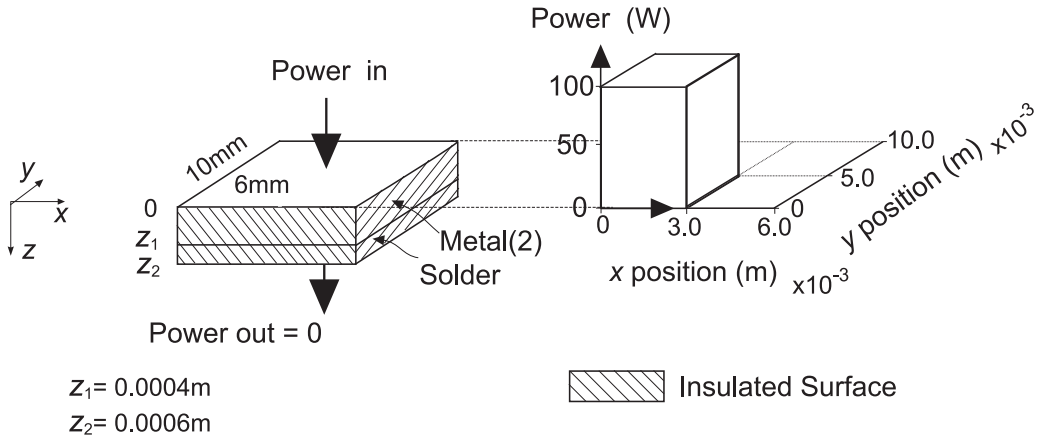

Figure 6.19: 3-D heat conduction problem containing vertically stacked materials with a constant x-y cross-sectional area. The power input is applied for 0.5 seconds. Diagram not to scale.

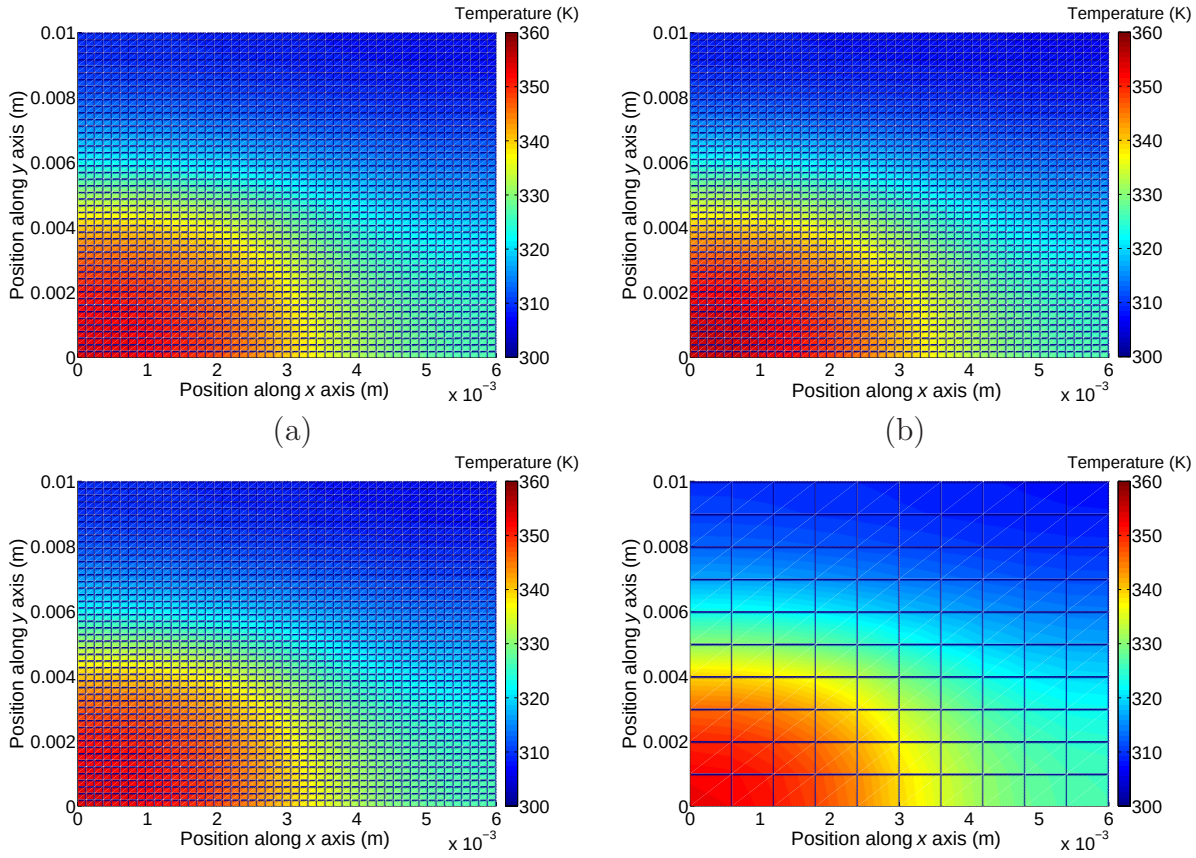

Figure 6.20: Thermographs illustrating the simulation results from modelling the heat conduction problem in Fig. 6.19. The thermographs represent the x-y plane at z=z_2, at time t=0.5s.
(a) Fourier model K=M=N=3. Simulation time: 0.09s.
(b) Fourier model K=M=N=5. Simulation time: 0.21s.
(c) Fourier model K=M=N=8. Simulation time: 1.17s.
(d) FLOTHERM model. Simulation time: 1hr 27 mins.

In order to gain a clear comparison between the results generated by FLOTHERM and the Fourier thermal mode, cut lines of the results in Fig. 6.20 were taken. Fig. 6.21 and Fig. 6.22 show the cut lines taken along the x and y axes respectively.

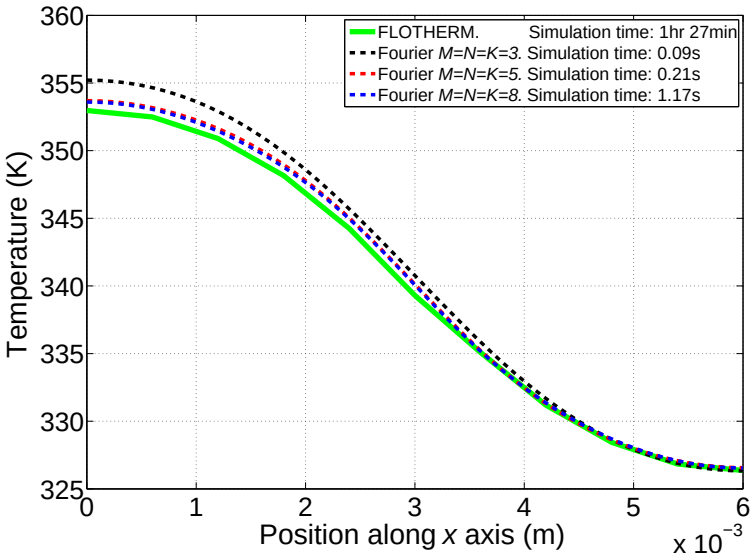

Figure 6.21: Graph showing a cut line from the results in Fig. 6.20 taken along the x axis.

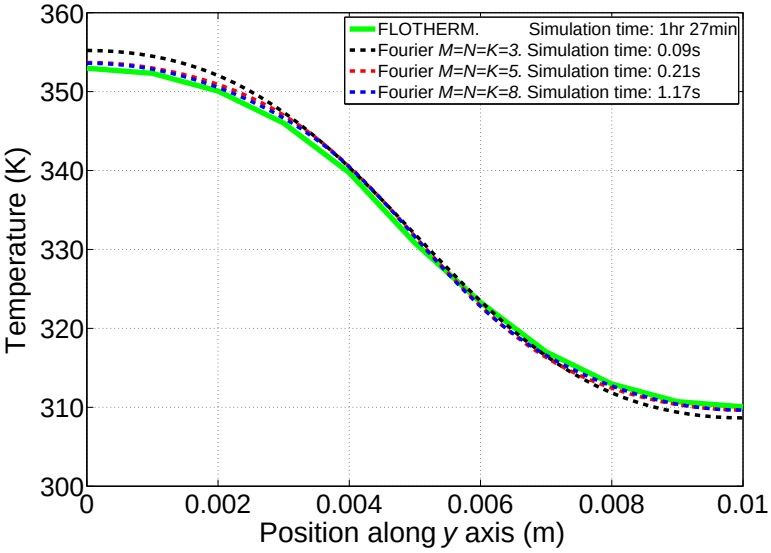

Figure 6.22: Graph showing a cut line from the results in Fig. 6.20 along y axis.

6.4.3 Different cross-sectional area

In this section the approach to modelling vertically stacked blocks with varying x-y cross-sectional areas will be validated. Namely, the approach shown in Fig. 6.7 which relied on the use of heat flux window and temperature extraction matrices.

6.4.3.1 MATLAB Code Test

The proposed method for dealing with a material interface where blocks are vertically stacked but have a different x-y cross-sectional area was presented in section 6.2. Prior to implementing the model designed to simulate this type of interface, shown in 6.7, it is worth testing MATLAB code which has been implemented. Namely, the code which creates a heat flux window and the code responsible for temperature distribution. These two scripts are vital since it is responsible for enabling the simulation of a change in x-y cross-sectional area at a material interface.

Heat Flux Window - The aim is to represent the heat flux passing into the top of block 2 in the heat conduction problem shown in Fig. 6.6, when $x_1 = 3$, $x_2 = 7$ and $x_3 = 10$. It is assumed that the heat flux passing through the material interface is uniform, and given an arbitrary value of 5 Wcm^{-2}; the results of the code test are shown in Fig. 6.23. It is clear that the more Fourier terms used to represent the flux, the closer the plot is to representing the flux as a pulse input in space. However, undershoot appears to occur in every case. Gibbs phenomenon is visible for a high number of Fourier terms.

Temperature Extraction - The test results from a temperature extraction process are shown in Fig. 6.24; this shows a 2-D plot of the arbitrary function $y = \sin x + x$. This function, a black dashed line, represents the temperature distribution along the x-axis. The temperature of various regions is extracted and plotted in Fig. 6.24. It is clear that the code is working correctly. The more Fourier terms that are used to represent a region, the more accurately the temperature distribution of that region follows the ideal curve.

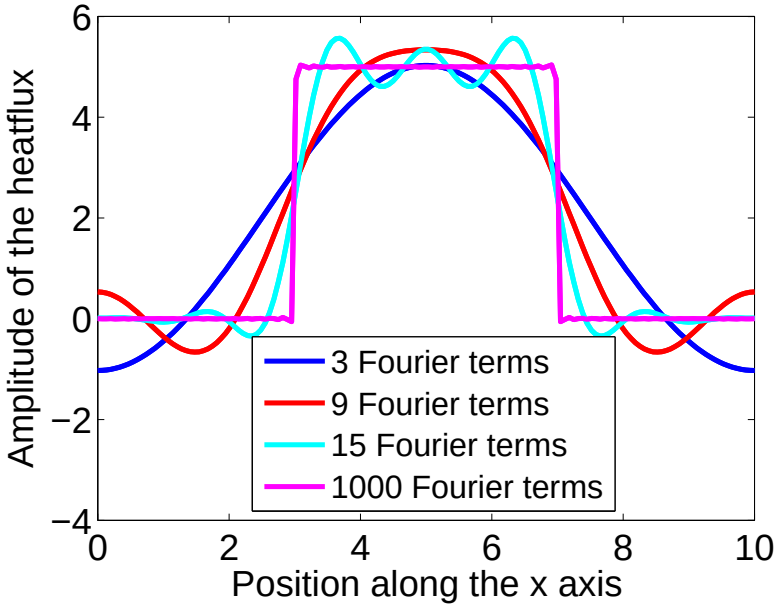

Figure 6.23: Graphical representation of the heat flux entering the top of block 2, using a different number of Fourier terms in each case.

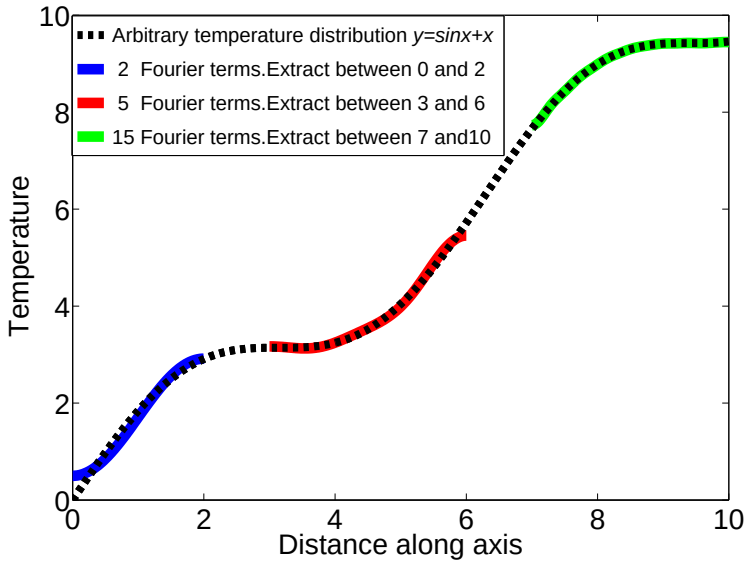

Figure 6.24: Extraction of the temperature distribution of various regions along the x-axis. The temperature distribution is assigned the function $y = \sin x + x$.

6.4.3.2 Cross-sectional change (x dimension only).

The 2-D Fourier thermal model and FLOTHERM have been used to model the heat conduction problem presented in Figure 6.25. The structure has an initial temperature of 300K. Simulated results showing the temperature distribution between x=0 and x=x_3, in the bottom of the aluminium block, appear in Fig. 6.26. The FLOTHERM model used contained a very coarse mesh of 28840 nodes and used 50 time steps. The Fourier model used a gain of 10^8. M and K represent the number of Fourier harmonics used in the x and z dimension respectively.

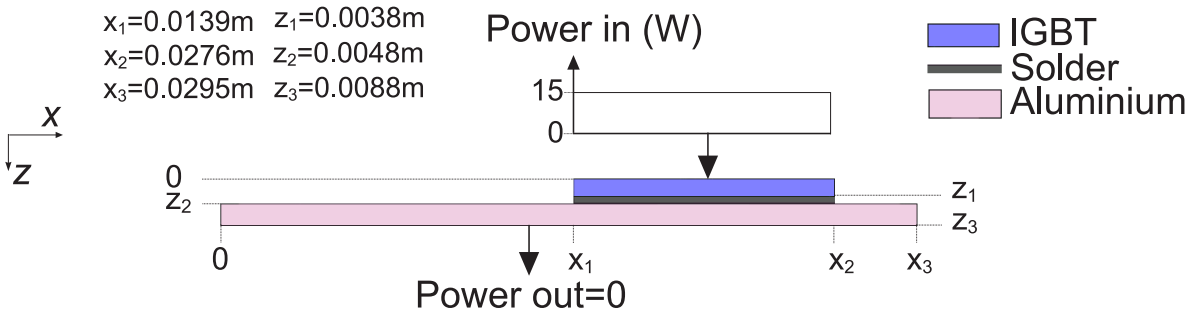

Figure 6.25: A 2-D heat conduction problem. The y dimension of the structure is fixed at 0.01m. The heat source is applied for a total of 0.5 seconds.

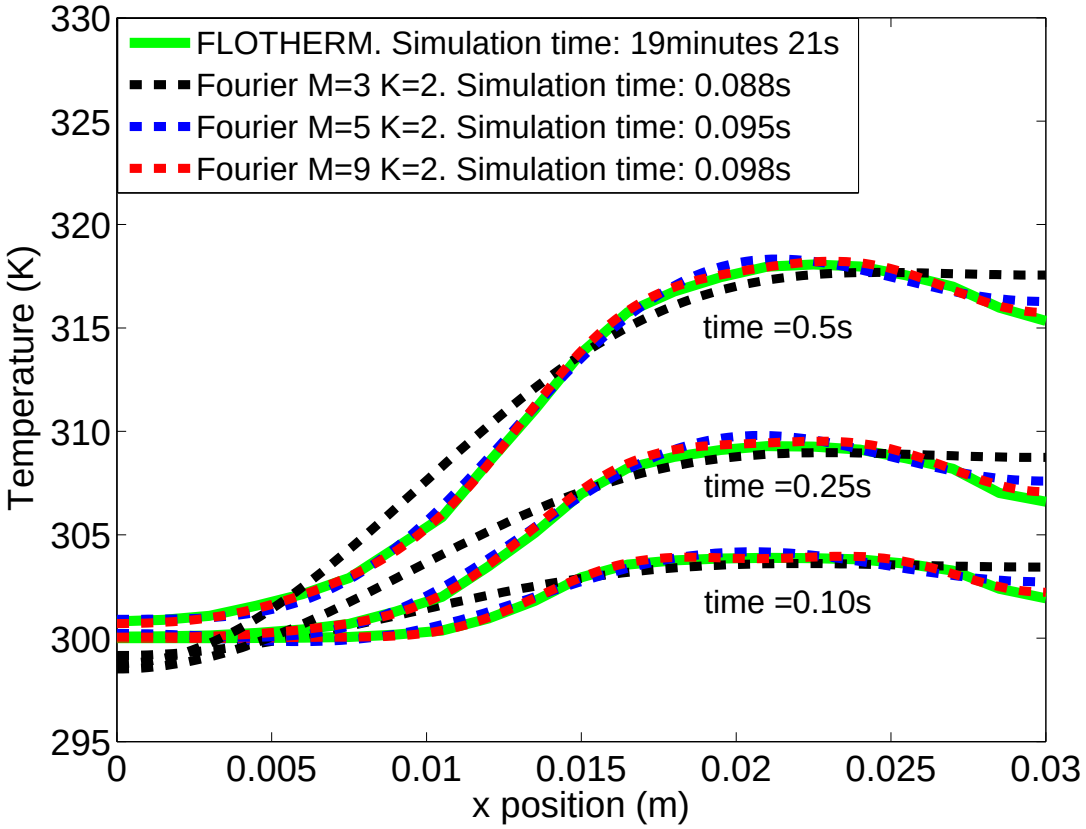

Figure 6.26: Temperature profile between x=0 and x=x_3, at depth z=z_2. The simulation times stated represents the time taken to simulate to time t=0.5s

6.4.3.3 Cross-sectional Change (x & y dimensions)

The 3-D Fourier thermal model and FLOTHERM have been used to simulate the 3-D heat conduction problem in Fig. 6.27. The results are displayed in the form of thermographs in Fig. 6.28. These thermographs represent the temperature distribution of the x-y surface at $z = z_3$, at time t=0.5s. The FLOTHERM model applied a coarse mesh with 34568 nodes and calculating results at 20 time steps. The FLOTHERM model relied on 121 temperature monitoring points to produce the thermograph in Fig. 6.28(d). Meanwhile, M, N and K represent the number of Fourier harmonics used in the Fourier model to represent the x, y and z dimensions. The Fourier model used a feedback gain of 10^8 to simulate the material interfaces.

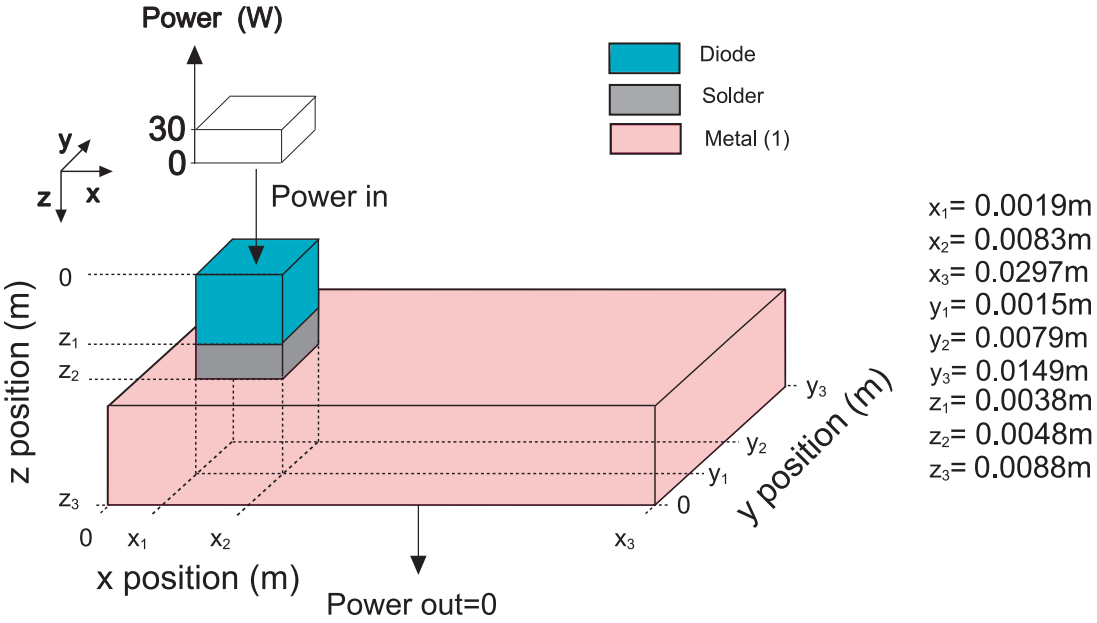

Figure 6.27: 3-D heat conduction problem. The power source is applied to the top of the diode block for total of 0.5 seconds. The structure is insulated everywhere except where the power enters the structure. The initial temperature of the structure is 300K.

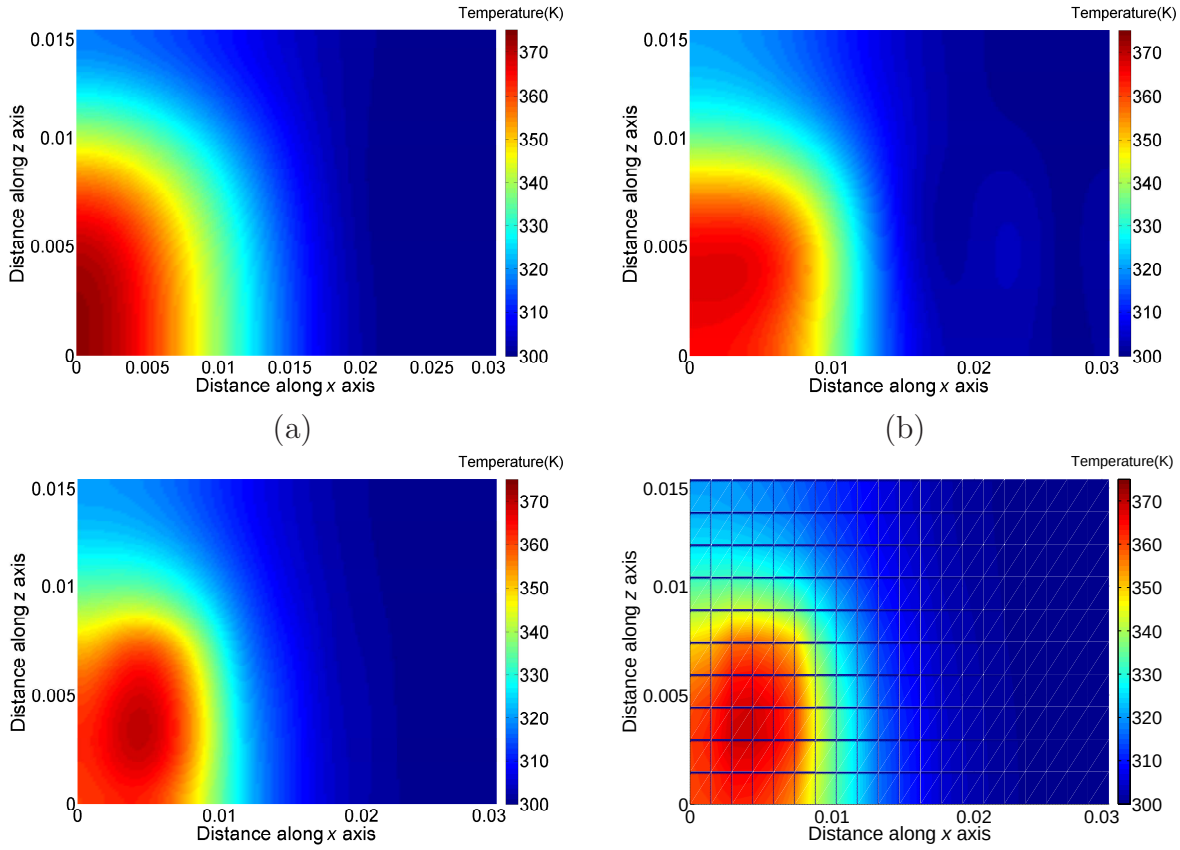

Figure 6.28: Thermographs illustrating the simulation results from modelling the heat conduction problem in Figure 6.27. The thermographs represent the x-y plane at z=z_2, at time t=0.5s.
(a) Fourier model M=N=3 K=2 . Simulation time: 0.008s.
(b) Fourier model M=N=5 K=2. Simulation time: 0.26s.
(c) Fourier model M=N=11 K=2. Simulation time: 2.16s.
(d) FLOTHERM model. Simulation time: 15min 34s.

Cut lines were taken from each of the four thermographs in Fig. 6.28 in order to investigate the results more closely. Fig. 6.29 displays cut lines taken beneath the centre of the diode and parallel to the x axis, while Fig. 6.29 shows cut lines taken beneath the centre of the diode and parallel to the y axis of Fig. 6.28.

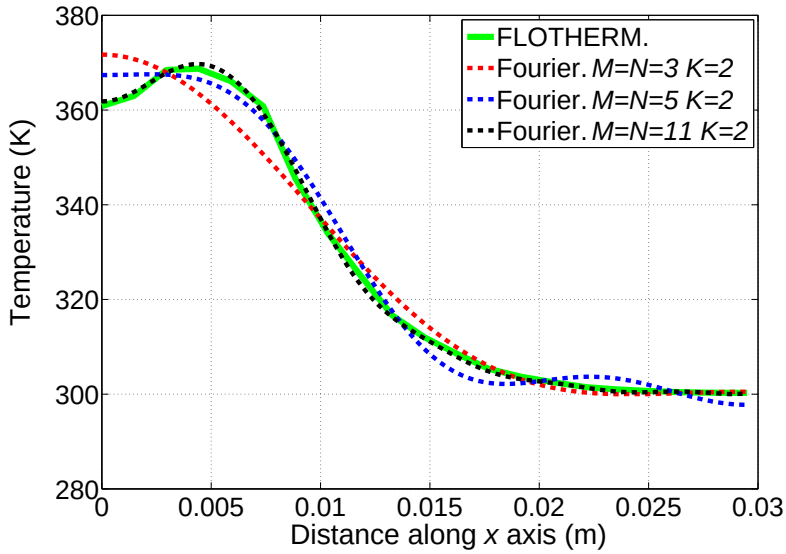

Figure 6.29: Cutline from Fig. 6.28 taken parallel to x axis, beneath the centre of the diode.

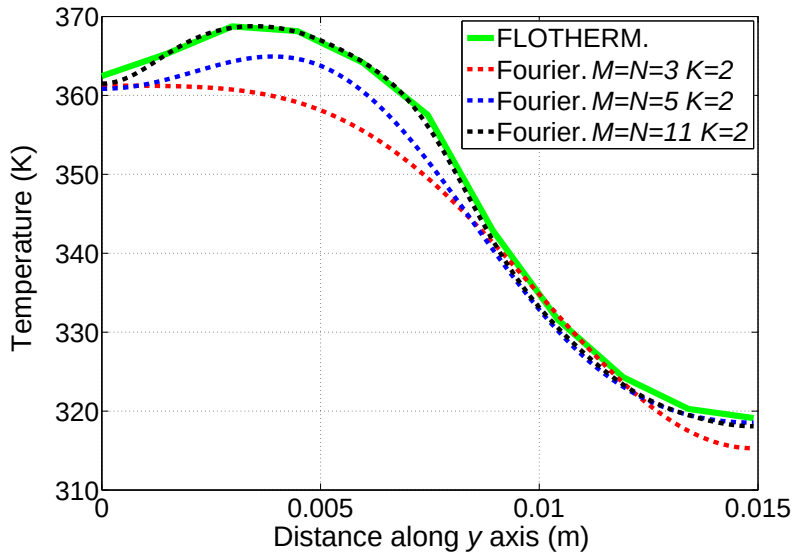

Figure 6.30: Cutline from Fig. 6.28 taken parallel to y axis, beneath the centre of the diode.

6.4.4 Multiple Heat Sources

In this section the use of applied the superposition principle in order to model multiple heat sources with a Fourier series model will be presented. Since the 3-D Fourier thermal model is easily adapted from the last section to validate this approach, only 3-D heat conduction is considered. The 3-D Fourier series model and FLOTHERM have modelled the situation shown in Fig. 6.31. This structure can be found in a Toyota Prius power converter; however, it would normally have many more blocks beneath it. Multiple heat sources are applied to the structure simultaneously for 0.5 seconds. The initial temperature of the structure is 300K.

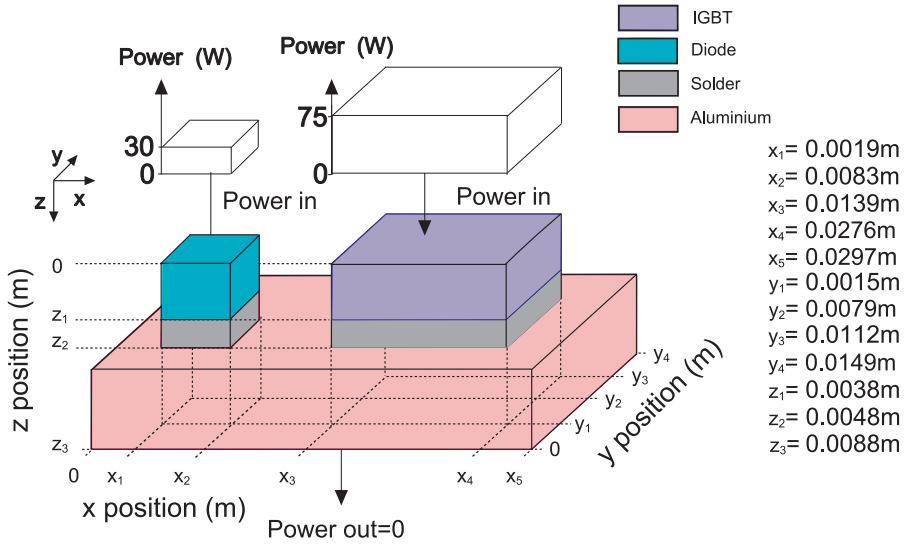

Figure 6.31: 3-D heat conduction problem. The heat sources are applied simultaneously for 0.5 seconds. The structure is insulated everywhere except where the power enters the structure.

Fig. 6.32 shows thermographs which represent the temperature distribution of the x-y surface at $z = z_2$, at time t=0.5s. The FLOTHERM model employed a medium density mesh with 328440 nodes and calculated results along 20 time steps. K, M and N represent the number of Fourier harmonics in the z, x and y dimensions respectively of the Fourier model. The Fourier model used a feedback gain of 100 million to simulate the material interfaces.

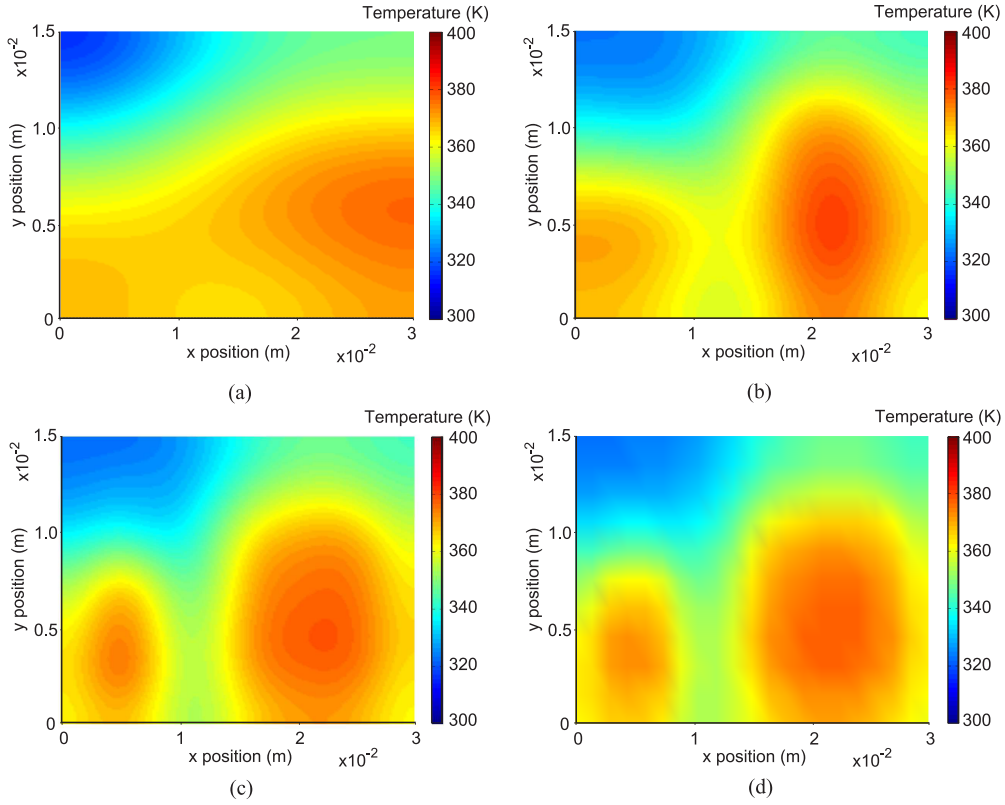

Figure 6.32: Thermographs illustrating the simulation results from modelling the heat conduction problem in Figure 6.31. The thermographs represent the x-y plane at z=z_2, at time t=0.5s.
(a) Fourier model M=N=3, K=2. Simulation time: 0.122s.
(b) Fourier model M=N=5, K=2. Simulation time: 0.436s.
(c) Fourier model M=N=7, K=2. Simulation time: 1.863s.
(d) FLOTHERM model. Simulation time: 1hr 6mins.

6.4.5 Modelling the Whole Simulation Domain

In chapter 5 it was established that if a thermal model could model the simulation domain in Fig. 5.1, it would also be able to accurately model the power converter packaging present in a Toyota Prius. The approaches to modelling material interfaces presented in this chapter have enabled the Fourier thermal model to simulate the simulation domain. This section will test whether the Fourier model can simulate it speedily and accurately. The most important output from the 3-D Fourier thermal model is the IGBT and diode temperature profiles because this is data which it will have to provide when it is placed inside the power converter simulator from section 1.3 at a later stage. Therefore the temperature profiles generated by the Fourier model will be compared with FLOTHERM in this section.

6.4.5.1 Single Heat Source

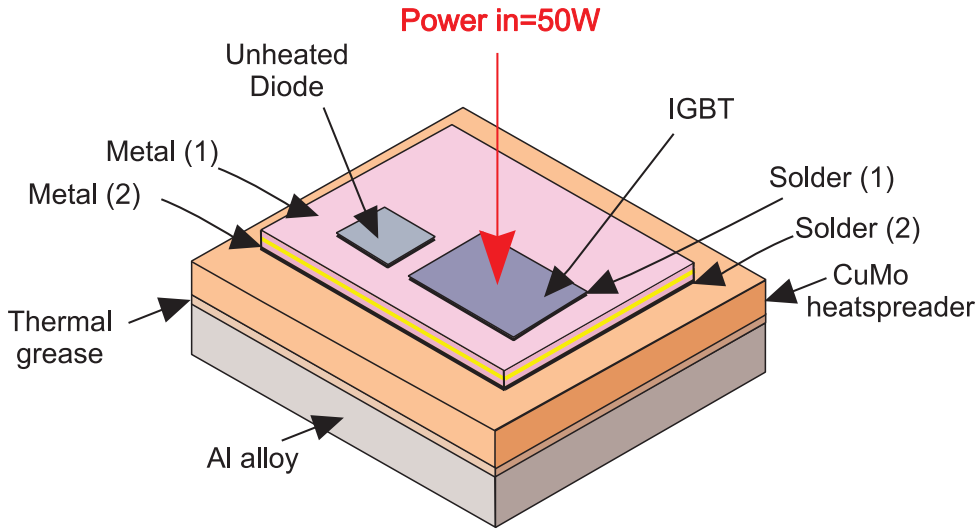

Figure 6.33: Diagram showing a 3-D heat conduction problem concerning the whole simulation domain. The IGBT is heated by 50W power for 10 seconds through its top surface. All other surfaces are insulated.

The Fourier thermal model and FLOTHERM were required to model the 3-D heat conduction problem in Fig. 6.33. The initial temperature of the structure was 300K. A FLOTHERM model and 3-D Fourier series model simulated the transient temperature profiles of the IGBT device, to produce the results shown in Fig 6.34. The FLOTHERM model used for validation employed a fine mesh consisting of 941,640 nodes and calculated at 80 time steps. The FLOTHERM model relied on 162 monitoring points, 81 over the surface of the IGBT and 81 over the surface of the unheated diode. This enables an average device temperature to be taken in each case. In the Fourier model M,N and K represent the number of Fourier terms used in the x, y and z direction respectively. The value of the feedback gain used by the Fourier model was varied to see how it would affect the Fourier model's performance. Up until now, the Fourier model has always used a feedback gain value of 10^8 in order to simulate a near perfect thermal contact. However, with so many material interfaces in this structure it is likely that using such a high gain value may adversely affect the Fourier model's simulation speed. The average device temperature was straightforward to ascertain using the Fourier model because it was simply the DC term inside the Simulink subsystem representing each device. Attention is also paid to the temperature of the unheated diode whilst solely heating the IGBT. The result for this case is given in Fig. 6.35, the Fourier model used a feedback gain of 10^4 and M=N=3, K=2. The same FLOTHERM simulation was used to validate this result.

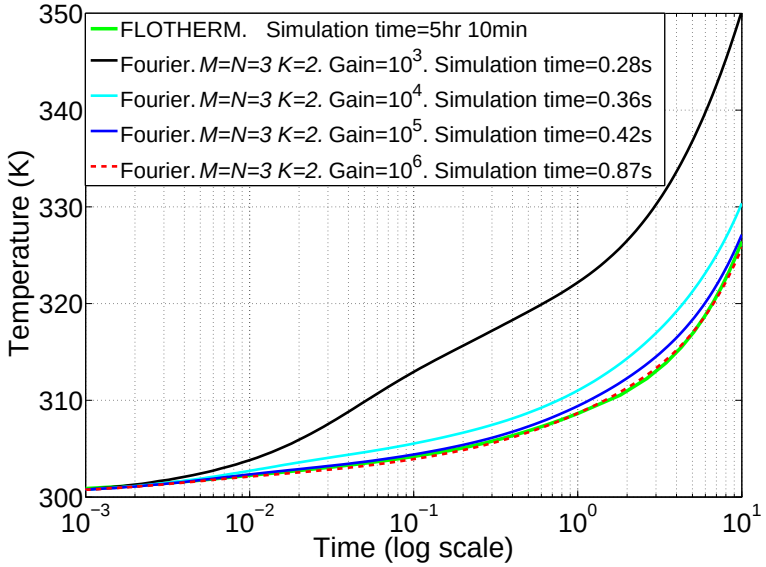

Figure 6.34: Temperature of the IGBT when heated by 50W of power (diode unheated). The 'gain' represents feedback gain.

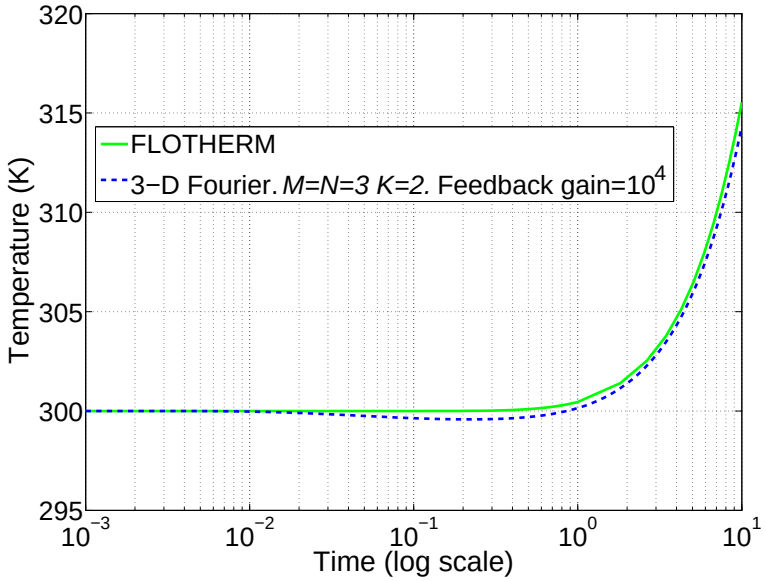

Figure 6.35: Temperature of the unheated diode when the IGBT is heated by 50W of power.

6.4.5.2 Dual Heating

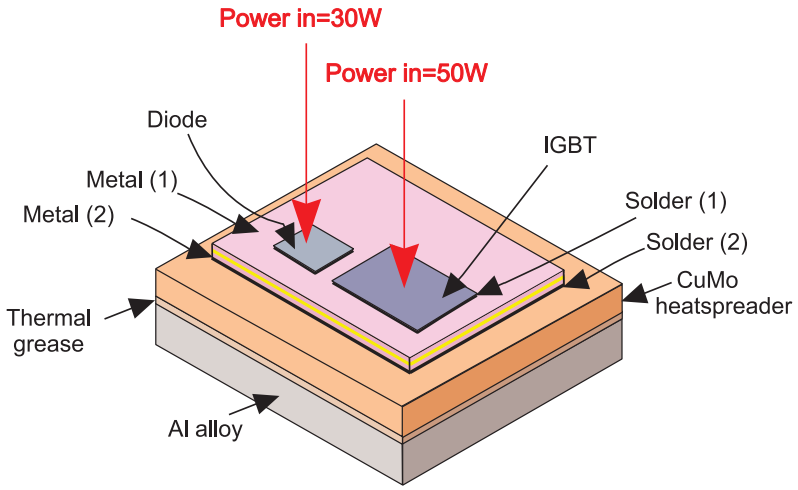

Figure 6.36: Diagram showing a 3-D heat conduction problem concerning the whole simulation domain. The IGBT and diode are heat simultaneously for 10 seconds. The IGBT is heated by 50W power, while the diode is heated by 30W of power. Both devices are heated through their top surfaces. All other surfaces are insulated.

This 3-D heat conduction problem also concerns the whole simulation domain. However, both devices are being heated simultaneously according the to power sources shown in Fig. 6.36. The structure has an initial temperature of 300K. The 3-D Fourier thermal model and FLOTHERM simulated the heat conduction problem in Fig. 6.36. The temperature profiles of the IGTB and diode which were generated by each of the thermal models appear in Fig. 6.37. The same number of Fourier terms were used as with the previous case (M=N=3, K=2). A feedback gain value of 10,000 was chosen as it was shown to give the best compromise of simulation speed and accuracy in Fig. 6.34. The FLOTHERM model was the same as the previous section 6.4.5.1.

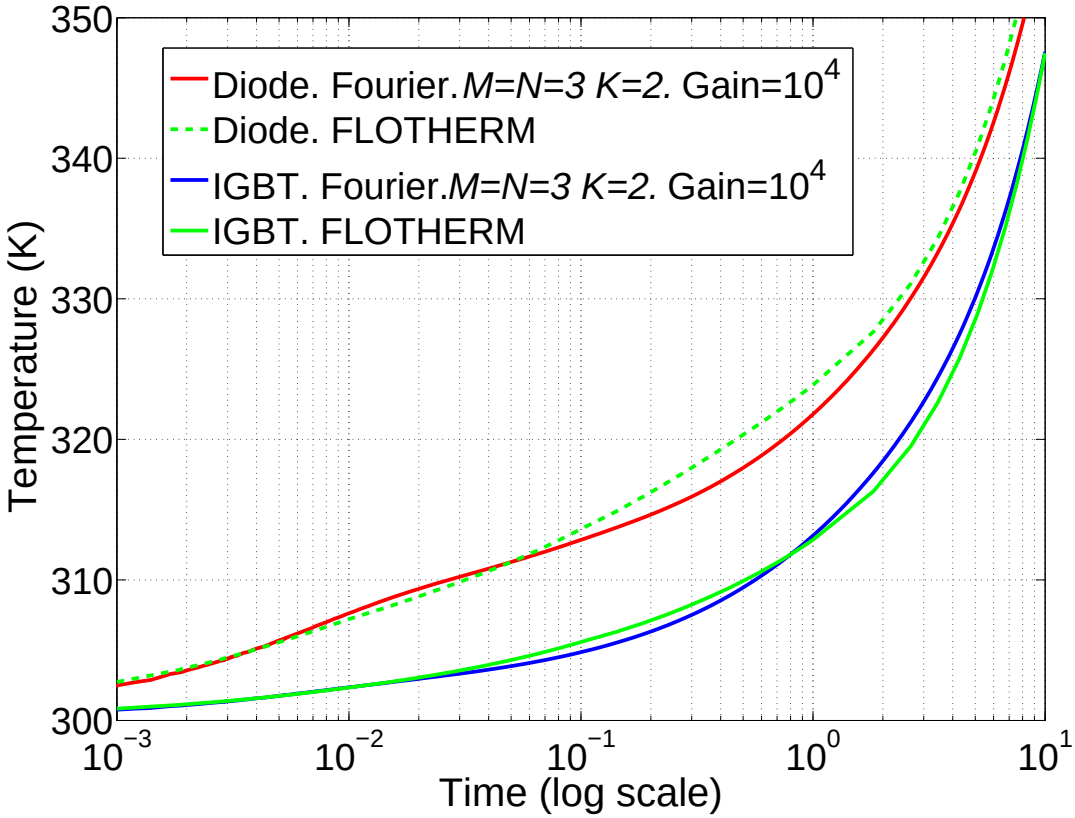

Figure 6.37: Transient temperature profiles of both the diode and IGBT. The results are generated by the 3-D Fourier model and FLOTHERM model when simulating the heat conduction problem in Fig. 6.36

6.5 Discussion

The transient temperature profiles in Fig. 6.16, produced by the Fourier model and FLOTHERM, matched very closely as the temperature at the centre of each block increased. However, the steady state temperatures generated by the Fourier model became more accurate as the number of Fourier terms used in the model increased. This is not surprising since an infinitely high number of terms would be required to solve the heat equation with complete accuracy.

The results in Fig. 6.18 show the expected behaviour, with the peak temperature occurring in the top of the silicon block for each result. Both models show that there is a large temperature difference across thin block of thermal grease at 0.005115m<z<0.005175m. As the number of Fourier terms used in the Fourier model increased, the closer the results matched FLOTHERM. However, the increased accuracy came at the expense of simulation speed.

Fig. 6.20 shows that the 3-D Fourier model is able to simulated the material interface in Fig. 6.19, where each block has the same x-y cross-sectional area. The Fourier model appears accurate whether using 3, 5 or 9 Fourier terms in each dimension. The cut lines in Fig. 6.21 and Fig. 6.22 support this point and they show that as the Fourier thermal model used more Fourier terms, it becomes more accurate. However, the improvement is only very slight and does not seem to warrant the substantial increase in simulation time.

The results in Fig. 6.26 show that the Fourier model can simulate a material boundary with a constant cross-section and a material boundary with a change in the x direction. The results support the use of the approach to modelling material interfaces which appeared in sections 6.1 and 6.2 because the Fourier model results match FLOTHERM closely over the time period which heat is applied. However, the Fourier model with

$M = 3$ and $K = 2$ harmonics seemed to undershoot the FLOTHERM result where $x < 0.005$m, and overshoot where $x > 0.025$m. This is potentially a consequence of having just three Fourier harmonics to describe the temperature distribution in the x dimension.

It is clear that the 3-D Fourier model can simulate 3-D heat diffusion correctly where the x-y cross-sectional area of the stack blocks changes. Fig. 6.28 shows that all the results generated by the Fourier model simulate the thermal behaviour of the problem in Fig. 6.27 very well, even when using very few Fourier harmonics.

The cut lines in Fig. 6.29 and Fig. 6.30 show that the Fourier thermal model case of M=N=11, K=2 is a near-identical match to the FLOTHERM. However, caution should be applied to this particular result; the extra computational cost of using so many Fourier terms is evident by its simulation time. That said, all the Fourier results are still far faster at simulating the 3-D diffusion than FLOTHERM. It is interesting to see the result in Fig. 6.29 where the Fourier M=N=5 K=2 result oscillates for the range 0.0175m<x<0.03m. This oscillation causes an undershoot of the 300K temperature mark where x>0.026m.

Fig. 6.32 shows that the 3-D Fourier thermal model can successfully simulate heat diffusion from multiple heat sources. It is clear that the superposition principle to represent multiple heat sources has been successful. The greater the value of M and N Fourier terms, the more accurately the 3-D Fourier model results matched FLOTHERM. Having just two Fourier terms in the z direction did not seem to have a negative impact on the results. The thermograph obtained using the M=N=7, K=2 Fourier model is almost identical to the result provided by FLOTHERM. Once again, the 3-D Fourier thermal model's simulation speed is far superior to that of FLOTHERM.

The trend shown in Fig. 6.34 is what would be expected: as the feedback gain increases, the Fourier model resembles the results of FLOTHERM more closely. The

FLOTHERM model used a very fine mesh and so it would simulate the interface as a near-perfect thermal contact, while the Fourier thermal model would require a feedback gain approaching infinity to achieve this. The disadvantage of using a higher feedback gain is that the Fourier model takes more time to simulate. A feedback gain value of 10^4 seems a good compromise of speed and accuracy. The result with a gain value of 10^3 is clearly not nearly accurate enough, whilst the improvement in accuracy as the gain increases from 10^4 to 10^5 is not sufficient to warrant the increase in simulation time.

Fig. 6.35 shows an unusual result. The temperature of the unheated diode appears to decrease between time $t = 0.01$ s and $t = 1$ s. This slight undershoot shows a cooling effect on the unheated diode while heat is applied to the IGBT. In reality, the temperature should not decrease since the structure is fully insulated. The undershoot appears to be occuring as a result of using too few Fourier terms. In this case the heat flux entering the metal (1) block must have a negative component beneath the unheated diode, as visualised in Fig. 6.38. Undershoot was also present in the results shown in Fig. 6.26 and during the heat flux window code test in Fig. 6.23 when too few Fourier terms were used. Clearly using only 3 Fourier harmonics to replicate a step heat flux in the lateral (x,y) direction is not ideal for the case shown in Fig. 6.27. The 3-D Fourier model does not show the unheated diode to be heating up until time t=1s. Beyond this point in time the result correlates well with FLOTHERM. The reason is that in the long transient the heat has diffused far enough for the area beneath the unheated diode to get warmer. The impact of the negative heat flux being passed down is overwhelmed by the overall heat diffusion which is occurring in the structure.

Simply increasing the number of Fourier terms in the metal (1) layer in order to overcome the undershoot issue will have a negative impact on the simulation time of the Fourier series model. A large attraction of the Fourier series model is a fast simulation

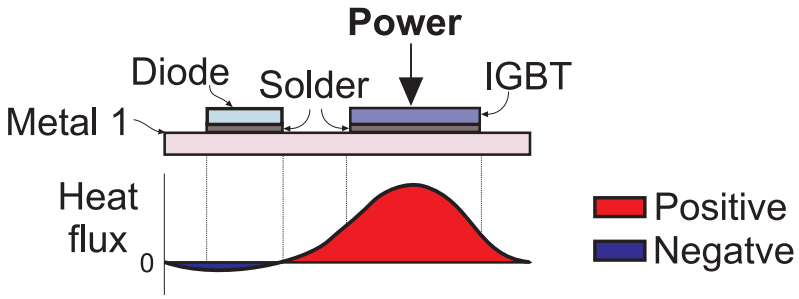

Figure 6.38: Diagram showing a spatial representation of the heat flux entering the metal (1) block during IGBT only heating. There is negative flux entering the metal (1) layer beneath the diode.

speed and this should be retained. Another method to overcome the problem of undershoot could be to use a filter which could remove the unwanted presence of negative heat flux. However, the drawback of this approach is that by smearing the heat flux one would be artificially altering the diffusion process. Undershoot is not a major issue because it only occurs on occasions and is very slight when it does occur as shown in Fig. 6.35. The benefit of the fast simulation speed associated with Fourier thermal model far outweighs this drawback.

The result from Fig. 6.37 shows that the 3-D Fourier series model is able to simulate multi-source heating accurately using a very few number of Fourier terms. The results showing the temperature of each device matched the FLOTHERM results closely throughout the 10 second period being simulated.

In order to extract the temperatures in a packaging structure using FLOTHERM for each validation, temperature monitoring points are placed at specific locations before the FEM solver begins. Meanwhile, using the Fourier thermal model a temperature distribution map of the whole structure is automatically generated during the simulation. In all the heat conduction problems faced in this chapter, the power inputs were either uniformly spread over a surface or a step input because FLOTHERM, unlike the Fourier

model, could not represent any arbitrary power source over a surface. A further difficulty of using FLOTHERM was the requirement to create a suitable mesh to model a structure. The Fourier model, in comparison, automatically had a suitable resolution to model every layer in a structure.

For all validation cases presented in this chapter, the speed of the Fourier model was far superior to that of FLOTHERM. The Fourier model was able to match the accuracy of the FLOTHERM model when a high number of Fourier harmonics were used. Although this chapter showed the validation of the 1-D and 2-D Fourier thermal models, this was more of a stepping stone towards the 3-D Fourier thermal model. The validation process in this section has shown that the 3-D Fourier thermal model can simulate heat diffusion through material boundaries of vertically stacked blocks, with:

- constant x-y cross-sectional area,
- changing x-y cross-sectional area,
- multiple heat sources.

The approach to simulating the material interfaces presented in this chapter is a significant step forward from that employed by Du et al [37, 38] (see chapter 4). Material interfaces are simulated by converting between two Fourier domains using a sound mathematical approach. There is no need to convert from the Fourier domain to space and back again as in [37, 38].

The Fourier model is versatile and not restricted to modelling simply the power converter of a Toyota Prius. The approaches presented for simulating material interfaces in this chapter make it possible for the Fourier thermal model to simulate any power module package which is made up of vertically stacked blocks of material.

The 3-D Fourier thermal model could simulate the structure which was identified as the simulation domain in Fig. 5.1 of chapter 5. However, one aspect of the simulation

domain was not simulated in Fig. 6.36 and Fig. 6.33 of this chapter, that is, the heat diffusing from the underside of the Al alloy block (heatsink). The next chapter will present a method for modelling the heat diffusing from the underside of the Al alloy block. The ability of the Fourier thermal model to co-simulate with an inverter simulator will be tested. Throughout this chapter the Fourier model was validated against FLOTHERM. Both models simulated pure heat conduction by solving the heat equation. A more relevant validation of the Fourier model will take place in the next chapter. The results generated from the 3-D Fourier thermal model simulating realistic load conditions will be compared with experiential results from a real power converter during operation.

Chapter

7 Experimental Validation

The work outlined in this chapter concerns the experimental validation of the fast electro-thermal converter simulator which was described in section 1.1.3. A 3-D Fourier thermal model is embedded within the framework of the fast electro-thermal converter simulator.

The operation of a single phase leg of an inverter during realistic inverter load conditions is replicated using an existing inverter 'back-to-back' rig. Experimental results are presented in the form of transient device temperatures which are recorded on the rig using an infrared camera. These experimental results are then compared with simulated transient device temperature profiles obtained by supplying the fast electro-thermal converter simulator mentioned in the previous chapter, with the same inverter load conditions.

7.1 Experimental Setup

7.1.1 Test Rig Operating Principle

The back-to-back rig is able to impose realistic inverter load conditions on a 3-phase test inverter. All three inverter phase legs do the same amount of work but are set 120° out of phase. Only one inverter phase leg is considered in this work. The inverter under test, rated at 50kW, is from a Toyota Prius HEV. This is the motor drive inverter, which is used to convert DC power from the battery to three-phase variable voltage variable frequency (VVVF) AC suitable for driving the permanent magnet traction motor. The back-to-back rig simulates the loaded motor of the HEV with an additional 3-phase inverter connected to the test inverter via an air-cored inductive load per phase.

The desired motor speed is related to the output of the test inverter phase leg by the rms voltage of the PWM output. The desired motor torque is set by the rms current through the load inductor by setting the voltage on the load side of the inductor by the equation $V = L(di/dt)$. The speed and torque versus time (motor drive cycle) are applied to the test inverter in this manner to operate the inverter switching devices with the same conditions that would be seen in the real vehicle when driven according to the drive cycle. The motor model from [183] is used here to convert the motor speed and torque into the resulting inverter conditions (V_{rms}, I_{rms}, power factor and switching frequency). For the purposes of this work the temperature of these devices is measured.

A back-to-back inverter test rig is used to validate the results generated by the power converter simulator in section 1.1.3 because the test inverter cannot be easily loaded for testing using an electric motor. Two electric motors would be required, one to load the test inverter and a second motor to provide resistance to the other motor in order to create the required torque. The second motor would require another converter to control

it, making the whole arrangement complicated. The recirculation of the power using the 'back-to-back' technique means that the overall power consumption of the test is significantly reduced and a smaller DC supply can be used.

7.1.2 The Back-to-Back Rig

A schematic of the back-to-back test rig is shown in Fig. 7.1. Fig. 7.2 shows a photograph of some of the main components of the rig housed in the white enclosure covered with a transparent lid. A timed interlock circuit locks the lid while the rig is operating to prevent access to the high voltages inside the enclosure.

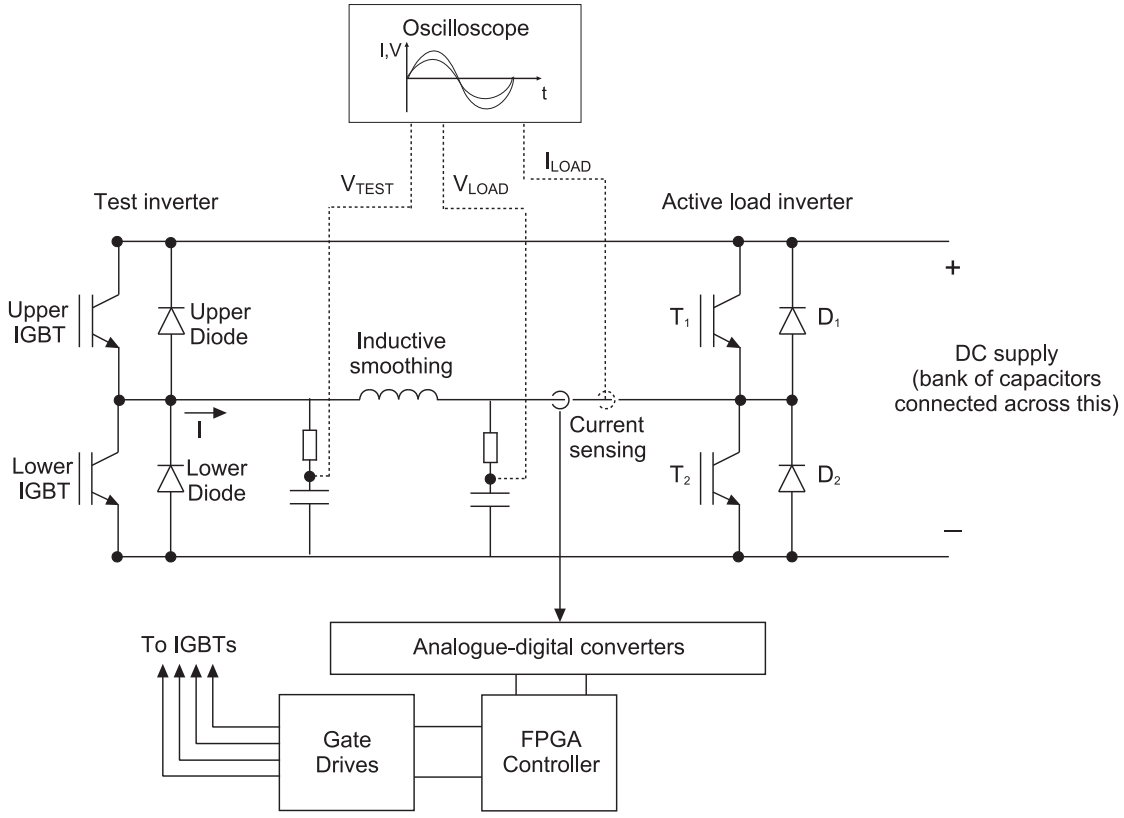

Figure 7.1: Simplified representation of the back-to-back rig operation for one phase leg only.

A capacitor bank minimises the ripple in the DC link. The capacitor bank consists of ten 470μF 450V capacitors connected directly onto the same terminals that deliver power to the inverters. A current transducer senses the current through the load inductor.

The current measurement is fed back to a controller, where it is compared to the set current value. The current is increased or reduced accordingly to maintain the desired condition, by varying the voltage at the output of the load inverter.

The FPGA controller operates the test inverter according to programmed inverter drive cycle. The IGBT gate drives are driven by logic signals from the controller. The gate drives contain opto-couplers for isolating logic from the high voltage inverter supply.

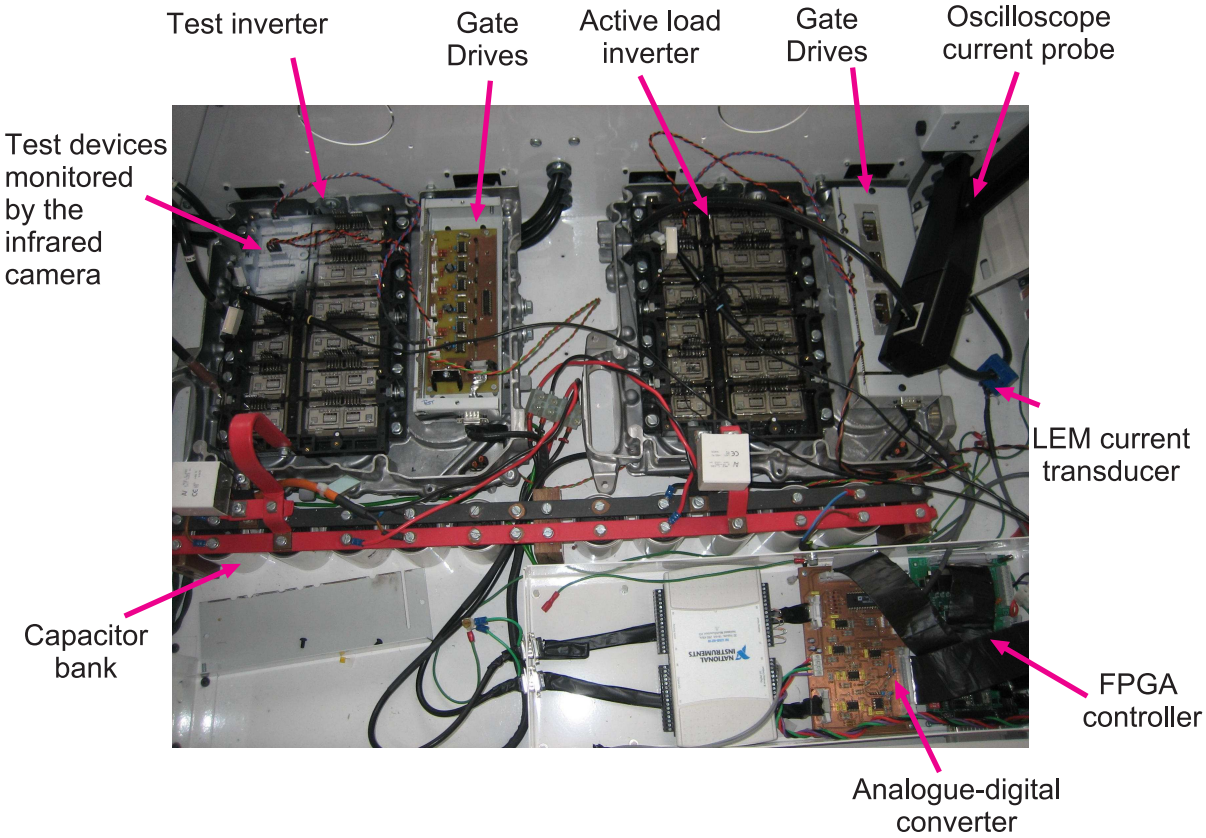

Figure 7.2: Photograph showing a plan view of the equipment from the test rig which was housed in a container as a safety precaution.

Fig. 7.3 shows the test environment. The power supply used is a Sorenson 600V/16A DC power supply. Although not shown clearly in Fig. 7.3, Toyota Prius water-cooled heatsinks are present beneath both power converter modules. These inverters are cooled in parallel by a constant water inlet temperature, as shown in the water cooling block diagram shown in Fig. 7.4.

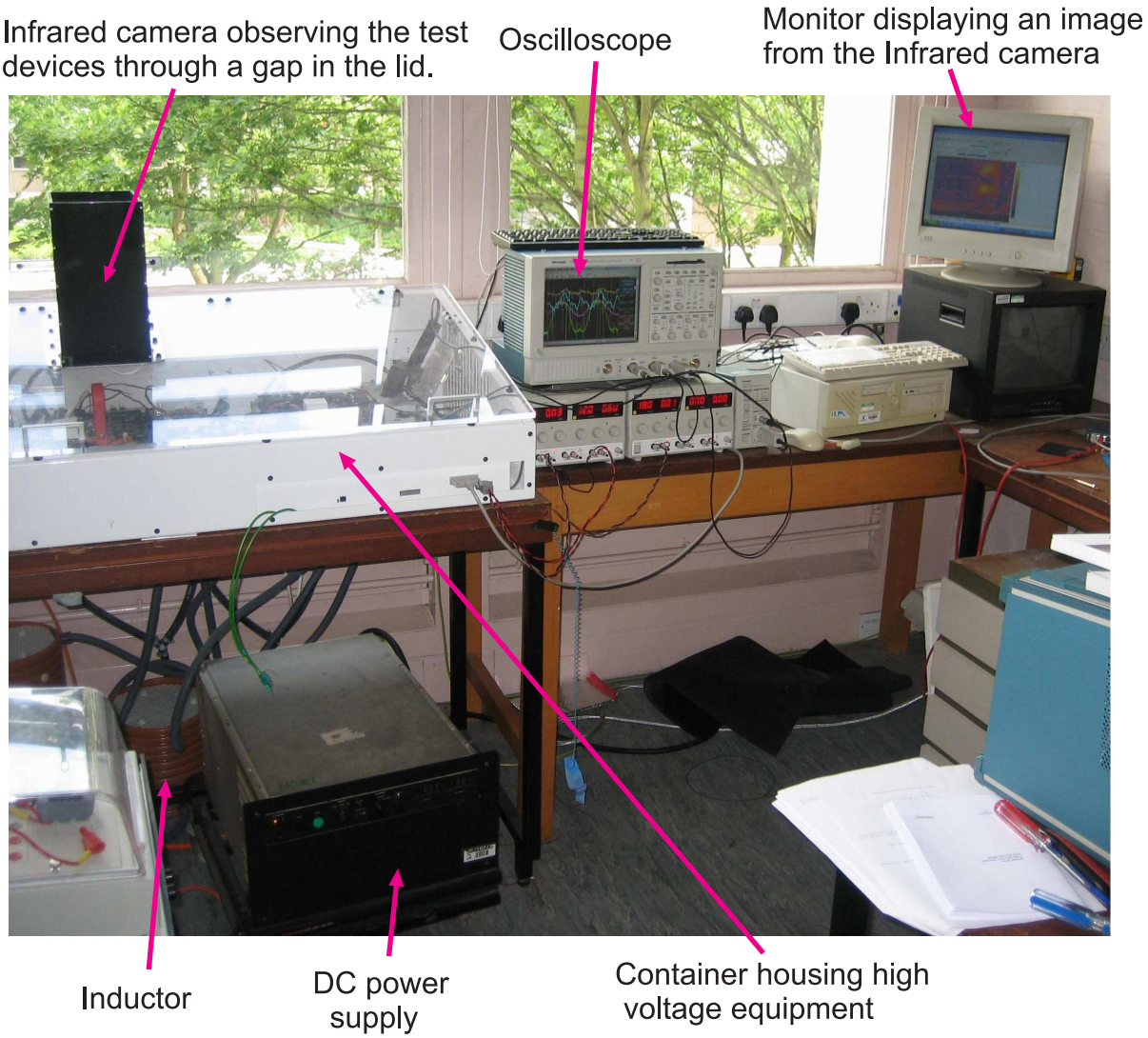

Figure 7.3: Photograph of some key elements of the back-to-back rig.

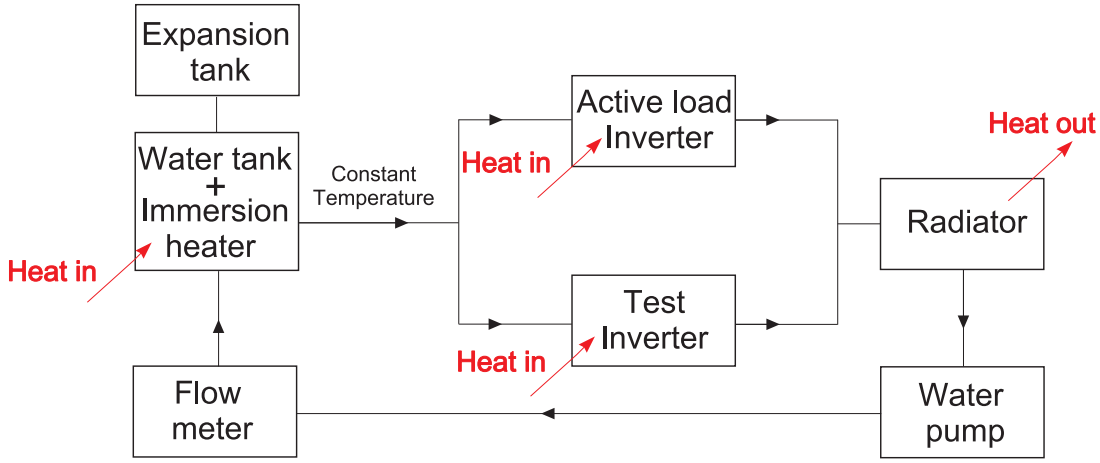

Figure 7.4: Block diagram of the heating/cooling system used to maintain the water flowing through the Prius heatsinks at a set temperature.

In this cooling/heating system, the inlet temperature is maintained constant by a combination of flow, heated pumped by the radiator, large thermal mass of the water tank and tank heat controller by a PID controller. The system is sized to pump a maximum of approximately 2.5kW of waste heat from the inverter under test and used standard domestic heating system components. The water is pre-heated to the start temperature (54°C) with the immersion heater. An expansion tank absorbs the excess water volume as it expands so that the pipes do not burst.

7.1.2.1 Oscilloscope

The Tektronic TDS 5054B Oscilloscope, shown in Fig. 7.3, measured the test inverter output conditions (pk-pk voltage, pk-pk current, phase angle and modulation frequency) which were monitored to ensure that the test inverter was operating correctly.

The raw test inverter output voltages are PWM square waves at the high voltage DC link voltage. In order to observe the average (modulated) voltage signal which would ordinarily be at the motor terminals, the PWM signals were filtered by a RC low-pass filter, as shown in Fig. 7.1. Fig. 7.5 shows a typical oscilloscope output displaying the I_{LOAD}, V_{TEST} and I_{TEST} waveforms.

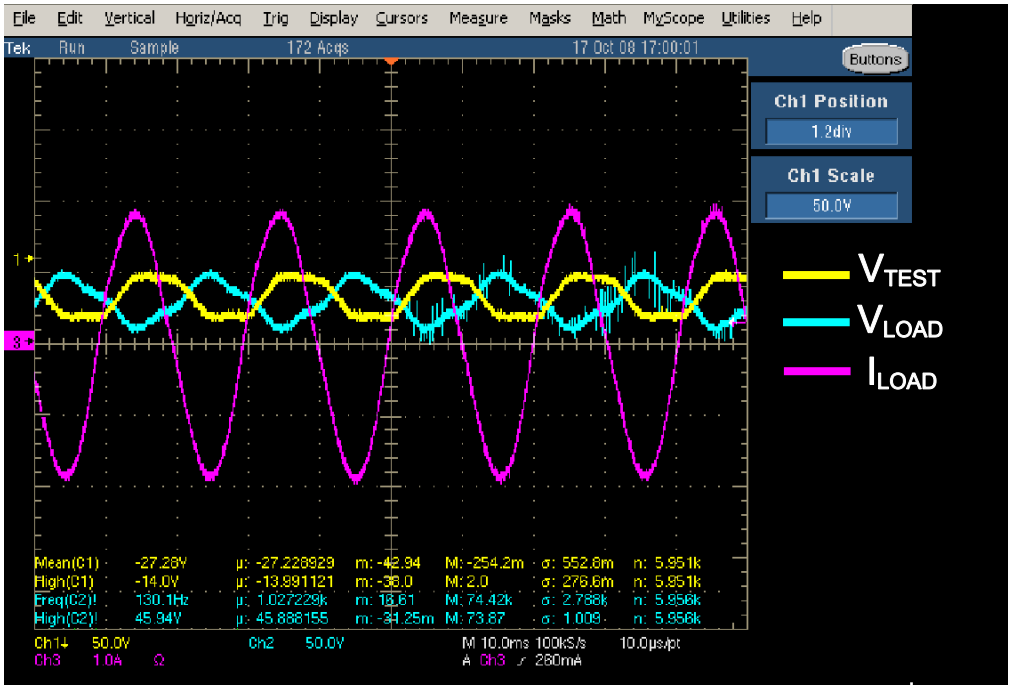

Figure 7.5: A screen grab from the oscilloscope located in the back-to-back circuit as shown in Fig. 7.1.

7.1.2.2 Infrared Camera

The transient device temperatures must be captured as the inverter load cycle proceeds in order to validate the electro-thermal converter simulator and therefore assess the performance of the Fourier thermal model developed in this work. The transient temperature measurements were performed with an FLIR Thermovision A20M infrared camera [184] with the following basic specifications:

- an accuracy of 2%,
- a resolution of 160 x 120 pixels,
- a temperature range of -20°C to 900°C,
- the ability to detect temperature variations as small as 0.12°C,
- standard 60 Hz colour video output.

It was possible to take infrared camera images of the devices and the surrounding area because the test inverter had its cover removed, with no silicon gel used for isolation. Before using the infrared camera a number of ambient measurement conditions were observed. The sensor ambient air temperature, the distance object-to-camera, and the emissivity ϵ of the measured object were programmed into the camera through its software interface. Since the material surfaces in the proximity of the test devices were reflective, a very thin coating of Magnaflux SKD-S2 solvent-based developer, with emissivity$\varepsilon \approx 1$, was sprayed over the area. This ensured a uniform emissivity was created which enabled accurate temperature readings to be taken across all the devices and all materials. A pair of test devices (upper and lower devices of a single phase leg) are shown in Fig. 7.6. The equivalent thermograph is shown in Fig. 7.7. Temperature variations caused by the bond wires were not visible due to the poor resolution of the infrared camera.

The transient device temperatures were measured at the hottest point of each device,by moving the cursors shown in Fig. 7.7. For simplicity, this was interpreted as the average temperature of the device surface rather than taking an average across the device surface area. Clearly, the average temperature would be slightly less than this reading; however, as a temperature drop is likely to occur across the developer coating above the devices, this was deemed to be a fair approximation.

The infrared camera results were recorded by a PC at a rate of 1Hz, which was the highest rate that the camera could update the real time image. The manufacturer's claim of a 60 Hz video output could not be achieved in practice. The accompanying thermal researcher software was used to convert the stored infrared images into spot transient device temperatures by analysing the colour scale on each of the frames.

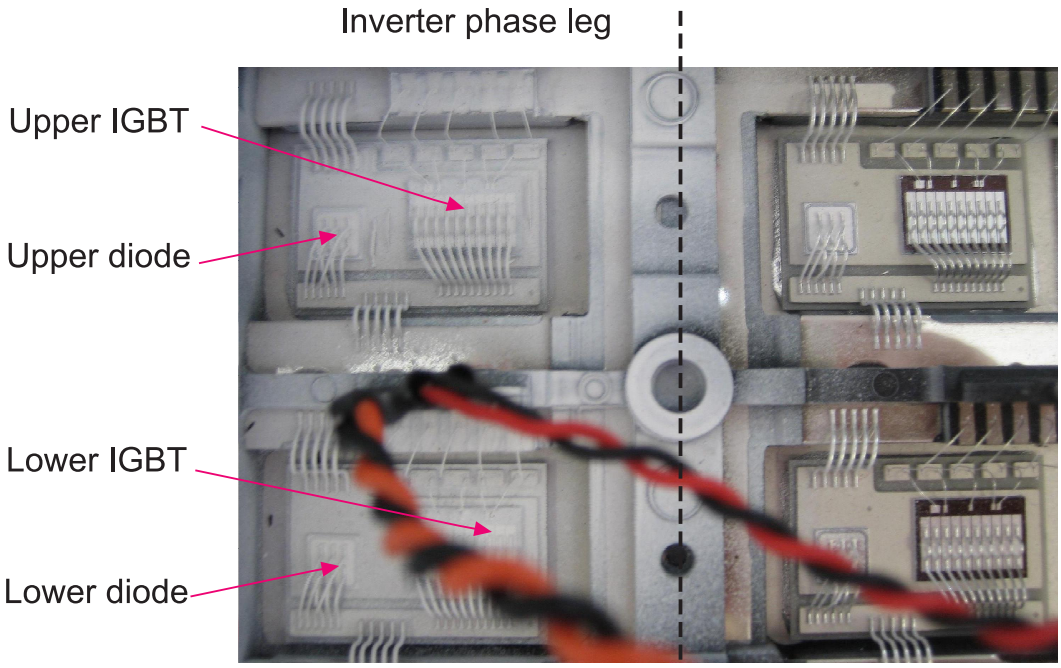

Figure 7.6: Photograph of the test devices covered by a thin layer of developer.

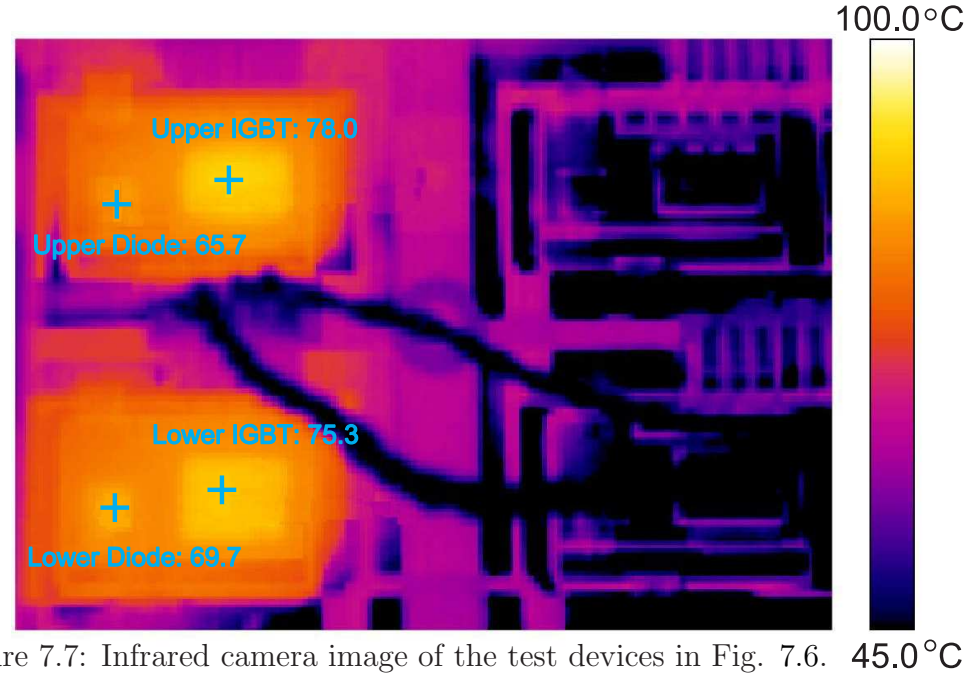

Figure 7.7: Infrared camera image of the test devices in Fig. 7.6.

7.2 Fast Electro-thermal Converter Simulator

In order for the fast electro-thermal converter simulator, illustrated in Fig. 1.3 of section 1.1.3, to operate as fast as possible, it required a fast and accurate compact 3-D thermal model which could simulate the structure of a power converter module and be implemented into the converter simulator framework. The Fourier thermal model, developed in chapters 5 and 6, was specifically designed to fulfil these requirements and was subsequently embedded into that framework.

In order to validate the electro-thermal converter simulator, and therefore assess the performance of Fourier thermal model embedded in it, the experimental test rig described earlier in this chapter was used. To enable a like for like comparison with the experiment test rig, the electro-thermal simulator models only one inverter phase leg only.

7.2.1 Packaging Structure of a Single Inverter Phase Leg

The Fourier series thermal model was programmed to simulate heat conduction through the device packaging structure shown in Fig. 7.8. To model the structure in Fig. 7.8 power is applied uniformly over the top surfaces of the devices. The packaging layers are identical to those shown in Fig. 5.1. The structure is made up purely of blocks which makes it an appropriate subject for the Fourier thermal model. In Fig. 7.8, R_h represents the thermal resistance while C_h represents thermal capacitance at the bottom of the Al alloy. This is the point at which the Al alloy comes into contact with water flowing through the cast channels beneath it.

7.2.2 Heatsink Model

The heatsink consists of the Al alloy block shown in Fig. 7.8 and water flowing through cast channels beneath it as depicted in Fig. 2.10. The 3-D Fourier thermal model can be applied to simulate heat transfer as far down as the bottom of the Aluminium alloy

block.

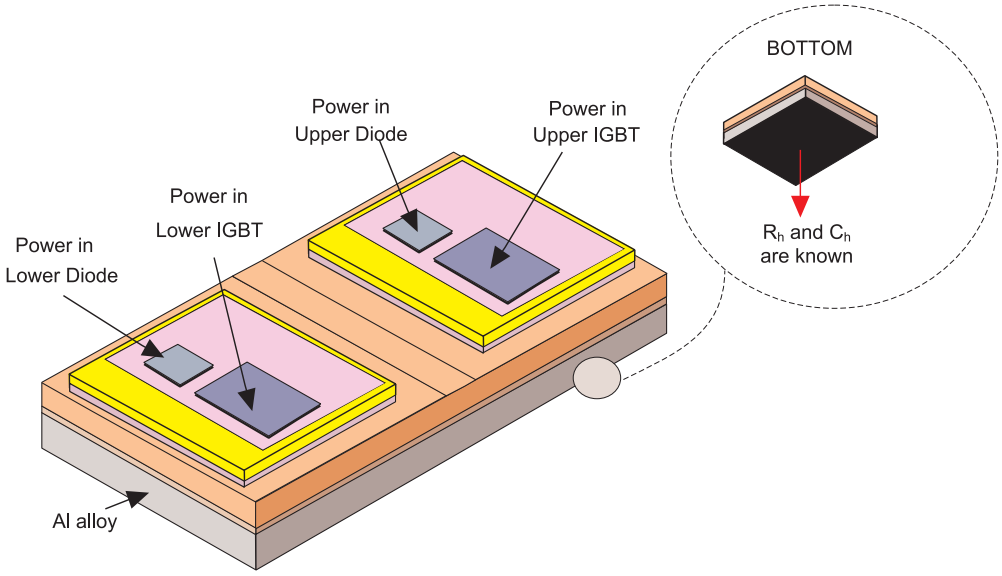

Figure 7.8: Isometric view of simplified packaging structure associated with one inverter leg.

Heat transfer from the underside of the Aluminium alloy into the water is not heat conduction. A fluid is contacting a solid which means that convection will occur. Therefore the Fourier model cannot be used.

Instead, a simple 1-D RC Cauer model is used; it is a simple and effective method of utilising the limited information available about the heat transfer from the underside of the Al alloy, represented by R_h and C_h. The rate of temperature change at the underside of the Al alloy is described by the following equation:

$$\frac{dT_{output}(t)}{dt} = \frac{1}{R_h C_h}(P_{in}(t)R_h - T_{output}(t) + T_{Ambient}) \tag{7.1}$$

The RC Cauer model subsystem shown in Fig. 7.9 represents Equation (7.1). It is implemented in MATLAB/Simulink so it may connect to the bottom of the Fourier thermal model of the Al alloy, as shown in Fig. 7.9. These two subsystems fit into the full inverter thermal model described in section 7.2.3.

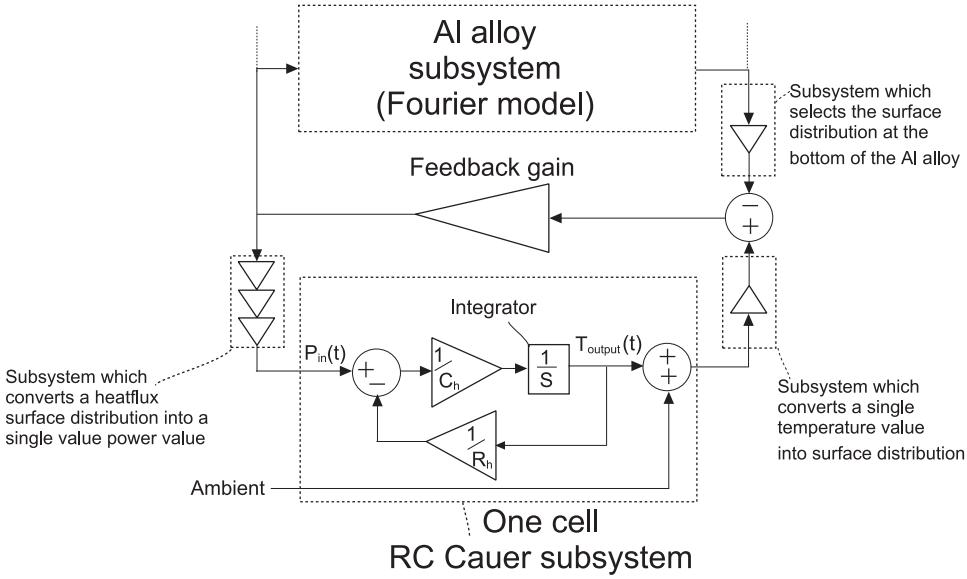

Figure 7.9: MATLAB/Simulink implementation of the heatsink model. A one cell Cauer network is used to model heat transfer away from the underside of the Al alloy to the water beneath it.

7.2.3 Thermal Model of a Single Inverter Phase Leg

The full Fourier thermal model of one inverter leg phase is implemented in Simulink as shown in Fig. 7.10. This Fourier model uses the methods described in chapters 5 and 6 to simulate heat diffusion through the whole of the packaging structure, with the exception of the underside of the Al alloy layer which relies on one cell RC Cauer model of Fig. 7.9. The full thermal model was embedded into the electro-thermal converter simulator using the input and output connections shown at the top of Fig. 7.10. Power losses are the inputs to the thermal simulator while the device temperatures are the outputs to the converter simulator. The blocks of material which make up the structure in Fig. 7.8 are represented in the Simulink model by subsystems labelled with the material name. The RC Cauer model subsystem described in section 7.2.2 can be seen at the very bottom of the structure.

The Fourier thermal model used a feedback gain of 10^4 at every material interface; this value was found to be the best compromise of simulation speed and accuracy in chapter 6. The number of Fourier terms in each of the Fourier subsystems (representing one block of material) was selected to optimise the simulation speed:

- Vertical $(z) : k = 0; 1$ (2 terms) for all layers;
- Lateral $(x; y) : m; n = 0; 1; 2$ (3 terms) for all layers.

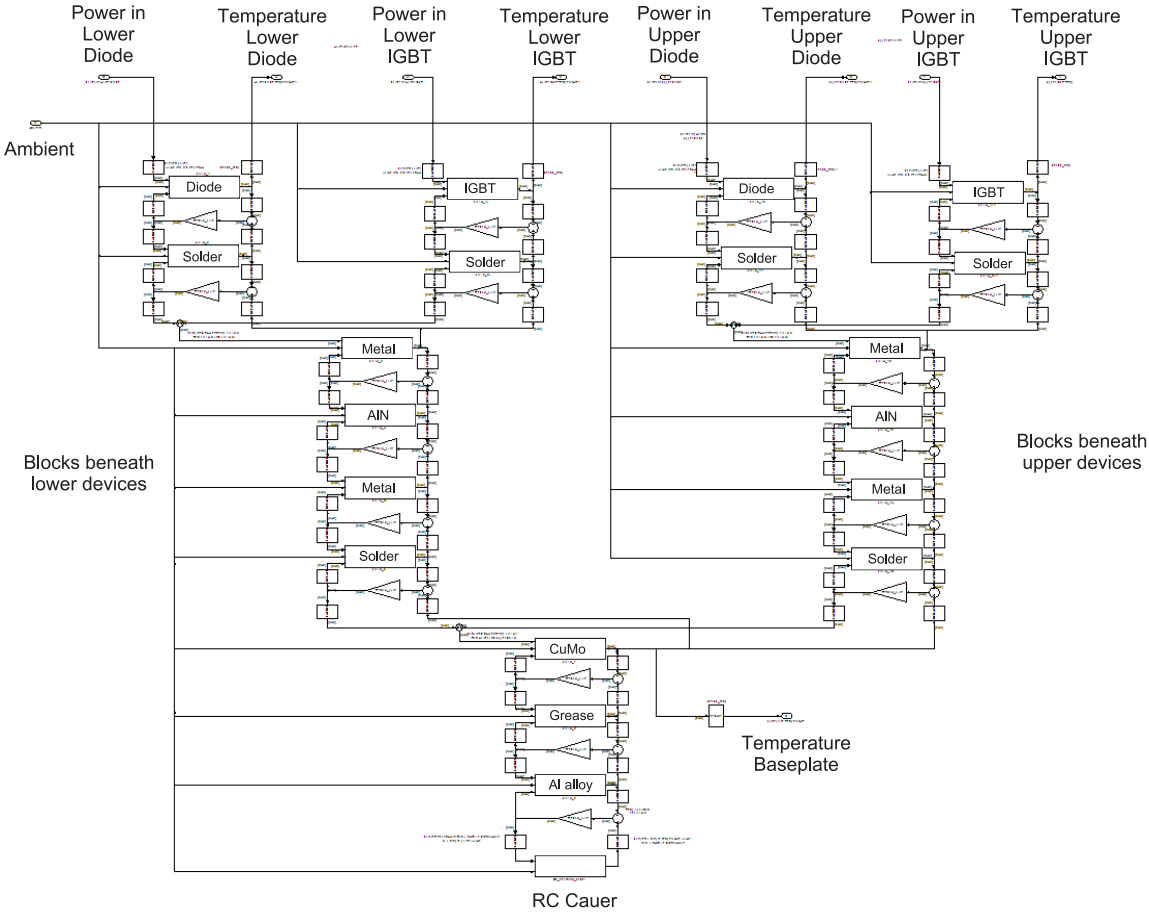

Figure 7.10: The Fourier series thermal model of one inverter phase leg implemented in MATLAB/Simulink. This model is embedded into the electro-thermal converter simulator in Fig. 1.3. The "Ambient" is the initial condition.

7.3 Results

The ARTEMIS and the Federal Urban Driving Schedule (FUDS) drive cycles have been created from data collected on the actual driving of vehicles in Europe and America respectively. These drive cycles are standardised for testing vehicle emissions. Realistic inverter load conditions may be investigated through use of these drive cycles because the drive cycle conditions can be transformed into inverter load cycle conditions using the method described in [183]. Therefore the inverter load conditions fed into the converter electro-thermal simulator will be identical to those demanded of the test inverter present in experimental set-up, leading to a meaningful validation of the electro-thermal converter simulator. Results are presented in the form of transient temperatures profiles of the upper and lower pairs of devices over the duration of the ARTEMIS (test 1) and FUDS (test 2) drive cycles. The validation of the electro-thermal converter simulator is carried out by the comparison of experimentally obtained results with simulated results.

7.3.1 Test 1: Artemis Driving Cycle

The inverter load conditions demanded during the ARTEMIS driving cycle are shown in Fig. 7.11. Experimentally obtained results are compared with simulated results over the duration of ARTEMIS load cycle in Fig. 7.12. The time taken for the electro-thermal converter simulation to run was 605 seconds; the look-up tables of device losses took an additional 119 seconds to run beforehand, giving a total of 724 seconds (approximately 12 minutes) using a Intel Dual Core 1.86GHz (each) and 3GB RAM computer.

7.3.2 Test 2: Federal Urban Driving Schedule (FUDS)

The inverter load conditions demanded during the FUDS drive cycle appear in Fig. 7.13. Experimentally obtained results are compared with simulated results over the duration of the FUDS drive cycle in Fig. 7.12. It took 7011 seconds (approx. 1hr 57mins) to simulate 640seconds of the FUDS cycle using the same computer as test 1.

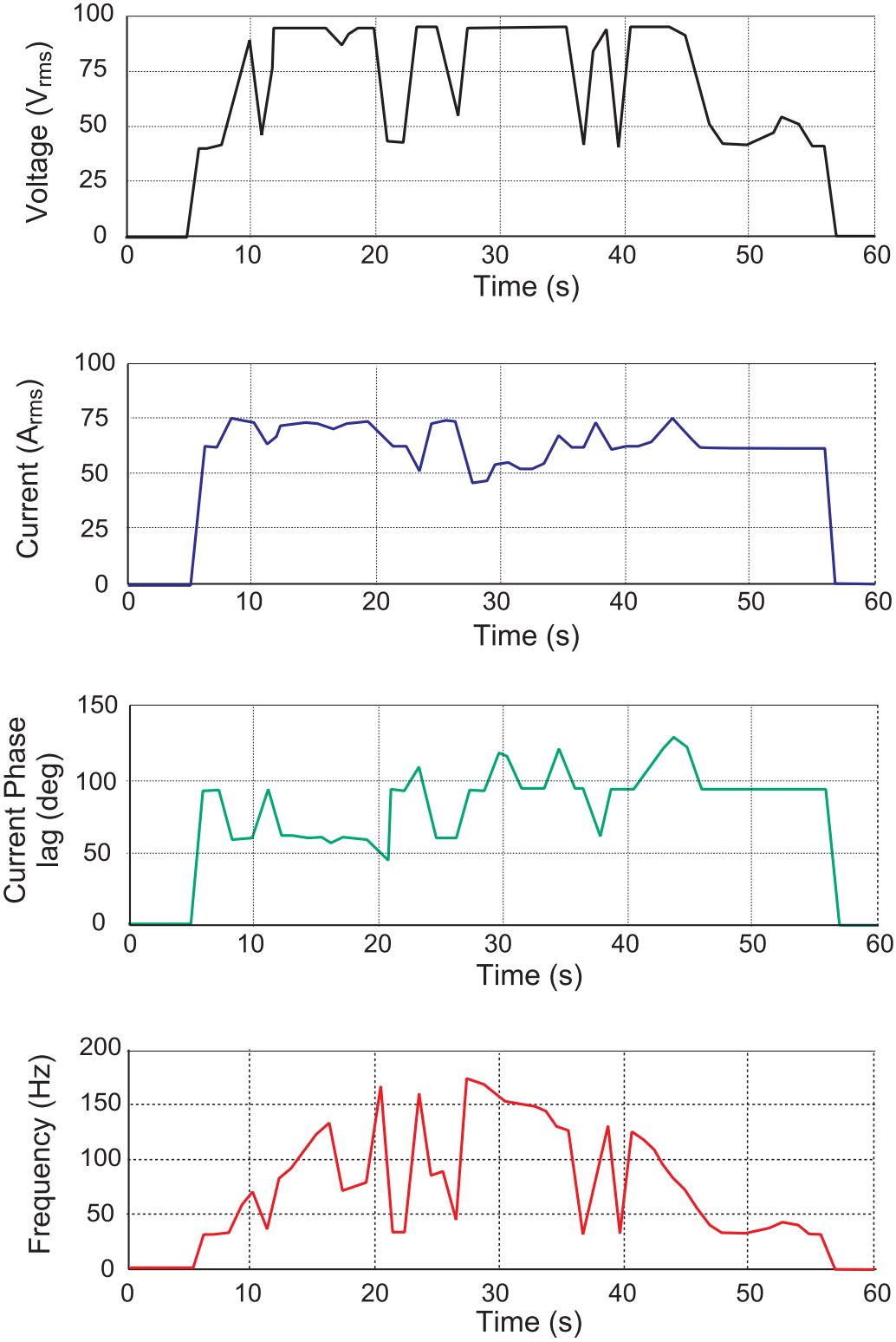

Figure 7.11: Inverter load conditions for one minute of the ARTEMIS drive cycle.

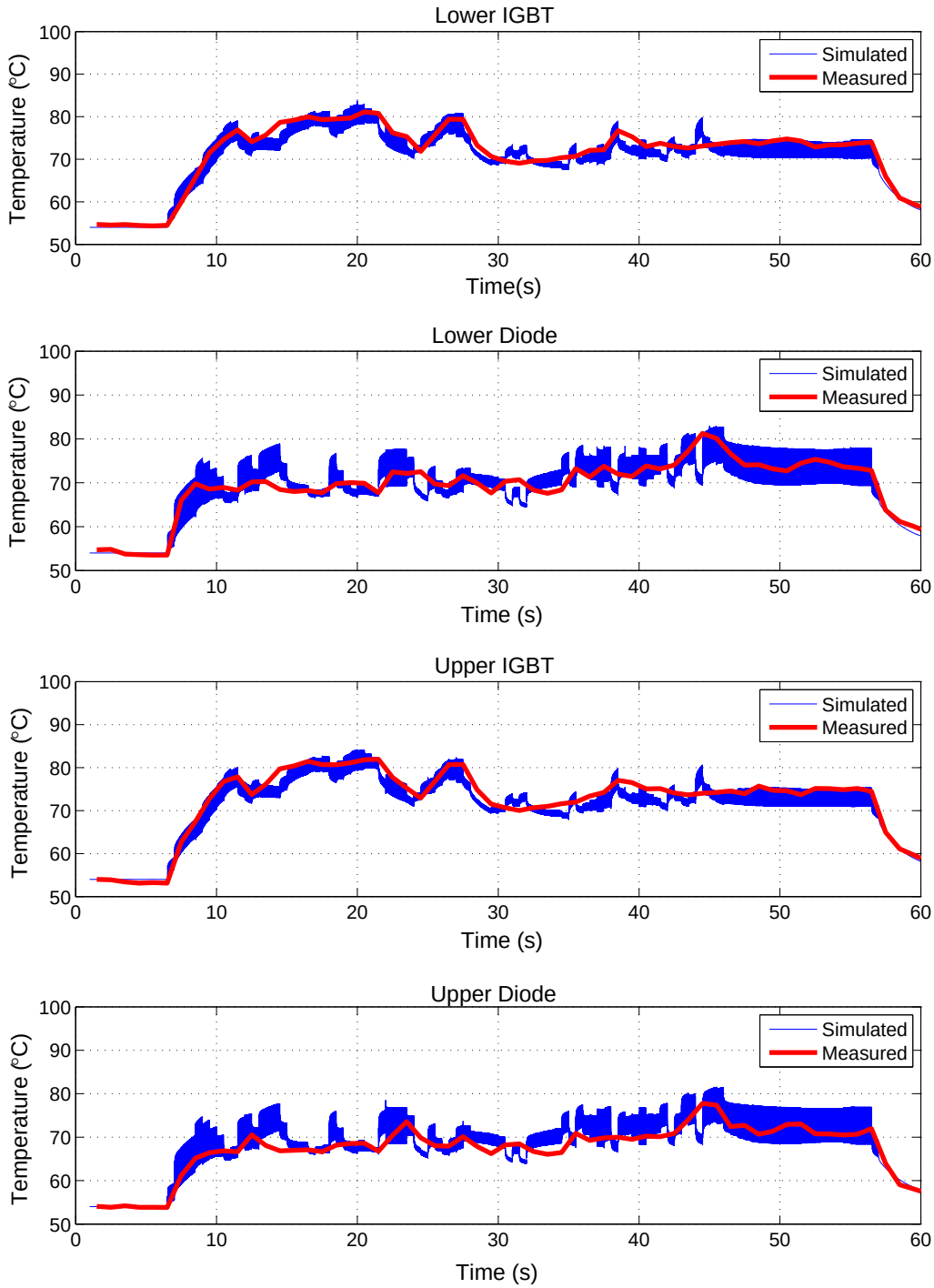

Figure 7.12: Phase leg device temperatures for the ARTEMIS load cycle.

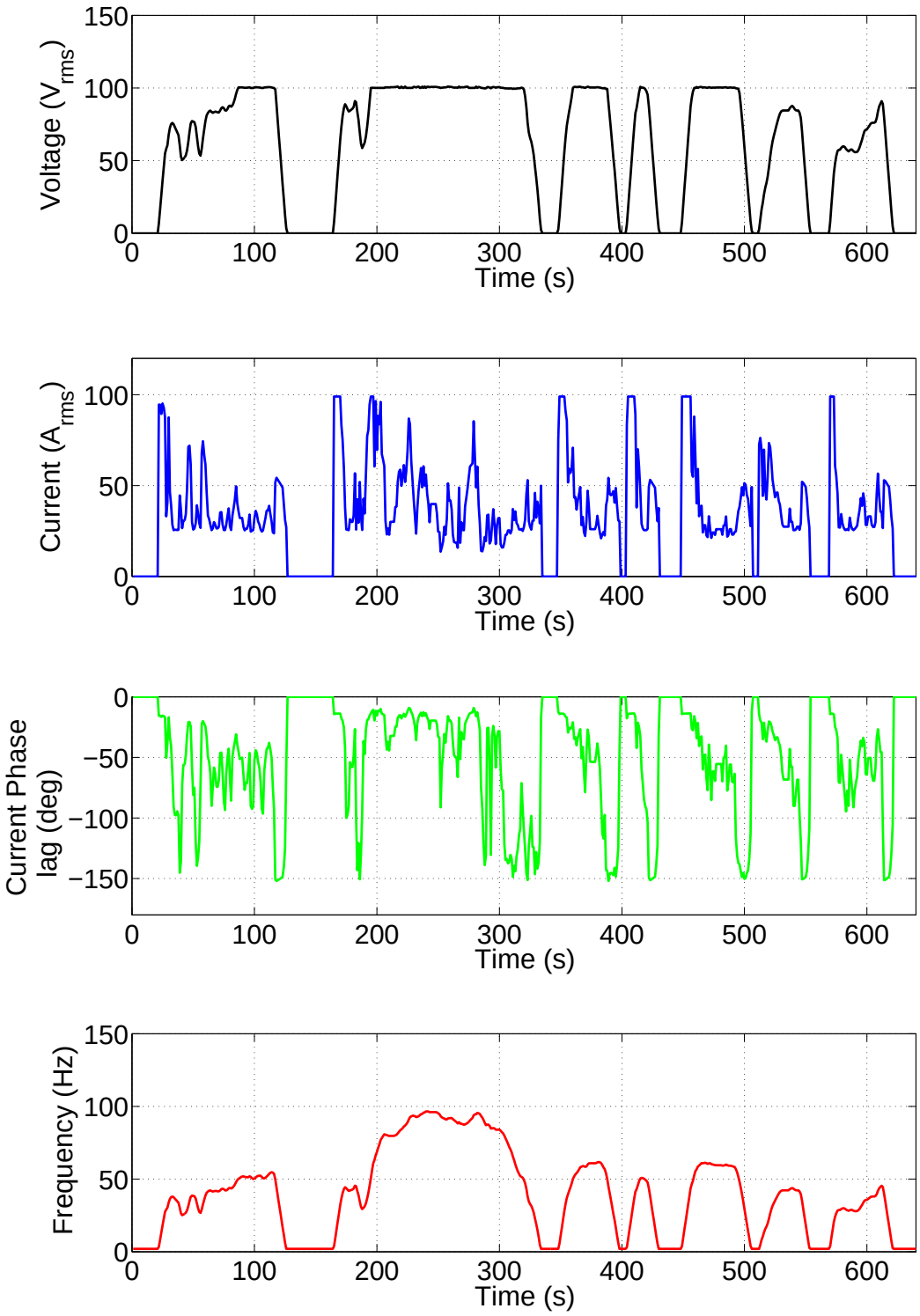

Figure 7.13: Inverter load conditions for 640 seconds of the FUDS drive cycle.

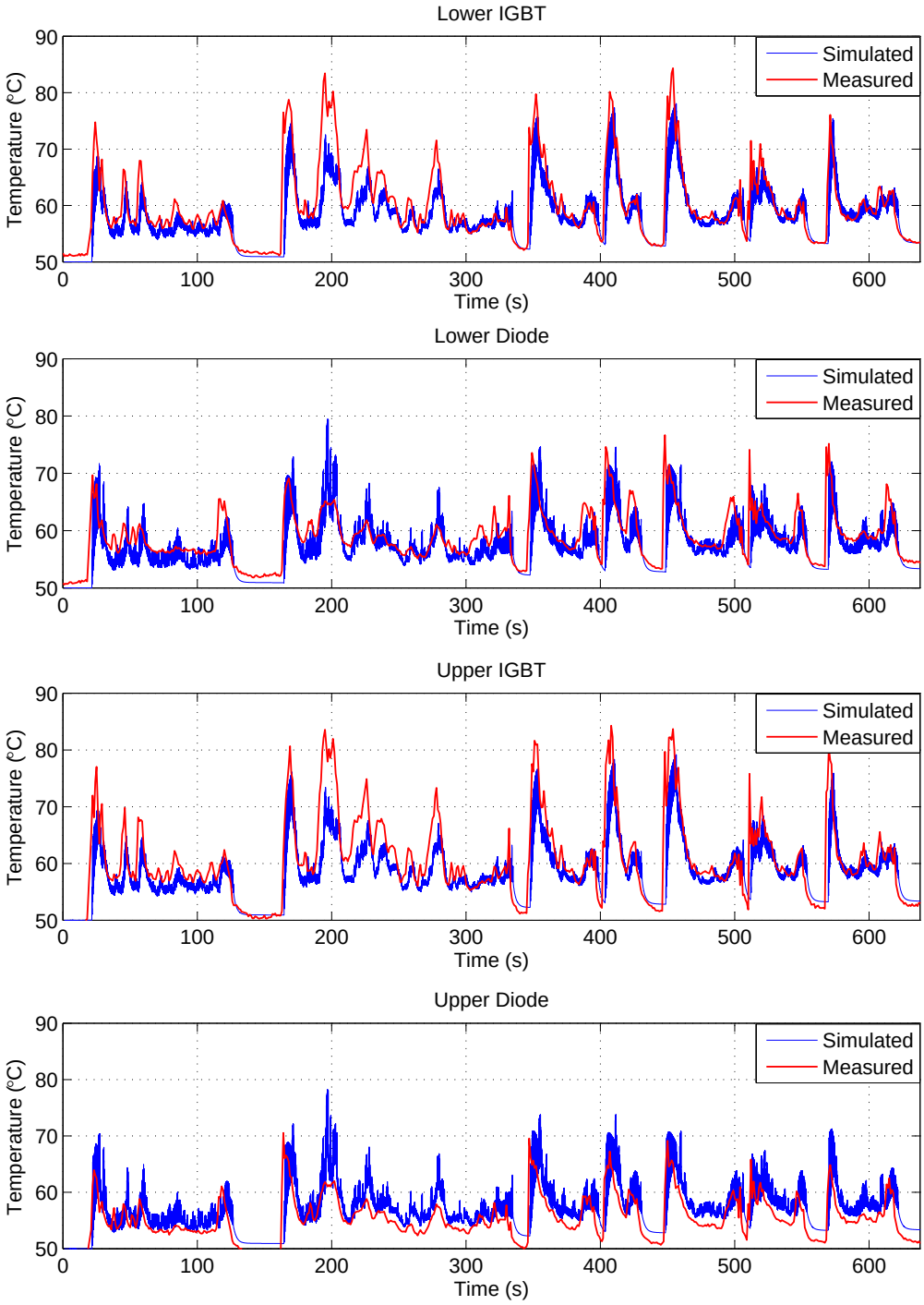

Figure 7.14: Phase leg device temperatures during the FUDS drive cycle.

7.4 Discussion

The results in Fig. 7.12 show that the transient device temperatures predicted by the fast electro-thermal converter simulator match the experimental results closely. The model has clearly captured the thermal transients during the ARTEMIS drive cycle. The measured temperature profile of the IGBT follows the load current. The simulated results show a greater degree of granularity than the measured results, this is because the infra-red camera was too slow to capture the high frequency temperature variations that the simulation predicted, the experimental device temperatures mostly stay within the envelopes of the simulated temperatures.

The transient device temperatures simulated by the fast electro-thermal converter simulator match the results captured by the infrared camera closely over the duration of the FUDS drive cycle. This shows the model works well, particularly as the plots from the FUDS drive cycle in Fig. 7.14 are taken over a time period which is ten times longer than that of the ARTEMIS drive cycle. That said, the results from the FUDS drive cycle seem to have sharper peaks. The peaks from the simulated and measured results line up well, although the measured magnitude of the IGBT temperature profiles does appear higher than the corresponding simulated results. Meanwhile the measured diode temperatures tend to be lower than the simulated results. This is potentially caused by the fact that very few Fourier terms were used in each layer of the thermal model ($M = N = 3$, $K = 2$) which led to some overshoot of the diode temperature and undershoot of the IGBT temperature. An anomalous result appears at time t=200s where the matching is poor for the temperature for every device. One potential reason for the poor matching could be the sampling frequency of the infrared camera which is 1Hz. Ideally, the sampling frequency of the infrared camera would by about 50 times that of the switching frequency

f_{sw}. Another possible reason for the anomalous result could be a glitch in the look-up table generation process which appears in Fig. 1.3. This would then show the transient temperature during each switching cycle which the thermal simulation does not predict. However, since the rate at which the electro-thermal converter simulator accesses the look-up tables is determined by the f_{sw}, a camera sampling rate to match f_{sw} would be sufficient since it would be possible to obtain direct comparison of experimental and simulated results at every time step.

The back-to-back test rig has proved to be effective in terms of providing a low cost means of experimentally validating the fast electro-thermal converter simulator. The successful validation of the fast electro-thermal converter simulator suggests it can play a important role in converter design. Numerical optimisation of the whole power converter is possible [183], including the devices, circuit and thermal system.

The close matching of the transient device temperatures from the test rig and converter simulator was dependent on several factors: the power losses from the devices, i.e. the switching and conduction behaviour of the device model, and the thermal model. The presence of the thermal model developed in this thesis within the electro-thermal simulator framework allows the thermal performance of power module packaging to be investigated during realistic operating conditions.

In contrast, existing approaches fail to test power converter packages using electro-thermal co-simulation, even though the ability to simulate realistic conditions is essential in order to accurately predict package reliability. Existing methods employ inverter simulators to create a power dissipation profile which is then fed into a RC thermal network. According to colleagues from the Toyota Motor Corporation, these inverter simulators can take up to two days to simulate a 60 second load cycle because they model every switching event. Further simulation delays are caused by the need to extract a RC network which is

a non-automatic time-consuming process, reliant on a prior FEM simulation. Therefore, using existing methods, a power module packaging designer must run a FEM solver for every packaging design which is tested and then extract a RC network from those results in order to create a thermal model. Meanwhile, the Fourier thermal model is a useful early stage design tool since it allows various packaging geometries and materials to be investigated efficiently, without recourse to finite element methods.

The electro-thermal converter simulator accurately simulates transient device temperatures at a speed approximately ten times slower than real-time. This compares extremely favourably with existing methods which are employed commercially. Therefore, the Fourier thermal model presented in this work is a significant step forward for power converter packaging design.

Chapter

8 Concluding Remarks and Further Work

This chapter presents the general conclusions of the research work carried out. The future benefits of the work are stated and valid avenues for further work are considered. Methods of increasing the capabilities of the Fourier thermal model are also discussed.

8.1 Conclusions

Power converters are essential for supplying energy for today's society in a more efficient, sustainable and controllable manner. Thermally induced failure modes are the main cause of power converter reliability issues. The introductory remarks within this thesis highlighted the need for a fast and accurate 3-D thermal model, capable of simulating 3-D heat diffusion through power converter packaging during realistic operating conditions. This need was met by the development of the Fourier thermal model in this work.

Chapters 5 and 6 showed the development of the Fourier thermal model. Validation using FLOTHERM proved that the Fourier model could successfully simulate 3-D heat conduction through many blocks of material with different x-y cross-sectional areas. It was evident that the Fourier model could also simulate heat diffusion from multiple heat

sources. Using the approaches presented for simulating material interfaces in chapter 6, any power module package made up of vertically stacked blocks of material could be modelled. The Fourier thermal model was computationally efficient, with a simulation speed far superior to that of the FVM software package FLOTHERM for every test case.

The Fourier thermal model had many advantages over FLOTHERM other its superior simulation speed. The Fourier thermal model was easier to use because it did not require mesh refinement prior to a simulation. Instead it operated directly from the material properties and the geometry of a structure. Furthermore, the results generated by the Fourier thermal model were in the form of a continuous wave and looked more realistic than those generated by FLOTHERM. The Fourier model had the advantage of being able to determine the temperature distribution across the whole converter package rather than just at monitoring points. This would be of benefit for locating hotspots and visualising the heat flow. A further advantage of the Fourier thermal model was its ability to describe any arbitrary heat flux, which was not possible using FLOTHERM.

In chapters 5 and 6, the accuracy of the Fourier thermal model was dependent on the number of Fourier terms used in the model; the more terms used, the greater accuracy. However, the benefit of using fewer terms was that the model simulated more quickly. The Fourier model appeared sufficiently accurate to provide a thermal designer with useful guidance in all the test cases, even when using very few terms. A drawback of the Fourier thermal model was the occasional presence of undershoot when simulating short transient periods, caused by using very few Fourier terms. However, this drawback is fairly insignificant when consideration is given to the model's simulation speed.

Chapter 7 showed the successful experimental validation of the fast electro-thermal converter simulator using a back-to-back rig. This suggests the electro-thermal simulator can play a important role in converter design. The whole power converter, including the

devices, circuit and thermal system can be numerically optimised. The similarity between the experimental and simulated results suggest the Fourier thermal model, which operates within the framework of the electro-thermal simulator, has clearly been fit for purpose.

The use of Simulink as the simulation environment takes advantage of the highly flexible programming facilities within MATLAB to couple the thermal and converter simulation. It has been shown to be an effective and compact means of simulating heat conduction in power module packaging during realistic load conditions. Thermally modelling devices during realistic load conditions is a major benefit of the work presented in this paper. Existing approaches fail to test power converter packages using electro-thermal co-simulation, even though the ability to simulate realistic conditions is essential in order to accurately predict package reliability.

The comparison between simulation speeds of existing approaches and the electro-thermal simulator suggest that the Fourier model enabled a significant step forward in power converter packaging design. Existing approaches can take up to two days to simulate a 60 second load cycle according to colleagues from Toyota. Meanwhile, the electro-thermal simulator, which contains the Fourier thermal model proposed in this work, operates with a simulation speed which is ten times real time. The fast simulation speed of the Fourier model ensures a more effective simulation based design phase. From an industrial perspective this is beneficial because 'time is money'.

The Fourier thermal model has the potential for commercial success as an early stage design tool. It allows various packaging geometries and materials to be investigated efficiently and in a meaningful way. Use of the Fourier thermal model to thermally optimise power converter packaging will hopefully give rise to cheaper, lighter, more compact and more reliable power converter packages in the future.

8.2 Suggestions for Further work

Although the experimental validation of the Fourier thermal model in chapter 7 was successful, the FLIR Thermovision A20M infrared camera, with a frame rate of 1Hz, did not record device temperature data quickly enough. This prevented a detailed comparison between experimental and simulated results. An alternative approach to transient temperature measurement should be sought. A faster frame rate could be achieved using a thermocouple or a thermistor, however, neither provides a contact-free method of temperature leading to issues caused by electromagnetic interference. An optical probe, which is essentially a one pixel version of an infrared camera, would be a good option. It would provide a contact-free device temperature measurement at a frame rate of 1000 Hz.

Device temperature profiles during realistic load conditions can be generated using the Fourier thermal model within the framework of the electro-thermal converter simulator. However, this data is of limited use in isolation. An essential line of further work is the integration of reliability lifetime models into the framework of electrothermal converter simulator. This would enable prediction of device reliability based on power converter packaging design.

The Fourier thermal model is capable of simulating thermal diffusion through a wide range of packaging configurations. In the future it would be worthwhile investigating the thermal performance of innovative designs, such as the substrate-free Copper leadframe package in [185]. The prospect of being able to identify the most effective packaging designs and optimise their geometrical layout is exciting.

In the Fourier thermal model of the Toyota Prius power converter package in chapter 7, the bond wires attached to the semiconductor devices were ignored. However, research in [186] has suggested that as many bond wires as possible should be connected to the

semiconductor devices, as shown in Fig. 8.1, because they play a significant role in conducting heat away from the devices. Furthermore, copper bond wires have been proposed in [187] because they have a higher thermal conductivity than Aluminium. Therefore, in future work, the thermal simulation of the bond wires should be considered.

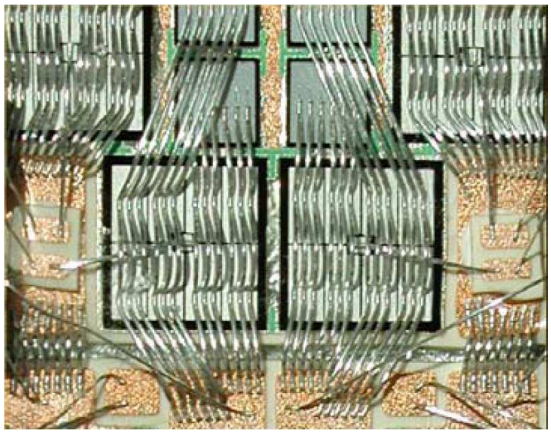

Figure 8.1: Photograph showing many bond wires connected in parallel to devices [186].

The model of the power converter heatsink used in chapter 7 is overly simplified. A RC network is used to model the thermal interface at the underside of Aluminium alloy packaging layer. In the future, it would be beneficial to investigate if the data provided by Toyota about this interface, i.e. the thermal resistance and thermal capacitance, is accurate. It would also be interesting to discover if heat is evenly distributed at this interface. This information would allow the formation of a more detailed and more accurate heatsink model which could possibly allow improvement in the design of water conduit.

Possibly, contact resistance at material interfaces could be simulated by the Fourier model. This might be possible by modifying the feedback gain value used at interface to reflect the contact resistance, this is worth exploration. Being able to model lateral Material interfaces would further add to the capability of the Fourier thermal model. Simulating a packaging design where a silicon device is embedded into another material would be possible. Another possible method of improving the Fourier thermal model

would to incorporate the fact that the material properties are temperature dependent into the model. However, this would add a degree of difficulty because the heat equation would become non linear.

Selecting the number of terms assigned to each layer based on the packaging structure, such as that shown in Fig. 8.2, may be of benefit. This has the potential to improve the model's accuracy, by preventing against undershoot, while maintaining a fast simulation speed. In the future, work could be carried out to automate the selection of the number of Fourier terms since it is time consuming for the model user.

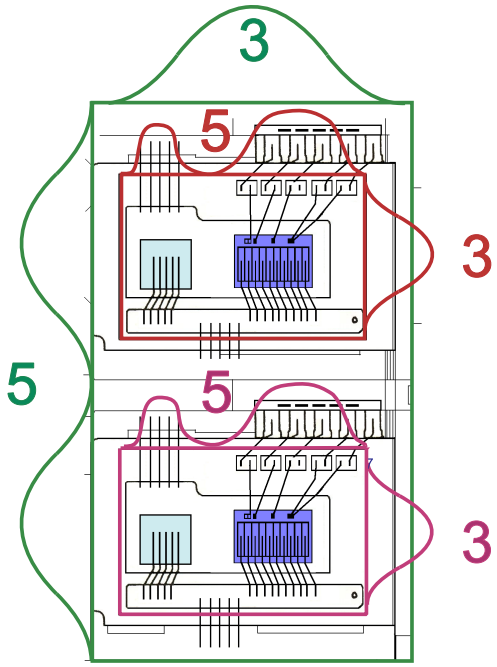

Figure 8.2: Diagram showing the number of Fourier terms which might be selected to represent some layers of this structure.

Finally, exploring possible means of increasing the simulation speed of the Fourier thermal model is important future work. Even though the model is far faster than FLOTHERM there might be further room for improvement. Simulation speed could potentially be increased using a Fast Fourier transform. According to [188], Fast Fourier transforms (FFTs) can reduce CPU time by a factor of 100 to 1000. However, a long-winded numerical integration procedure is required [189]. According to [153], each block of material in the power converter package would require its own fast Fourier transform, so FFTs might be impractical in this case.

References

[1] *World Energy Needs and Nuclear Power.* St James's Square, London, UK: World Nuclear association. Publication online: http://www.world-nuclear.org/info/inf16.html, 2010.

[2] P. Krein, *Power electronics and the New energy Revolution: The How of Energy in a Transitioning World and an introduction to ECE 464.* University of Illinois. Online: www.courses.engr.illinois.edu/ece464: Course notes ECE 464, 2010.

[3] B. Baliga, "Enhancement and depletion mode vertical-channel MOS gated thyristor," *IET Electronics Letters*, vol. 15, no. 20, pp. 645–647, 1979.

[4] P. Rousse, Yole Développment, "Power electronics in electric and hybrid vehicles," 2009.

[5] J. He, W. Morris, M. Shaw, J. Mather, *et al.*, "Reliability in large area die bonds and effects of thermal expansion mismatch and die size," *International Journal of Microelectronics And Packaging Society (IMAPS)*, vol. 21, no. 3, pp. 297–304, 1998.

[6] "Thermal aspects on DC/DC power modules," *Design Note: Ericsson Microelectronics AB*, no. 004, pp. 1–8, 2000.

[7] T. Stockmeier and W. Tursky, "Present and future of power electronics modules," in *the Center for Power Electronics Systems (CPES) Seminar, Blacksburg, VA, USA*, 2000, pp. 3–9.

[8] J. W. Kolar, U. Drofenik, J. Biela, M. Heldwein, *et al.*, "PWM converter power density barriers," *IEEJ Transactions on Industry Applications*, vol. 128, no. 4, pp. 1–14, 2008.

[9] G. Majumdar, "Recent technologies and trends of power devices," in *the 14th International Workshop on Physics of Semiconductor Devices (IWPSD), Mumbai, India*, 2007, pp. 1–6.

[10] U. Schlapbach, M. Rahimo, C. von Arx, A. Mukhitdinov, *et al.*, "1200V IGBTs operating at 200°C? An investigation on the potentials and the design constraints," in *the 19th International Symposium on Power Semiconductor Devices and ICs (ISPSD), Jeju, South Korea*, 2007, pp. 9–12.

[11] J. Biela and J. W. Kolar, "Impact of power density maximization on efficiency of DC−DC converter systems," *IEEE Transactions on Power Electronics*, vol. 24, no. 1, pp. 288–300, 2009.

[12] P. Jacob, M. Held, P. Scacco, and W. Wu, "Reliability testing and analysis of IGBT power semiconductor modules," in *the 20th International Symposium for Testing and Failure Analysis (ISTFA)*, 1994, pp. 1–5.

[13] L. G. Franquelo, J. Leon, and E. Dominguez, "New trends and topologies for high power industrial applications: the multilevel converters solution," in *the International Conference on Power Engineering, Energy and Electrical Drives (POWERENG), Lisbon, Portugal*, 2009, pp. 1–6.

[14] P. M. Igic, P. A. Mawby, M. S. Towers, and S. Batcup, "New physically based pin diode compact models for the diode and IGBT with full temperature dependent features," in *the IEE Circuits Devices Systems*, vol. 149, 2002, pp. 257–263.

[15] P. R. Palmer, E. Santi, J. L. Hudgins, X. Kang, *et al.*, "Circuit simulator models for the diode and IGBT with full temperature dependent features," *IEEE transactions on Power Electronics*, vol. 18, no. 5, pp. 1220–1229, 2003.

[16] A. Hefner, "A dynamic electro-thermal model for the IGBT," *IEEE Transactions on Industry Applications*, vol. 30, no. 2, pp. 394–405, 1994.

[17] T. Kojima, Y. Yamada, M. Ciappa, M. Chiavarini, *et al.*, "A novel eletcro-thermal simulation approach of power IGBT modules for automotive traction applications," in *in the 16th International Symposium on Power Semiconductor Devices and ICs (ISPSD), Kitakyushu, Japan*, 2004.

[18] A. Rajapakse, A. Gole, and P. Wilson, "Electromagnetic transient simulation models for accurate representation of switching losses and thermal performance in power electronic systems," *IEEE Transactions on Power Delivery*, vol. 20, no. 1, pp. 319–327, 2005.

[19] J. Reichl, J.-S. Lai, A. Hefner, T. McNutt, *et al.*, "Inverter dynamic electro-thermal modeling and simulation with experimental verification," in *the 36th Power Electronics Specialists Conference (PESC), Recife, Brazil*, vol. 3, 2005, pp. 2208–2215.

[20] H. Mantooth and J. Duliere, "A unified diode model for circuit simulation," *IEEE Transactions on Power Electronics*, vol. 12, no. 5, pp. 816–823, 1997.

[21] A. Bryant, P. Mawby, P. Palmer, E. Santi, *et al.*, "Exploration of power device

reliability using compact device models and fast electro-thermal simulation," *IEEE Transactions Industry Applications*, vol. 44, no. 3, pp. 894–903, 2008.

[22] A. Bryant, G. Roberts, A. walker, and P. Mawby, "Fast inverter loss and temperature simulation and silicon carbide device evaluation for hybrid electric vehicle drives," *IEEJ Transactions on Industry Applications*, vol. 128-D, no. 4, pp. 441–449, 2008.

[23] G. Coquery, R. Lallemand, D. Wagner, M. Piton, *et al.*, "Reliability improvement of the soldering thermal fatigue with AlSiC technology on traction high power IGBT modules," in *the 8th European Conference on Power Electronics and Applications, Lausanne, Switzerland*, 1999, pp. 1719–1722.

[24] F. Christiaens and B. Vandevelde, "A generic methodology for deriving compact dynamic thermal models, applied to the PSGA package," *IEEE Transactions on Components, Packaging, and Manufacturing Technology - Part A*, vol. 21, no. 4, pp. 565–576, 1998.

[25] P. Bagnoli, C. Casarosa, M. Ciampi, and E. Dallago, "Thermal resistance analysis by induced transient (TRAIT) method for power electronic devices thermal characterization - part I: Fundamentals and theory," *IEEE Transactions on Power Electronics*, vol. 13, pp. 1209–1219, 1998.

[26] V. Szekely, "THERMODEL: a tool for compact dynamic thermal model generation," *Microelectronics Journal*, vol. 29, pp. 257–267, 1998.

[27] V. Szekely, "A new evaluation method of thermal transient measurement results," *Microelectronics Journal*, vol. 28, pp. 277–292, 1997.

[28] C. Yun, P. Regli, J. Waldmeyer, and W. Fichter, "Static and dynamic thermal characteristics of IGBT power modules," in *Proceedings of the 11th International Symposium on Power semiconductor Devices and ICs*, 1999, pp. 37–40.

[29] P. Igic, P. Mawby, and M. Towers, "Thermal model of power semiconductor devices for electro-thermal circuit simulations," in *Proceedings of the 23rd International Conference on Microelectronics*, 2002, pp. 171–174.

[30] M. Rencz, V. Szekely, A. Poppe, and B. Courtois, "Inclusion of RC compact models of packages into board level thermal simulation tools," in *Proceedings of the 18th IEEE Semiconductor Thermal Measurement and Management (SEMITHERM) Symposim*, 2002, pp. 71–76.

[31] T. Kojima, Y. Nishibe, Y. Yamada, Y. Ueta, *et al.*, in *Conference Recordings of the Power Electronics Specialists Conference (PESC), Jeju, South Korea*, vol. 2, pp. 1–5.

[32] M. Ciappa, W. Fichtner, T. Kojima, Y. Yamada, *et al.*, "Extraction of accurate thermal compact models for fast electro-thermal simulation of IGBT modules in hybrid electric vehicles," in *Conference Recordings of ESREF, Arcachon, France*, vol. 45, no. 9-11, 2005, pp. 1694–1699.

[33] J. Hsu and L. Vu-Quoc, "A rational formulation of thermal circuit models for electrothermal simulation - part 1: finite element method," *IEEE Transactions on Circuits and Systems: Fundamental Theory and Application*, vol. 40, no. 9, pp. 721–732, 1996.

[34] J. Barnes and R. Lomax, "Finite element methods in semiconductor device simulation," *IEEE Transactions on Electron Devices*, vol. 34, pp. 1082–1088, 1997.

[35] K. Fukahori and P. Gray, "Computer simulation of integrated circuits in the presence of electrothermal interaction," *IEEE Journal of Solid-State Circuits*, vol. 11, pp. 834–846, 1976.

[36] A. Hefner and D. Blackburn, "Simulating the dynamic electrothermal behaviour of power electronic circuits and systems," *IEEE Transactions on Power Electronics*, vol. 8, pp. 376–385, 1993.

[37] B. Du, J. L. Hudgins, A. Bryant, E. Santi, *et al.*, "Expanded thermal model for IGBT models," in *the 41st Annual IEEE Industry Applications Conference (IAS), Tampa, FL, USA*, vol. 2, 2006, pp. 777–784.

[38] B. Du, J. Hudgins, E. Santi, A. Bryant, *et al.*, "Transient thermal analysis of power devices based on Fourier-series thermal model," in *Conference recordings of the IEEE Power Electronics Specialists Conference (PESC), Rhodes, Greece*, 2008, pp. 3129–3135.

[39] S. Pekarev and T. Skvarenina, "ACSL/graphic modeller component models for electric power education," *IEEE Transactions on Education*, vol. 41, no. 4, p. 4, 1998.

[40] A. Keyhani, "Pulse width modulation techniques," *Lecture 25, Online: www.ece.osu.edu/ems/*, 2010.

[41] O. Mueller, "Cryo-MOSFET and IGBT: a Comparison," *Journal de Physique IV*, vol. 6, pp. C3–219–24, 1996.

[42] B. Maurice and L. Wuidart, "Drive circuits for power MOSFETs and IGBTs," *Application note: AN524/0994 1/10. www.st.com.*

[43] A. Lostetter, F. Barlow, and A. Elshabini, "An overview to integrated power module design for high power electronics packaging," *Microelectronics Reliability*, vol. 40, pp. 365–379, 2000.

[44] T. Kojima, Y. Yamada, Y. Nishibe, and K. Torii, "Novel RC compact thermal model of hv inverter module for electro-thermal coupling simulation," in *the 4th Power Conversion Conference (PCC), Nagoya, Japan*, 2007, pp. 1025–1029.

[45] M. Ishiko and T. Kondo, "A simple approach for dynamic junction temperature estimation of IGBTs on PWM operation conditions," in *Power Electronics Specialist Conference (PESC), Orlando, Florida, USA*, 2007, pp. 916–920.

[46] S. Narumanchi, M. Mihalic, K. Kelly, and G. Eesley, "Thermal interface materials for power electronics applications," in *the 11th Intersociety Conference on Thermal and Thermomechanical Phenomena in Electronic Systems (ITHERM), Orlando, Florida, USA*, 2008, pp. 395–404.

[47] A. Birolini, *Reliability Engineering: Theory and Practice*, 5th ed. Springer Berlin Heidelberg, NY, USA, 2007.

[48] A. Bryant, *University of Warwick Undergraduate Lecture notes: ES4D4 Power electronics and devices.* Lecture 21, 2009, p. 5.

[49] V. K. Khanna, *Insulated Gate Bipolar Transistor IGBT Theory and Design.* Wiley-IEEE Press, Piscalaway, NJ, USA, 2003.

[50] D. A. Murdock, J. E. R. Torres, J. J. Connors, and R. D. Lorenz, "Active thermal control of power electronic modules," *IEEE Transactions on Industry Applications*, vol. 42, no. 2, pp. 552–558, 2006.

[51] N. Y. A. Shammas, "Present problems of power module packaging technology," *Microelectronics Reliability*, vol. 43, no. 4, pp. 519–527, 2003.

[52] R. A. Amro, "Packaging and interconnection technologies of power devices, challenges and future trends," *World Academy of Science, Engineering and Technology (WASET)*, vol. 49, pp. 691–694, 2009.

[53] S. Ramminger, G. Mitic, P. Tiirkes, and G. Wachutka, "Thermo-mechanical simulation of wire bonding joints in power modules," in *the 2nd International Conference on Modeling and Simulation of Microsystems (MSM), San Juan, PR, USA*, 1999, pp. 483–486.

[54] M. Bouarroudj, Z. Khatir, J. Ousten, F. Badel, *et al.*, "Degradation behavior of 600V−200A IGBT modules under power cycling and high temperature environment conditions," *Microelectronics Reliability*, vol. 47, pp. 1719–1724, 2007.

[55] V. Mehrotra, "Wirebond reliability in IGBT-power modules: Application of high resolution strain and temperature mapping," in *the 11th International Symposium on Power Semiconductor Devices and ICs (ISPSD), Toronto, Ontario, Canada*, 1999, pp. 113–116.

[56] C. V. Godbold, A. Sankaran, and J. Hudgins, "Thermal analysis of high-power modules," *IEEE Transactions on Power Electronics*, vol. 12, no. 1, pp. 3–11, 1997.

[57] J. He, W. Morris, M. Shaw, and N. Sridhar, "Reliability in large area solder joint assemblies and effects of thermal expansion mismatch and die size," *Advancing Microelectronics*, no. 9, pp. 39–46, 1999.

[58] Z. Khatir and S. Lefebvre, "Thermal analysis of power cycling effects on high power

IGBT modules by the boundary element method," in *the 17th Semiconductor Thermal Measurement and Management (SEMITHERM) Symposium, San Jose, CA, USA*, 2001, pp. 27–34.

[59] E. Herr, T. Frey, R. Schlegel, A. Stuck, *et al.*, "Substrate-to-base solder joint reliability in high power IGBT modules," vol. 37, pp. 1719–1722, 1997.

[60] G. Muralidharan and A. Kercher, Oak Hill National Laboratory, U.S Department of energy, "Solder joints of power electronics," 2009.

[61] M. Ciappa, "Selected failure mechanisms of modern power modules," *Microelectronics Reliability*, vol. 42, no. 4-5, pp. 653–667, 2002.

[62] N. Shammas, M. Rodrigues, A. Plumpton, and D. Newcombe, "Finite element modelling of thermal fatigue effects in IGBT modules," in *IEE Circuits, Devices & Systems*, vol. 148, no. 2, 2001, pp. 95–100.

[63] Y. S. Touloukian, R. K. Kirby, R. E. Taylor, and T. Y. R. Lee, *Thermo-physical properties of matter - Thermal expansion - Nonmetallic solids.* IFI/Plenum Publication Data Company, New York, USA, 1977, vol. 13.

[64] H. Ye, M. Lin, and C. Basaran, "Failure modes and FEM analysis of power electronic packaging," *Finite Elements in Analysis and Design*, vol. 38, pp. 601–612, 2002.

[65] G. Mitica, R. Beinertb, P. Klofaca, H. J. Schultza, *et al.*, "Reliability of AlN substrates and their solder joints in IGBT power modules," *Microelectronics reliability*, vol. 39, pp. 1159–1164, 1999.

[66] M. Held, P. Jacob, G. Nicoletti, P. Scacco, *et al.*, "Fast power cycling test for

insulated gate bipolar transistor modules in traction application," *International Journal of Electronics*, vol. 86, no. 10, p. 11931204, 1999.

[67] S. Manson, "Creep-fatigue analysis by strain range portioning," *NACA Technical Memorandum X-67838*, 1971.

[68] L. Coffin, "Fatigue at high temperature- prediction and interpretation," in *Proceedings of the institute of mechanical engineers, London, UK*, vol. 188, 1974, pp. 109–127.

[69] J. Kotz, P. Treichel, and J. Townsend, *Chemistry and chemical reactivity.* Belmont, CA, USA: Thomson Brooks/Cole, Thomson Higher Education, 2009, vol. 2, ch. 15, p. 696.

[70] A. Bryant, P. Mawby, P. Palmer, E. Santi, *et al.*, "Exploration of power device reliability using compact device models and fast electrothermal simulation," *IEEE Transaction on Industrial Applications*, vol. 44, no. 3, pp. 894–903, 2008.

[71] R. Amro, J. Lutz, and A. Lindemann, "Power cycling with high temperature swing of discrete components based on different technologies," in *conference recordings of Power Electronics Specialists Conference (PESC), Aachen, Germany*, 2004, p. 25932598.

[72] C. Xiao, K. Ngo, and G.-Q. Lu, "Thermal design of power module to minimize peak transient temperature," in *International Conference on Electronic Packaging Technology & High Density Packaging (ICEPT-HDP), Xi'an, China*, 2009, pp. 248–254.

[73] F. P. Incropera and D. P. D. Witt, *Fundamentals of Heat and Mass Transfer*, 4th ed. New York, NY: John Wiley & Sons, 1996, vol. 1.

[74] L. M. Latif, *Heat convection*, 2nd ed. Berlin, Germany: Springer-Verlag, 2009, vol. 1, p. 6.

[75] R. Siegel and J. Howell, *Thermal Radiation Heat transfer*, 4th ed. New York, NY: Taylor and Francis, 2002, vol. 1, p. 1.

[76] T. M. Tritt, *Physics of solids and liquids Thermal conductivity: theory,properties, and applications*, 2nd ed. New York, NY: Kluwer academic/Plenum publishers, 2004, vol. 1.

[77] S. L. Shind and J. Goela, *High thermal conductivity materials.* New York, NY: Springer Science+Business Media, inc, 2006, vol. 1.

[78] J. Kevorkian, *Partial Differential Equations:Analytical Solution Techniques*, international student ed. Pacific Grove, CA: Brooks/Cole, 1990, vol. 1, pp. 1–3.

[79] J. Crank, *The mathematics of diffusion*, 2nd ed. Oxford: Oxford science publications, Clarendon press, 1975, pp. 2–5.

[80] H. S. Carslaw and J. C. Jaeger, *Conduction of Heat in Solids*, 2nd ed. Oxford: Clarendon press, Oxford science publications, 1989, vol. 1, pp. 8–9.

[81] I. Müller and W. H. Müller, *Fundamentals of thermodynamics and applications: with historical annotations and many citations from Avogadro to Zermelo*, 1st ed. Berlin, Germany: Springer, 2009, vol. 1, p. 179.

[82] W. Huang, M. R. Stan, and K. Skadron, "Physically-based compact thermal modeling-achieving parametrization and boundary condition independence," in *10th*

International Workshop on THERMal INvestigations of ICs and Systems (THERMINIC), 2004.

[83] W. Wang, S. Liou, and Y. Sun, "Bridging the gap: Package level and system level thermal modelling," in *Proceedings of the 50th Electronic Components and Technology Conference, Las Vegas, NV. USA*, 2000, pp. 287–293.

[84] A. Bar-Cohen, T.Elperin, and R. Eliasi, "θ_{jc} charaterization of chip packages justification, limitations and future," *IEEE Transactions on Components, Hybrids, Manufacturing Technology (CHMT)*, vol. 12, pp. 724–731, 1989.

[85] H. Rosten and C. Lasance, "Final report to SEMITHERM XIII on the european-funded project DELPHI - the development of libraries and physical models for an integrated design environment," in *the 13th Annual IEEE Semiconductor Thermal Measurement and Management Symposium, Austin, TX, USA*, 1997, pp. 73–91.

[86] C. Lasance, H. Vinke, H. Rosten, and K.-L. Weiner, "A novel approach for the thermal characterization of electronic parts," in *the 11th Semiconductor Thermal Measurement and Management (SEMITHERM) Conference, San Jose, CA, USA*, 1995, p. 19.

[87] C. Lasance, "Thermal characterization of electronic parts with compact models: Interpretation, application, and the need for a paradigm shift," in *the 13th Semiconductor Thermal Measurement and Management (SEMITHERM) Conference, Austin, Texas, USA*, 1997, pp. 40–48.

[88] J. Andrews, "Package thermal resistance model: Dependency on equipment design," *IEEE Transactions on Components, Hybrids, and Manufacturing Technology*, vol. 11, pp. 528–537, 1988.

[89] *JEDEC JC15.1 is a committee of JEDEC standardisation organisation of the Electronic Industries Alliance (EIA)*, Published specifications are available at http://www.jedec.org.

[90] W. Xu, S. Shidore, and P. Gauch, "Creation and validation of a two-resistor compact model of a plastic quad flat pack (PQFP) using CFD," in *International conference on high-density interconnect and systems packaging, Denver, CO*, 2000, pp. 420–425.

[91] E. Garcia and C.-P. Chiu, "Two-resistor compact modeling for multiple die and multi-chip packages," in *Proceedings of the 21st Semiconductor Thermal Measurement and Management (SEMITHERM) Symposium, San Jose, CA*, 2005, pp. 327–334.

[92] B. Joiner and V. Adams, "Measurement and simulation of junction to board thermal resistance and its application in thermal modeling," in *Proceedings of the 15th Semiconductor Thermal Measurement and Management (SEMITHERM) Symposium, San Diego, CA*, 1999, p. 212220.

[93] S. Shidore, V. Adams, and T. Lee, "A study of compact thermal model topologies in CFD for a flip chip plastic ball grid array package," *IEEE transactions on Components, Packaging and Manufacturing Technology (CPMT)*, vol. 24, no. 2, pp. 191–198, 2001.

[94] W. Krueger and A. Bar-Cohen, "Thermal characterization of a PLCC - expanded R_{jc} methodology," *IEEE Transactions on Components, Hybrids, Manufacturing Technology*, vol. 15, no. 5, pp. 691–698, 1992.

[95] A. Bar-Cohen and W. Krueger, "Thermal characterization of chip packages - evolutionary development of compact models," in *Proceedings of the 13th Semiconductor*

Thermal Measurement and Management (SEMITHERM) Symposium, Austin, TX, 1997, pp. 180–197.

[96] J. Le-Jannou and Y. Huon, "Representation of thermal behaviour of electronic components for the creation of a databank," *IEEE Transactions on Components, Hybrids, Manufacturing Technology (CHMT)*, vol. 14, pp. 366–373, 1991.

[97] C. Lasance, D. den Hertog, and P. Stehouwer, "Creation and evaluation of compact models for thermal characterization using dedicated optimization software," in *Proceedings of the 15th Semiconductor Thermal Measurement and Management (SEMITHERM) Symposium, San Diego, CA, USA*, 1999, p. 189200.

[98] S. Shidore, "Design, test & measurement: Compact thermal modeling in electronics design," *Electronic cooling. Online article: http://www.electronics-cooling.com/2007/05/compact-thermal-modeling-in-electronics-design/*, 2007.

[99] Y. Assouad, F. Gatfosse, and T. Gautier, "Thermal characterization and modelling of EFD transformer, applying DELPHI methodology," in *Proceedings of the EUROTHERM Seminar no. 58,Thermal Management of Electronic Systems, Nantes, France*, 1997, pp. 238–245.

[100] J. He, V. Mehrotra, and M. Shaw, "Thermal design and measurements of igbt power modules: Transient and steady state," in *Proceedings of the IEEE Industry Aplications Society conference, Phoenix, Arizona*, 1999, pp. 1440–1444.

[101] N. Shammas, M. Rodriguez, and F. Masana, "A simple method for evaluating the transient thermal response of semiconductor devices," *Microelectronics Reliability*, vol. 42, pp. 109–117, 2002.

[102] B. Siegel, "Measuring thermal resistance is the key to a cool semiconductor," *Electronics*, pp. 121–126, 1978.

[103] U. Drofenik, D. Cottet, A. Musing, J. Meyer, *et al.*, "Computationally efficient integration of complex thermal multi-chip power module models into circuit simulators," in *Proceedings of the 4th Power Conversion Conference (PCC)*, 2007, pp. CD–ROM, ISBN: 1–4244–0844–X.

[104] Y. Gerstenmaier and G. Wachutka, "Efficient calculation of transient temperature fields responding to fast changing heat sources over long duration in power electronic systems," *IEEE Transactions on Components and Packaging Technologies*, vol. 27, no. 1, pp. 104–111, 2004.

[105] V. Szekely and T. V. Bien, "Fine structure of heat flow path in semiconductor devices: A measurement and identification method," *Solid-State Electronics*, vol. 31, no. 9, pp. 1363–1368, 1998.

[106] P. Johns and G. Butler, "The consistency and accuracy of the TLM method for diffusion and its relationship to existing methods," *International Journal for Numerical Methods in Engineering*, vol. 19, pp. 1549–1554, 1983.

[107] R. Hocine, M. Boudghene-Stambouli, and A. Saidane, "A three-dimensional TLM simulation method for thermal effect in high power insulated gate bipolar transistors," *Microelectronic Engineering*, vol. 65, pp. 293–306, 2003.

[108] R. Hocine, S. Pulko, M. Boudghene-Stambouli, and A. Saidane, "TLM method for thermal investigation of IGBT modules in PWM mode," *Microelectronis Engineering*, vol. 86, pp. 2053–2062, 2009.

[109] F. Masana, "A new approach to the dynamic thermal modelling of semiconductor packages," *Microelectronics Reliability*, vol. 41, pp. 901–912, 2001.

[110] F. Masana, "A straightforward analytical method for extraction of semiconductor device transient thermal parameters," *Microelectronics Reliability*, vol. 47, pp. 2122–2128, 2007.

[111] K. Murthy and R. Bedford, "Transformation between Foster and Cauer equivalent networks," *IEEE Transactions on Circuits and Systems*, vol. 25, no. 4, pp. 238–239, 1978.

[112] M. D. Greenberg, *Advanced Engineering Mathematics*, 2nd ed. Upper Saddle River, NJ, USA: Prentice-Hall, 1998.

[113] J. Koh, G. Noebauer, and C. An, "Generation of the electrothermal Cauer RC model using a recursive method," in *Proceedings of the 31st European Solid-State Device Research Conference*, 2001, pp. 495–498.

[114] J. W. Sofia, "Analysis of thermal transient data with synthesized dynamic models for semiconductor devices," *IEEE Transactions on Components, Packaging, and Manufacturing Technology (CPMT) - Part A*, vol. 18, no. 1, pp. 39–47, 1995.

[115] J. G. Korvink and E. B. Rudnyi, "Computer-aided engineering of electro-thermal mst devices: moving from device to system simulation," in *Proceedings of the 4th international conference on thermal and mechanical simulation and experiments in micro-electronics and micro-systems (EuroSimE), Aix-en-Provence, France, CD-ROM version: ISBN 0-7803-7056-2*, no. 6, 2003.

[116] A. Augustin and T. Hauck, "Transient thermal compact models for circuit simulation," in *Proceedings of the 24th CADFEM meeting, International Congress on FEM Technology with 2006 German ANSYS Conference, Stuttgart, Germany*, no. 2.5.3, 2006.

[117] S. X.-D. Tan and L. He, *Advanced Model Order Reduction Techniques in VLS Design.* Cambridge: Cambridge University press, 2007.

[118] R. Freund, "Krylov subspace methods for reduced order modelling in circuit simulation," *Journal of Computational and Applied Mathematics*, vol. 123, no. 1-2, pp. 395–421, 2000.

[119] P. Evans and M. Johnson, "Fast extraction of dynamic thermal impedance for multichip power modules," in *Proceedings of the 6th International Conference on Integrated Power Electronics Systems (CIPS), Nuremberg, Germany*, vol. P 07, pp. 1–6.

[120] L. Codecasa, D. D'Amore, and P. Maffezzoni, "An Arnoldi based thermal network reduction method for electro-thermal analysis," *IEEE Transactions on Componenet Packaging Technologies*, vol. 26, no. 1, pp. 186–192, 2003.

[121] Z. Bai, R. Stone, and W. Smith, "Error bound for reduced system model by Pade approximation via the Lanczos process," *IEEE Transactions on Computer aided design of Integrated circuits and systems*, vol. 18, no. 2, pp. 133–141, 1999.

[122] G. Obinata and B. Anderson, *Model Reduction for Control System Design.* New York: Springer-Verlag, 2004.

[123] R. Guyan, "Reduction of stiffness and mass matrices," *The American Institute of Aeronautics and Astronautics (AIAA) Journal*, vol. 3, no. 2, p. 380, 1965.

[124] Z.-Q. Qu, *Model Order Reduction Techniques with applications in finite element analysis.* London: Springer-Verlag, 2004.

[125] ANSYS. http://www.ansys.com/: ANSYS Inc.

[126] E. Rudnyi, J. Lienemann, A. Greiner, and J. G. Korvink, "mor4ansys: Generating compact models directly from ANSYS models," in *technical Proceedings of the Nanotechnology Conference and Trade Show (Nanotech), Boston, MA, USA*, 2004.

[127] T. Bechtold, E. Rudnyi, and J. Korvink, "Automatic generation of compact electrothermal models for semiconductor devices," *IEICE Transactions on Electronics*, vol. E86C, no. 3, pp. 459–465, 2003.

[128] M. N. Sabry and S. Hossam, "Compact thermal models: A global approach," in *1st Theta Workshop, Cairo, Egypt*, 2007, pp. 51–57.

[129] G. Strang and G. Fix, *An Analysis of The Finite Element Method.* Englewood, NJ, USA: Prentice Hall, 1973.

[130] J. Korvink and O. Paul, *MEMS a practical guide to design, analysis and applications.* Norwich, NY, USA: William Andrew Publishing.

[131] L. Zhaohui, "A thermal model for IGBT modules and its implementation in a real time simulator," *PhD Thesis*, 2002.

[132] Z. Luo, H. Ahn, and M. El-Nokali, "A thermal model for insulated gate bipolar transistor module," *IEEE Transactions on Power Electronics*, vol. 19, no. 4, pp. 902–907, 2004.

[133] S. Ryu, H. Ahn, D. Han, and M. El-Nokali, "Thermal analysis of PT IGBT by using ANSYS," in *Proceedings of the 7th International conference on Power electronics, Daegu, Korea*, no. PA2, 2007, pp. 59–61.

[134] R. LeVeque, *Finite Volume Methods for Hyperbolic Problems*, 1st ed. Cambridge, UK: Cambridge University Press, 2002, p. 5.

[135] *Mentor Graphics Corporation.* Wilsonville, OR, USA: Online: www.mentor.com/products/mechanical/multimedia/flotherm, 2008.

[136] Z. Zhou, P. Holland, and P. Igic, "Compact thermal model of a three-phase IGBT inverter power module," in *Proceedings of the 26th international conference on microelectronics (MIEL), NI, SERBIA*, 2008, pp. 167–170.

[137] E. Cho, E. Tan, and Y.-T. Lin, "Thermal characterization of cavity-down tbga package with flotherm simulation," in *Proceedings of the 16th IEEE Semiconductor Thermal Measurement and Management (SEMITHERM) Symposium, San Jose, CA, USA*, 2008, pp. 68–75.

[138] I. Swan, A. Bryant, and P. Mawby, "Fast thermal models for power device packaging," in *Conference Recordings of the IEEE Industry Applications Society (IAS) Annual Meeting, Edmonton, Canada*, vol. 41, 2008, pp. 1–8.

[139] R. Courant, K. Friedrichs, and H. Lewy, "Uber die partiellen differenzengleichungen der mathematischen physik," *Annals of Mathematics*, vol. 100, pp. 32–74, 1928.

[140] F. Incropera and D. Dewitt, *Fundamentals of Heat and Mass Transfer*, 5th ed. New York, NY, USA: John Wiley & sons, 2002.

[141] G. Forsythe and W. Wasow, *Finite-Difference Methods for Partial Differential Equations*. New York, NY, USA: Wiley, 1960.

[142] Z. Khatir and S. Lefebvre, "Thermal analysis of power cycling effects on high power IGBT modules by the boundary element method," in *Proceedings of the 17th IEEE Semiconductor Thermal Measurement and Management (SEMITHERM) Symposium, San Jose, CA*, 2001, pp. 27–34.

[143] S. Carubelli and Z. Khatir, "Experimental validation of a thermal modelling method dedicated to multichip power modules in operating conditions," *Microelectronics Journal*, vol. 34, no. 12, pp. 1143–1151, 2003.

[144] I. Guven, C. Chan, and E. Madenci, "Transient two-dimensionnal thermal analysis of electronic packages by the boundary element method," *IEEE Transactions on advanced packaging*, vol. 22, no. 3, pp. 476–486, 1999.

[145] N. Rinaldi, "Generalized image method with application to the thermal modeling of power devices and circuits," *IEEE Transactions on electron devices*, vol. 49, no. 4, pp. 679–686, 2002.

[146] A. Haji-Sheikh and J. Beck, "Temperature solution in multi-dimensional multi-layer bodies," *International Journal of Heat and Mass Transfer*, vol. 45, no. 9, pp. 1865–1877, 2002.

[147] J. Beck, K. Cole, A. Haji-Sheikh, and B. Litkouhi, *Heat conduction using Green's functions*. Hemisphere Publishing Corporation, Washington, DC, USA, 1992.

[148] M. Janicki, G. Mey, and A. Napieralski, "Thermal analysis of layered electronic

circuits with Green's functions," *Microelectronics Journal*, vol. 38, no. 2, pp. 177–184, 2007.

[149] A. Haji-Sheikh, "Peak temperature in high-power chips," *IEEE Transactions on Electron Devices*, vol. 37, no. 4, pp. 902–907, 1990.

[150] Y. Gerstenmaier, A. Castellazzi, and G. Wachutka, "Electrothermal simulation of multi-chip-modules with novel transient thermal model and time-dependent boundary conditions," *IEEE Transactions on Power Electronics*, vol. 21, no. 1, pp. 45–55.

[151] R. Lindsted and R. Surty, "Steady state junction temperatures of semiconductor chips," *IEEE Transactions on Electron Devices*, vol. 191, pp. 41–44, 1972.

[152] A. G. Kokkas, "Thermal analysis of multiple-layer structures," *IEEE Transactions on Electron Devices*, vol. 21, no. 11, pp. 674–681, 1974.

[153] P. Tounsi, J.-M. Dorkel, P. Leturcq, P. Vales, *et al.*, "3D thermal modelling for electronic devices based on the two-port network theory," in *the 2nd THERMINIC Workshop, Budapest, Hungary*, 1996, pp. 27–34.

[154] V. Koval and I. Farmaga, "A complete thermal simulator of electronic systems," in *the 31st Design Automation Conference (DAC), San Diego, CA, USA*, 1994, pp. 570–575.

[155] V. Szekely, A. Poppe, M. Rencz, M. Rosental, *et al.*, "THERMAN: a thermal simulation tool for IC chips, microstructures and PW boards," *Microelectronics Reliability*, vol. 40, pp. 517–524, 2000.

[156] P. Lall, M. Pecht, and E. B. Hakim, *Influence of temperature on microelectronics and system reliability*. CRC Press New York, USA, 1997.

[157] J. Parry, J. Rantala, and C. Lasance, "Enhance electronic system reliability- challenges for temperature prediction," *IEEE Transactions on Components and Packaging Technologies*, vol. 25, no. 4, pp. 533–538, 2002.

[158] M. Pecht, "Why the traditional reliability prediction models do not work is there an alternative?" *Electronic cooling*, vol. 2, no. 1, pp. 10–12, 1996.

[159] B. Chambers, T. Lee, and W. Blood, "Steady state and transient thermal analysis of chip scale packages," *The Journal of Electronics Manufacturing*, vol. 9, no. 2, pp. 131–139, 1999.

[160] R. Li and E. Larson, "An approach to thermal analysis of PCB with components having cyclic electrical loading," in *the 7th Intersociety Conference on Thermal and Thermomechanical Phenomena in Electronic Systems (ITHERM), Las Vegas, NV, USA*, 2000.

[161] Y. S. Ju and K. E. Goodson, "Thermal mapping of interconnects subjected to brief electrical stresses," *IEEE Electron Device Letters*, vol. 18, no. 11, pp. 512–514, 1997.

[162] L. Weinberg, *Network analysis and synthesis*, 1st ed. New York, NY: McGraw-Hill, 1962.

[163] A. Hefner and D. Blackburn, "Thermal component models for electrothermal network simulation," *IEEE Transactions on Components, Packaging, and Manufacturing Technology (CPMT)*, vol. 17, no. 3, pp. 413–423, 1994.

[164] A.Ammous, S.Ghedira, and B. Allard, "Choosing a thermal model for electrothermal simulation of power semiconductor devices," *IEEE Transactions on Power Electronics*, vol. 14, no. 2, pp. 300–307, 1999.

[165] A. Lakhsasi and Y. Hamri, "Transient thermal analysis of fast switching devices by partially coupled FEM method," in *Conference Recordings of the Canadian Conference on Electrical and Computer Engineering (CCECE), Ottawa, Canada*, 2006, pp. 1098–1103.

[166] M. Marz and P. Nance, in *PCIM Europe Magazine*, vol. 2, pp. 20–27.

[167] C. Lasance, in *Proceedings of the 19th IEEE Semiconductor Thermal Measurement and Management (SEMITHERM) Symposium*, pp. 290–299.

[168] A. Augustin, T. Hauck, B. Maj, J. Czernohorsky, *et al.*, "Model reduction for power electronics systems with multiple heat sources," in *Proceedings of the 12th International Workshop on Thermal Investigations of ICs and Systems (THERMINIC), Nice, France*, 2006, pp. 113–117.

[169] U. Drofenik, D. Cottet, A. Müsing, J.-M. Meyer, *et al.*, "Modelling the thermal coupling between internal power semiconductor dies of a water-cooled 3300v/1200a hipak igbt module," in *in proceedings of the Conference for Power Electronics, Intelligent Motion, Power Quality (PCIM), Nuremberg, Germany*, 2007.

[170] B. Smith, T. Brunschwiler, and B. Michel, "Utility of transient testing to characterize thermal interface materials," in *the proceedings of the 13th International Workshop on Thermal Investigations of ICs and Systems (THERMINIC), Budapest, Hungary*, 2007, pp. 6–11.

[171] A. Hamidi, G. Coquery, R. Lallmand, P. Vales, *et al.*, "Temperature measurements and thermal modeling of high power IGBT multichip modules for reliability investigations in traction applications," *Microelectronics Reliability*, vol. 38, pp. 1353–1359, 1998.

[172] L. Shampine and M. Reichelt, "The matlab ode suite," *SIAM Journal of Scientific Computing*, vol. 18, no. 1:1, 1997.

[173] L. Shampine and C. Gear, "A user's view of solving stiff ordinary differential equations," *SIAM Review*, vol. 21, no. 1:1, 1979.

[174] M. Janicki, A. Napieralski, D. Fedasyuk, and D. Petrov, "Thermal modelling of hybrid circuits: simulation method comparison," *Microelectronics Reliability*, vol. 40, pp. 541–546, 2000.

[175] P. Letureq, J.-L. Debrie, and M. Berraies, "A distributed model of IGBTs for circuit simulation." in *proceedings of the European Conference on Power Electronics and Applications (EPE), Trondheim, Norway*, vol. 1, 1997, pp. 494–501.

[176] T. Hemingway, *Electronic designer's handbook: a practical guide to circuit design*, 3rd ed. Blue Ridge Summit, PA, USA: Tab books inc., 1979.

[177] K. Warwick, *An introduction to control systems*, 2nd ed. World Scientific Publishing, 1996, vol. 8 of Advanced series in electrical and computer engineering.

[178] M. Ayadi, S. Abid, and A. Ammous, "Thermal modelling of hybrid power modules," in *Proceedings of the 11th International Workshop on Thermal Investigation of ICs and Systems (THERMINIC), Belgirate, Italy*, 2005, pp. 157–163.

[179] M. Rencz, V. Szekely, A. Pahi, and A. Poppe, "An alternative method for electro-thermal circuit simulation," in *Proceedings of the Southwest Symposium on Mixed-Signal Design (SSMSD), Tuscon, AZ, USA*, 1999, pp. 117–122.

[180] R. Schact, M. Kasper, and H. Reichl, "Macro modelling for transient simulation of coupled electro-thermal problems for an IGBT module," in *Proceedings of the*

5th International Workshop on Thermal Investigation of ICs and Systems (THERMINIC), Rome, Italy, 1999, pp. 121–124.

[181] Y. Gerstenmairer and G. Wachutka, "A new procedure for the calculation of temperature development in electronic systems," in *Proceedings of the 8th European Conference on Power Electronics and Applications (EPE), Lausanne, Switzerland. CD-ROM, ISBN:90-75815-04-2*, 1999.

[182] T. Franke, G. Zaiser, J. Otto, M. Honsberg-Riedl, *et al.*, "Current and temperature distribution in multi-chip modules under inverter operation," in *Proceedings of the 8th European Conference on Power Electronics and Applications (EPE), Lausanne, Switzerland*, 1999.

[183] A. Bryant, N.-A. Parker-Allotey, and P. Palmer, "The use of condition maps in the design and testing of power electronic circuits and devices." *IEEE Transactions on Industry Applications*, vol. 43, no. 4, pp. 1–8, 2007.

[184] FLIR A20 Infrared Camera datasheet: Online: http://www.movimed.com/files/Flir/A20M%20Datasheet.pdf.

[185] R. Bredtmann, K. Olesen, F. Osterwald and R. Eisele, "Substrate free molded power module," in *Proceedings of the Power Conversion Intelligent Motion conference (PCIM Europe), Nuremburg, Germany.*, 2008, pp. 494–499.

[186] R. Bredtmann, K. Olesen, F. Osterwald, and R. Eisele, "Options for electric power steering modules; a reliability challenge," in *Proceedings of the 2nd International Automotive Power Electronics Conference (APE), Paris, France.*, 2007.

[187] R. Bayerer, "Advanced packaging yields higher performance and reliability in power electronics," *Microelectronics Reliability*, vol. 50, no. 9-11, pp. 1715–1719, 2010.

[188] C. C. Lee, Y. J. Min, and A. L. Palisoc, "A general integration algorithm for the inverse Fourier transform of four-layer infinite plate structures," *IEEE Transactions on Components, Hybrids, and Manufacturing Technology*, vol. 12, no. 4, pp. 710–716, 1989.

[189] M. Pesare, A. Giorgio, and A. G. Perri, "Optimized electrothermal design of integrated devices through the solution to the non-linear 3-D heat flow equation," *Microelectronics Journal*, vol. 32, pp. 823–831, 2001.

Appendix

A Appendix 1 - Fourier series solution (DC terms)

This appendix links in with chapter 5. To have stated all the working of the Fourier series solution for the 1-D, 2-D and 3-D case would have been too exhaustive to include in the main body of this thesis.

A.1 1-D Fourier series solution DC term

The workings for the 1-D Fourier series solution DC term follows:

When $k = 0$, the following expression represents I_1:

$$I_1 = \alpha \int_{z_1}^{z_2} \left(\frac{\partial^2 T(z,t)}{\partial z^2} \right) dz. \tag{A.1}$$

Applying integration gives:

$$I_1 = \alpha \left[\left(\frac{\partial T(t)}{\partial z} \Big|_{z_2} \right) - \left(\frac{\partial T(t)}{\partial z} \Big|_{z_1} \right) \right]. \tag{A.2}$$

When k=*0*, I_2 is represented by:

$$I_2 = \int_{z_1}^{z_2} \frac{\partial T(z,t)}{\partial t} dz. \tag{A.3}$$

Substitution of the Fourier cosine series definition produces the following expression for I_2:

$$I_2 = (z_2 - z_1) \frac{dT_0(t)}{dt}. \tag{A.4}$$

Equating I_1 and I_2 leads to the expression:

$$\frac{dT_0(t)}{dt} = \frac{\alpha}{(z_2 - z_1)} \left[\frac{\partial T(t)}{\partial z}\bigg|_{z_2} - \frac{\partial T(t)}{\partial z}\bigg|_{z_1} \right]. \tag{A.5}$$

A.2 2-D Fourier series solution DC terms

The workings for 2-D Fourier series solution DC terms follows:

When *k=0*, *m=0*:

$$I_1 = \alpha \int_{x_1}^{x_2} \left[\int_{z_1}^{z_2} \frac{\partial^2 T(z,x,t)}{\partial z^2} dz \right] dx + \alpha \int_{z_1}^{z_2} \left[\int_{x_1}^{x_2} \frac{\partial^2 T(z,x,t)}{\partial x^2} dx \right] dz. \tag{A.6}$$

$$I_1 = \alpha \int_{x_1}^{x_2} \left[\frac{\partial T(x,t)}{\partial z}\bigg|_{z_2} - \frac{\partial T(x,t)}{\partial z}\bigg|_{z_1} \right] dx + \alpha \int_{z_1}^{z_2} \left[\frac{\partial T(z,t)}{\partial x}\bigg|_{x_2} - \frac{\partial T(z,t)}{\partial x}\bigg|_{x_1} \right] dz \tag{A.7}$$

Substitute in $\frac{\partial T(z,t)}{\partial z}\Big|_{x_2} = 0$ and $\frac{\partial T(z,t)}{\partial z}\Big|_{x_1} = 0$. Then represent $\frac{\partial T(x,t)}{\partial z}\Big|_{z_2}$ and $\frac{\partial T(x,t)}{\partial z}\Big|_{z_1}$ in Fourier series form, which leads to:

$$I_1 = \frac{(x_2 - x_1)}{\alpha} \left[\frac{\partial T_0(t)}{\partial z}\bigg|_{z_2} - \frac{\partial T_0(t)}{\partial z}\bigg|_{z_1} \right]. \tag{A.8}$$

$$I_2 = \int_{x_1}^{x_2}\int_{z_1}^{z_2} \frac{\partial T(x,z,t)}{\partial t} dxdz. \tag{A.9}$$

Using the relationship:

$$(x_2{-}x_1)(z_2{-}\mathrm{z}_1)\frac{dT_{00}(t)}{dt} = \int_{x_1}^{x_2}\int_{z_1}^{z_2} \frac{\partial T(x,z,t)}{\partial t} dxdz, \tag{A.10}$$

and then equating I_2 to I_1 leads to the expression:

$$\frac{dT_{00}(t)}{dt} = \frac{\alpha}{(z_2{-}z_1)}\left[\left.\frac{\partial T_o(t)}{\partial z}\right|_{z_2} - \left.\frac{\partial T_o(t)}{\partial z}\right|_{z_1}\right]. \tag{A.11}$$

When *k=0, m≥1*:

$$\begin{aligned} I_1 &= \alpha \int_{z_1}^{z_2}\int_{x_1}^{x_2} \frac{\partial^2 T(x,z,t)}{\partial x^2} \cos\left(\frac{\pi m(x-x_1)}{(x_2-x_1)}\right) dxdz \\ &\quad +\alpha \int_{z_1}^{z_2}\int_{x_1}^{x_2} \frac{\partial^2 T(x,z,t)}{\partial z^2} \cos\left(\frac{\pi m(x-x_1)}{(x_2-x_1)}\right) dxdz. \end{aligned} \tag{A.12}$$

$$I_1 = I_{1x} + I_{1y}. \tag{A.13}$$

$$I_{1x} = \alpha \int_{z_1}^{z_2} \left[\int_{x_1}^{x_2} \frac{\partial^2 T(x,y,t)}{\partial x^2} \cos\left(\frac{\pi m(x-x_1)}{(x_2-x_1)} \right) dx \right] dz. \tag{A.14}$$

$$\begin{aligned} \int_{x_1}^{x_2} \frac{\partial^2 T(x,z,t)}{\partial x^2} \cos\left(\frac{\pi m(x-x_1)}{(x_2-x_1)} \right) dx &= \left[\frac{\partial T(z,t)}{\partial x}\bigg|_{x_2} \cos(\pi m) - \frac{\partial T(z,t)}{\partial x}\bigg|_{x_1} \right] \\ &\quad - \left(\frac{\pi m}{(x_2-x_1)} \right)^2 \int_{x_1}^{x_2} T(x,z,t) \cos\left(\frac{\pi m(x-x_1)}{(x_2-x_1)} \right) dx, \end{aligned} \tag{A.15}$$

$\frac{\partial T(z,t)}{\partial x}\Big|_{x_2} = 0$ and $\frac{\partial T(z,t)}{\partial x}\Big|_{x_1} = 0$, and using the relationship:

$$\int_{z_1}^{z_2} \int_{x_1}^{x_2} T(x,z,t) \cos\left(\frac{\pi m(x-x_1)}{(x_2-x_1)} \right) dx dz = \frac{(x_2-x_1)(z_2-z_1)}{2} \frac{dT_{0m}(t)}{dt}, \tag{A.16}$$

leads to:

$$I_{1x} = -\frac{\alpha \pi^2 m^2 (z_2-z_1)}{2(x_2-x_1)} \frac{dT_{0m}(t)}{dt}. \tag{A.17}$$

$$I_{1y} = \alpha \int_{z_1}^{z_2} \frac{\partial^2 T(x,z,t)}{\partial z^2} dz \int_{x_1}^{x_2} \cos\left(\frac{\pi m(x-x_1)}{(x_2-x_1)} \right) dx. \tag{A.18}$$

$$I_{1y} = \alpha \int_{x_1}^{x_2} \frac{\partial T(x,t)}{\partial z}\bigg|_{z_2} \cos\frac{\pi m(x-x_1)}{(x_2-x_1)} dx - \alpha \int_{x_1}^{x_2} \frac{\partial T(x,t)}{\partial z}\bigg|_{z_1} \cos\frac{\pi m(x-x_1)}{(x_2-x_1)} dx. \tag{A.19}$$

Therefore:

$$I_1 = \alpha\frac{(x_2-x_1)}{2}\left[\left.\frac{\partial T_m(t)}{\partial t}\right|_{z_2} - \left.\frac{\partial T_m(t)}{\partial t}\right|_{z_1}\right] - \alpha\frac{(z_2-z_1)(x_2-x_1)}{2}\left(\frac{\pi m}{(x_2-x_1)}\right)^2 T_{0m}(t) \quad \text{(A.20)}$$

$$I_2 = \int_{y_1}^{y_2}\int_{x_1}^{x_2}\frac{\partial T(x,z,t)}{\partial t}\cos\left(\frac{\pi m(x-x_1)}{(x_2-x_1)}\right)dxdz. \quad \text{(A.21)}$$

Substituting in:

$$\int_{z_1}^{z_2}\int_{x_1}^{x_2}\frac{\partial T(x,z,t)}{\partial t}\cos\left(\frac{\pi m(x-x_1)}{(x_2-x_1)}\right)dxdz = \frac{(x_2-x_1)(z_2-z_1)}{2}\frac{dT_{0m}(t)}{dt}, \quad \text{(A.22)}$$

results in the following expression:

$$I_2 = \frac{(x_2-x_1)(z_2-z_1)}{2}\frac{dT_{0m}(t)}{dt}. \quad \text{(A.23)}$$

Equating I_1 and I_2, and rearranging, leads to:

$$\frac{dT_{0m}(t)}{dt} = \frac{\alpha}{(z_2-z_1)}\left[\left.\frac{\partial T_m(t)}{\partial t}\right|_{z_2} - \left.\frac{\partial T_m(t)}{\partial t}\right|_{z_1}\right] - T_{0m}(t)\left[\alpha\pi^2\left(\frac{m^2}{(x_2-x_1)^2}\right)\right]. \quad \text{(A.24)}$$

When $k \geq 1$, $m=0$:

$$I_1 = \alpha \int_{z_1}^{z_2} \int_{x_1}^{x_2} \left(\frac{\partial^2 T(x,z,t)}{\partial x^2} + \frac{\partial^2 T(x,z,t)}{\partial z^2} \right) \cos\left(\frac{\pi k (z - z_1)}{(z_2 - z_1)} \right) dx dz. \tag{A.25}$$

$$\begin{aligned} I_1 = \alpha \int_{z_1}^{z_2} \int_{x_1}^{x_2} \frac{\partial^2 T(x,z,t)}{\partial x^2} \cos\left(\frac{\pi k (z - z_1)}{(z_2 - z_1)} \right) dx dz \\ + \alpha \int_{z_1}^{z_2} \int_{x_1}^{x_2} \frac{\partial^2 T(x,z,t)}{\partial z^2} \cos\left(\frac{\pi k (z - z_1)}{(z_2 - z_1)} \right) dx dz \end{aligned} \tag{A.26}$$

$$I_1 = I_{1x} + I_{1y}, \tag{A.27}$$

$$I_{1x} = \alpha \int_{x_1}^{x_2} \left[\int_{z_1}^{z_2} \frac{\partial^2 T(x,z,t)}{\partial z^2} \cos\left(\frac{\pi k (z - z_1)}{(z_2 - z_1)} \right) dz \right] dx. \tag{A.28}$$

$$\begin{aligned} \int_{z_1}^{z_2} \frac{\partial^2 T(x,z,t)}{\partial z^2} \cos\left(\frac{\pi k (z - z_1)}{(z_2 - z_1)} \right) dz = \left[\frac{\partial T(x,t)}{\partial z}\bigg|_{z_2} \cos(\pi k) - \frac{\partial T(x,t)}{\partial z}\bigg|_{z_1} \right] \\ - \left(\frac{\pi k}{(z_2 - z_1)} \right)^2 \int_{z_1}^{z_2} T(x,z,t) \cos\left(\frac{\pi k (z - z_1)}{(z_2 - z_1)} \right) dz \end{aligned} \tag{A.29}$$

Substituting leads to:

$$I_{1x} = \alpha (-1)^k \int_{x_1}^{x_2} \frac{\partial T(x,t)}{\partial x}\bigg|_{z_2} dx - \int_{x_1}^{x_2} \frac{\partial T(x,t)}{\partial x}\bigg|_{z_1} dx \tag{A.30}$$

$$- \left(\frac{\pi k}{(z_2-z_1)}\right)^2 \int_{z_1}^{z_2}\int_{x_1}^{x_2} T(x,z,t)\cos\left(\frac{\pi k(z-z_1)}{(z_2-z_1)}\right)dxdz$$

$$\frac{\partial T_{k,x}(t)}{\partial x} = \frac{1}{(z_2-z_1)}\int_{z_1}^{z_2}\left.\frac{\partial T(x,t)}{\partial x}\right|_z dz \tag{A.31}$$

$$I_{1x} = \alpha(z_2-z_1)\left[\left.\frac{\partial T_m(t)}{\partial z}\right|_{z_2}(-1)^k - \left.\frac{\partial T_m(t)}{\partial z}\right|_{z_1}\right] - \left(\frac{\pi k}{(z_2-z_1)}\right)^2 \frac{(x_2-x_1)(z_2-z_1)}{2} T_{k0}(t). \tag{A.32}$$

$$I_{1y} = \alpha\frac{\partial^2 T(x,z,t)}{\partial z^2}\int_{z_1}^{z_2}\int_{x_1}^{x_2}\cos\left(\frac{\pi k(z-z_1)}{(z_2-z_1)}\right)dxdz. \tag{A.33}$$

The following expression:

$$\int_{z_1}^{z_2}\cos\left(\frac{\pi k(z-z_1)}{(z_2-z_1)}\right)dz = \frac{(z_2-z_1)}{k\pi}\left[\sin\left(\frac{\pi k(z-z_1)}{(z_2-z_1)}\right)\right]_{z_1}^{z_2}, \tag{A.34}$$

results in:

$$I_{1y} = 0. \tag{A.35}$$

$$I_2 = \int_{z_1}^{z_2}\int_{x_1}^{x_2}\frac{\partial T(z,x,t)}{\partial x}\cos\left(\frac{\pi k(z-z_1)}{(z_2-z_1)}\right)dzdx, \tag{A.36}$$

which by this stage is a standard result:

$$I_2 = \frac{(x_2-x_1)(z_2-z_1)}{2}\frac{dT_{k0}(t)}{dt}. \tag{A.37}$$

Substitution leads to the following expression:

$$\frac{dT_{k0}(t)}{dt}=\frac{2\alpha}{(z_2-z_1)}\left[\left.\frac{\partial T_0(t)}{\partial z}\right|_{z_2}(-1)^k\left.\frac{\partial T_0(t)}{\partial z}\right|_{z_1}\right]-T_{k0}(t)\left[\alpha\pi^2\left(\frac{k^2}{(z_2-z_1)^2}\right)\right]. \tag{A.38}$$

A.3 3-D Fourier series solution DC terms

The workings for 3-D Fourier series solution DC terms follows:

When *m=0*, *n=0*, *k=0*:

$$I_1 = \alpha\int_{x_1}^{x_2}\int_{y_1}^{y_2}\int_{z_1}^{z_2}\left(\frac{\partial^2 T(x,y,z,t)}{\partial x^2}+\frac{\partial^2 T(x,y,z,t)}{\partial y^2}+\frac{\partial^2 T(x,y,z,t)}{\partial z^2}\right)dxdydz. \tag{A.39}$$

$$I_1=I_{1x}+I_{1y}+I_{1z}. \tag{A.40}$$

$$I_{1x} = \alpha\int_{z_1}^{z_2}\int_{y_1}^{y_2}\left[\int_{x_1}^{x_2}\frac{\partial^2 T(x,y,z,t)}{\partial x^2}dx\right]dydz. \tag{A.41}$$

$$I_{1x} = \alpha\int_{z_1}^{z_2}\int_{y_1}^{y_2}\left[\left.\frac{\partial T(y,z,t)}{\partial x}\right|_{x_2}-\left.\frac{\partial T(y,z,t)}{\partial x}\right|_{x_1}\right]dydz. \tag{A.42}$$

$\partial T(y,z,t)/\partial x\big|_{x_2} = 0$ and $\partial T(y,z,t)/\partial x\big|_{x_1} = 0$ and so:

$$I_{1x} = 0 \tag{A.43}$$

$$I_{1y} = \alpha \int_{z_1}^{z_2} \int_{x_1}^{x_2} \left[\int_{y_1}^{y_2} \frac{\partial^2 T(x,y,z,t)}{\partial y^2} dy \right] dxdz \tag{A.44}$$

$$I_{1y} = \alpha \int_{z_1}^{z_2} \int_{x_1}^{x_2} \left[\frac{\partial T(x,z,t)}{\partial y}\bigg|_{y_2} - \frac{\partial T(x,z,t)}{\partial y}\bigg|_{y_1} \right] dxdz. \tag{A.45}$$

$\partial T(x,z,t)/\partial y\big|_{y_2} = 0$ and $\partial T(x,z,t)/\partial y\big|_{y_1} = 0$ and so:

$$I_{1y} = 0 \tag{A.46}$$

$$I_{1z} = \alpha \int_{x_1}^{x_2} \int_{y_1}^{y_2} \left[\int_{z_1}^{z_2} \frac{\partial^2 T(x,y,z,t)}{\partial z^2} dz \right] dydx \tag{A.47}$$

$$I_{1z} = \alpha(x_2 - x_1)(y_2 - y_1) \frac{\partial T_{mn}(t)}{\partial z}\bigg|_{z_2} - \alpha(x_2 - x_1)(y_2 - y_1) \frac{\partial T_{mn}(t)}{\partial z}\bigg|_{z_1} \tag{A.48}$$

$$I_2 = \int_{x_1}^{x_2} \int_{y_1}^{y_2} \int_{z_1}^{z_2} \frac{\partial T(x,y,z,t)}{\partial t} dxdydz. \tag{A.49}$$

Substituting:

$$\int_{x_1}^{x_2}\int_{y_1}^{y_2}\int_{z_1}^{z_2}\frac{\partial T(x,y,z,t)}{\partial t}dxdydz=(z_2{-}z_1)(y_2{-}y_1)(x_2{-}x_1)\frac{dT_{000}(t)}{dt}. \tag{A.50}$$

$$I_2=(z_2{-}z_1)(y_2{-}y_1)(x_2{-}x_1)\frac{dT_{000}(t)}{dt}. \tag{A.51}$$

Equating I_2 and I_1 yields:

$$\begin{aligned}\alpha(x_2{-}x_1)(y_2{-}y_1)\left.\frac{\partial T(x,y,t)}{\partial z}\right|_{z_2}-\alpha(x_2{-}x_1)(y_2{-}y_1)\left.\frac{\partial T(x,y,t)}{\partial z}\right|_{z_1}\\ =0+(z_2{-}z_1)(y_2{-}y_1)(x_2{-}x_1)\frac{dT_{000}(t)}{dt}.\end{aligned} \tag{A.52}$$

This results in the following ODE (for $m=0$, $n=0$, $k=0$):

$$\frac{dT_{000}(t)}{dt}=\frac{\alpha}{(z_2{-}z_1)}\left[\left.\frac{\partial T_{00}(t)}{\partial z}\right|_{z_2}-\left.\frac{\partial T_{00}(t)}{\partial z}\right|_{z_1}\right]. \tag{A.53}$$

When $m{\geq}1$, $n{=}0$, $k{=}0$:

$$\begin{aligned}I_1=\alpha\int_{x_1}^{x_2}\int_{y_1}^{y_2}\int_{z_1}^{z_2}\left(\frac{\partial^2T(x,y,z,t)}{\partial x^2}+\frac{\partial^2T(x,y,z,t)}{\partial y^2}+\frac{\partial^2T(x,y,z,t)}{\partial z^2}\right)\times\\ \cos\left(\frac{\pi m(x{-}x_1)}{(x_2{-}x_1)}\right)dxdydz\end{aligned} \tag{A.54}$$

$$I_1{=}I_{1x}{+}I_{1y}{+}I_{1z} \tag{A.55}$$

$$I_{1x} = \alpha \int_{z_1}^{z_2} \int_{y_1}^{y_2} \left[\int_{x_1}^{x_2} \frac{\partial^2 T(x,y,z,t)}{\partial x^2} \cos\left(\frac{\pi m (x - x_1)}{(x_2 - x_1)} \right) dx \right] dydz \tag{A.56}$$

Using the same approach as before:

$$I_{1x} = -\frac{\alpha \pi^2 m^2 (z_2 - z_1)(y_2 - y_1)}{2(x_2 - x_1)} T_{m00}(t). \tag{A.57}$$

$$I_{1y} = \alpha \int_{z_1}^{z_2} \int_{x_1}^{x_2} \left[\int_{y_1}^{y_2} \frac{\partial^2 T(x,y,z,t)}{\partial y^2} dy \right] \cos\left(\frac{\pi m (x - x_1)}{(x_2 - x_1)} \right) dydz, \tag{A.58}$$

$$I_{1y} = \alpha \int_{z_1}^{z_2} \int_{x_1}^{x_2} \left[\left. \frac{\partial T(x,z,t)}{\partial y} \right|_{y_2} - \left. \frac{\partial T(x,z,t)}{\partial y} \right|_{y_1} \right] \cos\left(\frac{\pi m (x - x_1)}{(x_2 - x_1)} \right) dxdz. \tag{A.59}$$

$\partial T(x,z,t)/\partial y|_{y_2} = 0$ and $\partial T(x,z,t)/\partial y|_{y_1} = 0$ and so:

$$I_{1y} = 0 \tag{A.60}$$

$$I_{1z} = \alpha \int_{x_1}^{x_2} \int_{y_1}^{y_2} \left[\int_{z_1}^{z_2} \frac{\partial^2 T(x,y,z,t)}{\partial z^2} dz \right] \cos\left(\frac{\pi m (x - x_1)}{(x_2 - x_1)} \right) dydx \tag{A.61}$$

$$I_{1z} = \alpha \int_{y_1}^{y_2} \int_{x_1}^{x_2} \left[\left. \frac{\partial T(x,y,t)}{\partial z} \right|_{z_2} - \left. \frac{\partial T(x,y,t)}{\partial z} \right|_{z_1} \right] \cos\left(\frac{\pi m (x - x_1)}{(x_2 - x_1)} \right) dxdy, \tag{A.62}$$

$$I_{1z} = \frac{\alpha(x_2-x_1)(y_2-y_1)}{2}\left[\left.\frac{dT_{m0}(t)}{dt}\right|_{z_2} - \left.\frac{dT_{m0}(t)}{dt}\right|_{z_1}\right]. \tag{A.63}$$

$$I_2 = \int_{x_1}^{x_2}\int_{y_1}^{y_2}\int_{z_1}^{z_2} \frac{\partial T(x,y,z,t)}{\partial t}\cos\left(\frac{\pi m(x-x_1)}{(x_2-x_1)}\right)dxdydz. \tag{A.64}$$

Using the Fourier definition:

$$I_2 = \frac{(z_2-z_1)(y_2-y_1)(x_2-x_1)}{2}\frac{dT_{m00}(t)}{dt} \tag{A.65}$$

Equating I_1 and I_2 yields:

$$-\frac{\alpha\pi^2 m^2(z_2-z_1)(y_2-y_1)}{2(x_2-x_1)}T_{m00}(t) + \frac{\alpha(x_2-x_1)(y_2-y_1)}{2}\left[\left.\frac{dT_{m0}(t)}{dt}\right|_{z_2} - \left.\frac{dT_{m0}(t)}{dt}\right|_{z_1}\right] \tag{A.66}$$
$$= 0 + \frac{(z_2-z_1)(y_2-y_1)(x_2-x_1)}{2}\frac{dT_{m00}(t)}{dt}.$$

This results in the following ODE (for $m = 1$,$n = 0$,$k = 0$):

$$\frac{dT_{m00}(t)}{dt} = \frac{\alpha}{(z_2-z_1)}\left[\left.\frac{dT_{m0}(t)}{dt}\right|_{z_2} - \left.\frac{dT_{m0}(t)}{dt}\right|_{z_1}\right] - T_{m00}(t)\left[\alpha\pi^2\left(\frac{m^2}{(x_2-x_1)}\right)\right]. \tag{A.67}$$

When *m=0, n≥1, k=0*:

$$I_1 = \alpha\int_{x_1}^{x_2}\int_{y_1}^{y_2}\int_{z_1}^{z_2}\left(\frac{\partial^2 T(x,y,z,t)}{\partial x^2} + \frac{\partial^2 T(x,y,z,t)}{\partial y^2} + \frac{\partial^2 T(x,y,z,t)}{\partial z^2}\right)\times \tag{A.68}$$
$$\cos\left(\frac{\pi n(y-y_1)}{(y_2-y_1)}\right)dxdydz$$

$$I_1{=}I_{1x}{+}I_{1y}{+}I_{1z} \tag{A.69}$$

$$I_{1x} = \alpha \int_{z_1}^{z_2}\int_{y_1}^{y_2}\left[\int_{x_1}^{x_2}\frac{\partial^2 T(x,y,z,t)}{\partial x^2}dx\right]\cos\left(\frac{\pi n(y{-}y_1)}{(y_2{-}y_1)}\right)dydz. \tag{A.70}$$

$$I_{1x} = \alpha \int_{z_1}^{z_2}\int_{y_1}^{y_2}\left[\left.\frac{\partial T(y,z,t)}{\partial x}\right|_{x_2} - \left.\frac{\partial T(y,z,t)}{\partial x}\right|_{x_1}\right]\cos\left(\frac{\pi n(y{-}y_1)}{(y_2{-}y_1)}\right)dydz. \tag{A.71}$$

$\partial T(x,z,t)/\partial x\big|_{x_2} = 0$ and $\partial T(x,z,t)/\partial x\big|_{x_1} = 0$ and so:

$$I_{1x} = 0. \tag{A.72}$$

$$I_{1y} = \alpha \int_{z_1}^{z_2}\int_{x_1}^{x_2}\left[\int_{y_1}^{y_2}\frac{\partial^2 T(x,y,z,t)}{\partial y^2}\cos\left(\frac{\pi n(y{-}y_1)}{(y_2{-}y_1)}\right)dy\right]dxdz. \tag{A.73}$$

Using the same approach as before:

$$I_{1y} = -\frac{\alpha\pi^2 n^2(z_2{-}z_1)(x_2{-}x_1)}{2(y_2{-}y_1)}T_{0n0}(t). \tag{A.74}$$

$$I_{1z} = \alpha \int_{x_1}^{x_2}\int_{y_1}^{y_2}\left[\int_{z_1}^{z_2}\frac{\partial^2 T(x,y,z,t)}{\partial z^2}dz\right]\cos\left(\frac{\pi n(y{-}y_1)}{(y_2{-}y_1)}\right)dydx, \tag{A.75}$$

$$I_{1z} = \frac{\alpha(x_2{-}x_1)(y_2{-}y_1)}{2}\left[\left.\frac{dT_{0n}(t)}{dt}\right|_{z_2} - \left.\frac{dT_{0n}(t)}{dt}\right|_{z_1}\right]. \tag{A.76}$$

$$I_2 = \int_{x_1}^{x_2}\int_{y_1}^{y_2}\int_{z_1}^{z_2} \frac{\partial T(x,y,z,t)}{\partial t} \cos\left(\frac{\pi n(y-y_1)}{(y_2-y_1)}\right) dxdydz. \tag{A.77}$$

From the relationship:

$$\int_{x_1}^{x_2}\int_{y_1}^{y_2}\int_{z_1}^{z_2} \frac{\partial T(x,y,z,t)}{\partial t} \cos\left(\frac{\pi n(y-y_1)}{(y_2-y_1)}\right) dxdydz = \frac{(z_2-z_1)(y_2-y_1)(x_2-x_1)}{2} \frac{dT_{0n0}(t)}{dt} \tag{A.78}$$

$$I_2 = \frac{(z_2-z_1)(y_2-y_1)(x_2-x_1)}{2} \frac{dT_{0n0}(t)}{dt}. \tag{A.79}$$

Equating I_1 and I_2:

$$-\frac{\alpha\pi^2 n^2 (z_2-z_1)(x_2-x_1)}{2(y_2-y_1)} T_{0n0}(t) + \frac{\alpha(x_2-x_1)(y_2-y_1)}{2}\left[\left.\frac{dT_{0n}(t)}{dt}\right|_{z_2} - \left.\frac{dT_{0n}(t)}{dt}\right|_{z_1}\right] = 0 + \frac{(z_2-z_1)(y_2-y_1)(x_2-x_1)}{2}\frac{dT_{0n0}(t)}{dt} \tag{A.80}$$

This results in the following ODE (for $m = 0$, $n = 1$, $k = 0$):

$$\frac{dT_{0n0}(t)}{dt} = \frac{\alpha}{(z_2-z_1)}\left[\left.\frac{dT_{0n}(t)}{dt}\right|_{z_2} - \left.\frac{dT_{0n}(t)}{dt}\right|_{z_1}\right] - T_{0n0}(t)\left[\alpha\pi^2\left(\frac{n^2}{(y_2-y_1)}\right)\right] \tag{A.81}$$

When *m=0, n=0, k≥1*:

$$I_1 = \alpha \int_{x_1}^{x_2}\int_{y_1}^{y_2}\int_{z_1}^{z_2} \left(\frac{\partial^2 T(x,y,z,t)}{\partial x^2} + \frac{\partial^2 T(x,y,z,t)}{\partial y^2} + \frac{\partial^2 T(x,y,z,t)}{\partial z^2}\right) \times \tag{A.82}$$

$$\cos\left(\frac{\pi k(z-z_1)}{(z_2-z_1)}\right) dxdydz. \tag{A.83}$$

$$I_1{=}I_{1x}{+}I_{1y}{+}I_{1z}. \tag{A.84}$$

$$I_{1x} = \alpha \int_{z_1}^{z_2}\int_{y_1}^{y_2}\left[\int_{x_1}^{x_2}\frac{\partial^2 T(x,y,z,t)}{\partial x^2}dx\right]\cos\left(\frac{\pi k(z{-}z_1)}{(z_2{-}z_1)}\right)dydz, \tag{A.85}$$

$$I_{1x} = \alpha \int_{z_1}^{z_2}\int_{y_1}^{y_2}\left[\left.\frac{\partial T(y,z,t)}{\partial x}\right|_{x_2} - \left.\frac{\partial T(y,z,t)}{\partial x}\right|_{x_1}\right]\cos\left(\frac{\pi k(z{-}z_1)}{(z_2{-}z_1)}\right)dydz \tag{A.86}$$

$\partial T(y,z,t)/\partial x\big|_{x_2} = 0$ and $\partial T(y,z,t)/\partial x\big|_{x_1} = 0$ and so:

$$I_{1x} = 0. \tag{A.87}$$

$$I_{1y} = \alpha \int_{z_1}^{z_2}\int_{x_1}^{x_2}\left[\int_{y_1}^{y_2}\frac{\partial^2 T(x,y,z,t)}{\partial y^2}dy\right]\cos\left(\frac{\pi k(z{-}z_1)}{(z_2{-}z_1)}\right)dxdz \tag{A.88}$$

Due to the insulated sides:

$$I_{1y} = 0. \tag{A.89}$$

$$I_{1z} = \alpha \int_{x_1}^{x_2}\int_{y_1}^{y_2}\left[\int_{z_1}^{z_2}\frac{\partial^2 T(x,y,z,t)}{\partial z^2}\cos\left(\frac{\pi k(z{-}z_1)}{(z_2{-}z_1)}\right)dz\right]dydx. \tag{A.90}$$

$$I_{1z} \;=\; \int_{y_1}^{y_2}\int_{x_1}^{x_2}(-1)^k\left(\left.\frac{\partial T(x,y,t)}{\partial z}\right|_{z_2}\right)dxdy - \int_{y_1}^{y_2}\int_{x_1}^{x_2}\left(\left.\frac{\partial T(x,y,t)}{\partial z}\right|_{z_1}\right)dxdy$$

$$-\frac{\alpha\pi^2k^2}{(z_2-z_1)^2}\int_{z_1}^{z_2}\int_{y_1}^{y_2}\int_{x_1}^{x_2}T(x,y,z,t)\cos\left(\frac{\pi k(z-z_1)}{(z_2-z_1)}\right)dzdxdy. \tag{A.91}$$

Using the following relationships:

$$\int_{y_1}^{y_2}\int_{x_1}^{x_2}\left.\frac{\partial T(x,y,t)}{\partial t}\right|_z dxdy=\frac{(x_2-x_1)(y_2-y_1)}{1}\left.\frac{dT_{mn}(t)}{dt}\right|_z, \tag{A.92}$$

$$\int_{x_1}^{x_2}\int_{y_1}^{y_2}\int_{z_1}^{z_2}T(x,y,z,t)\cos\left(\frac{\pi k(z-z_1)}{(z_2-z_1)}\right)dxdydz=\frac{(z_2-z_1)(y_2-y_1)(x_2-x_1)}{2}T_{00k}(t), \tag{A.93}$$

$$\begin{aligned}I_{1z}=\frac{(x_2-x_1)(y_2-y_1)}{1}(-1)^k\left.\frac{dT_{00}(t)}{dt}\right|_{z_2}-\frac{(x_2-x_1)(y_2-y_1)}{1}(-1)^k\left.\frac{dT_{00}(t)}{dt}\right|_{z_1}\\-\frac{\alpha\pi^2k^2}{(z_2-z_1)^2}\frac{(z_2-z_1)(y_2-y_1)(x_2-x_1)}{2}T_{00k}(t).\end{aligned} \tag{A.94}$$

$$I_2=\int_{x_1}^{x_2}\int_{y_1}^{y_2}\int_{z_1}^{z_2}\frac{\partial T(x,y,z,t)}{\partial t}\cos\left(\frac{\pi k(z-z_1)}{(z_2-z_1)}\right)dxdydz. \tag{A.95}$$

Use the relationship:

$$\int_{x_1}^{x_2}\int_{y_1}^{y_2}\int_{z_1}^{z_2}\frac{\partial T(x,y,z,t)}{\partial t}\cos\left(\frac{\pi k(z-z_1)}{(z_2-z_1)}\right)dzdxdy=\frac{(z_2-z_1)(y_2-y_1)(x_2-x_1)}{2}\frac{dT_{00k}(t)}{dt}, \tag{A.96}$$

$$I_2=\frac{(z_2-z_1)(y_2-y_1)(x_2-x_1)}{2}\frac{dT_{00k}(t)}{dt}. \tag{A.97}$$

Equating I_1 and I_2:

$$\frac{(x_2-x_1)(y_2-y_1)}{1}(-1)^k\left.\frac{dT_{00}(t)}{dt}\right|_{z_2}-\frac{(x_2-x_1)(y_2-y_1)}{1}\left.\frac{dT_{00}(t)}{dt}\right|_{z_2}+0$$
$$-\frac{\alpha\pi^2k^2}{(z_2-z_1)^2}\frac{(z_2-z_1)(y_2-y_1)(x_2-x_1)}{2}T_{00k}(t)=\frac{(z_2-z_1)(y_2-y_1)(x_2-x_1)}{2}\frac{dT_{00k}(t)}{dt}. \quad (A.98)$$

This results in the following ODE (for $m=0$, $n=0$, $k=1$):

$$\frac{dT_{00k}(t)}{dt}=\frac{2}{(z_2-z_1)}\left[(-1)^k\left.\frac{dT_{00}(t)}{dt}\right|_{z_2}-\left.\frac{dT_{00}(t)}{dt}\right|_{z_2}\right]-T_{00k}(t)\left[\alpha\pi^2\left(\frac{k^2}{(z_2-z_1)^2}\right)\right] \quad (A.99)$$

When $m\geq 1$,$n\geq 1$, $k\geq 0$):

$$I_1=\alpha\int_{x_1}^{x_2}\int_{y_1}^{y_2}\int_{z_1}^{z_2}\left(\frac{\partial^2T(x,y,z,t)}{\partial x^2}+\frac{\partial^2T(x,y,z,t)}{\partial y^2}+\frac{\partial^2T(x,y,z,t)}{\partial z^2}\right)$$
$$\cos\left(\frac{\pi m(x-x_1)}{(x_2-x_1)}\right)\cos\left(\frac{\pi n(y-y_1)}{(y_2-y_1)}\right)dxdydz. \quad (A.100)$$

$$I_1=I_{1x}+I_{1y}+I_{1z}. \quad (A.101)$$

$$I_{1x}=\alpha\int_{z_1}^{z_2}\int_{y_1}^{y_2}\left[\int_{x_1}^{x_2}\frac{\partial^2T(x,y,z,t)}{\partial x^2}\cos\left(\frac{\pi m(x-x_1)}{(x_2-x_1)}\right)dx\right]\cos\left(\frac{\pi n(y-y_1)}{(y_2-y_1)}\right)dydz \quad (A.102)$$

Using integration by parts:

$$\int_{x_1}^{x_2}\frac{\partial^2T(x,y,z,t)}{\partial x^2}\cos\left(\frac{\pi m(x-x_1)}{(x_2-x_1)}\right)dx=\left[\cos(\pi m)\left(\left.\frac{\partial T(y,z,t)}{\partial x}\right|_{x_2}\right)-\left(\left.\frac{\partial T(y,z,t)}{\partial x}\right|_{x_1}\right)\right]$$

$$+\frac{\pi m}{(x_2-x_1)}\int_{x_1}^{x_2}\left(\frac{\partial T(x,y,z,t)}{\partial x}\right)\sin\left(\frac{\pi m(x-x_1)}{(x_2-x_1)}\right)dx$$

$\partial T(y,z,t)/\partial x\big|_{x_2}=0$ and $\partial T(y,z,t)/\partial x\big|_{x_1}=0$ and so:

$$I_{1x}=-\frac{\alpha\pi^2m^2}{(x_2-x_1)^2}\int_{z_1}^{z_2}\int_{y_1}^{y_2}\int_{x_1}^{x_2}T(x,y,z,t)\cos\left(\frac{\pi m(x-x_1)}{(x_2-x_1)}\right)\cos\left(\frac{\pi n(y-y_1)}{(y_2-y_1)}\right)dxdydz \quad \text{(A.103)}$$

Resulting in:

$$I_{1x}=-\frac{\alpha\pi^2m^2(y_2-y_1)(z_2-z_1)}{4(x_2-x_1)}T_{mn0}(t), \quad \text{(A.104)}$$

Now use the same method for I_{1y}:

$$I_{1y}=\alpha\int_{z_1}^{z_2}\int_{x_1}^{x_2}\left[\int_{y_1}^{y_2}\frac{\partial^2T(x,y,z,t)}{\partial y^2}\cos\left(\frac{\pi n(y-y_1)}{(y_2-y_1)}\right)dy\right]\cos\left(\frac{\pi m(x-x_1)}{(x_2-x_1)}\right)dxdz \quad \text{(A.105)}$$

Here $\partial T(x,z,t)/\partial y\big|_{y_2}=0$ and $\partial T(x,z,t)/\partial y\big|_{y_1}=0$. and so we get the following expression by applying the same method as for I_{1x}

$$I_{1y}=-\frac{\alpha\pi^2n^2(x_2-x_1)(z_2-z_1)}{4(y_2-y_1)}T_{mn0}(t). \quad \text{(A.106)}$$

Now for I_{1z}:

$$I_{1z}=\alpha\int_{y_1}^{y_2}\int_{x_1}^{x_2}\left[\int_{z_1}^{z_2}\frac{\partial^2T(x,y,z,t)}{\partial z^2}dz\right]\cos\left(\frac{\pi m(x-x_1)}{(x_2-x_1)}\right)\cos\left(\frac{\pi n(y-y_1)}{(y_2-y_1)}\right)dydx. \quad \text{(A.107)}$$

In Fourier form this becomes:

$$I_{1z} = \frac{\alpha(x_2-x_1)(y_2-y_1)}{4}\left[\left.\frac{dT_{mn}(t)}{dt}\right|_{z_2} - \left.\frac{dT_{mn}(t)}{dt}\right|_{z_1}\right]. \tag{A.108}$$

Therefore:

$$\begin{aligned} I_1 = {} & \frac{(x_2-x_1)(y_2-y_1)}{4}\left.\frac{\partial T_{mn}(t)}{\partial z}\right|_{z_2} - \frac{(x_2-x_1)(y_2-y_1)}{4}\left.\frac{\partial T_{mn}(t)}{\partial z}\right|_{z_1} \\ & -\frac{\alpha\pi^2 n^2(x_2-\mathrm{x}_1)(z_2-z_1)}{4(y_2-y_1)}T_{mn0}(t) - \frac{\alpha\pi^2 m^2(y_2-y_1)(z_2-z_1)}{4(x_2-x_1)}T_{mn0}(t) \end{aligned} \tag{A.109}$$

$$I_2 = \int_{x_1}^{x_2}\int_{y_1}^{y_2}\int_{z_1}^{z_2}\frac{\partial T(x,y,z,t)}{\partial t}\cos\left(\frac{\pi m(x-x_1)}{(x_2-x_1)}\right)\cos\left(\frac{\pi n(y-y_1)}{(y_2-y_1)}\right)dxdydz \tag{A.110}$$

Successive substitution produces:

$$\begin{aligned} & \frac{(x_2-x_1)(y_2-y_1)}{4}\left.\frac{\partial T_{mn}(t)}{\partial z}\right|_{z_2} - \frac{(x_2-x_1)(y_2-y_1)}{4}\left.\frac{\partial T_{mn}(t)}{\partial z}\right|_{z_1} \\ & -\frac{\alpha\pi^2 n^2(x_2-\mathrm{x}_1)(z_2-z_1)}{4(y_2-\mathrm{y}_1)}T_{mn0}(t) - \frac{\alpha\pi^2 m^2(y_2-y_1)(z_2-z_1)}{4(x_2-x_1)}T_{mn0}(t) \\ & = 0 + \frac{(x_2-x_1)(y_2-y_1)(z_2-z_1)}{4}\frac{dT_{mn0}(t)}{dt}. \end{aligned} \tag{A.111}$$

This brings us to the following ordinary differential equation $m\geq 1, n\geq 1, k\geq 0$:

$$\frac{dT_{mn0}(t)}{dt} = \frac{\alpha}{(z_2-z_1)}\left[\left.\frac{\partial T_{mn}(t)}{\partial z}\right|_{z_2} - \left.\frac{\partial T_{mn}(t)}{\partial z}\right|_{z_1}\right] - T_{mn0}(t)\left[\alpha\pi^2\left(\frac{m^2}{(x_2-x_1)^2} + \frac{n^2}{(y_2-\mathrm{y}_1)^2}\right)\right] \tag{A.112}$$

When $m \geq 1, n=0, k \geq 1$:

$$I_1 = \alpha \int_{x_1}^{x_2}\int_{y_1}^{y_2}\int_{z_1}^{z_2} \left(\frac{\partial^2 T(x,y,z,t)}{\partial x^2} + \frac{\partial^2 T(x,y,z,t)}{\partial y^2} + \frac{\partial^2 T(x,y,z,t)}{\partial z^2} \right) \cos\left(\frac{\pi m(x-x_1)}{(x_2-x_1)}\right) \cos\left(\frac{\pi k(z-z_1)}{(z_2-z_1)}\right) dxdydz. \tag{A.113}$$

$$I_1 = I_{1x} + I_{1y} + I_{1z}. \tag{A.114}$$

$$I_{1x} = \alpha \int_{z_1}^{z_2}\int_{y_1}^{y_2} \left[\int_{x_1}^{x_2} \frac{\partial^2 T(x,y,z,t)}{\partial x^2} \cos\left(\frac{\pi m(x-x_1)}{(x_2-x_1)}\right) dx \right] \cos\left(\frac{\pi k(z-z_1)}{(z_2-z_1)}\right) dydz. \tag{A.115}$$

Using the same approach as before:

$$I_{1x} = -\frac{\alpha \pi^2 m^2 (z_2-z_1)(y_2-y_1)}{4(x_2-x_1)} T_{m0k}.(t) \tag{A.116}$$

$$I_{1y} = \alpha \int_{z_1}^{z_2}\int_{x_1}^{x_2} \left[\int_{y_1}^{y_2} \frac{\partial^2 T(x,y,z,t)}{\partial y^2} dy \right] \cos\left(\frac{\pi m(x-x_1)}{(x_2-x_1)}\right) \cos\left(\frac{\pi k(z-z_1)}{(z_2-z_1)}\right) dxdz \tag{A.117}$$

$\partial T(x,z,t)/\partial y\big|_{y_2} = 0$ and $\partial T(x,z,t)/\partial y\big|_{y_1} = 0$ and so:

$$I_{1y} = 0. \tag{A.118}$$

$$I_{1z} = \alpha \int_{x_1}^{x_2}\int_{y_1}^{y_2} \left[\int_{z_1}^{z_2} \frac{\partial^2 T(x,y,z,t)}{\partial z^2} \cos\left(\frac{\pi k(z-z_1)}{(z_2-z_1)}\right) dz \right] \cos\left(\frac{\pi m(x-x_1)}{(x_2-x_1)}\right) dydx. \tag{A.119}$$

$$I_{1z} = \int_{y_1}^{y_2}\int_{x_1}^{x_2}\left[\left.\frac{\partial T(x,y,t)}{\partial z}\right|_{z_2}(-1)^k - \left.\frac{\partial T(x,y,t)}{\partial z}\right|_{z_1}\right]\cos\left(\frac{\pi m(x-x_1)}{(x_2-x_1)}\right)dxdy$$
$$-\frac{\alpha\pi^2k^2}{(z_2-z_1)^2}\int_{z_1}^{z_2}\int_{y_1}^{y_2}\int_{x_1}^{x_2}T(x,y,z,t)\cos\left(\frac{\pi m(x-x_1)}{(x_2-x_1)}\right)\cos\left(\frac{\pi k(z-z_1)}{(z_2-z_1)}\right)dzdxdy. \quad \text{(A.120)}$$

$$I_{1z} = \frac{\alpha(x_2-x_1)(y_2-y_1)}{2}\left[\left.\frac{dT_{m0}(t)}{dt}\right|_{z_2}(-1)^k - \left.\frac{dT_{m0}(t)}{dt}\right|_{z_1}\right] \quad \text{(A.121)}$$
$$-\frac{\alpha\pi^2k^2(x_2-x_1)(y_2-y_1)}{4(z_2-z_1)}T_{m0k}(t) \quad \text{(A.122)}$$
$$\text{(A.123)}$$

$$I_2 = \int_{x_1}^{x_2}\int_{y_1}^{y_2}\int_{z_1}^{z_2}\frac{\partial T(x,y,z,t)}{\partial t}\cos\left(\frac{\pi m(x-x_1)}{(x_2-x_1)}\right)\cos\left(\frac{\pi k(z-z_1)}{(z_2-z_1)}\right)dxdydz \quad \text{(A.124)}$$

$$I_2 = \frac{(z_2-z_1)(y_2-y_1)(x_2-x_1)}{4}\frac{dT_{m0k}(t)}{dt}, \quad \text{(A.125)}$$

Equating I_1 and I_2 leads to:

$$\frac{\alpha(x_2-x_1)(y_2-y_1)}{2}\left[\left.\frac{dT_{m0}(t)}{dt}\right|_{z_2}(-1)^k - \left.\frac{dT_{m0}(t)}{dt}\right|_{z_1}\right] - \frac{\alpha\pi^2k^2(x_2-x_1)(y_2-y_1)}{4(z_2-z_1)}T_{m0k}(t)$$
$$-\frac{\alpha\pi^2m^2(z_2-z_1)(y_2-y_1)}{4(x_2-x_1)}T_{m0k}(t) = 0 + \frac{(z_2-z_1)(y_2-y_1)(x_2-x_1)}{4}\frac{dT_{m0k}(t)}{dt} \quad \text{(A.126)}$$

This results in the following ODE (for $m = 1$, $n = 0$, $k = 1$):

$$\frac{dT_{m0k}(t)}{dt} = \frac{2\alpha}{(z_2-z_1)}\left[\left.\frac{dT_{m0}(t)}{dt}\right|_{z_2}(-1)^k - \left.\frac{dT_{m0}(t)}{dt}\right|_{z_1}\right] - T_{m0k}(t)\left[\alpha\pi^2\left(\frac{m^2}{(x_2-x_1)^2}+\frac{k^2}{(z_2-z_1)^2}\right)\right] \tag{A.127}$$

When *m=0, n≥1, k≥1* :

$$I_1 = \alpha\int_{x_1}^{x_2}\int_{y_1}^{y_2}\int_{z_1}^{z_2}\left(\frac{\partial^2 T(x,y,z,t)}{\partial x^2}+\frac{\partial^2 T(x,y,z,t)}{\partial y^2}+\frac{\partial^2 T(x,y,z,t)}{\partial z^2}\right) \cos\left(\frac{\pi n(y-y_1)}{(y_2-y_1)}\right)\cos\left(\frac{\pi k(z-z_1)}{(z_2-z_1)}\right)dxdydz \tag{A.128}$$

$$I_1 = I_{1x}+I_{1y}+I_{1z} \tag{A.129}$$

$$I_{1x} = \alpha\int_{z_1}^{z_2}\int_{y_1}^{y_2}\left[\int_{x_1}^{x_2}\frac{\partial^2 T(x,y,z,t)}{\partial x^2}dx\right]\cos\left(\frac{\pi n(y-y_1)}{(y_2-y_1)}\right)\cos\left(\frac{\pi k(z-z_1)}{(z_2-z_1)}\right)dydz \tag{A.130}$$

Due to insulation on the sides of the block:

$$I_{1x} = 0. \tag{A.131}$$

$$I_{1y} = \alpha\int_{z_1}^{z_2}\int_{x_1}^{x_2}\left[\int_{y_1}^{y_2}\frac{\partial^2 T(x,y,z,t)}{\partial y^2}\cos\left(\frac{\pi n(y-y_1)}{(y_2-y_1)}\right)dy\right]\cos\left(\frac{\pi k(z-z_1)}{(z_2-z_1)}\right)dxdz \tag{A.132}$$

$$I_{1y} = -\frac{\alpha\pi^2 n^2}{(y_2-y_1)^2}\int_{z_1}^{z_2}\int_{y_1}^{y_2}\int_{x_1}^{x_2} T(x,y,z,t)\cos\left(\frac{\pi n(y-y_1)}{(y_2-y_1)}\right)\cos\left(\frac{\pi k(z-z_1)}{(z_2-z_1)}\right)dxdydz \quad \text{(A.133)}$$

Using similar procedures to earlier:

$$I_{1y} = -\frac{\alpha\pi^2 n^2(z_2-z_1)(x_2-x_1)}{4(y_2-y_1)}T_{0nk}(t). \quad \text{(A.134)}$$

$$I_{1z} = \alpha\int_{x_1}^{x_2}\int_{y_1}^{y_2}\left[\int_{z_1}^{z_2}\frac{\partial^2 T(x,y,z,t)}{\partial z^2}\cos\left(\frac{\pi k(z-z_1)}{(z_2-z_1)}\right)dz\right]\cos\left(\frac{\pi n(y-y_1)}{(y_2-y_1)}\right)dydx, \quad \text{(A.135)}$$

$$I_{1z} = \int_{y_1}^{y_2}\int_{x_1}^{x_2}\left[\left.\frac{\partial T(x,y,t)}{\partial z}\right|_{z_2}(-1)^k - \left.\frac{\partial T(x,y,t)}{\partial z}\right|_{z_1}\right]\cos\left(\frac{\pi n(y-y_1)}{(y_2-y_1)}\right)dxdy$$
$$-\frac{\alpha\pi^2 k^2}{(z_2-z_1)^2}\int_{z_1}^{z_2}\int_{y_1}^{y_2}\int_{x_1}^{x_2} T(x,y,z,t)\cos\left(\frac{\pi n(y-y_1)}{(y_2-y_1)}\right)\cos\left(\frac{\pi k(z-z_1)}{(z_2-z_1)}\right)dzdxdy, \quad \text{(A.136)}$$

$$I_{1z} = \frac{\alpha(x_2-x_1)(y_2-y_1)}{2}\left[\left.\frac{dT_{0n}(t)}{dt}\right|_{z_2}(-1)^k - \left.\frac{dT_{0n}(t)}{dt}\right|_{z_1}\right] \quad \text{(A.137)}$$
$$- \frac{\alpha\pi^2 k^2(x_2-x_1)(y_2-y_1)}{4(z_2-z_1)}T_{0nk}(t). \quad \text{(A.138)}$$

$$I_2 = \int_{x_1}^{x_2}\int_{y_1}^{y_2}\int_{z_1}^{z_2}\frac{\partial T(x,y,z,t)}{\partial t}\cos\left(\frac{\pi m(x-x_1)}{(x_2-x_1)}\right)\cos\left(\frac{\pi n(y-y_1)}{(y_2-y_1)}\right)dxdydz \quad \text{(A.139)}$$

$$I_2 = \frac{(z_2-z_1)(y_2-y_1)(x_2-x_1)}{4}\frac{dT_{0nk}(t)}{dt} \tag{A.140}$$

Equating I_1 and I_2 yields:

$$\frac{\alpha(x_2-x_1)(y_2-y_1)}{2}\left[\left.\frac{dT_{0n}(t)}{dt}\right|_{z_2}(-1)^k - \left.\frac{dT_{0n}(t)}{dt}\right|_{z_1}\right] - \frac{\alpha\pi^2k^2(x_2-x_1)(y_2-y_1)}{4(z_2-z_1)}T_{0nk}(t)$$
$$-\frac{\alpha\pi^2n^2(z_2-z_1)(x_2-x_1)}{4(y_2-y_1)}T_{0nk}(t) = 0 + \frac{(z_2-z_1)(y_2-y_1)(x_2-x_1)}{4}\frac{dT_{0nk}(t)}{dt} \tag{A.141}$$

This results in the following ODE (for $m = 0$,$n = 1$,$k = 1$):

$$\frac{dT_{0nk}(t)}{dt} = \frac{2\alpha}{(z_2-z_1)}\left[\left.\frac{dT_{0n}(t)}{dt}\right|_{z_2}(-1)^k - \left.\frac{dT_{0n}(t)}{dt}\right|_{z_1}\right] - T_{0nk}(t)\left[\alpha\pi^2\left(\frac{n^2}{(y_2-y_1)^2} + \frac{k^2}{(z_2-z_1)^2}\right)\right]. \tag{A.142}$$

Appendix

B Appendix 2 - Fourier to space conversion for 3-D implementation

This chapter looks at the creation of the conversion matrices featured in section 5.2.3.2. The conversion matrices convert data from the Fourier domain to the spatial domain. In order to use MATLAB/Simulink, 3-D conversion matrices are implemented in 2-D form.

B.1 Conversion in the z dimension only

Converting between the Fourier (m-n-k) domain and the spatial (x-y-z) domain is achieved using the Fourier cosine series geometrical expansion of the 3-D heat equation which is given below:

$$T(x,y,z) \sim \sum_{m=0}^{\infty}\sum_{n=0}^{\infty}\sum_{k=0}^{\infty} T_{mnk}\cos\left(\frac{\pi m(x-x_1)}{(x_2-x_1)}\right)\cos\left(\frac{\pi n(y-y_1)}{(y_2-y_1)}\right)\cos\left(\frac{\pi k(z-z_1)}{(z_2-z_1)}\right), \qquad \text{(B.1)}$$

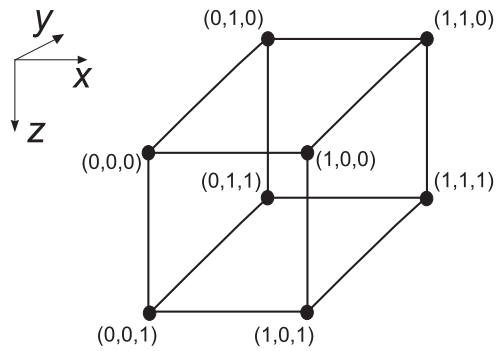

Figure B.1: Cube labelled with x-y-z co-ordinates.

Using Equation (B.1), the eight co-ordinates in the x-y-z space shown in Fig.B.1 may be defined as follows:

$$
\begin{aligned}
T(0,0,0) = {} & T_{000}\cos(0)\cos(0)\cos(0) \\
& + T_{001}\cos(0)\cos(0)\cos(0) \\
& + T_{010}\cos(0)\cos(0)\cos(0) \\
& + T_{011}\cos(0)\cos(0)\cos(0) \\
& + T_{100}\cos(0)\cos(0)\cos(0) \\
& + T_{101}\cos(0)\cos(0)\cos(0) \\
& + T_{110}\cos(0)\cos(0)\cos(0) \\
& + T_{111}\cos(0)\cos(0)\cos(0)
\end{aligned}
\qquad
\begin{aligned}
T(0,1,0) = {} & T_{000}\cos(0)\cos(\pi)\cos(0) \\
& + T_{001}\cos(0)\cos(\pi)\cos(0) \\
& + T_{010}\cos(0)\cos(\pi)\cos(0) \\
& + T_{011}\cos(0)\cos(\pi)\cos(0) \\
& + T_{100}\cos(0)\cos(0)\cos(0) \\
& + T_{101}\cos(0)\cos(0)\cos(0) \\
& + T_{110}\cos(0)\cos(\pi)\cos(0) \\
& + T_{111}\cos(0)\cos(\pi)\cos(0)
\end{aligned}
$$

$$
\begin{aligned}
T(0,0,1) = {} & T_{000}\cos(0)\cos(0)\cos(0) \\
& + T_{001}\cos(0)\cos(0)\cos(\pi) \\
& + T_{010}\cos(0)\cos(0)\cos(0) \\
& + T_{011}\cos(0)\cos(0)\cos(\pi) \\
& + T_{100}\cos(0)\cos(0)\cos(0) \\
& + T_{101}\cos(0)\cos(0)\cos(\pi) \\
& + T_{110}\cos(0)\cos(0)\cos(0) \\
& + T_{111}\cos(0)\cos(0)\cos(\pi)
\end{aligned}
\qquad
\begin{aligned}
T(0,1,1) = {} & T_{000}\cos(0)\cos(0)\cos(0) \\
& + T_{001}\cos(0)\cos(0)\cos(\pi) \\
& + T_{010}\cos(0)\cos(\pi)\cos(0) \\
& + T_{011}\cos(0)\cos(\pi)\cos(\pi) \\
& + T_{100}\cos(0)\cos(0)\cos(0) \\
& + T_{101}\cos(0)\cos(0)\cos(\pi) \\
& + T_{110}\cos(0)\cos(\pi)\cos(0) \\
& + T_{111}\cos(0)\cos(\pi)\cos(\pi)
\end{aligned}
$$

$$
\begin{aligned}
T(1,0,0) = {} & T_{000}\cos(0)\cos(0)\cos(0) \\
& + T_{001}\cos(0)\cos(0)\cos(0) \\
& + T_{010}\cos(0)\cos(0)\cos(0) \\
& + T_{011}\cos(0)\cos(0)\cos(0) \\
& + T_{100}\cos(\pi)\cos(0)\cos(0) \\
& + T_{101}\cos(\pi)\cos(0)\cos(0) \\
& + T_{110}\cos(\pi)\cos(0)\cos(0) \\
& + T_{111}\cos(\pi)\cos(0)\cos(0)
\end{aligned}
\qquad
\begin{aligned}
T(1,1,0) = {} & T_{000}\cos(0)\cos(0)\cos(0) \\
& + T_{001}\cos(0)\cos(0)\cos(0) \\
& + T_{010}\cos(0)\cos(\pi)\cos(0) \\
& + T_{011}\cos(0)\cos(\pi)\cos(\pi) \\
& + T_{100}\cos(\pi)\cos(0)\cos(0) \\
& + T_{101}\cos(\pi)\cos(0)\cos(0) \\
& + T_{110}\cos(\pi)\cos(\pi)\cos(0) \\
& + T_{111}\cos(\pi)\cos(\pi)\cos(0)
\end{aligned}
$$

$$
\begin{aligned}
T(1,0,1) = \; & T_{000}\cos(0)\cos(0)\cos(0) \\
& + T_{001}\cos(0)\cos(0)\cos(\pi) \\
& + T_{010}\cos(0)\cos(0)\cos(0) \\
& + T_{011}\cos(0)\cos(0)\cos(\pi) \\
& + T_{100}\cos(\pi)\cos(0)\cos(0) \\
& + T_{101}\cos(\pi)\cos(0)\cos(\pi) \\
& + T_{110}\cos(\pi)\cos(0)\cos(0) \\
& + T_{111}\cos(\pi)\cos(0)\cos(\pi)
\end{aligned}
\qquad
\begin{aligned}
T(1,1,1) = \; & T_{000}\cos(0)\cos(0)\cos(0) \\
& + T_{001}\cos(0)\cos(0)\cos(\pi) \\
& + T_{010}\cos(0)\cos(\pi)\cos(0) \\
& + T_{011}\cos(0)\cos(\pi)\cos(\pi) \\
& + T_{100}\cos(\pi)\cos(0)\cos(0) \\
& + T_{101}\cos(\pi)\cos(0)\cos(\pi) \\
& + T_{110}\cos(\pi)\cos(\pi)\cos(0) \\
& + T_{111}\cos(\pi)\cos(\pi)\cos(\pi)
\end{aligned}
$$

Consider the situation depicted in Fig. B.2.

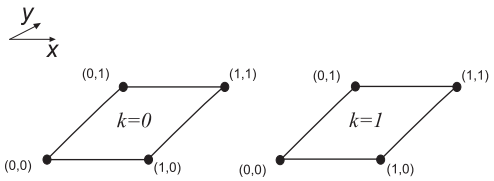

Figure B.2: x-y is in the space domain but z is in the Fourier domain

The Fourier cosine series geometrical expansion of the 2-D heat equation, with the z direction remaining in the Fourier domain, is given below:

$$T(x,y)_k \sum_{m=0}^{\infty}\sum_{n=0}^{\infty} T_{mnk}\cos\left(\frac{\pi m(x-x_1)}{(x_2-x_1)}\right)\cos\left(\frac{\pi n(y-y_1)}{(y_2-y_1)}\right), \tag{B.2}$$

Defining x-y co-ordinates, when k=0, gives:

$$
\begin{aligned}
T(0,0)_0 = \; & T_{000}\cos(0)\cos(0) \\
& + T_{010}\cos(0)\cos(0) \\
& + T_{100}\cos(0)\cos(0) \\
& + T_{110}\cos(0)\cos(0)
\end{aligned}
\qquad
\begin{aligned}
T(0,1)_0 = \; & T_{000}\cos(0)\cos(0) \\
& + T_{010}\cos(0)\cos(\pi) \\
& + T_{100}\cos(0)\cos(0) \\
& + T_{110}\cos(0)\cos(\pi)
\end{aligned}
$$

$$
\begin{aligned}
T(1,0)_0 = \; & T_{000}\cos(0)\cos(0) \\
& + T_{010}\cos(0)\cos(0) \\
& + T_{100}\cos(\pi)\cos(0) \\
& + T_{110}\cos(\pi)\cos(0)
\end{aligned}
\qquad
\begin{aligned}
T(1,1)_0 = \; & T_{000}\cos(0)\cos(0) \\
& + T_{010}\cos(0)\cos(\pi) \\
& + T_{100}\cos(\pi)\cos(0) \\
& + T_{110}\cos(\pi)\cos(\pi)
\end{aligned}
$$

Defining x-y co-ordinates, when k=1, gives:

$$
\begin{aligned}
T(0,0)_1 = \; & T_{001}\cos(0)\cos(0) \\
& + T_{011}\cos(0)\cos(0) \\
& + T_{101}\cos(0)\cos(0) \\
& + T_{111}\cos(0)\cos(0)
\end{aligned}
\qquad
\begin{aligned}
T(0,1)_1 = \; & T_{001}\cos(0)\cos(0) \\
& + T_{011}\cos(0)\cos(\pi) \\
& + T_{101}\cos(0)\cos(0) \\
& + T_{111}\cos(0)\cos(\pi)
\end{aligned}
$$

$$
\begin{aligned}
T(1,0)_1 = \; & T_{001}\cos(0)\cos(0) \\
& + T_{011}\cos(0)\cos(0) \\
& + T_{101}\cos(\pi)\cos(0) \\
& + T_{111}\cos(\pi)\cos(0)
\end{aligned}
\qquad
\begin{aligned}
T(1,1)_1 = \; & T_{001}\cos(0)\cos(0) \\
& + T_{011}\cos(0)\cos(\pi) \\
& + T_{101}\cos(\pi)\cos(0) \\
& + T_{111}\cos(\pi)\cos(\pi)
\end{aligned}
$$

All definitions featured so far in this chapter lead to the creation of the z conversion matrix shown in Fig. B.3, which converts from the Fourier domain to the spatial domain in the z direction only.

$$
\begin{bmatrix}
1 & 0 & 1 & 0 \\
0 & 1 & 0 & 1 \\
1 & 0 & -1 & 0 \\
0 & 1 & 0 & -1
\end{bmatrix}
*
\begin{bmatrix}
T(0,0)_0 & T(0,1)_0 \\
T(1,0)_0 & T(1,1)_0 \\
T(0,0)_1 & T(0,1)_1 \\
T(1,0)_1 & T(1,1)_1
\end{bmatrix}
=
\begin{bmatrix}
T(0,0,0) & T(0,1,0) \\
T(1,0,0) & T(1,1,0) \\
T(0,0,1) & T(0,1,1) \\
T(1,0,1) & T(1,1,1)
\end{bmatrix}
$$

z conversion matrix space(x,y) Fourier (k) space(x,y,z)

Figure B.3: The creation of the z conversion matrix.

Upon inspection, it is clear how to construct the z conversion matrix above. The z conversion matrix is a pre-multiplier. Identity matrices (with m-by-m dimensions) are present within another matrix. They appear within the conversion matrix as:

$$
\begin{bmatrix}
\begin{bmatrix} I \end{bmatrix} & \begin{bmatrix} I \end{bmatrix} \\
\begin{bmatrix} I \end{bmatrix} & \begin{bmatrix} -I \end{bmatrix}
\end{bmatrix}
$$

Figure B.4: Identity matrices within the z conversion matrix.

The pre-multiplying matrix does not affect the x co-ordinates thanks to the presence of the identity matrices. It is desirable to convert in the z direction only at this stage. The dimension of the square identity matrix I matches the number of Fourier terms (M=2) in the x dimension.

Each identity matrix 'I' is multiplied by the element it replaces in the conversion matrix which links $T(z)$ to T_k in the formula:

$$T(z) = \sum_{k=0}^{\infty} T_k \cos\left(\frac{k\pi\,(z - z_1)}{(z_2 - z_1)}\right), \tag{B.3}$$

where k represents each of the Fourier coefficients and the z terms are described as follows:

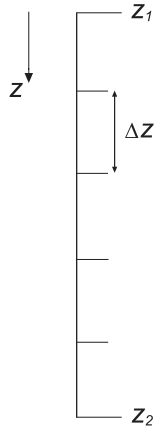

The following equation therefore holds true:

$$z - z_1 = num_z \Delta z = \frac{num_z(z_2 - z_1)}{N_z} \tag{B.4}$$

where num_z is the number of segments along the z dimension and N_z is the total number of segments.

This is how the expression in Equation (B.3) is implemented:

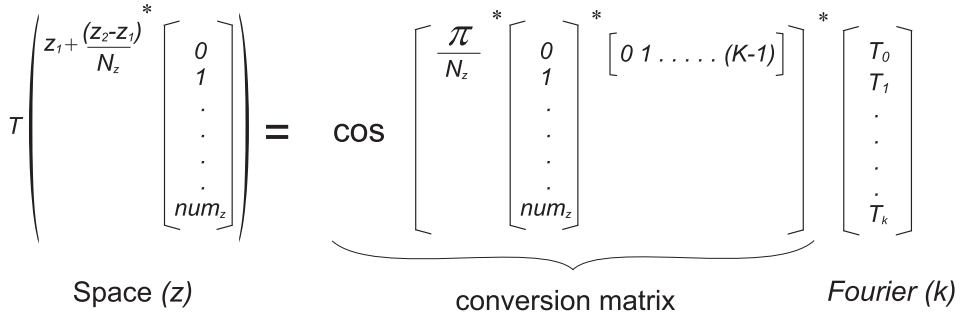

In this example $K = 2$, and so each I (M by M) identity matrix is multiplied by the element it replaces in the resulting z conversion matrix:

$$\begin{bmatrix} 1 & 1 \\ 1 & -1 \end{bmatrix}$$

Therefore a conversion matrix which converts from the Fourier to space in the z dimension only can be easily constructed for any positive integer value assigned to M and K.

B.2 Conversion in the x dimension only

In order to convert in the x direction a pre-multiplying conversion matrix is used. In this case, it is necessary to convert from the Fourier domain to the space domain in the x direction only. This means that the x conversion matrix must operate within each value of the Fourier coefficient k (k=0, k=1 ..) if it is to allow the z direction to remain in Fourier domain.

Looking closely, it is clear how to construct the x conversion matrix above for any value of M and K. Start with an identity matrix with dimensions (K by K). Each element is multiplied by and replaced with a mini conversion matrix.

The mini x conversion matrices come from the relationship between $T(x)$ and T_m in

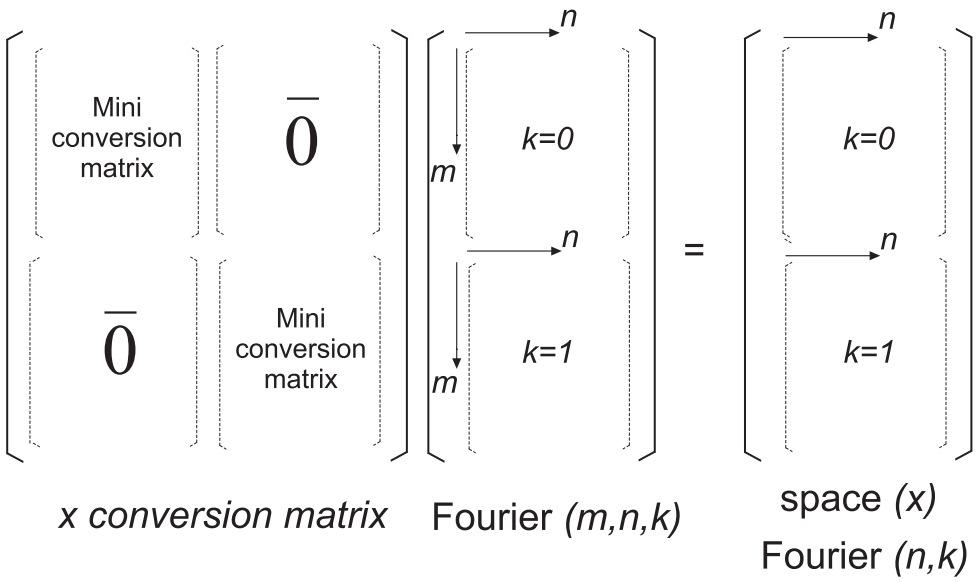

the formula:

$$T(x) = \sum_{k=0}^{\infty} T_m \cos\left(\frac{m\pi\,(x - x_1)}{(x_2 - x_1)}\right), \tag{B.5}$$

where m represents each of the Fourier coefficients and the x terms are described as follows:

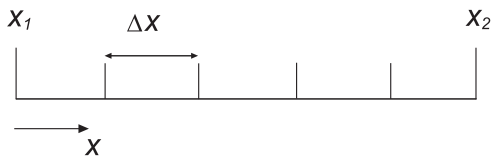

The following equation therefore holds true:

$$x - x_1 = num_x \Delta x = \frac{num_x(x_2 - x_1)}{N_x} \tag{B.6}$$

where num_x is the number of segments along the x dimension and N_x is the total number of segments.

This is how the expression in Equation (B.5) is implemented:

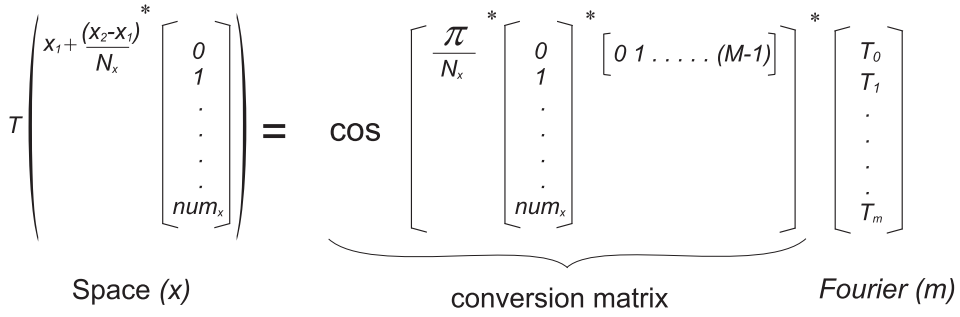

It is possible to convert in x dimension and z dimension at once with one premultiplying matrix which is x conversion matrix * z conversion matrix.

B.3 Conversion in the y dimension only

In order to convert from Fourier domain to space in the y dimension, matrix postmultiplication is required. The y conversion matrix has no baring on the x and z directions thanks to the vertical stacking of each k Fourier coefficient. The matrix postmultiplication appears like this:

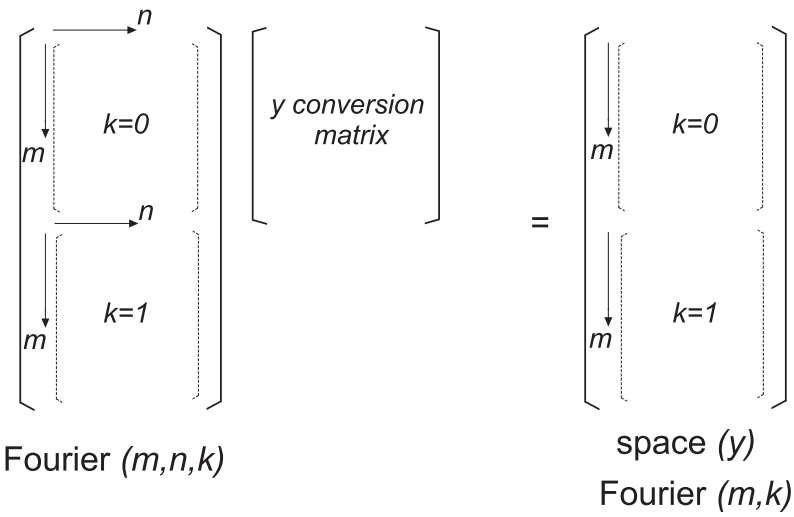

The y conversion post multiplying matrix describes the relationship between $T(y)$ and T_n in the following expression:

$$T(y) = \sum_{n=0}^{\infty} T_n \cos\left(\frac{n\pi\,(y - y_1)}{(y_2 - y_1)}\right), \tag{B.7}$$

Equation (B.7) is implemented as follows in order to create the y post multiplying conversion matrix:

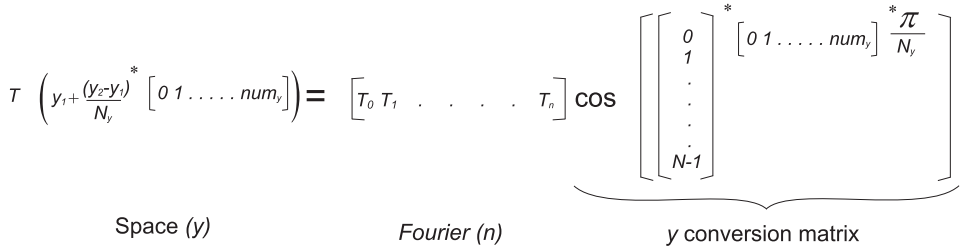

where num_y is the number of segments along the y dimension and N_y is the total number of segments. The y terms are determined in the same fashion as the x terms were.

Appendix

C List of Publications

Journal Publications

1. I.R. Swan, A.T. Bryant and P.A. Mawby, "Fast 3-D thermal simulation of power module packaging", *International Journal of Numerical Methods in Engineering*, vol. 1, pp. 1–25, 2010.

2. I.R. Swan, A. T. Bryant, P.A. Mawby, T. Ueta, T. Nishijima and K. Hamada, "A Fast Loss and Temperature Simulation Method for Power Converters, Part II: 3-D Thermal Model of Power Module", *Conference on Integrated Power Electronics System (CIPS)*, pp. 1–9, 2010.

3. A. T. Bryant, N.-A. Parker-Allotey, I.R. Swan, P.A. Mawby, T. Ueta, T. Nishijima and K. Hamada, "A Fast Loss and Temperature Simulation Method for Power Converters, Part I: Electro-thermal Modelling and Validation", *Conference on Integrated Power Electronics System (CIPS)*, vol. 1, pp. 1–8, 2010.

International Conference Publications

1. I.R. Swan, A.T. Bryant, N.-A. Parker-Allotey and P.A. Mawby, "3-D Thermal Simulation of Power Module Packaging", *IEEE Energy Congress and Conversion Exposition (ECCE)*, San Jose, California, USA, 2009.

2. I.R. Swan, A.T. Bryant and P.A. Mawby, "Fast Thermal Models for Power Device Packaging", *IEEE Industry Applications Society (IAS)*, Edmonton, Canada, 2008.